Characterisation of a Vascular Self-healing Cementitious Material System

Doctor of Philosophy Thesis

Tharmesh Selvarajoo

School of Engineering

Cardiff University

2020

To my parents,

for everything and more.

Summary

Over the last few decades, researchers have shown conclusively that is it possible to incorporate self-healing systems into concrete structures. Some of these are enhanced natural autogenic mechanisms, while others are based on autonomic (or engineered healing) techniques. One promising approach involves embedding channel networks in cementitious matrices as a delivery system for healing agents. These vascular healing systems have the advantage that they can be pressurised and provide a continuous supply of healing agent, which enables multiple cycles of damage to be healed. Although much experimental work had been undertaken on vascular systems for cementitious structural elements, the author found that there was not a complete characterisation study on any one system that was adequate for developing a comprehensive design or numerical model of the system. This provided the motivation for the work reported in the thesis, which involved an extensive experimental programme of work aimed at characterising the transport and mechanical behaviour of a cementitious vascular material system with cyanoacrylate as a healing agent.

The tests series undertaken included (i) three-point flexural bending tests on unreinforced notched prisms, in which the effects of varying the healing period, healing agent pressure and loading rate were explored; (ii) flexural tests on notched beams with an offset arrangement of discontinuous reinforcement that were undertaken to study healing behaviour when complex crack patterns occur; (iii) direct tension tests on notched cubes with different crack openings for a range of healing periods; (iv) dynamic healing-agent flow tests that investigated the variation of the capillary meniscus contact angle with velocity; (v) the sorption of healing agent into a concrete specimen through a natural crack surface; and (vi) tests in which healing-agent curing adjacent to a cementitious substrate was studied. A particular focus of the present work is simultaneous damage-healing behaviour and the various properties that influence the associated response. This requirement governed the range of loading rates (crack opening rates), healing agent pressures and fixed healing periods considered in the test series.

The test series successfully characterised the mechanical behaviour of the healing system for situations in which damage and healing are separated in time as well as for cases in which these processes overlap. In addition, the experimental programme provided data on the curing response of the healing agent and on its dynamic flow characteristics in flow channels, discrete cracks and within the cementitious continuum. This work guided the development of a series of constitutive models for both mechanical and transport behaviour. These formed the basis of a numerical model, which was developed by others, but used in a material tailoring exercise in the current study.

This work is part of the EPSRC funded Resilient Materials for Life, (RM4L) project, undertaken by researchers at Cardiff, Cambridge, Bath and Bradford universities (EP/P02081X/1 and http://rm4l.com/).

Acknowledgements

I would like to express my sincere gratitude to Prof. Tony Jefferson whose optimism had inspired me the most. Thank you for the continuous support and encouragement. Your guidance, passion and enthusiasm on my topic had helped me through my doctorate degree. You have always kept your sense of humour even when I lost mine. I would also like to extend my appreciation to Dr. Robert Davies. Thank you for your advice and feedback. I have learnt so much from you and I have always enjoyed our conversations. This would not have been possible without the both of you so thank you for believing in me.

I would also like to acknowledge the contribution from the laboratory technical and support staff in Cardiff University. Carl, Jack, Richard, Ian, Harry, Steve and Paul, thank you for all the help throughout these years. I know I have not been the easiest to work with but thanks for sticking around when things fail. Thanks to my friends and colleagues in W1.31 and W1.32 for sharing this journey with me; you know who you are. Thank you to Brubeck who I worked very closely with. Keep spreading positivity because we need more of that. Thanks also to Zac and I hope it all goes well for you. I will remember this experience for years to come so thanks again for this opportunity.

I would also like to thank my family, my relatives and my godparents for the love and support. Thanks to my brothers, Jegan and Eswaran who I have nothing but love and admiration for. I would rather be stuck with the both of you than anyone else. Thanks also to my sister-in-law, Priya who is now part of our family. Finally, thank you to my parents who will go above and beyond for anything I could ever ask for. *ILYWAMH* and I hope I have made you proud.

Contents

List of Figures

List of Tables

List of Symbols

A	Cross-sectional area
b	Capillary width/crack width
β_c	Transfer coefficient
β_m	Frictional dissipation factor at the meniscus
β_s	Stick-slip factor at the meniscus
β_w	Wall slip factor at meniscus
c	Healing recovery or softening constant
c_1, c_2	Model parameters
C_a	As defined in equation (7.18)
D	Diffusion coefficient or spreading parameter
D_1	Maximum value of D
E	Young's modulus
E_h	Young's modulus of the healed material
f_t	Tensile strength
f_{th}	Tensile strength of the healed material
g	Gravity
h	Degree of healing
h_ω	Healing parameter
H_K	Stiffness healing index
H_σ	Strength healing index
$\mathrm{J_q}$	Moisture flux
k	Permeability
K	Stiffness of the crack band
K, $\bar{K}$, K_2	As defined in equation (7.22) (Appendix C)
nv	An exponent which defines the rate of change with μ with φ
η	Total viscous resistance
P	Load
P_0, P_1, P_2	As defined in equation (3.1)
P_{app}	Applied pressure
P_c	Capillary pressure
ρ	Density
Q	Moisture source/sink term representing flow between the concrete matrix and discrete cracks
S_h	Degree of saturation in the porous medium
u	Relative displacement
u_{el}	As defined in equations (7.2a) and (7.2b)
u_h	Relative displacement at which healing takes place
u_t	As defined in equations (7.4) and (7.5)
Δu	As defined in equation (7.24) (Appendix C)
μ	Dynamic viscosity
μ_0	Initial viscosity

v	Meniscus velocity
ν	Poisson's ratio
ν_h	Poisson's ratio of the healed material
w_b	Width of the crack band
w_{crit}	Healing agent release at crack opening
ω	Damage variable
ω_h	Damage variable of the healed material
ω_2	As defined in equation (7.23) (Appendix C)
z	Meniscus height
z	Position of the meniscus front
z_c	Position of the curing front
z_{c0}	Critical curing depth at which the transport ceases
σ	Stress
σ_v	Stress of the virgin material
σ_h	Stress of the healed material
σ_1, σ_2	As defined in Figure C1 (Appendix C)
σ_3, σ_{3c}	As defined in Figure C1 (Appendix C)
σ_g, σ_{gc}	As defined in Figure C1 (Appendix C)
α, n, S_{h_c}	Model parameters
θ_d	Dynamic contact angle
θ_s	Static contact angle
γ	Capillary surface tension
τ	Curing time parameter or healing rate
ζ	Inelastic relative displacement
ζ_h	Inelastic relative displacement of the healed material
ζ_m	Effective relative displacement at the end of the softening curve
ζ_{mh}	Effective relative displacement at the end of the softening curve of the healed material
φ	Inclination of the capillary or degree of cure
φ_g	Degree of cure at the gel point (where a rapid increase of viscosity is observed)
ϕ_2	As defined in equation (7.24) (Appendix C)
Φ	Strength decay function

List of Acronyms

AE	Acoustic emission
CA	Cyanoacrylate
CAP	Single encapsulated compound
CHT	Cementitious hollow tubes
CMOD	Crack mouth opening displacement
CSH	Calcium silicate hydrate
DCA	Dynamic contact angle
DE	Diatomaceous earth
DIC	Digital image correlation
ECC	Engineered cementitious composite
EVA	Ethylene vinyl acetate
FRCC	Fibre reinforced cementitious composite
FTIR	Fourier transform infrared analysis
GHG	Greenhouse gasses
HPFRCC	High performance fibre reinforced cementitious composite
LVDT	Linear variable displacement transducer
LWA	Lightweight aggregate
MMA	Methyl methacrylate
PET	Polyurethane terephthalate
PP	Polypropylene
PU	Polyurethane
PVA	Polyvinyl alcohol
SAP	Superabsorbent polymer
SCM	Supplementary cementitious material
SEM	Scanning electron microscopy
SH	Self-healing
SHCM	Self-healing cementitious material
SMM	Shape memory material
SMP	Shape memory polymer
SS	Sodium silicate
UPV	Ultrasonic pulse-wave velocity

Chapter 1 Introduction

1.1 An introduction to self-healing cementitious materials

The ongoing problem of the deterioration of concrete structures has been a major concern in the construction industry and engineering community. It is estimated that between 35% and 50% of the annual construction budget in Britain and the EU (Cailleux and Pollet 2009; Office of National Statistic 2019) is spent on repair, maintenance and rehabilitation of existing structures. In a market research survey by Gardner et al. (2018), it was shown that the problem most experienced with concrete structures (both old and new) is cracking. It is known that cementitious materials are inherently brittle and have a relatively low tensile strength and are therefore expected to crack. These cracks provide a pathway for aggressive substances from the surrounding environment to penetrate into the bulk matrix, and sometimes reach the reinforcement, which then leads to corrosion and a loss of serviceability. This results in repair and maintenance, which therefore increases the associated whole life cycle costs (Ferrara 2018).

The problems referred to above apply to modern structures designed to current codes of practice, for concrete structures for example, BS EN 1992-1-1:2004 (British Standard Institution 2004), which should lead to structures that have the required performance, durability, reliability and quality. Such codes ensure that crack widths remain satisfactorily small (i.e. 0.1 to 0.3mm) by controlling the reinforcement size, spacing and cover. Even though cracking in reinforced concrete elements does not result short-term collapse, excessive cracking can be unsightly and lead to long-term durability problems due to chemical ingress and the corrosion of the reinforcement (Sangadji, 2017). Such problems result in increases in whole life cycle costs due to the consequential expenditure on repair and maintenance (Ferrara, 2018).

A widely accepted method of crack prevention that improves durability is prestressing, which can be in the form of pre or post tensioning. Prestressed structures are generally designed to withstand serviceability loadings without cracking. However, the application of pre-stressing requires jacking operations that are costly and there are also a number of health and safety issues related to their use. In addition, many existing prestressed structures have cracked and have suffered significant durability problems (Li et al. 2011). One solution to the jacking issues is to use shape memory materials (SMMs) to apply the prestress (Kuang and Ou 2008a; 2008b; Pilegis et al. 2015; Teall et al. 2016). Other methods, such as including fibres in the cementitious matrix as means of crack control, have also been reported (Ferrara et al. 2018a). This dispersed fibre reinforcement distributes stresses throughout the matrix, which encourages multiple smaller cracks to form, and prevents or delays the formation of macro-cracks (Neville 2012; Sangadji, 2017).

The development of self-healing cementitious materials (SHCMs) can potentially be a solution to the problem of cracking and deterioration, which would also improve the socio-economic costs and sustainability of civil engineering infrastructure. SHCMs are inspired by biological systems and have the ability to adapt and respond to a changing environment in such a way that they recover some of their performance after being exposed to damage. The RILEM committee TC-211 defines self-healing

as *'any process by the material itself involving the recovery and hence improvement of a performance after an earlier action that had reduced the performance of the materials'* (de Rooij et al. 2013). In the present work, healing is generally quantified in terms of mechanical strength and stiffness, although the change in durability properties are also discussed.

Self-healing technologies may appear promising but there is still scepticism from clients, designers and contractors on how it may be used by the construction industry. The market research reported by Gardner et al. (2018) suggested that highway structures and specialised water-retaining structures will benefit most from self-healing technologies. Despite having an increased capital cost, the use of SHCMs may generate cost savings over the lifetime of such structures, with significantly lower future repair and maintenance costs. The whole life cost savings will produce substantial economic, social and environment benefits. There is also a potential for resource efficiency by reducing element cross-sectional areas and steel reinforcement volumes when incorporating such technologies into concrete structures (Gardner et al. 2018).

It is also necessary to tailor self-healing techniques to different applications and initially it is believed that self-healing technologies should be applied to specialised applications where reliability and durability plays an important role. These include areas where it is difficult to gain the required access to undertake maintenance and repair such as high rise or underground structures (de Rooij et al. 2013). Although such technologies are in their infancy, progress towards large scale applications in a construction environment have already been achieved by a team of researchers at Cardiff, Cambridge, Bath and Bradford universities (Davies et al. 2018).

1.2 Aim and objectives

The overall motivation for this research arises from the need to improve durability of concrete structures. More specifically, the work aims to provide a comprehensive data set for a selected self-healing cementitious material system that provides the information necessary for developing a design procedure and/or numerical model for the system. The self-healing system selected for study is a vascular system in which healing agents are delivered to damage (crack) sites via a network of channels embedded in a cementitious matrix. The healing agent used in the present study is cyanoacrylate (CA), of which further details are given in Chapter 3.

The self-healing processes considered in the present work are illustrated in Figure 1.1, which shows (a) the formation of micro- and macro-cracks; (b) the flow of the healing agent through delivery channels and into the cracks; (c) the gradual curing of the healing agent, which proceeds as a diffuse front that gradually develops from the crack walls; and finally (d) crack healing. These processes result in partial or full restoration of a range of performance properties.

The objectives of this research work are as follows:

- Develop an experimental methodology for characterising the behaviour of a vascular self-healing cementitious material system;
- Understand different aspects of the mechanical and transport behaviour of the healing system;
- Determine a consistent set of mechanical damage and healing, and transport parameters for the chosen cementitious material system;
- Devise and validate a set of constitutive relationships that could form the basis of a design procedure and/or numerical model of the selected material system;
- Validate a numerical model, developed by others in the M4L Group at Cardiff, and then use the model to determine the most ideal healing agent for a selected structural element under a predetermined loading scenario;
- Assess the accuracy of the above material design exercise by conducting experimental tests on the structural element designed.

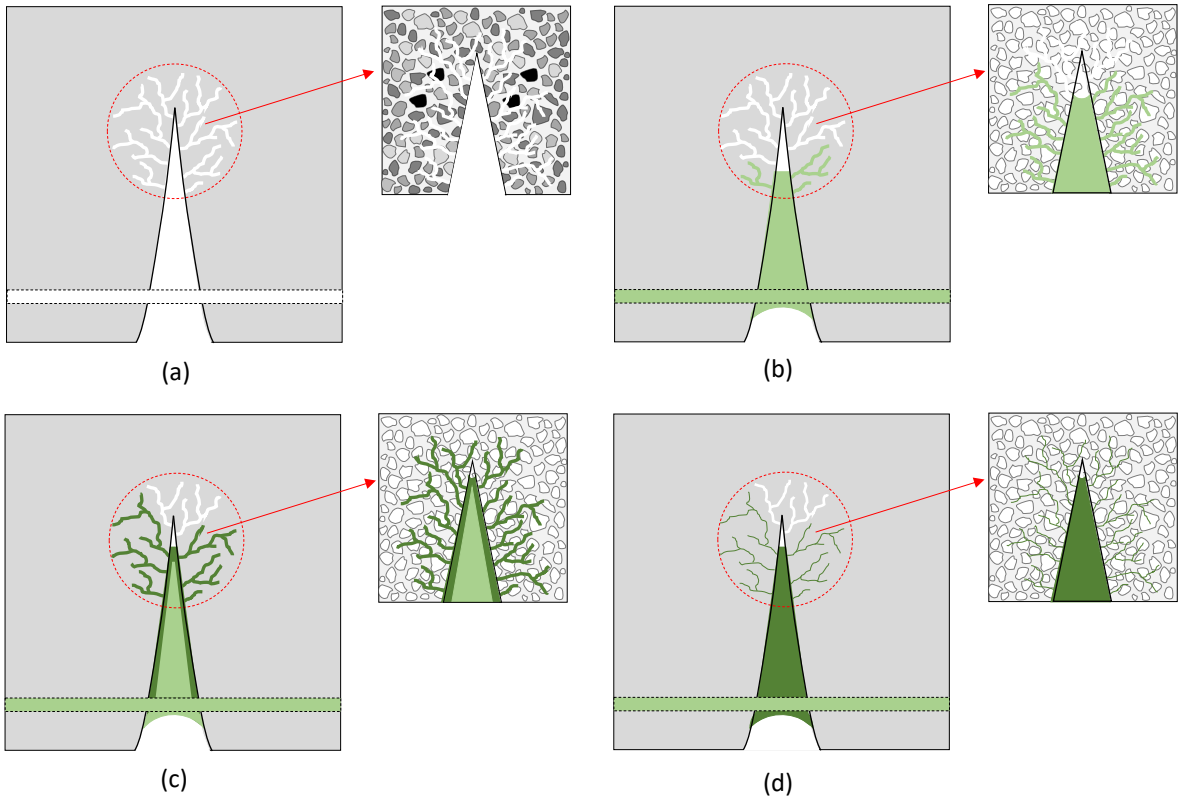

Figure 1.1. Characterisation of the self-healing processes showing (a) microcracks forming in the FPZ along the macrocrack, (b) some cracks filled with healing agent, (c) further filling with subsequent polymerisation of healing agent and (d) healing of some cracks partially restoring material performance

1.3 Outline of the remainder of the thesis

The thesis describes the various experimental test series and associated theoretical work undertaken to characterise the chosen autonomic vascular healing system. The remainder of this thesis is organised as follows:

Chapter 2 provides a literature review on SHCMs, which considers both autogenic and autonomic healing. This review discusses a range of healing techniques that includes the use of supplementary cementitious materials (SCMs), engineered cementitious composites (ECCs), shape memory polymers (SMPs), micro and macro capsules, flow networks and bacteria. This chapter also focuses on the characterisation of self-healing and the different approaches employed to evaluate self-healing efficiency.

Chapter 3 describes a detailed experimental investigation on the performance of the healing system in unreinforced notched concrete beams, that examined the effects of (i) varying the loading (crack opening) rate, (ii) the healing agent delivery pressure and (iii) the fixed crack healing period.

Chapter 4 presents the results from larger-scale laboratory tests on self-healing beams that contained a discontinuous arrangement of reinforcement. The chapters report on the behaviour of the healing system when applied to structural elements in which complex crack patterns develop.

Chapter 5 describes a series of direct tension tests on notched concrete specimens with different healing periods and crack openings. The results from these tests are compared with those of the beam tests reported in Chapter 3.

In Chapter 6 the focus is shifted towards transport and curing properties of healing agent in the vascular healing system. The tests reported in this chapter include the capillary flow of CA in an evolving crack, the sorption of CA through a cracked surface into a cementitious specimen, the development and progress of a CA curing front adjacent to a cementitious substrate and the dynamic flow CA in capillary channels. Chapter 6 also presents a series of constitutive models for the various aspects of transport and curing behaviour, as well as providing the associated parameters.

Chapter 7 presents a validation – undertaken by the author – of a new coupled finite element model for the material system, which was developed by the author's colleagues in Cardiff. The validation is followed by a description of a material design exercise which aimed to find an ideal healing agent for a selected structural element subjected to a predetermined loading rate. Subsequently, an experimental study is described which aimed to determine the accuracy of the numerical model as a material design tool.

Finally, Chapter 8 provides a summary of the conclusions made from each chapter and recommendations for future work. It also includes a brief discussion, with reference to the aim and objectives of the research.

1.4 Publications

The author is named on the following journal publications and conference proceedings:

- Selvarajoo, T., Davies, R. E., Freeman, B. L. and Jefferson, A. D. (2020). Mechanical response of a vascular self-healing cementitious material system under varying loading conditions. *Construction and Building Materials*.

- Selvarajoo, T., Davies, R. E., Gardner, D. R., Freeman, B. L. and Jefferson, A. D. (2020). Characterisation of a vascular self-healing cementitious material system: Flow and curing properties. *Construction and Building Materials* **245**:118332.

- Selvarajoo, T., Davies, R. and Jefferson, T. (2019). Characterisation of a vascular self-healing cementitious material system. *7th International Conference on Self-Healing Materials*, 2nd-5th June 2019, Yokohama, Japan.

- Jefferson, A., Selvarajoo, T., Freeman, B. and Davies, R. (2019). An experimental and numerical study on vascular self-healing cementitious materials. *MATEC Web of Conferences* **289**.

Chapter 2 State-of-the-art review

2.1 Introduction

This chapter provides an extensive literature review on the development of SHCMs relevant to the construction industry. In order for SHCMs to have significant influence, they will have to be compatible with, and partially replace conventional concrete structures. The scope of the study includes the development of a more sustainable cementitious material with an increased life span and fewer repair and maintenance requirements.

The chapter gives the background to the emerging field of SHCMs and, in particular, to self-healing concrete. These materials are designed to adapt and respond to their surrounding environment, and to improve the durability and longevity of structural elements from which they are formed. Self-healing concrete also has the potential to reduce the carbon footprint of concrete structures and reduce their whole-life cost (Van Tittelboom and De Belie 2013; De Belie et al. 2018).

Cementitious materials exhibit the natural ability to heal small cracks (Edvardsen 1999; Neville 2012) but this is usually insufficient to heal all the cracks that form in the matrix (Jefferson et al. 2018). Over the last few decades, enhanced autogenic and autonomic healing techniques have been developed that involve the inclusion of mineral additions, crystalline admixtures, polymers, hollow fibres, encapsulation or microorganisms within structural elements (Joseph et al. 2011; Davies et al. 2018; Xue et al. 2019; Al-Tabbaa et al. 2019). A topic that will be explored further in this review is vascular healing systems, which use embedded flow networks to transport healing agents to crack sites. Experimental techniques and methodologies developed to evaluate and characterise the efficiency of these self-healing systems will also be addressed.

As discussed in Chapter 1, the motivation for exploring such systems arises from the problems encountered with concrete structures, such as cracking and poor workmanship, and the high costs associated with these problems (Gardner et al. 2018). Before discussing previous work on SHCMs, it is worth considering the current issues faced by the cement and concrete industries. Details of the healing agent transport processes and numerical models for SHCMs are also given in Chapters 6 and 7 respectively.

2.1.1 Current issues

It has always been a challenge for the construction industry to integrate sustainability with constructability. These issues are linked to the environment, economic and social implications associated with the cement and concrete production processes. There are many environmental hazards associated with Portland cement production. The consumption and production of cement requires large quantities of raw materials (about 2 tonnes of limestone and shale per tonne of cement) and natural resources to generate the heat required (about 4GJ per tonne of cement) (Ferrara 2018). On average it is estimated that 1 tonne of concrete is produced for every person in the world which adds up to 10 billion tonnes every year making concrete the most used construction materials (Ferrara

2018; Naqi and Jang 2019). The cement industry also produces 1 tonne of CO_2 for every tonne of cement due to fuel combustion required to power the kiln and calcination of limestone in the manufacture of clinker, which is a product responsible for at least 80% of total energy consumed in cement production (Worrell et al. 2001; Van Oss 2005). The CO_2 emissions associated with cement production are estimated at 5% to 7% of the total CO_2 production in the world (Turner and Collins 2013; de Rooij et al. 2013). This also contributes to emission of the greenhouse gasses (GHG) such as methane (CH_4) and nitrogen oxide (N_2O) (Valipour et al. 2014).

According to the European Cement Association (2017) the world cement production surpassed 4.1 billion tonnes in 2017 while China is responsible for almost 56.5%. As the global population rises and urbanisation continues, global cement consumption is expected to increase to 4.68 billion tonnes annually by 2050 (International Energy Agency 2018). Given the rapid growth of economies especially in developing countries, this figure is more than likely to increase unless cement production can be less carbon and energy intensive (de Rooij et al. 2013). Since the cement industry plays a key role in GHG emissions, an integrated mitigation plan should be implemented to cope with threats posed by climate change and global warming (Wang et al. 2013a; Supino et al. 2016). It is of upmost importance to understand the environmental implications of concrete and cement manufacturing. The cement and concrete industry have been making significant progress on moving towards the adoption of a more sustainable approach with improved cement efficiency and incorporating waste materials such as mineral additions to reduce the adverse environmental impacts.

The repair and maintenance cost of concrete structures also has significant economic impact due to their lack of quality and durability. For example, in the UK alone, 40% of the annual expenditure is spent on restoring existing structures (Department of Trade and Industry 2014). In the USA, the average maintenance cost for bridges is estimated at $5.2 billion (de Rooij et al. 2013). In the Netherlands about 33% of the annual budget is spent on inspection, monitoring, maintenance, upgrading, and repair (van Breugel 2012; Sangadji 2017).

Social issues include public nuisance caused by maintenance and inspection as well as reduced safety for the general public due to poorly maintained infrastructure. For example, in a press release by the European Commission, it was reported that there were 28 traffic fatalities per million inhabitants in UK in 2018, some of which attributed to inadequate roadway conditions (European Commission DG 2018). In addition to this, traffic congestions could be linked to billions of pounds of wasted fuel and time each year (Li et al. 2004). Therefore, with such impacts on our daily lives there is a need to step forward and look closely into other alternatives means of building and maintaining the nation's infrastructure.

2.1.2 Existing solutions

The OPEC oil embargo in the mid-1970s forced the cement industry to reduce its dependency on oil which resulted in improved production energy efficiency. Since then the average specific kiln energy has reduced approximately 40% over just two decades. With growing legislative pressure to reduce GHG emissions, cement manufacturers are continually improving plant efficiency by increasing energy efficiency and using alternative fuels (i.e. agricultural or non-agricultural biomass, chemical and hazardous waste, and petroleum-based fuels) as substitution for raw materials (Supino et al. 2016).

At Imperial College in London, researchers developed a way of producing concrete that absorbs CO_2 from the atmosphere (Kennett 2009). The cement used contains magnesium oxide which requires lower temperatures and does not produce any CO_2 during the reaction process resulting in total CO_2 absorption of 0.4 tonnes for every tonne of cement produced. In addition to this, the cement absorbs 1.1 tonnes of CO_2 when it hardens, making net absorption of CO_2 at 0.7 tonnes per tonne. OPC (ordinary Portland cement) does this too, but in relatively small quantities between 0.2 and 0.5 tonnes (Kennett 2009). Blended cements are those in which a portion of clinker is replaced with either an industrial by-product or waste such as blast furnace slag, fly ash, silica fumes, or biomass ash (Newlands and Paine 2010; Yang et al. 2015; Crossin 2015; European Commission DG 2018). These alternatives have shown to achieve the same if not greater strength than that of OPC whist reducing CO_2 emissions and consuming less energy (Van Oss 2005; Li et al. 2010; Jones et al. 2011; Scrivener et al. 2018). However, the primary disadvantage of these industrial by-products is the limited availability compared to the abundance of quarried limestone (Gartner 2004). The savings in CO_2 sought using cement replacement materials strongly depends on the transportation cost, which can out-weigh the environmental gain (Worrell et al. 2001). Additionally, geopolymer cements are often referred to as a suitable option to help reduce emissions linked to OPC. However, geopolymers, which contain aluminosilicate, are also obtained from either natural sources or waste materials. The curing occurs through polycondensation activated in a highly alkaline environment, which results in a much lower CO_2 emission rate compared to OPC (Schneider et al. 2011). Finally, because of the good availability of raw materials, the associated transportation costs and emissions are reduced (Davidovits 2010). The conservative approach of the construction industry and reluctance to uptake geopolymers could be due to the issues surrounding High Alumina Cement Concrete, which led to several collapses in the early 1970s (Currie and Crammond 1994). In order to explore the full potential of all the material solutions described above, the construction industry will have to take the initiative to adopt new methods and innovative technologies to achieving widespread implementation and transition towards a low carbon economy. An alternative or additional solution to reducing the impact of cement manufacture is to make structures much more durable and one way to achieve this is to introduce self-healing systems.

2.2 Self-healing cementitious materials

In recent years, there has been growing interest in SHCMs, which to date is focused on exploring other alternatives and formulating preventive repair methods due to increasing awareness on sustainability issues. Researchers worldwide are aiming to develop materials with superior properties in order to address durability concerns associated with concrete. A summary of self-healing techniques is presented in Table 2.1 and these are discussed in detail in the sections that follow. Table 2.1 groups these techniques by the system, technology and healing processes employed. It is noted that a number of review articles have been published covering the breadth of techniques employed across the world. An exhaustive literature review on was undertaken by Joseph et al. (2011) on the recent work of self-healing technologies. This was followed by Van Tittelboom et al. (2013) who provided a detailed comparison on different self-healing approaches. A state-of-the-art report of RILEM TC-221 SHC entitled *'Self-Healing Phenomena in Cement-based Materials'* published in 2013 (de Rooij et al. 2013) also provided an extensive overview on the recent progress. A systematic in-depth summary was given in De Belie et al. (2018). It encompasses autogenous and non-encapsulated autonomic self-healing, encapsulated autonomic self-healing, self-healing bio concrete, and outlook and drawbacks. Similarly, Xue et al. (2019) provided a review on encapsulated autonomic self-healing systems with various healing agents, encapsulation techniques and experimental approaches. Also, Ferrara et al. (2018a) provided a state-of-the-art report on a range of experimental characterisation techniques used to evaluate self-healing efficiency. In linked work, Jefferson et al. (2018) considered the recent developments on numerical models for SHCMs.

Table 2.1. Summary of self-healing techniques developed for cementitious materials

Self-healing system	Self-healing technology	Ways and techniques	Healing processes
Autogenic	Supplementary cementitious materials (Section 2.2.1)	Inclusion of SCMs into the cementitious mix.	The presence of water allows the precipitation of $CaCO_3$ crystals.
	Microfibers (i.e. steel, PVA, PE) (Section 2.2.1)	Microfibres randomly dispersed throughout the cementitious mix.	Restricting crack widths so that autogenic healing can occur.
	Shape memory polymers (Section 2.2.1)	PET strips or strands formed into tendons anchored within the cementitious matrix similar to post-tensioning. Heat activation via electric current resulting in shrinkage.	Compressive stresses help create contact between the crack surfaces and reduce crack widths which facilitates autogenic healing.
Autonomic	Microencapsulation (Section 2.2.2.2)	Microcapsules distributed into the cementitious matrix.	The rupture of the micro/macro capsules releases healing agent into the cementitious matrix.
	Macro encapsulation (Section 2.2.2.2)	Hollow tubes (glass or ceramic) embedded into the cementitious matrix. Usually preferred because more healing agent can be stored to achieve multiple healing.	
	Bacteria healing systems (Section 2.2.2.3)	Bacterial spores and nutrients included in the cementitious matrix.	Exposure of bacterial spores and nutrients to water promotes deposition of $CaCO_3$ crystals.
	Vascular healing systems (Section 2.3)	Hollow channels formed in the cementitious matrix as a delivery system for the healing agent into cracks. Potentially pressurised to allow multiple healing.	The healing agent flows into crack plane when cracking reaches flow channels. This system can be connected to an external reservoir to increase supply of healing agent.

2.2.1 Autogenic healing of cementitious materials

The first observation of autogenic healing was made by The French Academy of Science in 1836 in water retaining structures, pipes, and culverts (Hearn 1998) but it was not until the end of the nineteenth century that Hyde and Smith (1889) studied the self-healing capability of concrete. van Breugel (2012) reported that Glenville carried out a more systematic study of these phenomena in 1931 by introducing the distinction between self-healing and self-sealing. In self-healing, the original strength of concrete was recovered whereas in self-sealing, the cracks were closed without any strength recovery. This phenomenon was also explored by Soroker and co-workers, and Brandeis in 1926 and 1937 respectively. The physical, chemical, and mechanical mechanisms of autogenic healing have been discussed by Kishi et al. (2007), Wu et al. (2012) and de Rooij et al. (2013) and are illustrated below in Figure 2.1.

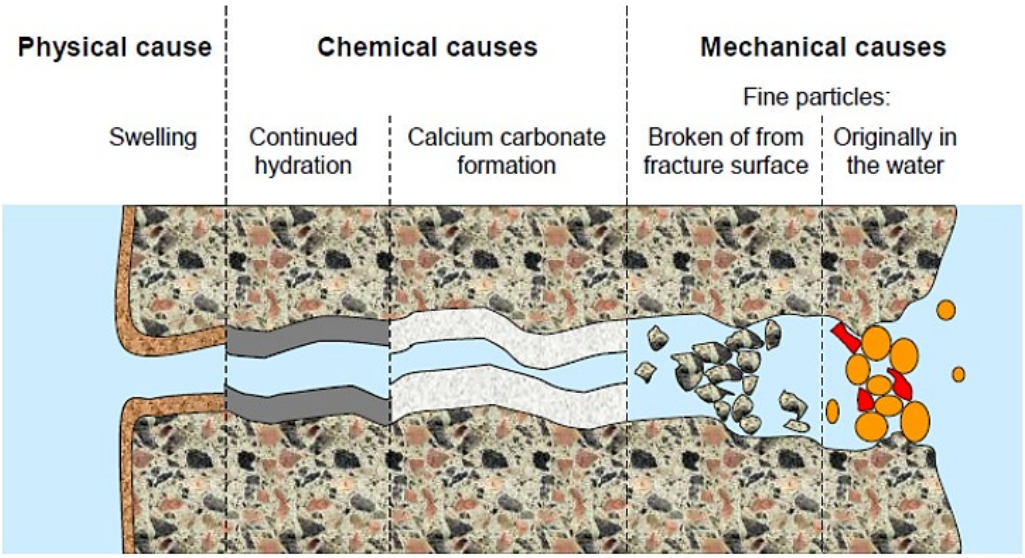

Figure 2.1. Causes of autogenic healing (de Rooij et al. 2013)

There has been significant amount of research which considers the autogenic healing efficiency with regards to the recovery of mechanical and durability properties. The intrinsic healing potential of concrete can be enhanced by factors such as (i) the age and composition, (ii) the presence of water and (iii) the width and shape of the crack. Neville (2012) suggested that if cracking occurs at an early age, there will be more unhydrated cement for continued hydration within the matrix while if cracking occurs at a later age, carbonation due to the precipitation and growth of $CaCO_3$ crystals from the crack surfaces will most likely be the cause of self-healing. ter Heide and Schlangen (2007) also found that specimens which cracked at a younger age achieved more strength compared to specimens that cracked at a later age. The use of coarser cement in modern concrete structures can also improve autogenic healing due to availability of more unhydrated cement (Van Tittelboom et al. 2012a). A low water-cement ratio is also important to induce large amount of unhydrated cement to promote autogenic healing (Granger et al. 2007). However, according to van Breugel (2007), healing may not be guaranteed under all circumstances.

In similar studies, Ranaivomanana et al. (2013) investigated the healing process caused by precipitation of $CaCO_3$ crystals in cracks. The authors performed percolation tests with liquid (carbonated water) and gas (CO_2 and humid air) with a relative humidity of 60% on fractured specimens. The results for tests with gas showed that the formation of $CaCO_3$ crystals is dependent on the relative humidity. However, from the liquid tests, it was suggested that the pressure gradient in the liquid through the crack was a limiting factor for self-healing. It was proven that there was a threshold cracks width value associated with the pressure gradient, as shown in previous study by Edvardsen (1999) in which cracks cannot be sealed if the initial crack width value exceeded the threshold. This threshold crack width was between 0.2mm and 0.3mm for the pressure gradient of 0.625bar/m and 1.25bar/m. Ranaivomanana et al. (2013), alongside other researchers (Edvardsen 1999; Wiktor and Jonkers 2011; Palin et al. 2015), agreed that the presence of water is essential to stimulate the precipitation of $CaCO_3$ into cracks for self-healing.

The influence of temperature (i.e. 20°C to 80°C) and crack width (i.e. 0.05mm to 0.15mm) on self-healing was studied by Reinhardt and Jooss (2003) and the authors concluded that a higher temperature could yield a faster self-healing process. They also concluded that narrow cracks (i.e. less than 0.10mm) heal more quickly and are more likely to completely heal than wider cracks. The authors suggested that the formation of $CaCO_3$ crystals depends on the crack width and temperature, which is consistent with Edvardsen's (1999) findings. A study by ter Heide and Schlangen (2007) found that healing is consistent in cracks with openings between 0.02mm to 0.15mm but that strength recovery is enhanced in closed cracks when a compressive stress of 0.5N/mm^2 is applied across the crack surfaces.

Various methods developed to stimulate autogenic healing such as by incorporating mineral additions, crystalline admixtures, superabsorbent polymers (SAPs) and using SMMs will be discussed in the following sections.

The use of mineral additions has been shown to have a positive effect on the hydration kinetics in cementitious materials. Van Tittelboom et al. (2012a) considered alternative binder materials for autogenic healing. It was found that cement replacement materials such as blast furnace slag and fly ash could increase the self-healing efficiency with continued hydration. A reduced water/binder ratio was also shown to heal cracks with openings below 0.2mm. A higher capacity of self-healing was also observed (Şahmaran et al. 2013) with mixtures incorporating blast furnace slag instead of fly ash in although, the latter have more unreacted binder materials. This was attributed to the mixed cementitious and pozzolanic activity which causes delayed hydration even in the presence of low calcium hydroxide (Huang et al. 2016a; De Belie et al. 2018). A crack closure of 0.41mm was also recorded for specimens containing blast furnace slag as oppose to 0.17mm for OPC specimens in Palin et al. (2015). In a study by Ahn and Kishi (2010), cracks were healed after 33 days of re-curing for specimens containing mineral additions i.e. aluminosilicate and various modified calcium composite materials. A 0.15mm wide crack was completely healed after 3 days and a crack width of 0.22mm decreased to 0.16mm after 7 days.

Self-healing in enhanced ECCs has been explored by a number of authors (Yang et al. 2009; Yang et al. 2011a and Zhu et al. 2012a). As for plain cementitious materials, it was found that the addition of cement replacement materials enhances the healing capacity of ECC. These studies explored the self-healing ability of ECCs subject to freeze-thaw (Zhu et al. 2012b) and wetting and drying cycles (Yang et al. 2009) with positive results.

There have been studies on the effectiveness of using crystalline admixtures to promote self-healing (De Belie et al. 2018). Crystalline admixtures can increase the density of calcium silicate hydrate (CSH) and react with water to form water insoluble pore or crack blocking precipitation of outside impurities. In addition to blocking pores, crystalline admixtures can continue to activate in the presence of moisture to seal any additional gap over the lifetime of the structure (American Concrete Institute 2010). Silva et al. (2017) explored the use of crystalline admixtures in an anti-flotation reinforced concrete slab and showed that its use improved water tightness. An improvement of self-healing properties of concrete with crystalline admixtures was also reported by Ferrara et al. (2014) in which the presence of crystalline admixtures accelerated crack healing process. Additionally, the authors also found that the synergy between the dispersed fibre reinforcement in high performance fibre reinforced cementitious composites (HPFRCC) and crystalline admixtures resulted in a *'chemical pre-stressing'* which benefited in the mechanical recovery (Ferrara et al. 2016b). In a more recent study, Cuenca et al. (2018) investigated autogenic and stimulated self-healing capacity of steel fibre reinforced concrete specimens with and without crystalline admixtures under cracking and healing cycles up to a year. The results suggested improved self-sealing capacity due to the delayed hydration and carbonation reactions by both the cement and crystalline admixtures.

Several researchers have investigated whether the inclusion of SAPs in concrete mixes promotes self-healing (Lee et al. 2010; Kim and Schlangen 2011; Dejonghe et al. 2011; Snoeck and De Belie 2012; Lee et al. 2016). SAP inclusions are used to store water within the cementitious matrix and this water is released when cracking occurs, and subsequently reacts with unhydrated cement to help heal cracks. The effectiveness of SAPs in self-healing concrete depends on several factors such as the type, shape, size and amount of SAPs, water/cement ratio, and mixing procedures (Snoeck et al. 2014b; Snoeck et al. 2017). These authors have shown that SAP inclusions can be highly effective despite earlier work which suggested that they can severely weaken concrete (Yao et al. 2012).

A very different approach to self-healing is to use shape memory polymer tendons to close cracks in concrete elements (Jefferson et al. 2010; Isaacs et al. 2013; Hazelwood 2015; Teall et al. 2016). Much of this work is not of direct relevance to the present research other than the fact that the closure (or reduction in width) of cracks facilitates autogenous self-healing (Isaacs et al. 2013).

From the work reviewed in this section, it is concluded that some autogenous healing may occur in cracks up that are up to 0.25mm wide but 0.05mm is the upper limit required for promoting strength and stiffness recovery. Despite this, autogenic healing can be enhanced by introducing SCMs into the mix to enhance the self-healing process especially at early age. Other methods such as using microfibers and SMPs to restrict crack widths so that autogenic healing can occur has also shown to be effective. The presence of water which result in swelling and expansion effects, and re-crystallisation is also essential to ensure complete healing. However, a significant disadvantage of autogenic healing behaviour is that healing is restricted to smaller crack widths. To overcome this shortfall, autonomic healing techniques have been developed (see Section 2.2.2).

2.2.2 Autonomic healing of cementitious materials

Autonomic crack healing in concrete refers to the self-healing mechanisms which are artificially triggered within the matrix through chemical or biological agents. For example, when damage occurs (i.e. intrusion of cracks), the self-healing mechanism is triggered due to the release and reaction of healing agents in the region of damage (Van Tittelboom and De Belie 2013). These healing agents are usually supplied through encapsulation (see Section 2.2.2.2) or vascular networks (see Section 2.3).

2.2.2.1 Healing agents

The efficacy of self-healing systems that employs autonomic healing agents have been demonstrated in a number of studies over the past 25 years (Dry 1994; Mihashi et al. 2000; Joseph et al. 2010; Wang et al. 2012a; Minnebo et al. 2017; Araújo et al. 2018). A range of healing agents have been employed which includes CA which polymerises upon contact with moisture (Li et al. 1998; Joseph et al. 2010; Sun et al. 2011, Huang et al. 2014; Davies et al. 2018), alkali-silica and sodium silicate which reacts with the portlandite (Mihashi et al. 2010; Pelletier 2019; Huang and Ye 2011; Mostavi et al. 2015; Kanellopoulos et al. 2015; Kanellopoulos et al. 2016; Alghamri et al. 2016; Beglarigale et al. 2018; Al-Tabbaa et al. 2019), polyurethane (PU) that have been applied as an single component agent (Van Tittelboom et al. 2011; Maes et al. 2014; Van den Heede et al. 2016; Gilabert et al. 2017; Van Belleghem et al. 2018) and as a two-component agent comprising of a prepolymer and an accelerator (Feiteira et al. 2016; Van Tittelboom et al. 2016; Feiteira et al. 2017; Gilabert et al. 2017; Hu et al. 2018) through encapsulation, methyl methacrylate (MMA) which was originally employed in a three-component system by Dry and McMillan (1996) but was later developed as a two-component system by Van Tittelboom et al. (2011) that used compounds of MMA monomers with an initiator and MMA with an activator, and epoxy resin which have been tested by encapsulation as a two-component system (Li et al. 2013). This was also used as a single encapsulated compound (CAP) with a dispersed hardener or with functionalised silica nanoparticles (Perez et al. 2015; Li et al. 2017).

The delivery of these healing agents is partly dependent on the capillary forces, which is determined by the crack width, and the viscosity of the agent, with lower viscosity agents generally reaching larger crack areas (Joseph et al. 2010). In addition, it must also have sufficient strength to avoid crack reopening. Other factors such as easy availability, cost effectiveness and sufficient longevity are essential for application in bulk construction product such as concrete (Joseph et al. 2011).

The categories of healing agents used in cementitious materials according to their activation mechanism can be found in Van Tittelboom and De Belie (2013). The first category is the reaction due to moisture, air or heat within the cementitious matrix. Dry (1994) used porous, cylindrical polypropylene (PP) capsules filled with MMA embedded in the cementitious materials. Heat is applied to cause the melting of wax fibres and the release of healing agents into cracks. In later publication, CA was used in cylindrical glass capsules which releases and cured upon contact with air when damage occurs (Dry 2000). Some researchers including (Van Tittelboom and De Belie 2010; Joseph et al. 2011; Sun et al. 2011) also used CA in cylindrical capsules. However, due to the highly reactive nature of CA, it can cure prematurely, which leads to limited dispersion (Joseph et al. 2011; Gardner et al. 2014). Instead of CA, Thao et al. (2009) suggested the use of one-part epoxy healing agent because it is less reactive.

The second category is the reaction with cementitious materials. Pelletier (2019) and Huang and Ye (2011) used microencapsulated sodium silicate (SS) embedded into the cementitious materials. Upon the appearance of one or more cracks, the healing agents reacts with the calcium hydroxide, which is naturally present in concrete. Premature hardening is not an issue because activation can only occur when the SS comes into contact with the cementitious matrix. Despite being suitable for OPC, this reaction may not occur when used with SCMs which requires calcium hydroxide to induce pozzolanic reactions.

The last category requires the components of multi-part healing agents to come in contact with each other for healing to occur. Dry and McMillan (1996) suggested the use of multi-component healing agents because they have greater stability than single-component healing agents and can be activated at a later date (i.e. in situ). Van Tittelboom et al. (2011) raised the issue of insufficient mixing of both components upon their release. To overcome the latter problem, Yang et al. (2011b) and Wang et al. (2013b) used MMA monomers and triethylborane as the healing agent and catalyst respectively. The authors showed that this pairing led to reduced permeability of the mortar and improved crack resistance and toughness.

2.2.2.2 Encapsulation methods

The types of encapsulation methods used to deliver healing agents to the micro and macrocracks consist of microcapsules with internal diameters of below 1mm (White et al. 2001; Yang et al. 2011b; Wang et al. 2013b; Kanellopoulos et al. 2017; Souza and Al-Tabbaa 2018), continuous hollow glass and ceramic capillary tubes with internal diameters ranging from 0.8mm to 4mm (Li et al. 1998; Kuang and Ou 2008a; Kuang and Ou 2008b; Joseph et al. 2010; Van Tittelboom et al. 2011; Gardner et al. 2014; Maes et al. 2014; Formia et al. 2015; Van Tittelboom et al. 2016; Gilabert et al. 2017; Araújo et al. 2018; Van Belleghem et al. 2018), and flow networks or channels embedded within the cementitious matrices (Dry et al. 2003; Joseph et al. 2010; Sun et al. 2011; de Rooij et al. 2013; Pareek et al. 2014; Davies et al. 2015; Davies et al. 2016; Minnebo et al. 2017). These approaches provide direct internal delivery of healing agents to damage zones and can be divided into two categories, i.e. discrete and continuous. All of these approaches rely on the embedded capsules (or channel walls) rupturing when crossed by a crack and the subsequent flow and curing of the healing agent (Gilabert et al. 2017; De Belie et al. 2018). The various factors influencing the curing processes include the composition of healing agents, the structure of the capsule materials, accelerators, surrounding conditions and type of cracks (Xue et al. 2019).

The present research programme considers vascular healing systems, which will be discussed in more detail in Section 2.3.

Micro-encapsulation

A potential drawback of microencapsulation is that the microcapsules may break during mixing. An approach to ensure the survivability of microcapsules during the mixing process was developed by Kanellopoulos et al. (2016) (see also Kanellopoulos et al. 2017), who designed microcapsules with switchable mechanical properties, which exhibit a soft and rubbery like behaviour when hydrated and transitioned into a stiff and glassy like behaviour when dried. Additionally, Mostavi et al. (2015)

proposed the use of double-walled polyurethane/urea-formaldehyde microcapsules to provide improved durability and survivability at high temperatures.

In other studies, formaldehyde and acrylate shells were adopted to increase the hydrophilic behaviour of the shells and to enhance the bonds between the microcapsules and the cementitious materials (Lv et al. 2016a; Souza and Al-Tabbaa 2018). Lv et al. (2016b) reported using a new type of polymeric microcapsules with phenol–formaldehyde which reported positive outcomes such as high thermal stability and excellent bonding properties. Yang et al. (2011b) also explored the potential of microcapsules made with silica gel. Similarly, Wang et al. (2013b) used urea formaldehyde for the shell material. It was found that adding appropriate amount of microcapsules could reduce pore content and surface area thus, improving its durability and impermeability through a microfiller effect.

Some researchers considered the microfluidic techniques to produce double emulsions microcapsules as shown in Figure 2.2, where drops of core material within drops of another fluid which subsequently solidifies the middle phase and yield solid shell microcapsules (Vilanova et al. 2013; Datta et al. 2014). As a result, the microcapsules exhibit a mechanical behaviour that can be adjusted (i.e. geometric parameters, outer radius, shell thickness and elastic modulus of the cross-linked network) depending on the desired application (Chen et al. 2012; Vilanova et al. 2013; Chen et al. 2014; Datta et al. 2014). The hydrophilicity of the shell can also be modified to enhance the interfacial bonding in the cementitious matrix (Souza and Al-Tabbaa 2018).

A full-scale site trial as part of the Material for Life (M4L) research project was developed in the interest of facilitating the adoption of microcapsules containing healing agents into practice (Davies et al. 2018). The inclusion of microcapsules in SHCMs in the field study appeared to be very promising to which the results suggested significant improvement in crack width and depth reductions and recovery in permeability (Al-Tabbaa et al. 2018; Al-Tabbaa et al. 2019).

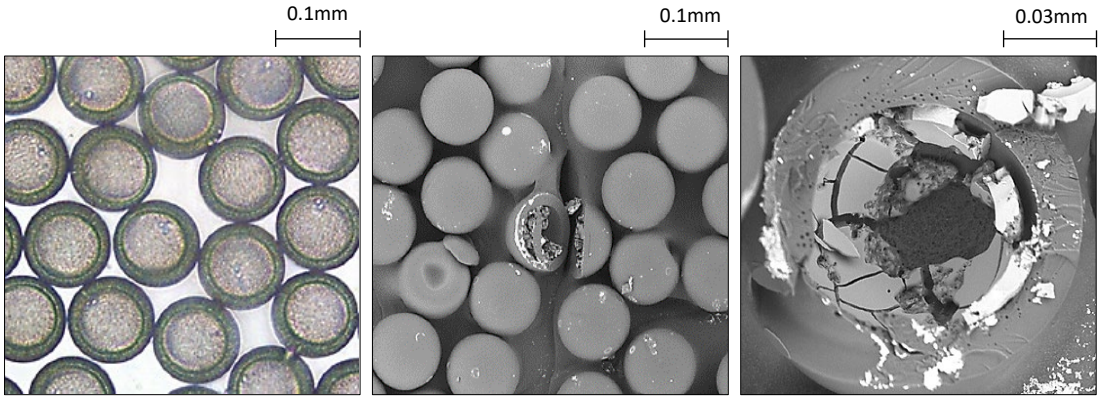

Figure 2.2. Microcapsules produced in the microfluidics device (a) optical microscope image of monodispersed double emulsion, (b) SEM images of the dried microcapsules and (c) a close up of a ruptured microcapsule (Souza and Al-Tabbaa 2018)

Macro-encapsulation

In most studies involving macro encapsulation, hollow glass tubes were used (Li et al. 1998; Mihashi et al. 2000; Joseph et al. 2011; Van Tittelboom et al. 2011; Sun et al. 2011; Kanellopoulos et al. 2015; Feiteira et al. 2016; Van Tittelboom et al. 2016). This method of encapsulation was usually preferred because of its ability to store larger amount of healing agents and potentially achieve multiple healing (De Belie et al. 2018). The earliest study was carried out by Dry (1994) where MMA was encapsulated in hollow PP and glass tubes. Both active and passive mode of activation are considered feasible for self-healing.

Li et al. (1998) carried out a study using hollow glass fibres (1.0mm outer diameter, 0.8mm inner diameter and 100mm length) and a 0.05ml capacity containing CA with both ends sealed with silicon. It was found that most specimens showed recovery in stiffness. The authors also suggested that the crack width of the matrix should be limited to less than the inner diameter of the tubes to ensure higher capillary action within cracks. Joseph et al. (2010) found only small amount of CA was drawn into cracks when closed-end tubes were used (3mm diameter and 100mm length) which was attributed to the suction effects. Therefore, to ensure the efficient release of healing agents the authors used a delivery system with open ends. With this opened ended delivery system, the healed specimens showed improved mechanical properties such as an increase in stiffness, peak strength and post peak ductility.

Additionally, Van Tittelboom et al. (2011) compared the use of glass and ceramic for macro encapsulation with varying diameters and the results showed that the ceramic tubes released more healing agents than its counterpart due to the difference in surface tension. Thao et al. (2009) chose the use of glass tubes (4mm inner diameter and 6mm outer diameter) over Perspex tubes, the latter were found to have visible cracks on the surface as the result of chemical reaction between the healing agents and the tubes. Also, the Perspex tubes were found to be stronger and more ductile hence, delaying the rupture of tubes.

As an alternative, Nishiwaki et al. (2006) developed a self-diagnosis composite made with fibre reinforced composites and electro-conductive materials. When the temperature rises due to heating, the embedded ethylene vinyl acetate (EVA) pipe (3.4mm outer diameter and 2mm inner diameter) selectively melts which then releases the epoxy resin in the crack. In a more recent study, extruded cementitious hollow tubes (CHT) with different internal diameters of 2mm and 7.5mm were used to contain and release SS and potassium silicate solutions (Formia et al. 2015; Formia et al. 2016). Hydrophobic coating was also applied to the inner surfaces of some hollow tubes to enhance the release of healing agents into cracks. The results exhibited an improvement in the mechanical properties and reached a recovery in load and stiffness of more than 70% and 50% respectively.

Sisomphon et al. (2011) studied the potential of expanded clay lightweight aggregate (LWA) containing sodium monofluorophosphate solutions coated with cement paste layers used as a self-healing agent in a blast furnace slag mortar. Similarly, Alghamri et al. (2016) and Alghamri et al. (2018) impregnated SS solutions into LWAs with 4mm to 8mm in diameter which were sprayed with polyvinyl alcohol (PVA) and left to dry. It was found that the specimens showed 80% recovery in pre-cracking strength and 50% reduction in sorptivity index. These studies suggested that the impregnation of LWAs by healing agents (with coatings) can be employed to improve the self-healing performance of cementitious materials.

2.2.2.3 Bacteria healing systems

Jonkers (2007) proposed the use of bacteria as a self-healing agent for concrete. The idea is to include microorganisms into the concrete mix for the purpose of assisting the precipitation of $CaCO_3$ crystals into microcracks during reaction with water. Interestingly, Jonkers (2011) found that these bacteria are able to form spores which are dormant cells that can withstand mechanical and chemical stresses and remain viable for over 50 years. However, the authors noticed a decrease in lifespan when bacterial spores were added into the concrete mix due to early age processes such as cement hydration which develops compressive stresses that crushes the micro sized cells (Jonkers et al. 2010). Although there was no loss of viability after six months, the addition of lightweight aggregates caused a decrease in compressive strength of the specimens. Additionally, Soltmann et al. (2011) found that the bacteria only survived 19 days despite the ideal pH conditions, which concluded its viability is mostly caused by cement hydration rather than alkalinity.

Some researchers had suggested that the compressive strength of concrete might increase with the amount of bacteria. They may act as a nucleation point for reactions or even precipitate free calcium ions to $CaCO_3$ crystals given their quantity (Paine 2016). For example, the addition of *Sporosarcina pasteuri* increases concrete strength from 55MPa to 65MPa (Ramachandran et al. 2001), and the use of *Shewanella* showed a 25% increase in compressive strength of cement mortar at 28 days (Ghosh et al. 2005). However, in Basaran Bundur et al. (2015) the inclusion of *Sporosarcina pasteuri* seem to slow the hydration resulting in lower strength concrete at early ages but it was similar to or greater than the compressive strength of the control mortar at later ages.

It is also necessary to encapsulate bacteria spores so they can survive longer. Wang et al. (2012b) suggested the use of diatomaceous earth (DE) as a protective carrier for the bacteria from the high pH environment of concrete. It was found that DE had a profound protective effect on the bacteria. DE immobilized bacteria also showed a higher ureolytic activity (25 g/L on average) than that of un-immobilized bacteria, which had almost no urea decomposed in cement slurry. The optimal concentration of DE for immobilization was 60% (weight of DE/volume of bacteria suspension). The cracks ranging from 0.15mm to 0.17mm were also filled with $CaCO_3$ crystals in specimens containing DE immobilized bacteria and showed increased water tightness. Alternatively, Wang et al. (2012a) took a slightly different approach by using silica gel or PU as a bacterial carrier. The results showed that PU microencapsulation yielded higher strength regain compared to silica gel. It was also found that the PU foam caused more healing than the bacterially precipitated $CaCO_3$.

A field study was carried out by Wictor and Jonkers (2015) in a parking garage using a bacteria-based repair system by combining the traditional repair system and the bio-based methods. The authors concluded that the bacteria-based repair system was very promising as it showed an increased resistance to freeze/thaw and icing salts, alongside the improvement of water tightness. A long-term assessment of the bacteria-based repair system will be subjected to ongoing research.

2.3 Vascular healing systems

Vascular healing systems are based on a biomimetic approach to self-healing that mimics the human cardiovascular system. In this framework, healing agents are delivered to damage sites via tube networks that are embedded in cementitious structural elements. It is worth noting that this is a type of encapsulation method (see Section 2.2.2.2) that allows single or multiple channels to be included within the cementitious matrix.

In an earlier study by Dry (1994) proposed using glass capillary tubes containing adhesive embedded within the matrix but it was found that there were difficulties during casting and mixing due to the brittleness of the glass capillary tubes. This was also scaled up and cast into a bridge deck for a full-scale site trials (Dry and McMillan 1996; Dry 2000). Instead of using glass tubes, round steel rods were cast into the concrete and pulled out after 24 hours of curing. The channels throughout the length of the specimen were coated with sealant to ensure low permeability. A more comprehensive early work is given in de Rooij et al. (2013).

Joseph and co-workers (Joseph et al. 2010; Joseph et al. 2011) carried out a study on mortar beam samples that contained four hollow glass tubes of inner diameter 3mm with one end open to the atmosphere and filled with air-curing CA, as illustrated in Figure 2.3.

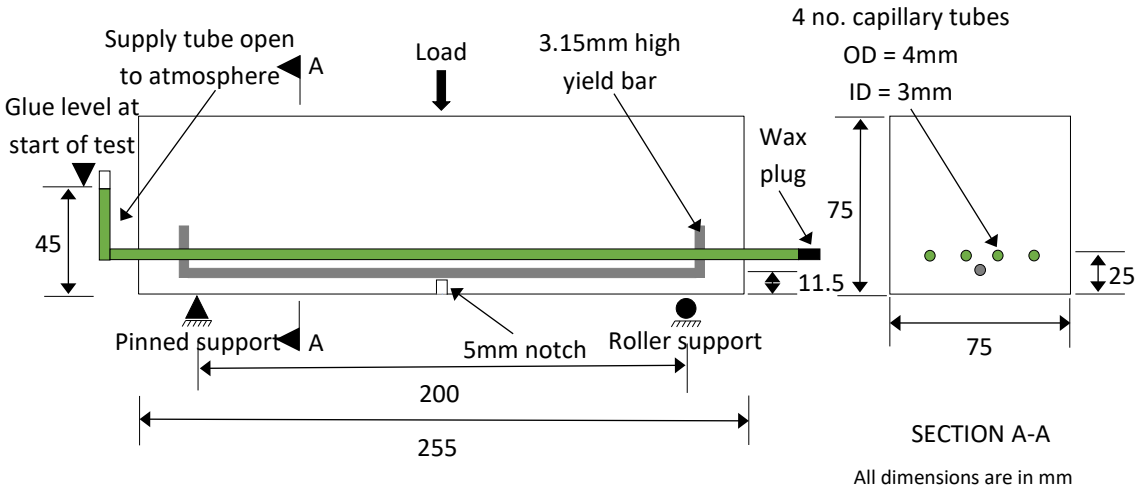

Figure 2.3. Experimental setup for continuous flow arrangement (Joseph et al. 2010)

The tests involved the beam specimens being loaded in a three-point flexural bending test until a crack mouth opening displacement (CMOD) of 0.3mm was reached, followed by unloading. The specimens were then left for 24 hours being reloaded to failure. The results of these tests, illustrated in Figure 2.4, show that SH beams increased in stiffness due to primary healing (i.e. during the first loading stage) and increased in strength and post-peak ductility after secondary healing (i.e. after the 24hour healing period). The primary healing is attributed to the fast curing rate of CA causing rapid macro and macro-crack healing.

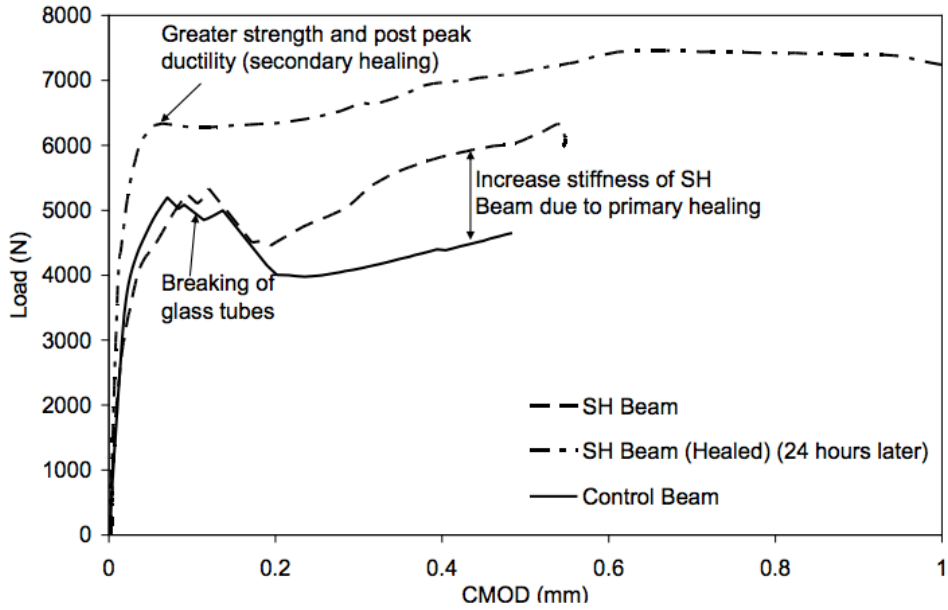

Figure 2.4. Typical load-CMOD responses for notched SH and control specimens (Joseph et al. 2011)

Joseph et al. (2010; 2011) reported that the supply of healing agent was exhausted in some tests. Earlier, Mihashi et al. (2000) had avoided such problems by attaching an external reservoir filled with healing agent to the outer ends of the supply tubes. Even earlier, Dry (1994) had connected a vacuum pump to an external reservoir so healing agents could be supplied whenever needed. Kuang and Ou (2008a; 2008b) incorporated SMA wires in this approach using continuous glass tubes filled with adhesive to reduce crack widths. The glass tubes break upon damage and due to the super elasticity of SMA wires the deflection of the beams are recovered immediately after unloading. This allows the release of adhesive from the broken glass tubes to fill and repair cracks.

The major advantage of vascular systems is that the healing agent can be continuously supplied through the flow networks, allowing repeated cracking and healing cycles (Dry 2000; Joseph et al. 2010; Huang et al. 2014; Gardner et al. 2018). The healing agent in the flow networks can also be flushed out so that the channels can be reused. Such systems also have the potential to be pressurised to ensure flow and delivery of the healing agent to the required damage zones (Davies et al. 2015; 2018), in contrast to most of the delivery systems described above (see Section 2.2.2.2) which rely only on capillary forces (Van Tittelboom and De Belie 2013; De Belie et al. 2018). Despite that, the addition of vascular networks may provide preferential pathways for harmful materials to bypass the concrete cover protection layer and compromise the durability of the concrete structures if left open to the atmosphere (De Belie et al. 2018). This could be countered by ensuring the channels are sealed when not in used. Various forms of vascular networks have been proposed. The simplest comprised a 1D flow networks, in which both ends can be accessed externally (Dry 2000; Mihashi et al. 2000; Joseph et al. 2010; Huang et al. 2014), by contrast, more complex 3D flow networks were created by using multi flow junction nodes within the cementitious matrix (Davies et al. 2015) to provide multiple pathways for healing agents.

A different approach to creating channels in cementitious elements was developed by Davies et al. (2015), who used removable shrinkable polyolefin or polyurethane terephthalate (PET) tubes to create single or multi-path flow networks. To facilitate the latter, the authors made 3D printed joints that accommodated the removal tubes. Another method for transporting healing agents to fracture zones involved embedding a porous concrete core within a concrete specimen (Sangadji and Schlangen 2012). In this work, healing agent was manually injected through the porous core. Even though the healing agents were distributed across the porous core, more agent was required to achieve the same healing efficiency as a tube network.

In a study by Minnebo et al. (2017), the authors assembled a 3D printed vascular network distribution piece allowing one inlet to be connected to multiple channels embedded in the matrix. This was also attached to a reservoir to accommodate a relatively high volume of healing agent. The authors suggested that that network could be positioned around or near the main tensile reinforcement to improve the efficiency of the system (De Belie et al. 2018).

The shelf life of the healing agent, the reliability of the self-healing system for on-site, the durability of the system and the relative cost are all relevant to the viability of vascular-based self-healing technologies. As discussed in Section 2.2.1, autogenic healing is restricted to narrow crack widths (i.e. below 0.25mm) and its efficiency depends on the composition of the matrix. Therefore, autonomic healing (see Section 2.2.2) by means of different encapsulation methods (see Section 2.2.2.2) including bacteria (see Section 2.2.2.3) and vascular healing systems (see Section 2.3) should be explored further. In autonomic healing, wider crack widths (i.e. above 0.25mm) can be healed in addition to having more flexibility and also the ability to achieve repeated healing cycles. However, the challenge to remotely activate these self-healing systems still remains a topic of interest. In vascular healing systems, overlapping damage and healing behaviour can be studied through the active release of healing agents via an external reservoir. These systems have the potential to be pressurised (Davies et al. 2015; 2018) and multiple channels can be embedded into the cementitious matrix to maximize flow into cracks.

2.3.1 Process and design steps

Figure 2.5 shows a flow diagram of the self-healing processes for a system in which healing agent can be repeatedly flushed out so that the channels can be re-used. This would allow multiple healing cycles to take place over the lifetime a structure.

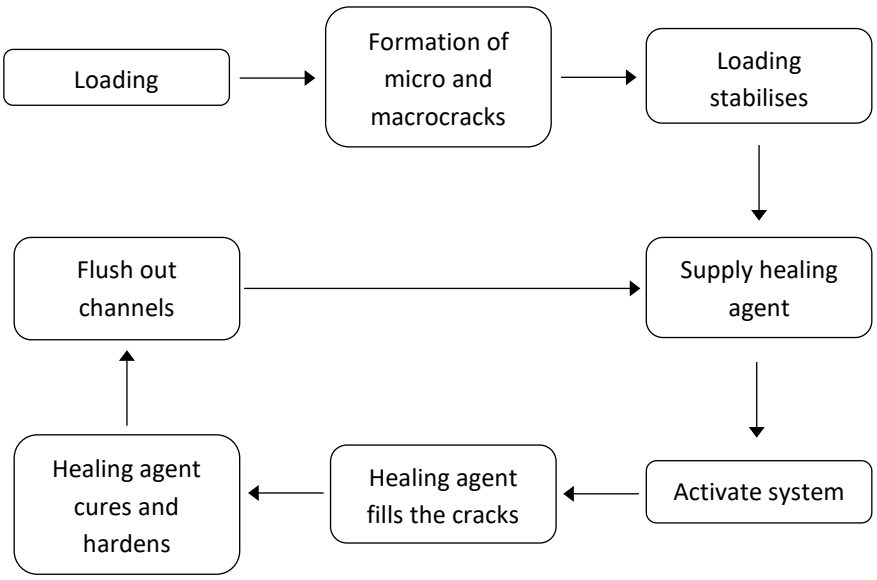

Figure 2.5. Processes of the vascular healing mechanisms in concrete structures

Data gained from experiments have been used to develop a numerical model for the self-healing system, details of which are given in Chapter 7.

The data are also relevant to the development of a design procedure for a structure formed from a self-healing material system. The steps of such a procedure for a structural member would be as follows:

- Predict initial cracking using serviceability crack width calculations (Eurocode 2 – clause 7.3);
- Evaluate degree and duration of crack filling;
- Evaluate the degree of curing and healing, accounting for load changes during the healing period;
- Compute the healing indices and assess whether the member fulfils the durability criteria in its healed state.

2.4 Characterisation of self-healing

The following sections describe a range of experimental methodologies used to characterise and evaluate self-healing efficiency of the SHCM systems described above.

2.4.1 Preliminary damage

In order to evaluate the self-healing efficiency of autogenic or autonomic healing systems, one or more cracks should first be induced in the specimen (Ferrara et al. 2018a). The effectiveness of the self-healing system can then be measured by the degree of crack closure or sealing, and/or by the recovery of mechanical or durability properties (Muhammad et al. 2016). The type of test employed for pre-cracking is dependent on the behaviour of the material. For example, plain concrete under flexural bending requires a closed loop crack controlled opening setup whereas, in the case of fibre reinforced cementitious composites (FRCCs) or HPFRCCs, flexural bending under machine stroke control is normally sufficient to create a stable crack opening (Ferrara et al. 2018a). The type of tests used to induce pre-cracking does not have any significant influence when evaluating the recovery in durability properties but is related to factors such as the type of test, the geometry of the crack and the type of material, as explained in Ferrara et al. (2018a).

Table 2.2 provides an overview of the techniques and the self-healing systems for pre-cracking used by previous researchers. It has been suggested that the type of test used for pre-cracking and that used for evaluating of self-healing should be compatible. Three and four-point flexural bending tests have most frequently been employed to determine the recovery of flexural strength and stiffness (Ferrara et al. 2018a). A notch is usually introduced to induce a pre orientated crack path in three-point flexural bending tests. However, in four-point flexural bending tests, cracking is normally designed to occur anywhere in the central bending moment region. This normally leads to the formation of multiple cracks, particularly in fibre-reinforced material samples (Ferrara et al. 2018a). Compression tests have also been reported to investigate compressive strength recovery (De Nardi et al. 2017a; De Nardi et al. 2017b; De Nardi et al. 2018). In an investigation by Homma et al. (2009), multiple cracking was achieved by stretching the specimens at different strain levels in order to obtain different maximum crack widths. In most studies, it was highlighted that there was an effect of elastic regain on the crack opening upon load removal and this was confirmed in a round robin test by Tziviloglou et al. (2016). This can affect the accuracy of self-healing efficiency measurements (Gruyaert et al. 2016). As a result, it is important to have a controlled pre-cracking method to produce a lower variation of residual crack width. Ferrara et al. (2018a) also pointed out that the crack width measured on the surface provides limited information about the crack within the matrix. For example, different specimens can have similar crack openings on the surface but with a completely different crack geometry. This issue has been studied by Van Tittelboom et al. (2016), who used x-ray tomography to visualise the interior of cracks, before and after healing. Splitting tests were also used to pre-crack specimens by several researchers, to measure the water tightness or crack sealing via water flow (Roig-Flores et al. 2015; 2016).

Table 2.2. Summary on the techniques for pre-cracking (definitions, AG: Autogenic; IAG: Improved Autogenic; AN: Autonomic; E: Encapsulation; V: Vascular; B: Bacteria)

Description	Techniques for pre-cracking	Type of cementitious materials	Authors
Mechanical properties	Three-point flexural bending test	Mortar Plain concrete Fibre reinforced cementitious composites High performance fibre reinforced cementitious composites	Alghamri et al. (2016) **AG/AN/E**; Wang et al. (2012a) **AN/E/B**; Ferrara et al. (2014) **IAG**; Kanellopoulos et al. (2015) **AG/AN/E**; Li and Li (2011) **AG**; Qureshi et al. (2016) **AG/AN/E**; Van Tittelboom et al. (2012a) **AN/E**; Wang et al. (2012b) **AN/B**; Wang et al. (2014a) **AN/E/B**; Wang et al. (2014b) **AN/E/B**; Wang et al. (2014c) **AG/AN/E/B**; Feiteira et al. (2016) **AN/E**; Feiteira et al. (2017) **AN/E**; Jefferson et al. (2010) **IAG**; Isaacs et al. (2013) **IAG**; Pilegis et al. (2015) **IAG**; Joseph et al. (2010) **AN/E**
	Four-point flexural bending test	Mortar Plain concrete Fibre reinforced cementitious composites High performance fibre reinforced cementitious composites	Ferrara et al. (2016a) **IAG**; Ferrara et al. (2017) **IAG**; Ferrara et al. (2016b) **IAG**; Ma et al. (2014) **AG**; Özbay et al. (2013a) **IAG**; Özbay et al. (2013b) **IAG**; Qian et al. (2009) **IAG**; Qian et al. (2010) **IAG**; Siad et al. (2015) **IAG**; Snoeck and De Belie (2012) **IAG**; Snoeck et al. (2012) **IAG**; Snoeck and De Belie (2015) **AG**; Snoeck et al. (2015) **IAG**; Snoeck and De Belie (2016) **IAG**; Snoeck et al. (2016) **IAG**; Snoeck et al. (2014) **IAG**; Yildirim et al. (2015a) **IAG**; Yildirim et al. (2015b) **IAG**; Snoeck and De Belie (2019) **IAG**; Snoeck et al. (2018a) **IAG**; Mignon et al. (2017) **IAG**
	Splitting test	Fibre reinforced cementitious composites	Ferrara et al. (2018b) **IAG**
	Direct tension test	Fibre reinforced composites	Homma et al. (2009) **IAG**; Feiteira et al. (2016) **AN/E**; Feiteira et al. (2017) **AN/E**; Wiktor and Jonkers (2011) **IAG/B**
	Drop-weight test	Mortar	Snoeck et al. (2018a) **IAG**
	Compression test	Mortar	De Nardi et al. (2017) **IAG**; De Nardi et al. (2017) **IAG/AN/E**; De Nardi et al. (2019) **IAG/AN/E**
Durability properties	Three-point flexural bending test Four-point flexural bending test	Mortar Plain concrete Fibre reinforced cementitious composites	Ma et al. (2014) **AG**; Zhang et al. (2014); Kanellopoulos et al. (2015) **AG/AN/E**; Kanellopoulos et al. (2016) **AN/E**; Alghamri et al. (2016); Tziviloglou et al. (2016) **AN/B**; Gruyaert et al. (2016) **IAG**; Van Tittelboom et al. (2016) **IAG/AN/E**; Van Mullem et al. (2019) **AG**; Van Belleghem et al. (2018) **AN/E**; Araújo et al. (2018) **AN/E**; Qureshi et al. (2018) **IAG**; Qureshi et al. (2019) **IAG**
	Three-point flexural bending test Four-point flexural bending test	High performance fibre reinforced cementitious composites	Homma et al. (2009) **IAG**; Lepech and Li (2009) **IAG**; Yang et al. (2009) **IAG**; Li and Li (2011) **AG**; Nishiwaki et al. (2014) **IAG**
	Compression test	Mortar	Ersan et al. (2018) **IAG/AN/B**; Jonkers (2011) **AN/B**
	Splitting test	Plain concrete Fibre reinforced cementitious composites	Van Tittelboom et al. (2012) **AN/E**; Snoeck et al. (2014a) **IAG**; Kanellopoulos et al. (2015) **AG/AN/E**; Roig-Flores et al. (2015) **IAG**; Roig-Flores et al. (2016) **IAG**; Olivier et al. (2016) **IAG**; Cuenca et al. (2018) **IAG**; Borg et al. (2018) **IAG**
		High performance fibre reinforced cementitious composites	Özbay et al. (2013a) **IAG**; Özbay et al. (2013b) **IAG**; Şahmaran et al. (2013) **IAG**; Şahmaran et al. (2014) **IAG**; Zhang et al. (2014) **IAG**; Siad et al. (2015); Yildirim et al. (2015b) **IAG**

2.4.2 Evaluation of self-healing efficiency

The self-healing capacity of SHCMs were evaluated after pre-cracking to determine the closure of cracks and/or the recovery of one or more mechanical and durability properties. Tables 2.3 and 2.4 summarise the techniques and the self-healing systems used to assess the effects of healing which will be discussed in following sections.

2.4.2.1 Recovery of mechanical properties

The majority of approaches to determine the self-healing efficiency have focused on the recovery of mechanical properties (see Table 2.3). In most test methods, specimens are pre-cracked, allowed a scheduled healing period under specific environmental conditions and then retested, with the post-healed properties being compared with their pre-healed counterparts (Ferrara et al. 2018a). The mechanical tests have also been combined with non-destructive techniques such as acoustic emission (AE) analysis (Van Tittelboom et al. 2012b) or ultrasonic pulse-wave velocity (UPV) tests (Ferrara et al. 2017) which according to Ferrara et al. (2018a), it can be useful to differentiate between ongoing bulk hydration and crack/damage healing.

Flexural bending test

The most commonly employed methods to evaluate self-healing efficiency in terms of recovery of the mechanical properties are three and four-point flexural bending tests (Ferrara et al. 2018a). Examples include tests on specimens with crystalline admixtures (Ferrara et al. 2014; Ferrara et al. 2016a), blast furnace slag and limestone powder (Qian et al. 2009), bacteria (Wang et al. 2012b), SAPs (Snoeck et al. 2014b; Snoeck and De Belie 2015; Van Tittelboom et al. 2016) or cement mixes formed from LWA impregnated with SS (Alghamri et al. 2016).

Three and four-point flexural bending tests were also used for the evaluation of the self-healing capacity of a range of plain and fibre reinforced materials (Ferrara et al. 2016a; Ferrara et al. 2016b). Li and Li (2011) studied healing in ECC specimens using three-point flexural bending tests. In Van Tittelboom et al. (2011; 2012a) notched mortar prisms containing embedded healing agent were subjected to three-point flexural bending test controlled by the rate of the crack openings. The recovery of flexural strength and stiffness of the specimens were measured by comparing the original and post healing values which in this case exhibited improvement of mechanical properties. Similarly, Feiteira et al. (2016; 2017) determined the self-healing efficiency for both healed and non-healed reinforced mortar containing encapsulated polymer precursors subjected to a three-point flexural bending test under displacement control. The authors found only 30% of the recovery of the mechanical stiffness with a crack width reduction of 0.02mm was obtained compared to the control specimens.

Four-point flexural bending tests was applied by Qian et al. (2009; 2010) to compared healing in pre-existing and newly form cracks in ECC specimens at different curing condition and pre-cracking time in an attempt to evaluate self-healing efficiency. Ferrara et al. (2016b; 2017) have also analysed the self-healing phenomenon in terms of recovery of stiffness, strength and ductility by employing four-point flexural bending tests. The healing recovery was determined by an index of crack healing

obtained from visual image analysis of the healed cracks and through a tailored indirect method proposed by Ferrara et al. (2014).

Direct tension and splitting tests

Far less work on SHCMs has been undertaken using direct tension and splitting tests than flexural bending tests; nevertheless, a significant number of studies have used such tests (Ferrara et al. 2018a). For example, Wang et al. (2014a; 2014b; 2014c; 2015) created multiple cracks in mortar prisms, which had a central reinforcing bar, using a direct tension test, with the degree crack-closure (or filling) being measured using optical microscopy. Nishiwaki et al. (2014) conducted direct tension tests on FRCC specimens to determine the effect of self-healing on the mechanical properties by comparing the energy absorption from both initial and reloading cycles. Yang et al. (2009) also measured the self-healing efficiency of ECC specimens using direct tension tests and employed the tensile strain capacity as a recovery indicator. Additionally, Gilabert et al. (2017) conducted direct tension tests on assembled concrete specimens which had two borosilicate glass tubes (containing PU and accelerator) crossing a preformed planar opening. The tubes were broken by the application of a relatively small force to the top of the specimen, which released the agents. After a recovery period, the specimens were reloaded at a controlled displacement rate of 0.04mm/min in order to evaluate the recovery of the mechanical strength. This study did not consider healing in a crack opening or captured the softening behaviour under tensile stresses and only measured the interfacial bonding strength of the healing agent between the glass and the concrete. Other authors had also used direct tension tests to assess the recovery of the strain capacity (Feiteira et al. 2016; Feiteira et al. 2017). In some cases, non-destructive test methods (see Table 2.3) have been employed to allow continuous monitoring of healing characteristics.

Splitting tests were employed by Şahmaran et al. (2014; 2015) to evaluate mechanical healing in ECC specimens with different mineral additions. The degree of self-healing was determined by the number of the multiple cracks formed and the average crack width recovery.

Compression tests

Compression tests, that produce a diffuse array of microcracks, have also been used to evaluate self-healing capacity of lime mortar specimens (De Nardi et al. 2017a; De Nardi et al. 2017b; De Nardi et al. 2018). The self-healing capacity was obtained through the recovery of compressive strength after the specimens were pre-cracked at different ages and levels of damage.

2.4.2.2 Recovery of durability properties

Self-healing efficiency can also be evaluated through the recovery of durability properties as described in Table 2.3. The improvement in gas or water tightness may be considered a good indication of concrete durability (Reinhardt and Jooss 2003; Song and Kwon 2007; Li et al. 2013; Huang et al. 2016a). Experimental methods used for the characterisation of the transport properties are discussed in the following sections.

Water permeability tests

There have been several investigations on the change in permeability of micro and macro cracked specimens to measure self-healing in respect to recovery in durability properties (Van Tittelboom et al. 2011; Van Tittelboom et al. 2015; Van Tittelboom et al. 2010; Gruyaert et al. 2016; Homma et al. 2009; Roig-Flores et al. 2015; Roig-Flores et al. 2016; Edvardsen 1999). There are two approaches to evaluate the permeability of healed cracks which are the evaluation of decrease in pressure (water height) with time and the evaluation of water flow passing through the crack at a certain period (Ferrara et al. 2018a). Van Tittelboom et al. (2010; 2011) explored the healing efficiency of an encapsulation-based self-healing system using this approach. In their work, they formed a single crack in cylindrical specimens, which were then saturated with water using an established vacuum saturation technique (Van Tittelboom et al. 2010). The specimens were glued inside PVC rings, mounted in a test setup and then submerged in water on one side. These water permeability tests were used to measure the change in flow through discrete cracks before and after healing. The work was later extended to specimens with multiple cracks (Van Tittelboom et al. 2015; Van Tittelboom et al. 2016), although, the authors concluded that their approach was far less effective because of the difficulty of properly sealing all of the cracks.

Homma et al. (2009) developed a test setup capable of imposing a tensile stress on specimens in order to have different maximum crack widths. The specimens were then exposed to water pressure to evaluate the water flow through the cracks. Instead of using the standard test methods to measure water depth penetration for concrete specimens (EN 12390-8), Roig-Flores et al. (2015; 2016) proposed measuring water flow. Following a similar approach, Gruyaert et al. (2016) and Tziviloglou et al. (2016) developed a water flow test using mortar prisms (40x40x160mm) consisting of two reinforcement wires (ø1mm) and a hole (ø5mm) at mid depth over the length of the specimens. A three-point flexural bending test was performed with a controlled crack opening and stored in water for two days. When the specimens were saturated, the side surfaces of the crack were wrapped with aluminium tape and the hole was sealed with MMA glue with another connected to a plastic tube. The plastic tube was attached to a water reservoir 500mm above the mid depth of the specimens to which the water can flow into the hole (ø5mm) formed within the matrix and leak out of the crack. The self-healing efficiency was measured using the change in water flow over time.

Sorptivity tests

de Rooij et al. (2013) investigated the healing efficiency of cracked mortar specimens using a capillary water absorption technique. The investigators used laboratory scale prismatic specimens (60x60x220mm) which were cracked and then oven cured for 3 days. The surfaces adjacent to the damage zone were then wrapped with aluminium tape thereby, exposing the crack to capillary suction. The specimens were placed on two rigid non-porous supports in a container filled with water such that at least 2mm of the specimen was immersed in water. The specimens were weighed to determine the uptake of water through both the crack and surrounding matrix and measured at prescribed time intervals. The results showed clear distinctions between healed and unhealed specimens, from which the authors concluded that this sorptivity test was an effective means of determining the degree of healing. A similar technique was used by a number of other investigators (Sabir et al. 1998; Şahmaran et al. 2008; Wang et al. 2012b). The weight change was recorded periodically over 8 hours (at 15mins, 30mins, 1hour, 2hours, 4hours, 6hours, 8hours) in Feiteira et al.

(2016) and every 4 hours in Alghamri et al. (2016). Van Belleghem et al. (2016) recorded the mass of the mortar specimens every 5 minutes for the first 30 minutes and every 30 minutes for 8 hours during the capillary sorption test. The specimens were then left overnight, and readings were recorded again at every 24 hours until a total exposure time of 96 hours. X-ray radiography was also used to visualise the moisture content distribution at specific time intervals during the ongoing test.

Gas permeability tests

Another technique used to evaluate the recovery of the microstructure properties in cementitious materials involves testing the gas permeability of samples. Yang et al. (2011b) used changes in gas permeability as a measure of healing in cementitious specimens with silica gel shell microcapsules containing MMA monomer or triethylborane. The authors prepared a set of cylinder specimens (ø50x100mm), cured for different periods (3 and 30 days), and then caused damage by subjecting them to a compressive load of 80% of their capacities. The specimens were then cut into 10mm thick cylindrical disk specimens, vacuum dried for 24 hours at room temperature, sealed and subjected to a gas permeability test. The authors reported a reduction in the permeability of both 3 and 30-days self-healing specimens of 50.2% and 66.8% respectively. More recently, Yildirim et al. (2015a; 2015b) investigated the influence of cracking and healing on the gas permeability of ECC specimens. It was found that the self-healing effect was determined by the changes of the chemical composition. The results also suggested that the preloading contributed to the increase of gas permeability in the specimens where even microcracks of below 0.05mm resulted in a gas permeability coefficient 50 times higher than that of control specimens.

Chloride penetration tests

A few studies on the effect of cracking on chloride ion diffusion in partially cracked, as well as single or multiple cracked, specimens have been reported (Win et al. 2004; Djerbi et al. 2008; Ye et al. 2012). It was found that chloride diffusion increases with crack widths and water/cement ratio (Win et al. 2004; Djerbi et al. 2008). The efficiency of self-healing through rapid chloride permeability tests was also investigated by several authors (Jacobsen et al. 1996; Li and Li 2011; Wang et al. 2013b; Şahmaran et al. 2013; Şahmaran et al. 2014; Özbay et al. 2013b; Zhang et al. 2014; Siad et al. 2015; Darquennes et al. 2016). A study by Wang et al. (2013b) explored the healing effectiveness of cementitious specimens embedded with microcapsules with respect to a chloride migration coefficient which was calculated from the results of the chloride ion permeability tests. The cylindrical mortar specimens (ø100x50mm) were cured in water at room temperature and were subjected to compression to induce initial damage. The specimens were surrounded by a hollow rubber cylinder containing 0.2 mol/L KOH water solution (as anolyte) which was later submerged into a mixed water solution (as catholyte) (with 5% NaCl and 0.2 mol/L KOH) and a 30 voltage was applied at room temperature for 24 hours. The specimens were split open and coloured with a 0.1 mol/L $AgNO_3$ water solution to show the chloride ion migration. The authors reported almost complete recovery of the chloride migration coefficient relative to that of the original material. In Şahmaran et al. (2013; 2014) chloride penetration tests were performed on ECCs and suggested that the effectiveness of crack sealing can reduce the chloride ion penetration.

Table 2.3. Summary of techniques to evaluate self-healing efficiency, recovery of mechanical and durability properties (definitions, AG: Autogenic; IAG: Improved Autogenic; AN: Autonomic; E: Encapsulation; V: Vascular; B: Bacteria)

Techniques for characterising self-healing efficiency	Type of test	Possibilities	Authors
Recovery of mechanical properties	Flexural bending tests Direct tension and splitting tests Compression tests	Strength and stiffness recovery (flexural, tensile or compression) Formation of new cracks or reopening of old cracks	Ferrara et al. (2014) **IAG**; Kanellopoulos et al. (2015) **AG/AN/E**; Li and Li (2011) **AG**; Qureshi et al. (2016) **AG/AN/E**; Van Tittelboom et al. (2012) **AN/E**; Wang et al. (2012b) **AN/B**; Wang et al. (2014a) **AN/E/B**; Wang et al. (2014b) **AN/E/B**; Ferrara et al. (2016a) **IAG**; Ferrara et al. (2017) **IAG**; Ferrara et al. (2016b) **IAG**; Ma et al. (2014) **AG**; Özbay et al. (2013a) **IAG**; Özbay et al. (2013b) **IAG**; Qian et al. (2009) **IAG**; Qian et al. (2010) **IAG**; Siad et al. (2015) **IAG**; Snoeck and De Belie (2012) **IAG**; Snoeck and De Belie (2015) **AG**; Snoeck et al. (2015) **IAG**; Snoeck and De Belie (2016) **IAG**; Snoeck et al. (2014a) **IAG**; Yildirim et al. (2015a) **IAG**; De Nardi et al. (2017a) **IAG**; De Nardi et al. (2017b) **IAG/AN/E**; Zhang et al. (2014) **IAG**; Kanellopoulos et al. (2016) **AN/E**; Van Tittelboom et al. (2016) **IAG/AN/E**; Homma et al. (2009) **IAG**; Lepech and Li (2009) **IAG**; Yang et al. (2009) **IAG**; Nishiwaki et al. (2014) **IAG**; Şahmaran et al. (2014) **IAG**; Feiteira et al. (2016) **AN/E**; Feiteira et al. (2017) **AN/E**; De Nardi et al. (2018) **IAG/AN/E**; Cuenca et al. (2018) **IAG**; Borg et al. (2018) **IAG**; Ferrara et al. (2018b) **IAG**; Snoeck and De Belie (2019) **IAG**; Snoeck et al. (2018a) **IAG**; Snoeck et al. (2018b) **IAG**; Mignon et al. (2017) **IAG**; Qureshi et al. (2018) **IAG**; Alghamri et al. (2018) **AN/E**; Xu et al. (2019a) **AN/E**; Xu et al. (2019b) **AN/E**; Davies et al. (2018) **IAG/AN/E/V/B**; Jefferson et al. (2010) **IAG**; Isaacs et al. (2013) **IAG**; Pilegis et al. (2015) **IAG**; Teall et al. (2016) **IAG**; Joseph et al. (2010) **AN/E**; Palin et al. (2015) **IAG**; Palin et al. (2017) **IAG/B**; Wiktor and Jonkers (2011) **IAG/B**
	Acoustic emission analysis	Regain in energy Breakage of capsules	Van Tittelboom et al. (2012) **AN/E**; Feiteira et al. (2017) **AN/E**
	Resonant frequency analysis	Stiffness recovery	Yildirim et al. (2015b) **IAG**; Yang et al. (2009) **IAG**; Snoeck et al. (2018a) **IAG**
Recovery of durability properties	Water permeability tests (low/high pressure)	Water flow through healed crack	Wang et al. (2012a) **AN/E/B**; Wang et al. (2014a) **AN/E/B**; Wang et al. (2014c) **AG/AN/E/B**; Snoeck et al. (2012) **IAG**; Snoeck et al. (2014a) **IAG**; Tziviloglou et al. (2016) **AN/B**; Gruyaert et al. (2016) **IAG**; Roig-Flores et al. (2015) **IAG**; Roig-Flores et al. (2016) **IAG**; Homma et al. (2009) **IAG**; Lepech and Li (2009) **IAG**; Yang et al. (2009) **IAG**; Nishiwaki et al. (2014) **IAG**; Van Mullem et al. (2019) **AG**; Ersan et al. (2018) **IAG/AN/B**; Palin et al. (2017) **IAG/B**; Wiktor and Jonkers (2015) **IAG/B**; Jonkers (2011) **AN/B**
	Sorptivity tests	Capillary water uptake of healed crack	Alghamri et al. (2016) **AG/AN/E**; Kanellopoulos et al. (2015) **AG/AN/E**; Qureshi et al. (2016) **AG/AN/E**; Wang et al. (2012b) **AN/B**; Wang et al. (2014c) **AG/AN/E/B**; Snoeck et al. (2012) **IAG**; Zhang et al. (2014) **IAG**; Snoeck et al. (2018b) **IAG**
	Gas permeability tests	Air flow through healed crack	Kanellopoulos et al. (2015) **AG/AN/E**; Yildirim et al. (2015b) **IAG**; Qureshi et al. (2019) **IAG**; Qureshi et al. (2018) **IAG**; Wang et al. (2018a) **IAG**
	Chloride penetration tests (w/ or w/o pressure)	Resistance against chloride ingress	Li and Li (2011) **AG**; Ma et al. (2014) **AG**; Özbay et al. (2013b) **IAG**; Siad et al. (2015) **IAG**; Zhang et al. (2014) **IAG**; Şahmaran et al. (2013) **IAG**; Şahmaran et al. (2014) **IAG**; Cuenca et al. (2018) **IAG**; Van Belleghem et al. (2018) **AN/E**; Araújo et al. (2018) **AN/E**
	Ultrasonic pulse-wave velocity tests	Continuity of material	Ferrara et al. (2014) **IAG**; Ferrara et al. (2017) **IAG**; De Nardi et al. (2017a) **IAG**; De Nardi et al. (2019) **IAG/AN/E**; Araújo et al. (2018) **AN/E**

2.4.2.3 Visualisation and determination

A number of authors have considered the closure of cracks as a measurement method to determine crack healing or crack sealing which were assessed by the recovery of mechanical and durability properties. Increasing use have been made of imaging techniques to explore internal crack patterns and the morphology of healing zones of materials (Beglarigale et al. 2018; Van Tittelboom et al. 2016; Ferrara et al. 2018a; Liu et al. 2016). The most common technique used to characterise the microstructure of cementitious materials is light microscopy. This allows for repeated observations during healing periods because the cementitious material can be preserved without the need to destroy the specimen (Ferrara et al. 2018a). Light microscopy is able to gather information on the surface of the cracks such as the composition of healing products (i.e. $CaCO_3$ crystals). Additional information can also be obtained using thin section analysis to detect the depth of the formation of $CaCO_3$ crystals (de Rooij et al. 2013). In a study by Van Tittelboom et al. (2016), the inside of cracks was investigated using florescence microscopy which was very effective to increase the contrast between space and solid phases (de Rooij et al. 2013). The use of scanning electron microscopy (SEM) and/or infrared analysis (FTIR) has also been reported by several authors (see Table 2.4) who used these techniques to analyse crystal depositions inside a crack or to characterise healing materials. Feiteira et al. (2017) used digital image correlation (DIC) combined with AE analysis to monitor the crack opening along the full height of the crack and to detect failure due to high energy emissions. Other techniques include topographies and CT scans where the self-healing efficiency can be assessed by means of waves propagation allowing the ability to examine the composition inside the cementitious matrix to differentiate by the density of the materials (between aggregates, pores and cracks). For example, in Alghamri et al. (2016), x-rays were applied to characterised healing products whereby it was reported that SS produced more CSH gels due to the reaction with the portlandite. As for CT scans, x-ray images at different angles create cross-sectional 2D images or 3D compositions (Ferrara et al. 2018a). Neutron tomography has also been used to evaluate water uptake (Snoeck et al. 2012; Alderete et al. 2019). These imaging techniques can provide considerable insights into the behaviour of the self-healing systems, but they have not been applied to capture real time damage and healing processes.

An overview of the experimental methods for characterising crack healing in cementitious materials has been given. As discussed earlier, the recovery of mechanical properties is carried out by subjecting the SH specimens to repeated pre-cracking followed by a scheduled healing period at different curing conditions whereby the comparison to the control specimens would determine the healing effectiveness. It is also essential to distinguish between crack healing and ongoing bulk hydration (Ferrara et al. 2018a) during the evaluation of self-healing capacity since, the presence of water or high relative humidity can promote the precipitation of $CaCO_3$ crystals which result in crack sealing or closure. Imaging techniques are usually employed in order to differentiate between the two. Conversely, the recovery of durability properties can be measured by changes in liquid or gas flow through a crack before and after healing.

An issue which will be discussed in the following chapters is overlapping damage and healing behaviour. This issue has been investigated in the programme of work using a combination of the experimental techniques described in Section 2.4 to measure the healing efficiency of a vascular model material system (see Chapter 3). Previous studies have only considered healing at specific time intervals in fixed crack openings, when in fact, healing can continuously progress as cracking occurs. To the best of the author's knowledge, there have yet been a study that provides a consistent body of data using the same set of parameters for characterising various aspects and properties of a self-healing system. This will be addressed in Chapters 3 to 6.

Table 2.4. Summary of techniques to evaluate self-healing efficiency, visualisation and determination (Definitions, AG: Autogenic; IAG: Improved Autogenic; AN: Autonomic; E: Encapsulation; V: Vascular; B: Bacteria)

Techniques for characterising self-healing efficiency	**Type of test**	**Possibilities**	**Authors**
Visualisation and determination	Light microscopy (optical, digital or stereo)	Visualisation of crystal deposition Determination of healing rate	Wang et al. (2012a) **AN/E/B**; Wang et al. (2014a) **AN/E/B**; Wang et al. (2014b) **AN/B**; Ferrara et al. (2016b) **IAG**; Snoeck and De Belie (2012) **IAG**; Snoeck et al. (2015) **IAG**; Snoeck and De Belie (2016) **IAG**; Snoeck et al. (2014a) **IAG**; Gruyaert et al. (2016) **IAG**; Roig-Flores et al. (2015) **IAG**; Roig-Flores et al. (2016) **IAG**; Homma et al. (2009) **IAG**; Lepech and Li (2009) **IAG**; Cuenca et al. (2018) **IAG**; Borg et al. (2018) **IAG**; Ferrara et al. (2018b) **IAG**; Farrugia et al. (2019) **AN/B**; Snoeck and De Belie (2019) **IAG**; Snoeck et al. (2018a) **IAG**; Al-Tabbaa et al. (2019) **AN/E**; Xu et al. (2019b) **AN/E**; Jonkers (2011) **AN/B**
	Scanning electron microscopy (SEM or ESEM)	Visualisation of crystal deposition Visualisation of crack closure (or healed crack) Visualisation of breakage of embedded capsules	Alghamri et al. (2016) **AG/AN/E**; Wang et al. (2012a) **AN/E/B**; Ferrara et al. (2014) **IAG**; Kanellopoulos et al. (2015) **AG/AN/E**; Qureshi et al. (2016) **AG/AN/E**; Wang et al. (2012b) **AN/B**; Wang et al. (2014c) **AG/AN/E/B**; Ferrara et al. (2017) **AG**; Ferrara et al. (2016b) **IAG**; Ma et al. (2014) **AG**; Özbay et al. (2013a) **IAG**; Özbay et al. (2013b) **IAG**; Qian et al. (2009) **IAG**; Siad et al. (2015) **IAG**; Snoeck et al. (2016) **IAG**; Yildirim et al. (2015b) **IAG**; De Nardi et al. (2017a) **IAG**; Zhang et al. (2014) **IAG**; Kanellopoulos et al. (2016) **AN/E**; Homma et al. (2009) **IAG**; Şahmaran et al. (2013) **IAG**; Yang et al. (2009) **IAG**; Feiteira et al. (2017) **AN/E**; De Nardi et al. (2018) **IAG/AN/E**; Cuenca et al. (2018) **IAG**; Farrugia et al. (2019) **AN/B**; Ersan et al. (2018) **IAG/AN/B**; Al-Tabbaa et al. (2019) **AN/E**; Qureshi et al. (2019) **IAG**; Qureshi et al. (2018) **IAG**; Souza and Al-Tabbaa (2018) **AN/E**; Alghamri et al. (2018) **AN/E**; Xu et al. (2019b) **AN/E**; Dong et al. (2018) **AN/E**; Yang et al. (2018) **AN/E**; Wang et al. (2018a) **IAG**; Wang et al. (2018b) **AN/E**; Wang et al. (2018c) **AN/E**; Palin et al. (2015) **IAG**; Palin et al. (2017) **IAG/B**; Wiktor and Jonkers (2011) **IAG/B**; Jonkers et al. (2010) **AN/B**; Jonkers (2011) **AN/B**
	Topographies and CT scans (x-rays and neutron)	Visualisation of release encapsulated agent from embedded capsule Determination of crystals (formation of C-S-H)	Alghamri et al. (2016) **AG/AN/E**; Wang et al. (2012a) **AN/E/B**; Kanellopoulos et al. (2015) **AG/AN/E**; Qureshi et al. (2016) **AG/AN/E**; Wang et al. (2014a) **AN/E/B**; Wang et al. (2014b) **AN/E/B**; Ma et al. (2014) **AG**; Qian et al. (2009) **IAG**; Snoeck et al. (2012) **IAG**; Snoeck et al. (2016) **IAG**; De Nardi et al. (2017a) **IAG**; De Nardi et al. (2017b) **IAG/AN/E**; Olivier et al. (2016) **IAG**; De Nardi et al. (2018) **IAG/AN/E**; Alderete et al. (2019) **IAG**; Snoeck et al. (2018b) **IAG**; Snoeck et al. (2018a) **IAG**; Ersan et al. (2018) **IAG/AN/B**; Araújo et al. (2018) **AN/E**; Al-Tabbaa et al. (2019) **AN/E**; Qureshi et al. (2019) **IAG**; Qureshi et al. (2018) **IAG**; Souza and Al-Tabbaa (2018) **AN/E**; Xu et al. (2019a) **AN/E**; Xu et al. (2019b) **AN/E**; Dong et al. (2018) **AN/E**
	Infrared analysis (FTIR)	Determination of precipitated products	Kanellopoulos et al. (2015) **AG/AN/E**; Qureshi et al. (2016) **AG/AN/E**; Farrugia et al. (2019) **AN/B**; Wiktor and Jonkers (2011) **IAG/B**

2.5 Conclusions

The following conclusions are drawn from the above review of literature:

- Autogenic healing in cementitious materials offers an immediate crack repair solution. The presence of water is necessary to increase the autogenic healing potential and to promote ongoing hydration and crystallisation. It also does not require the addition of expensive healing agents. However, the work to-date suggests that autogenic healing is only able to repair cracks up to 0.25mm in width and provides a relatively low degree of strength recovery;
- Improved autogenic healing through the inclusions of SCMs, microfibres and SMPs was also investigated. This includes the use of mineral additions, crystalline admixtures, SAPs and ECCs to stimulate crack healing. A different approach to restrict crack width by taking advantage of the super elastic effect of SMAs (Kuang and Ou 2008a; 2008b) and the shape memory effect of SMPs (Jefferson et al. 2010; Isaacs et al. 2013; Pilegis et al. 2015; Teall et al. 2016) was also developed. The latter techniques reduce the size of the cracks so that autogenic healing can occur;
- Autonomic healing in cementitious materials that include microcapsules containing healing agent or bacteria into the cementitious matrix or which allow delivery of healing agents to damage sites through vascular networks, have proven able to repair cracks with openings of more than 0.25mm to 0.4mm;
- Vascular healing systems provide more flexibility than the other autonomic deliver systems (Davies et al. 2015; 2018). These can be pressurised and are able to supply relatively large quantities of healing agent, which facilities multiple healing cycles;
- It is also important to develop standard techniques for the evaluation of self-healing over the lifetime of a cementitious structure to determine the most efficient and reliable self-healing approach. Experimental methods, which are already widely accepted to measure the recovery of mechanical and durability properties, alongside non-destructive testing techniques and numerical analysis, can collectively provide a better understanding of the self-healing phenomenon;
- Although, considerable experimental work has been devoted to proving the efficacy and characterising the various properties of self-healing systems, there have been less focus on developing an experimental programme directed towards the specific requirements of design procedures and numerical models (Jefferson et al. 2018; Ferrara et al. 2018a);
- Another factor relevant to practical applications relates to the simultaneous damage and healing behaviour of the autonomic healing systems which was ignored in previous studies.

Final remarks

The conclusions of the literature review have identified various gaps in current research data. Some of these gaps are addressed in the work described in the remaining chapters of thesis, which describe experiments that characterise the mechanical, curing and transport properties of vascular healing systems that use a pressurised autonomic healing agent. These experiments encompass studies on specimens with cracks ranging from 0 to 0.4mm, various crack configurations, crack opening conditions and applied pressure. These tests address situations in which overlapping damage-healing events occur. The overall aim of these studies is to provide sufficient data for the development and calibration of a comprehensive design and/or numerical model of such systems (see Chapter 3).

Chapter 3 Mechanical damage and healing

3.1 Introduction

This chapter presents a characterisation study on the damage-healing behaviour of an autonomic self-healing cementitious material system. The autonomic healing approach is based on capillary networks containing healing agents embedded within the cementitious matrix. The vascular network is connected to an external reservoir to allow continuous supply of healing agents throughout the working life of the structure. Once cracking occurs, the healing agent will flow out of the network channels, fill and then heal any cracks that have formed. The vascular healing system can also be pressurised to assist with the delivery of the healing agent. The objectives of this study are:

- To develop an experimental procedure to obtain self-healing in cementitious materials using vascular networks;
- To understand the relationship between the healing agent and cementitious materials;
- To determine the effects of loading rate, pressure and healing period on the damage and healing responses in autonomic self-healing systems;
- To explore the interaction of multiple healing agent flow paths;
- To provide a benchmark data for validating numerical and design models for SHCM systems.

The comprehensive study on the characterisation of the vascular healing system focuses on the healing behaviour of CA and provides data for the development of a generic numerical model for self-healing systems. The motivation for developing the present experimental programme is to obtain a consistent set of data for a model self-healing system since to date, there have been very few experiments directed towards the specific requirements of design and numerical model for a range of loading scenarios (Ferrara et al. 2018a; Jefferson et al. 2018). In this study, a series of tests under three and four-point flexural bending tests on notched prismatic beams were carried out to evaluate the damage and healing behaviour under transient (in Groups A, C, D, E and F) and fixed crack opening conditions (in Group B), each of which had different sets of parameters, as described and summarised in Section 3.3.5.

The Group A test series explores both the effect of loading rate on the beam and the healing agent delivery pressure while the Group B test series consider the effect of varying the healing period on the degree of healing recovery when the crack is held at a constant opening during the healing period. The healing period is defined as the period of time for which a crack is held stationary while healing takes place. The Group A and B test series relate to the creation and healing of one primary mode I crack whereas it is acknowledged that multiple interconnected micro and macrocracks may occur in practical applications. To explore this issue, four groups of tests (i.e. Groups C to F) were undertaken on specimens that had two discontinuous layers of reinforcement, arranged so that the reinforcement gaps were horizontally offset from each other. This arrangement of reinforcement produces the desired complex multiple crack patterns.

The tests in Groups A and B, reported in this chapter, consist of small-scale laboratory specimens (75x75x255mm), whereas larger scale laboratory specimens (100x100x500mm) were used for the tests in Groups C to F, which are reported in Chapter 4.

3.2 Model material system

In order to investigate simultaneous cracking and healing, a vascular healing system was selected because it allowed the healing agent to be externally pressurised and CA (Cyanotec 2019) was chosen as the healing agent because it has been proven to heal crack openings from 0.1mm to 0.5mm within seconds or minutes (Joseph et al. 2010). This means that it was possible to study simultaneous damage-healing behaviour in relatively short-term tests (i.e. test durations of 1 to 10 minutes), which facilitated the relatively large testing programme undertaken. It is worth mentioning that when domestic CA is used in a contact situation, in which two surfaces are pressed together and separated by a relatively thin film (i.e. 0.01-0.03mm) of CA, significant healing (bonding) takes place in a few seconds, whereas in openings greater than 0.1mm (up to 1mm), it can take several seconds or minutes before detectable healing occurs (Tomlinson et al. 2006). The CA used in this study has a relatively low viscosity (< 5cps) and a significant surface tension (0.034N/m), which facilitates its flow into micro and macro cracks (see Section 3.3.2). The flow network, which acts as the healing agent delivery system, is illustrated in Figure 3.1.

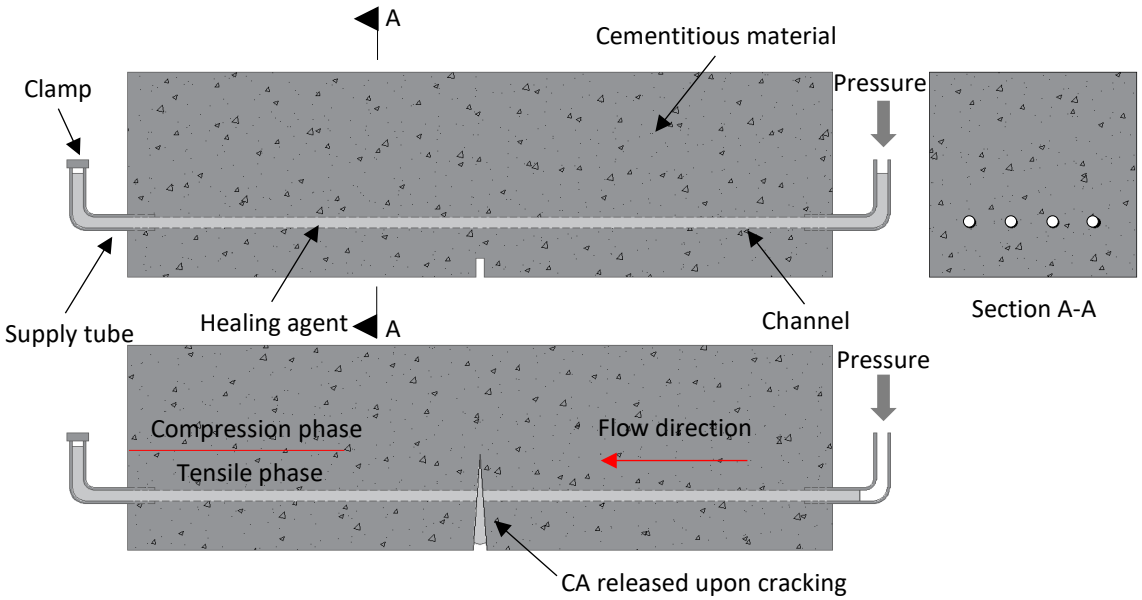

Figure 3.1. Generic autonomic vascular healing system

The network channels were formed using the method proposed by Davies et al. (2015; 2018), whereby PET tubes (4mm outer diameter and 3mm internal diameter) were cast into the specimens and subsequently removed to create hollow channels (see Section 3.3.3 below for more details). The

following section gives the material data and the experimental procedures used for the tests in Groups A to F.

3.3 Experimental programme

3.3.1 Concrete mix and mould preparation

The details of the mix ratio and materials used in this study are shown in Table 3.1. The standard concrete mix was designed in accordance with the BRE concrete mix design method (Teychenné et al. 1997). The quantities of the materials used in each batch were adjusted to account for the water absorption and moisture content of the coarse and fine aggregate, whilst maintaining a water/cement ratio of 0.46. This achieved a target slump value of between 110-130mm, which was in accordance to BS EN 12350-2:2009.

The coarse aggregate consisted of 4-10mm crushed limestone whereas the fine aggregate comprised 0-4mm natural sea-dredged sand with 0-2mm diameter limestone dust. The cement used was CEM II/A-L 32, 5R containing 80-94% of clinker, 6-20% of limestone and up to 5% of secondary constituents complying to BS EN 197-1 classifications. A maximum aggregate size of 10mm was used to ensure that the concrete was able to fill the spaces in between the PET tubes in the mould (see Figure 3.2). The materials were weighed and placed into plastic buckets prior to mixing. Concrete mixing was undertaken in a Belle Premier 200XT Mixer with a maximum drum and mixing capacity of 400 and 220 litres respectively.

Table 3.1. Concrete mix design details

Materials	**Cement**	**Coarse aggregate**	**Fine aggregate**	**Water**
Origin	Portland-limestone cement (CEM II/A-L 32, 5R)	Crushed limestone	Crushed marine sand with limestone	Tap water
Size (mm)	-	4 - 10	0 - 4	-
Mix ratio	1	2.1	1.55	0.46
Concrete (kg/m^3)	470	986	728	216

The twin moulds for the small-scale laboratory specimens in Groups A and B (see Figure 3.2) and the wooden mould for the large-scale laboratory specimens in Group C (reported in Chapter 4) had four pre-drilled holes in the mould stop-ends. By contrast, eight pre-drilled holes were required to form the two layers of channels used in the Group D to F series of tests (see Figure 4.3 in Chapter 4). The PET tubes were included to form flow networks. These tubes were lightly tensioned by hand and secured with crocodile clips. The moulds were lightly coated with grease to facilitate demoulding. The concrete mix was placed in the mould in three equal layers and compacted using a vibrating table. The

surface of the wet concrete was smoothed with a trowel as shown in Figure 3.3. The specimens were then demoulded, and the PET tubes removed the following day. It was found that the PET tubes could be pulled out by hand with relative ease.

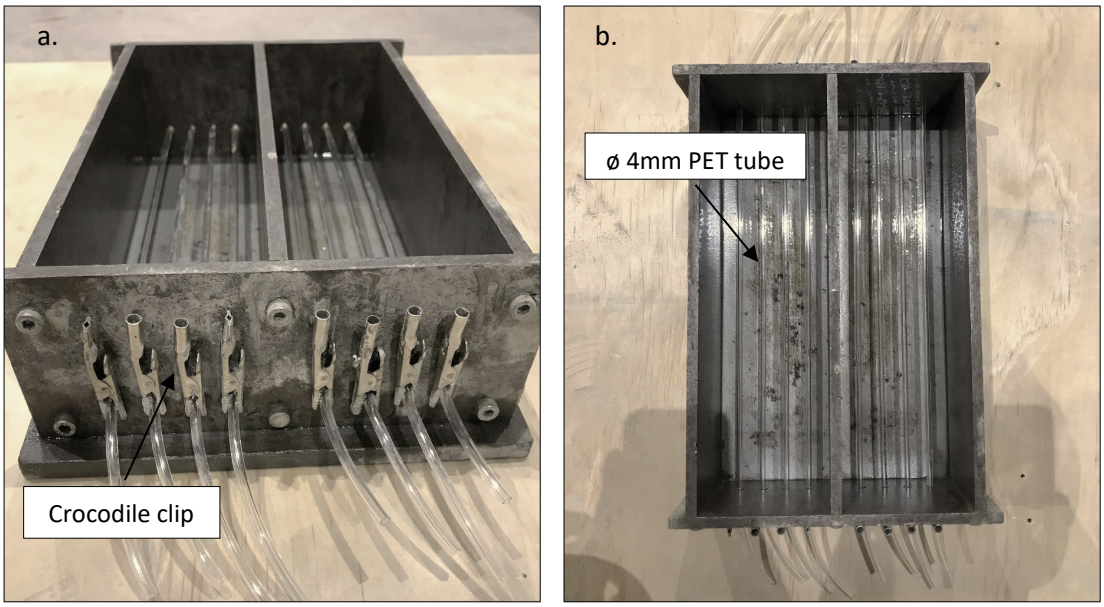

Figure 3.2. Specimen preparation for Groups A and B with twin moulds before casting (a) showing crocodile clip and (b) 4mm PET tube

3.3.2 Healing agent

The Procure PC20 CA (see Table 3.2) from AdCo Ltd has a quoted shelf-life of 12 months if stored at 5°C, and the safety and technical data sheets for this healing agent are included in Appendix B. The term CA is used throughout Chapters 3 and 6 to signify PC20 CA; however, in Chapter 7 a more specific designation is used since other cyanoacrylates are considered. CA requires moisture (OH^- ions) to cure and the curing rate accelerates in a highly alkaline environment, such as that found within a concrete matrix (Joseph et al. 2010). For this reason, the channels were dried prior to testing.

Table 3.2. Properties of Cyanoacrylate, Procure PC20

Chemical type	Ethyl
Appearance	Clear
Specific gravity	1.06
Viscosity (Ns/m^2)	0.004
Tensile strength (MPa)	21
Surface tension (N/m)	0.033
Shelf life at 5°C (months)	12

3.3.3 Curing regime and specimen preparation

The specimens underwent 5 days of water curing in a water tank, were oven dried for 1 day at a temperature of 90°C and allowed to cool at room temperature for another day. A nominal age of 8 days was chosen for testing unless noted otherwise. An oven temperature of 90°C was selected in order to accelerate hydration and remove the majority of the capillary water. At this temperature, little or no thermal damage can be expected (Gardner et al. 2005). It is also important to minimise any potential interaction between CA and excess capillary water to prevent polymerisation occurring before CA flows into the cracks (Joseph et al. 2010).

Once cured and demoulded, the specimens were notched (3mm width and 7mm depth) using a diamond blade masonry table saw (Controls Cernusco model 55-CO210/D) (see Figure 3.5 for Groups A and B, and Figure 4.2 in Chapter 4 for Groups C to F). The channels adjacent to the specimen ends were then enlarged to a diameter of 6mm for a depth of 10mm. Pressurised air was used to clean the channels and to remove any concrete dust before a set of 250mm long PET supply tubes were glued into position using CA. These supply tubes had an outer diameter of 6mm and an inner diameter of 4mm. Steel knife edges were then bonded to the underside of the specimen either side of the notch to accommodate a CMOD transducer. In addition, an aluminium arm and angle bracket were (see Figure 3.6) were attached to the specimen to support a linear variable displacement transducer (LVDT).

Figure 3.3. Specimen preparation for Groups A and B with twin moulds after casting

3.3.4 Healing agent and pressurising system

The healing agent was pressurised using a pressurised airline, which was connected to pressure regulator (SMC IR3000-03BG-R) with a 6mm diameter PET tube (see Figure 3.4). The system also included a pressure transducer connected to a computer in order to provide an accurate pressure reading. The flexible tubes were attached to an inlet manifold with multiple outlets to tee connectors which were then fastened to the PET supply tubes of the specimen. The pressure was applied to each of the PET supply tubes at one end of the specimen. The pressure varied between 0 bar to 1 bar depending on the test carried out. Each of the PET supply tubes were individually locked off using plastic clamps once the channels were empty. The PET supply tubes for the unpressurised (0 bar) tests were left open to the atmosphere. This avoided any negative suction pressures developing in the CA, which have been reported to occur when closed channels have been used (Joseph et al. 2010).

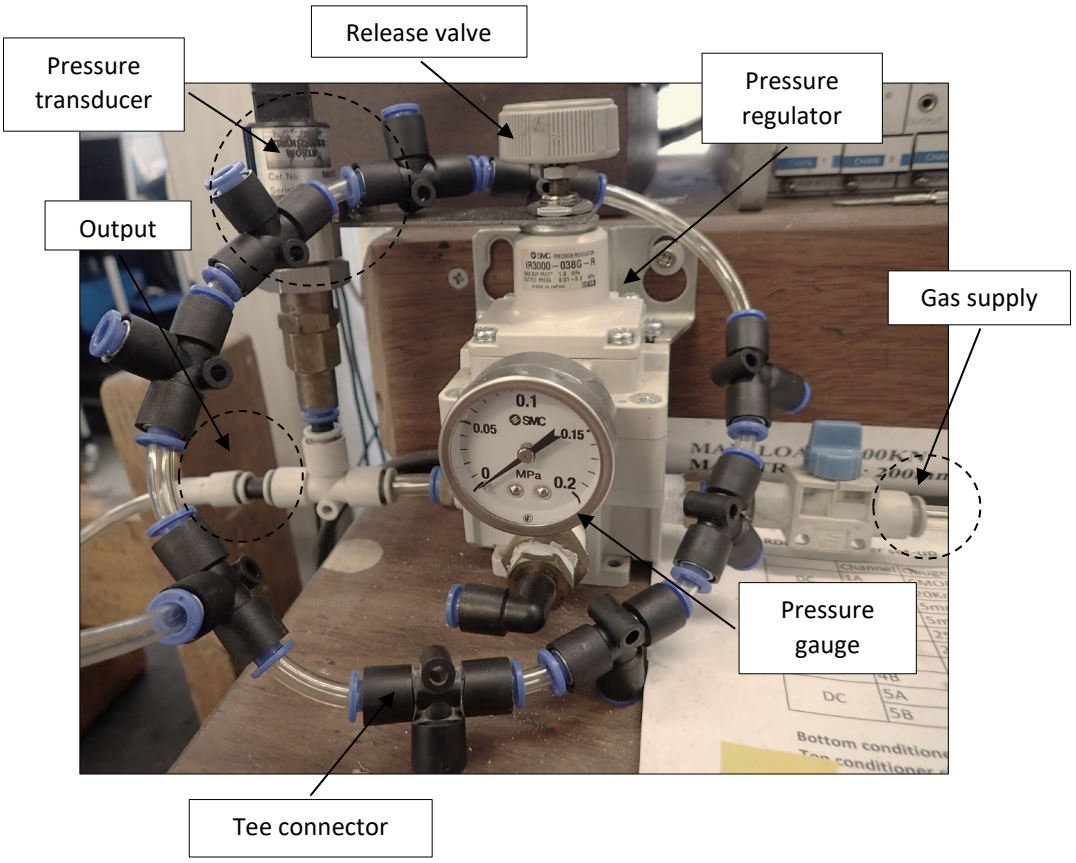

Figure 3.4. Pressure gauge

3.3.5 Testing procedure

The concrete cubes were tested using a calibrated Controls Automax 50-C52D02 machine following the BS EN12390-3:2009 standard. The specimens were tested on the face perpendicular to the cast face at a loading rate consistent with a stress rate of 0.5MPa/s. The reading at failure is assumed to be associated with the maximum compressive strength of the specimen. The same machine was also used for the cylinder splitting tests. The bearing blocks and other fixtures necessary were installed to allow the tests to be carried out according to BS EN12390-6:2009. The loading rate was consistent with a stress rate of 0.1MPa/s. The maximum load is assumed to be associated with the splitting tensile strength of the concrete. It is generally accepted that the true tensile strength (f_t) is approximately 0.85 times the f_{cyl}, (i.e. f_t = 0.85 f_{cyl}) and the true uniaxial strength (f_c) of 0.8 times the cube strength (f_{cu}) (i.e. f_c = 0.8 f_{cu}) (Neville 2012).

The three and four-point flexural bending tests were carried out using an Avery Denison 7152 Universal Hydraulics testing machine, with either a 20kN or 100kN load cell depending on the size of the specimens, using a displacement-controlled feedback loop. A similar procedure for supplying healing agent was used for all specimens containing CA, which allowed the CA to be supplied at either atmospheric or at an elevated pressure. This is explained as follows:

- Prior to testing, the PET supply tubes were filled with CA (except for Group B);
- For the pressurised specimens, the PET supply tubes were connected to the pressurised airline (at 0.5 bar) and the pressure regulator (as discussed in Section 3.3.4) which allowed different pressures to be applied, whist the PET supply tubes at the other end of the specimen were clamped to prevent CA from flowing out of the specimen (see Figures 3.5 and 3.6);
- For the unpressurised specimens, both sides of the PET supply tubes were left open to atmosphere;
- The PET supply tubes on the specimen were individually locked off using plastic clamps as soon as the channels were empty.

The CMOD clip gauge attached to the knife edges was used to measure the crack opening whist, the LVDT placed onto the aluminium angle bracket was used to measure the central deflection of the specimens. The loadings on all specimens were controlled using feedback from either the CMOD clip gauge or the LVDT. A plastic container filled with sand was also placed underneath the beam to absorb excess CA during the course of testing. The details of the experimental series with their respective parameters will be discussed in the following sections (Groups A and B in Chapter 3 and Group C to F in Chapter 4). The control specimens used the same loading rates and pause periods (or healing period in Group B) for the test series within the associated groups.

Table 3.3. Summary of the experimental details in Chapters 3 and 4

Description	**Group/ Chapter/ Section**	**Set(s)**	**No. and size of specimens (mm)**	**Controlled displacement rate (mm/s)**	**Pressure applied (bar)**	**Healing period (mins)**
Continuous loading on variable crack opening rates and CA pressure under 3-point flexural bending tests	**A Chapter 3 Section 3.4**	1 to 3	27 x self-healing (75x75x255) 9 x controls (75x75x255) 9 x cubes (100x100x100) 9 x cylinders (200xø100)	0.0002 0.0005 0.001 0.002	0 0.1 0.3 0.5 1.0	Variable
Paused loading on variable fixed crack healing period under 3-point flexural bending tests	**B Chapter 3 Section 3.5**	4 and 5	9 x self-healing (75x75x255) 3 x controls (75x75x255) 3 x cubes (100x100x100) 3 x cylinders (200xø100)	Gradual increase (from 0.0002 to 0.001)	No	2 5 10 15 30 60
Continuous loading under 4-point flexural bending tests with (vertically and/or laterally) offset discontinuous reinforcement	**C Chapter 4 Section 4.4**	6	4 x self-healing (100x100x500) 4 x controls (100x100x500) 3 x cubes (100x100x100) 3 x cylinders (200xø100)	0.002	0.5	Variable
	D Chapter 4 Section 4.5	7	4 x self-healing (100x100x500) 3 x controls (100x100x500) 3 x cubes (100x100x100) 3 x cylinders (200xø100)	0.002	0.5	Variable
	E Chapter 4 Section 4.5	8	4 x self-healing (100x100x500) 3 x controls (100x100x500) 3 x cubes (100x100x100) 3 x cylinders (200xø100)	0.002	0.3	Variable
	F Chapter 4 Section 4.6	9	4 x self-healing (100x100x500) 3 x controls (100x100x500) 3 x cubes (100x100x100) 3 x cylinders (200xø100)	0.002	0.3	Variable

3.3.6 Compressive and tensile values

The average compressive and tensile strengths along with the coefficient of variance (CoV) of the specimens in Groups A and B for sets 1 to 5 are shown in Table 3.4.

Table 3.4. Summary of concrete strengths after 8 days of curing in Chapter 3

Set	Average cube strength, f_{cu} (MPa)	CoV (%)	Average cylinder splitting strength, f_{cyl} (MPa)	CoV (%)	True uniaxial strength, f_c (MPa)	True tensile strength, f_t (MPa)
1	42.0	1.6	3.6	7.3	33.6	3.0
2	38.1	1.8	2.8	9.4	30.5	2.4
3	38.7	2.9	3.3	4.0	30.9	2.8
4	39.2	1.1	3.2	6.3	31.4	2.7
5	41.0	1.2	3.7	2.5	32.8	3.1

3.4 Group A: Varying crack opening rates and CA supply pressures

The details of the test series in Group A can be found in Table 3.3. The general arrangements and the dimensions of specimen are shown in Figure 3.5. The specimens from set 1 were tested at an age of 12 days due to a mechanical malfunction of the testing machine. Figure 3.6 shows the testing setup of the specimens used throughout this experiment.

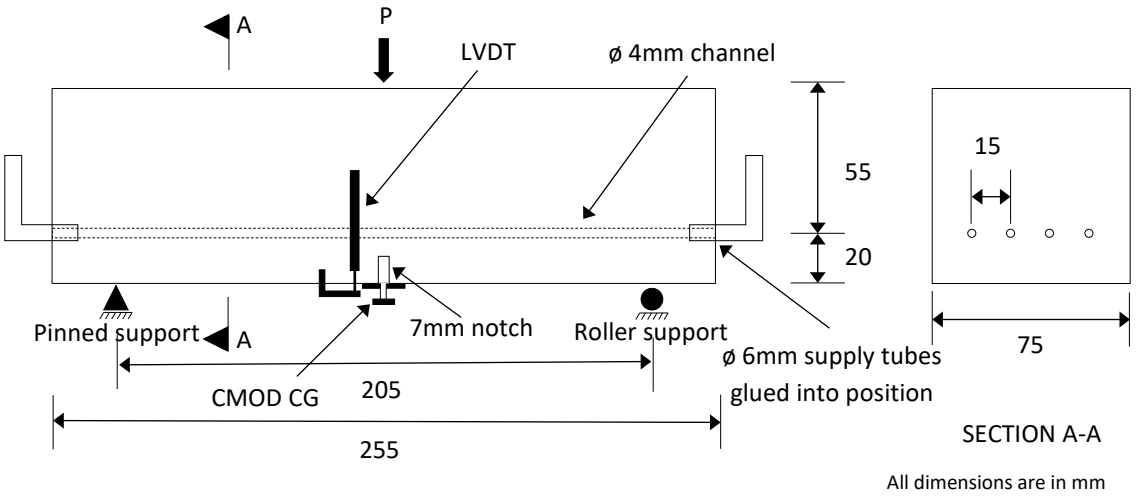

Figure 3.5. General arrangements for Groups A and B

The primary focus of this investigation was to explore the interaction between damage and healing under varying crack opening rates and CA supply pressures. The former measured the response of the specimens to continuous loading with the rate of loading being governed by the constant CMOD rate selected for each set of tests. A range of loading rates (see Table 3.3) were predetermined that ensured the damage and healing processes overlapped. The latter considered if capillary pressure

alone would be sufficient to transport the healing agent to the damage regions or whether it was beneficial for it to be pressurised and if so, to determine the optimum delivery pressure for the specimens considered in this study (see Table 3.3).

The hollow channels for the specimens in Groups A and B were created as shown in Figure 3.2. The central notch, introduced into all specimens, ensured that a crack initiated at the notch and propagated upwards as a primary mode I crack. A point load was applied at the centre of the beam as seen in Figures 3.5 and 3.6. The results from these test series are reported in Section 3.4.1.

The experimental procedure for the Group A test series with continuous loading is as follows:

- The CA supply system was set up as detailed in Section 3.3.5 with the CA initially being isolated from the specimen by plastic clamps;
- The CA supply was turned on;
- The specimen was loaded to maintain the designated loading rate (CMOD rate) until a maximum CMOD of 0.3mm was reached;
- The CA supply was turned off, following unloading and the remaining CA was drained from the specimen.

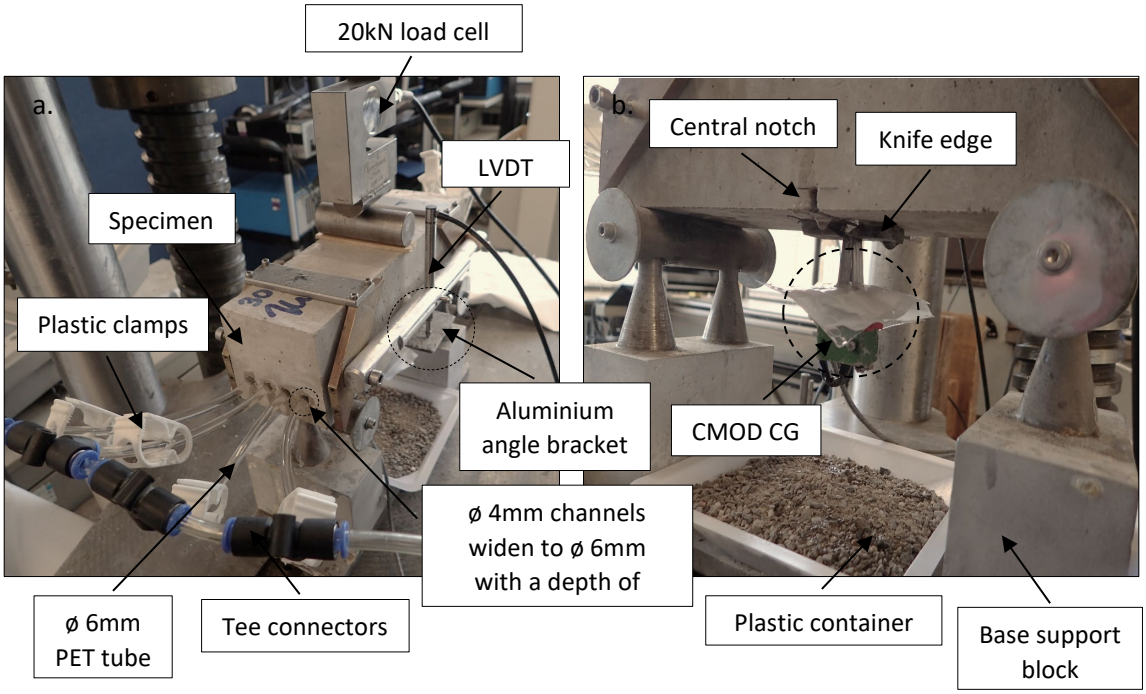

Figure 3.6. Testing arrangements for Groups A and B

3.4.1 Results and discussion

This section presents representative results from the Group A and B series of tests, with the full set of experimental results being given in Appendix A.

3.4.1.1 Effect of varying loading rates

The results for the variable CMOD rates are given in Figure 3.7(a-b), Figure 3.7(c-d), Figure 3.7(e-f) and Figure 3.7(g-h) for 0.0002mm/s, 0.0005mm/s, 0.001mm/s and 0.002mm/s tests respectively. The supply pressure was kept constant at 0.5 bar throughout each test. A representative control specimen for the associated CMOD rates is also plotted in the load-CMOD and load-displacement responses in Figure 3.8 for comparison.

It is clear, by comparing the results of the self-healing (SH) specimens with those of the corresponding control specimens in Figure 3.7 that significant healing occurred in all cases. The graphs in Figures 3.7 showed considerable variability both within the tests and between tests, and it is noticeable that the damage-healing responses become smoother when the loading rate increases. This is because as the loading rate increases so does the rate at which the healed material is restressed. Therefore, each component (or elemental area) of healed material reaches the re-damage threshold more quickly and, in any one location, the relative area of healed material that has reached this threshold is less. As a result, there were smaller jumps in the response due to re-healing and re-damage.

Additionally, slower loading rates (i.e. 0.0002mm/s and 0.0005mm/s) also allowed more time for the less viscous CA to polymerise which led to more pronounced peaks than those of the faster loading rate tests (i.e. 0.001mm/s and 0.002mm/s). The SH specimens also showed an increase in stiffness response after the initial cracking peak, relative to the control response, as well as an increase in the unloading stiffness. Joseph et al. (2010) suggested that this could be due to the rapid curing and hardening of CA at the crack surfaces that acted as a wedge and contributed to a higher CMOD values for the SH specimens at unloading. It was also evident that the CA started flowing into the cracks soon after the initial cracking peak, since healing occurred at a lower crack width at faster loading rates. This is believed to be due to there being less time for curing in the tests conducted at faster loading rates. It is believed that the SH specimens indicated multiple damage-healing events and that damage and healing progressed simultaneously. Bazant and Gettu (1992) showed that the rate of loading affects the fracture softening response of plain concrete, with the post peak response being more ductile and peak strength increasing with loading rate. This effect is seen in these tests, as illustrated in Figure 3.8.

It was also found that the CMOD and displacement values at which the response of the SH specimens starts to depart from that of the control specimens varied between tests. This occurred because the crack adjacent to the supply channels needs to reach a certain threshold before CA was released into the crack. There is also a lag in time from when the CA first flow into the crack to the point where healing actually began. It is estimated that the threshold for CA transport is between a crack opening of 0.03mm and 0.05mm. Additionally, it is suggested that there is a tendency for CA pipes to form in the channels, as illustrated in Figure 3.9. Although, the thickness of these CA pipes was negligible, due to the duration of the tests but if the SH specimens were left for longer (i.e. hours or days), the formation of the CA pipes becomes more distinct. It is possible that the CA pipes may have influenced the time and crack opening at which CA first enters the crack.

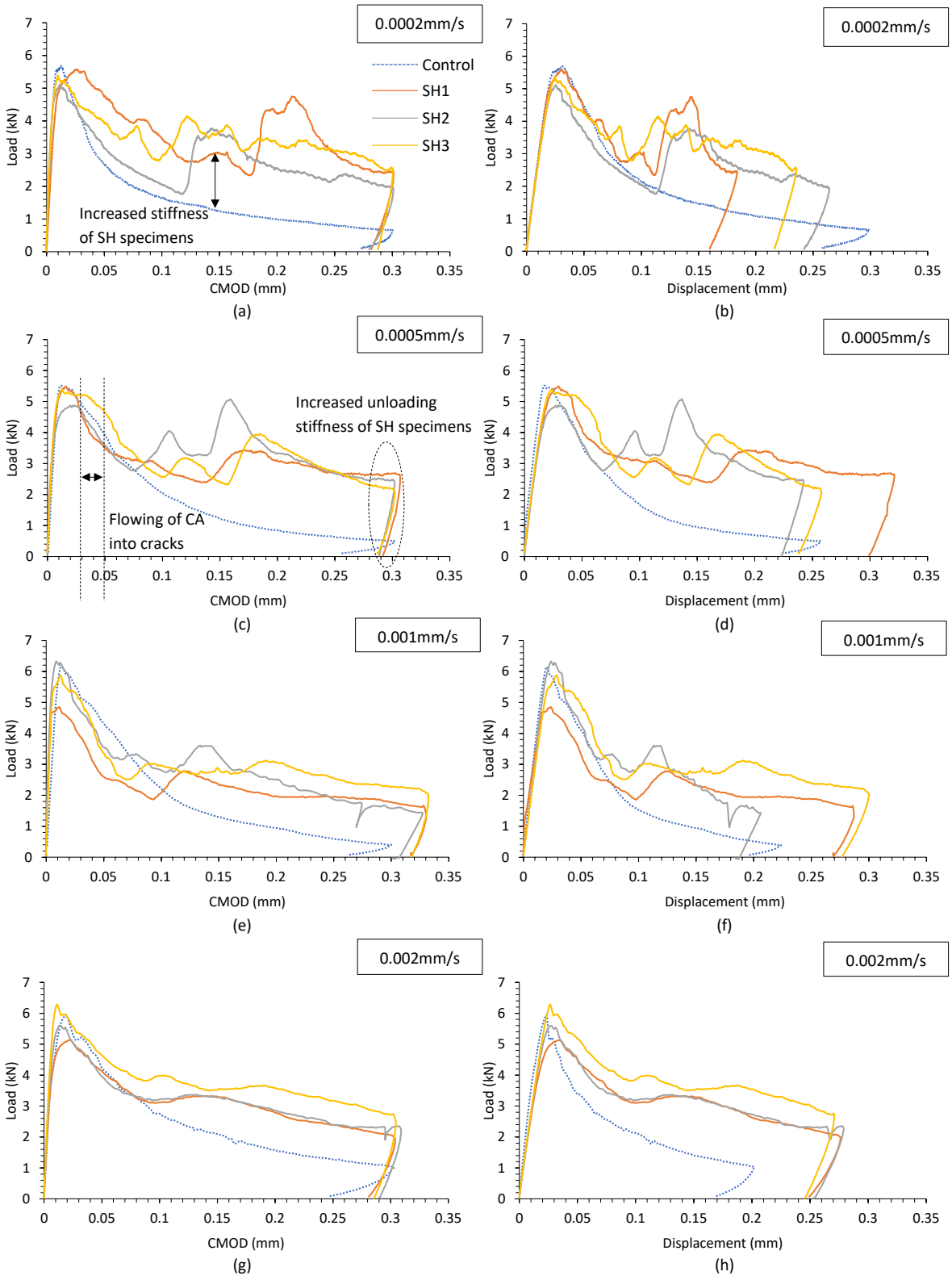

Figure 3.7. Load-CMOD and load-displacement responses at loading rate of (a-b) 0.0002mm/s, (c-d) 0.0005mm/s, (e-f) 0.001mm/s and (g-h) 0.002mm/s (Group A)

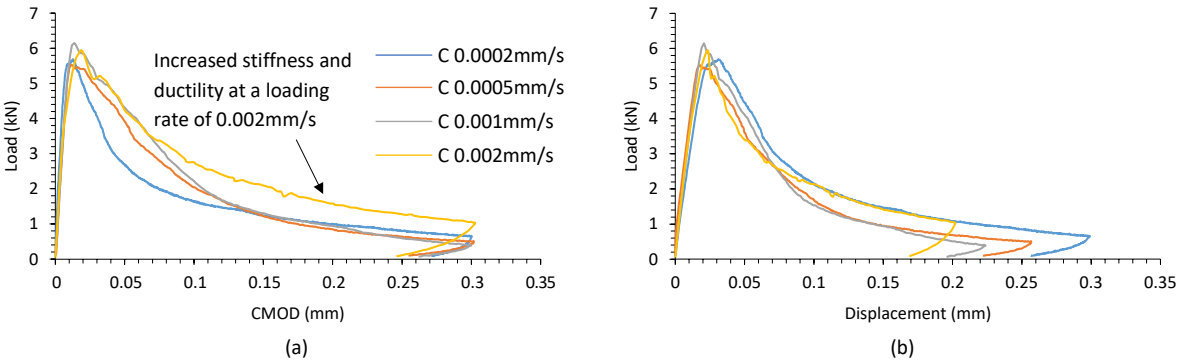

Figure 3.8. Controls at different loading rates (Group A)

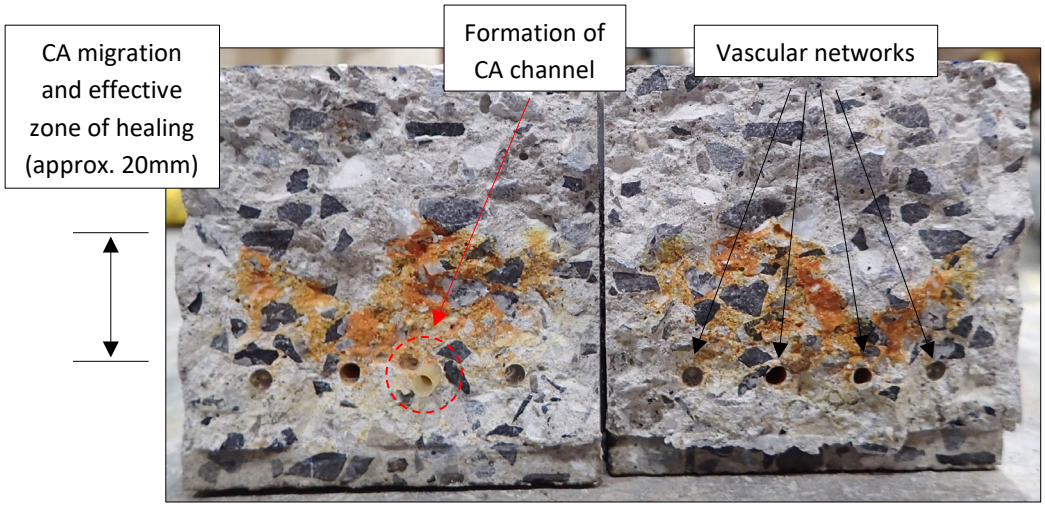

Figure 3.9. Two halves of a broken SH beam shown side by side indicating the extend of CA curing and formation of CA channels (circled)

3.4.1.2 Effect of varying pressures

The results for the variable pressures are given in Figure 3.10(a-b), Figure 3.10(c-d), Figure 3.10(e-f), Figure 3.11(g-h) and Figure 3.11(i-j) for 0 bar, 0.1 bar, 0.3 bar, 0.5 bar and 1 bar respectively. The loading rate was kept constant at a CMOD rate of 0.001mm/s throughout each test. The reference responses of the control specimens are also included in the load-CMOD and load-displacement responses in Figures 3.10 and 3.11.

It was suggested that significantly lower healing was recorded for specimens which solely relied on capillary tension to transport the healing agent into the crack (i.e. 0 bar) while the specimens which showed the most healing had a CA supply pressure of 0.3 bar. The post peak responses stayed below 2.5kN for specimens without pressure (i.e. 0 bar) where visible healing was only seen after 0.1mm crack opening upon which CA was able to flow and wick into crack because of capillary action. Conversely, there was a tendency of CA to flow out of the sides of the cracks at higher pressure (i.e. 1 bar) which implies that the body of healing fluid in the crack was in a flux and therefore less likely to cure. Pressure is required to assist the capillary action of CA in cementitious materials whereby when

applied, CA was able to accelerate glue flow into microcracks more efficiency for healing to occur. Based on the results, the SH specimens with 0.3 to 0.5 bar supply pressures at this CMOD rate (i.e. 0.001mm/s) were found to be the most effective to obtain a more consistent damage-healing response. Additionally, the CMOD and displacement (and time) at which measurable healing commences reduces as the delivery pressure increases which is believed to be due to the fact that pressurised liquid will flow through a smaller opening than unpressurised liquid. As would be expected, there is an increase in stiffness and ductility, also upon unloading.

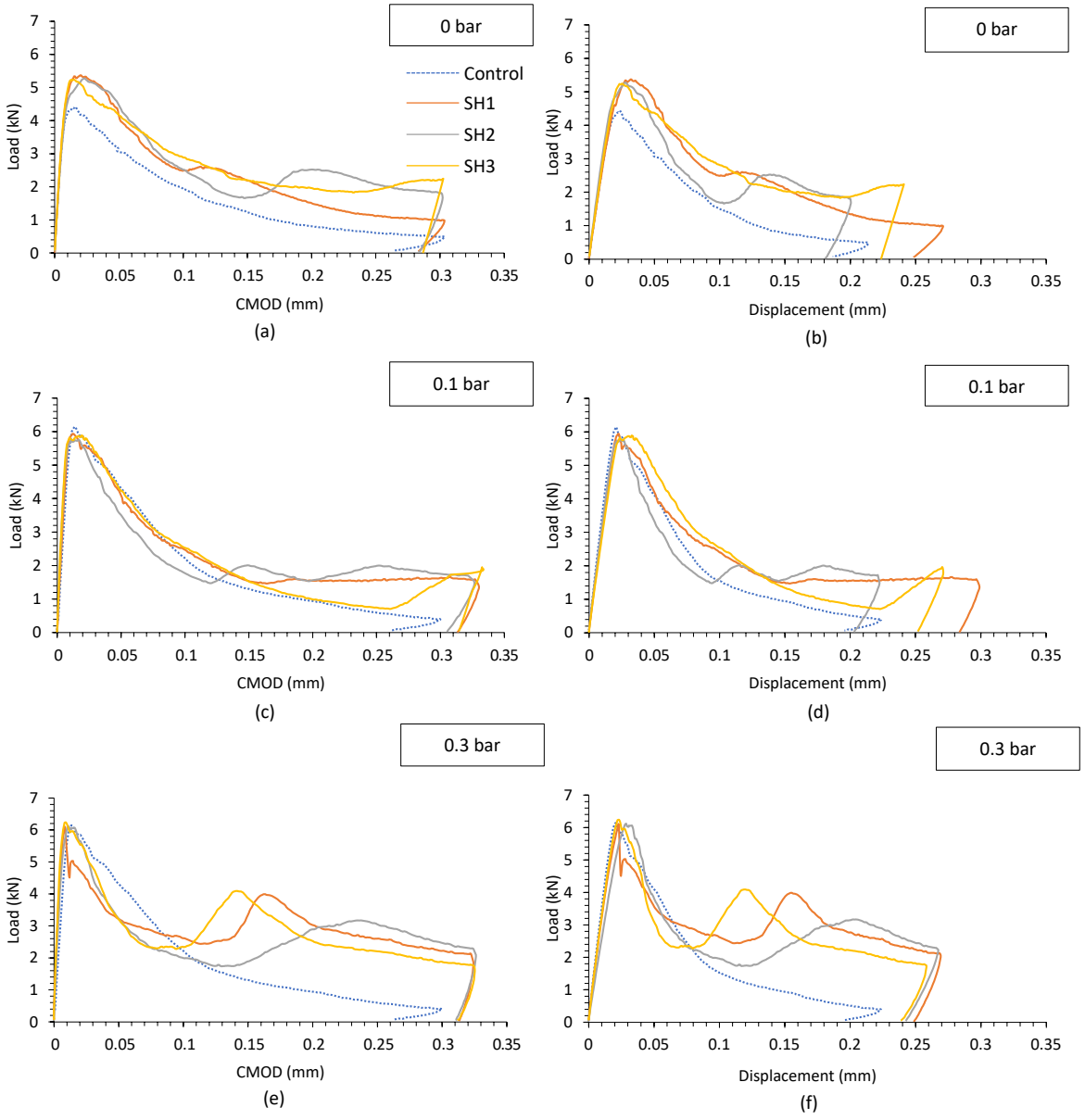

Figure 3.10. Load-CMOD and load-displacement responses at pressure of (a-b) 0 bar, (c-d) 0.1 bar and (e-f) 0.3 bar (Group A)

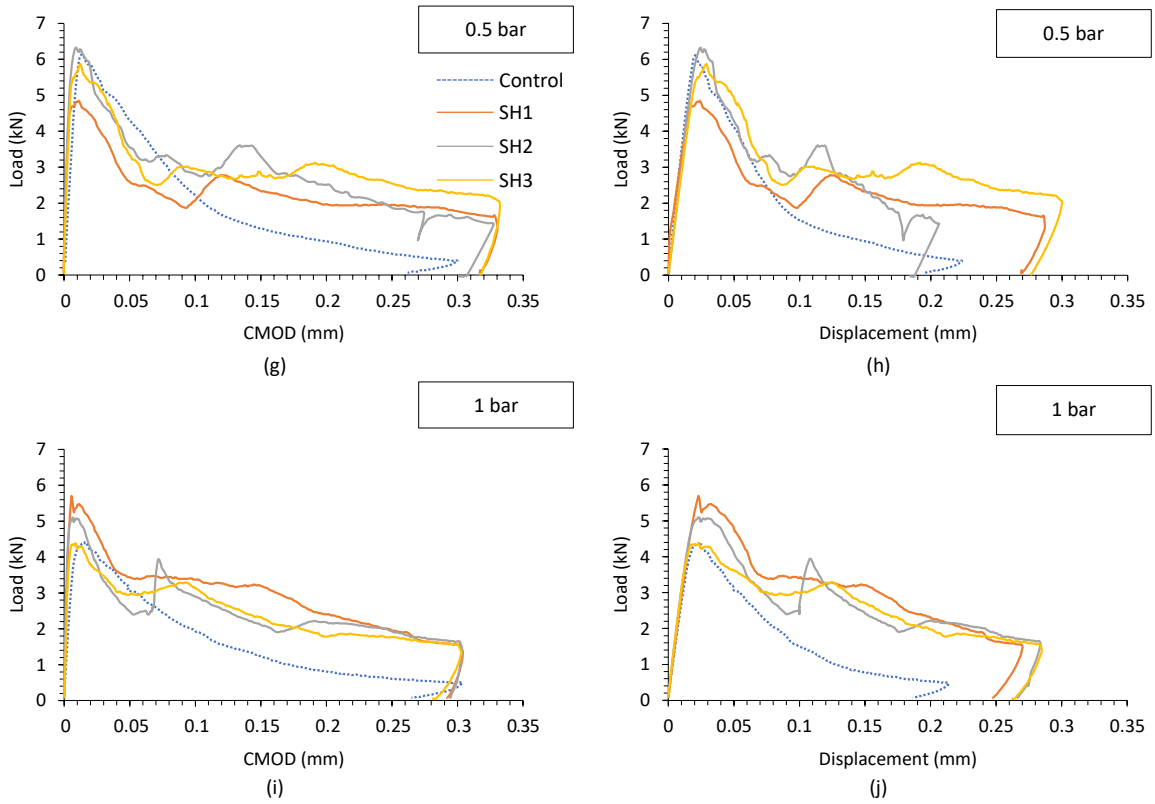

Figure 3.11. Load-CMOD and load-displacement responses at pressure of (g-h) 0.5 bar and (i-j) 1.0 bar (Group A)

3.4.1.3 Effect on damage-healing responses

The load-CMOD-displacement results in Figures 3.7, 3.10 and 3.11 showed that there were major variations in the damage-healing responses in cementitious materials when different loading rates and pressures were used. For example, an increase in loading rate shows a corresponding increase in the crack opening which allows healing to occur at a lower crack width. CA was also able to flow, due to capillary forces and pressure, into cracks much quicker with a faster loading rate and also allow it to fill and seal smaller cracks. It was also found that increasing the loading rate decreases the healing response thereby causing a decrease in the stiffness response shown by smoother peaks. This may be due to the effects the faster loading rate has on the rapid curing and hardening of CA between crack surfaces. A faster loading rate also showed a more regular damage-healing response, where the healing occurred at a rate similar to the damage rate. The effect of pressure was also evident where too much or too little pressure affects the damage-healing responses. The results suggested that the optimum pressure for achieving simultaneous damage and healing was between 0.3 and 0.5 bar with a CMOD rate of 0.001mm/s, for small scale laboratory specimens.

3.4.1.4 Healing indices

The degree of healing can be quantified using healing indices which is taken from the difference between the recovered strength and the peak strength. For the present work, the healing recovery (c) is quantified using an index proposed by Homma et al. (2009) (see also Ferrara et al. 2014; Davies et al. 2018), which may be expressed in the form of equation (3.1).

$$c = \frac{P_2 - P_0}{P_1 - P_0} * 100\% \tag{3.1}$$

This equation is typically used for a single measurement point. However, by taking P_1 as the peak load of the control and allowing P_2 and P_0, the corresponding loads of the SH beam response and control specimen at the same CMOD values, a time-varying healing index can be evaluated, as shown in Figure 3.12. The value of the healing recovery, c is the percentage of healing of the specimen during continuous damage. Values of c greater than 100%, indicate that the healed material has a higher strength than the original matrix.

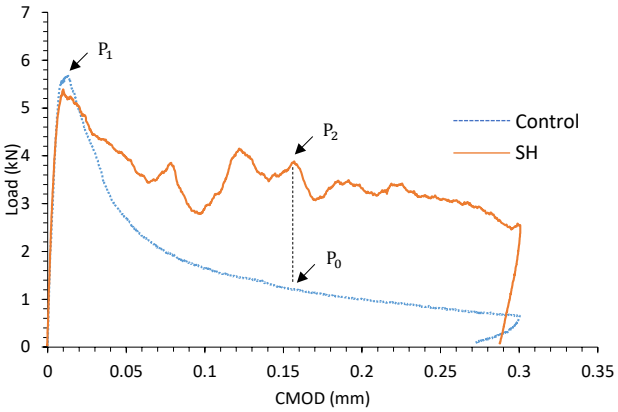

Figure 3.12. Healing index

Graphs of healing index plotted against the CMOD, for all of Group A tests, are given in Figures 3.13 and 3.14. In most cases, the highest healing recovery was recorded after the initial cracking peaks. This increase was usually coincided with the drop-in CA level in the PET supply tubes, signifying that the CA started to flow into the centre of the beam soon after cracking occurred. The findings suggest that the small crack width would have aided the curing of the CA to form stronger bond between the two crack surfaces as the layer of the CA was thinner, hence, achieving a greater healing recovery. Slower loading rates (i.e. 0.0002mm/s and 0.0005mm/s) suggested a higher healing recovery compared to the faster loading rate (i.e. 0.001mm/s and 0.002mm/s) but there was no positive correlation between the damage and healing responses. The SH specimens subjected to faster loading rates also fluctuated the least, approximately by 20% suggesting simultaneous damage and healing. CA was also able to flow into the cracks at the centre of the beams rapidly at a faster loading rate thus, achieving simultaneous damage and healing and showed the most conclusive results.

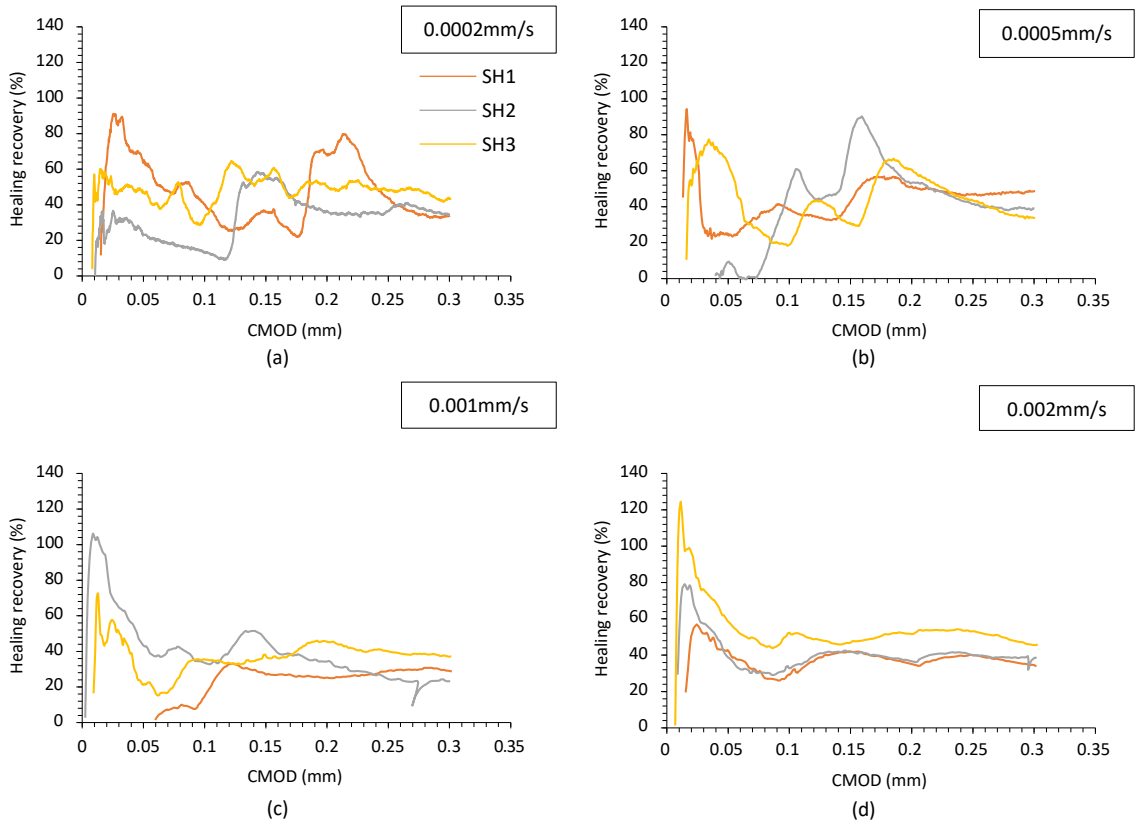

Figure 3.13. Healing recovery at loading rate of (a) 0.0002mm/s, (b) 0.0005mm/s, (c) 0.001mm/s, and (d) 0.002mm/s (Group A)

The SH specimens without or with low pressures (i.e. 0 bar, 0.1 bar) was insufficient to assist CA to flow into cracks, hence these specimens showed significantly lower healing. More consistent healing was achieved with the SH specimens subjected to 0.5 bar of pressure where healing took place soon after damage occurred. Despite this, too much pressure could also be a disadvantage where the SH specimens with a supply pressure of 1 bar showed the least healing recovery after the initial cracking peak where the response stayed reasonably low. From these results, it is concluded that a supply pressure of between 0.3 to 0.5 bar is optimal for the present specimens.

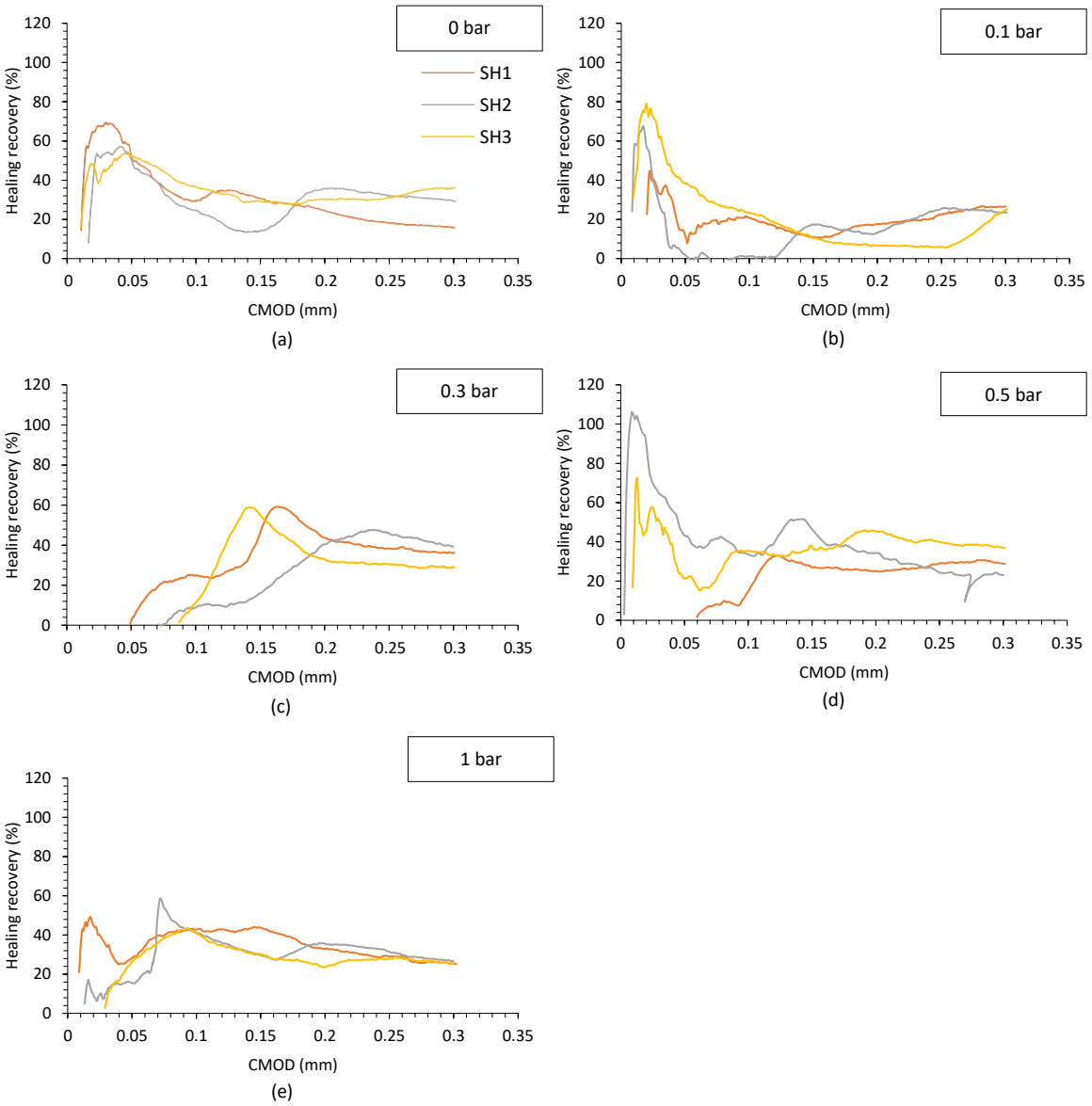

Figure 3.14. Healing recovery at pressure of (a) 0 bar, (b) 0.1 bar, (c) 0.3 bar, (d) 0.5 bar, and (e) 1.0 bar (Group A)

3.5 Group B: Fixed crack healing periods

This study expands on previous investigations to determine the degree of healing in specimens that contained a single stationary macrocrack. Each of these cracks was formed before the healing agent was released and then the specimens were held at a fixed crack opening displacement for a selected period of time (see Table 3.3) prior to being loaded to failure. The same fixed crack opening displacement was used throughout this test series. The mix design, the methods of including the channels, and the notching procedure for this study have already been discussed in Section 3.3. The details of the test series in Group B can be found in Table 3.3. The specimens were prepared similarly to those of Group A, illustrated in Figures 3.5 and 3.6 but in this case the specimens were not subjected to pressure and were only dependent on capillary forces to drive CA into the cracks.

Based on the outcomes of the preliminary studies in Section 3.5.1 below, the sequence of testing for specimens in Group B was also slightly different from that used in the Group A tests. The experimental procedure for the Group B test series with paused loading is as follows:

- The specimen was loaded at a CMOD rate of 0.001mm/s until a discrete central crack had formed and reached a CMOD of 0.15mm;
- The loading was then paused, and the CA supply was activated;
- The specimen was held (via feedback loop) such that the CMOD remained at the designated value for the required healing period;
- At the end of the healing period, the loading was resumed by gradually increasing the CMOD rate from 0.0002mm/s to 0.001mm/s until a CMOD value of 0.4mm was reached;
- The specimen was unloaded, and the remaining CA drained from the specimen.

The PET supply tubes were clamped on both sides at the end of the fixed healing period to prevent further CA flowing into the crack. The following section examines the main issues related to this study followed by a discussion of the Group B test results.

3.5.1 Preliminary investigations

Two sets of trial tests were carried out on 12 small scale laboratory specimens. The aim was to investigate the post-healing response of cementitious specimens, with CA as a healing agent, for certain crack openings (i.e. a CMOD of 0.15mm in the present case). The load-CMOD and load-displacement responses for different healing periods are shown in Figure 3.15. The specimens were prepared in a similar way as those in Group A until the testing; the only exception was that, the specimens were air cured for further 14 days and tested at 21 days. They were loaded in three-point flexural bending. The loading of the specimens was controlled using feedback from the CMOD clip gauge. The initial loading stage progressed until the CMOD reached 0.15mm, after which the specimen was unloaded. The CA was allowed to flow through the channels via the PET supply tubes which were left open to atmosphere. The specimens were then taken out of the testing machine and left to healing for the defined healing period (i.e. 10mins, 60mins, and 24hours), after which they were reloaded until the CMOD reached 0.4mm, at which point they were unloaded.

The post-crack CMOD rate employed for these tests was 0.001mm/s. It was found that some specimens (see Figure 3.15) failed during the reloading stages most likely due to the sudden increase in the loading rate at 0.001mm/s and hence, the loading rate was ramped up slowly from 0.0002mm/s in the Group B test series. The specimens became more brittle (i.e. at 10mins and 60mins), particularly in the reloading stages, because the uncured CA was still flowing into the cracks due to the open ends. Therefore, it was found better to seal the PET supply tubes at the end of the fixed healing period in order to avoid failure and to get a pure post-healing response. The results also suggested that shorter healing periods would be sufficient for the majority of healing to occur, since all of the healing periods resulted in similar secondary peak loads of between 4 to 5kN.

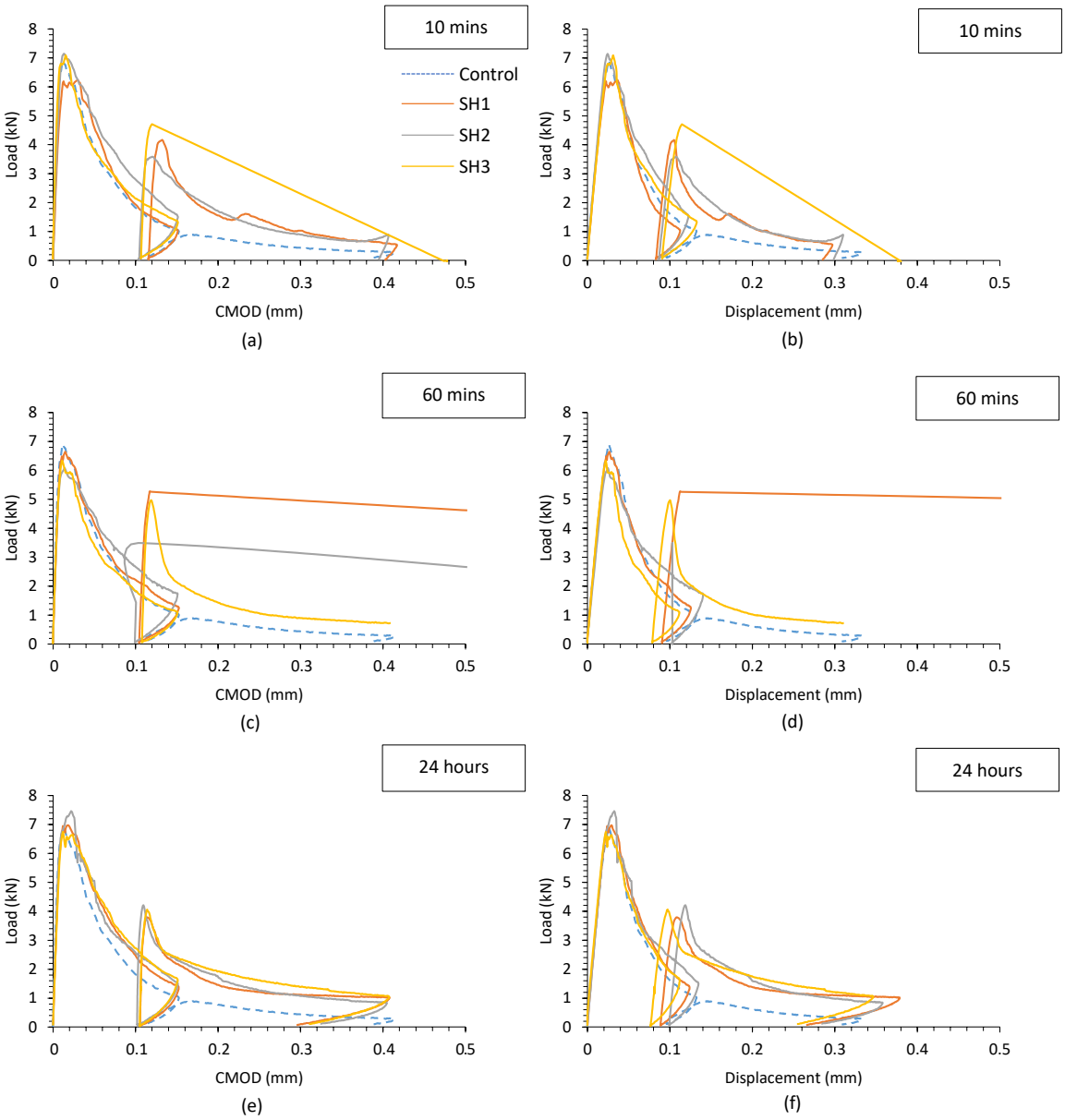

Figure 3.15. Load-CMOD and load-deflection responses at different healing periods for first trial test (a-b) 10mins, (c-d) 60mins and (e-f) 24hours

A different testing procedure was used for the second trial tests, which were tested on the 8th day after casting. As with the first trial set, the load was controlled using feedback from the CMOD clip gauge and loaded until the CMOD reached 0.15mm but this time the specimens were not unloaded but rather the CMOD of 0.15mm was maintained constant for the fixed healing period, with the periods now being 10mins, 60mins, and 120mins. At the end of the healing period, loading was recommenced at the same CMOD rate until the CMOD clip gauge reached 0.45mm, after which the specimen was unloaded. This loading regime was considered to better simulate a realistic situation of a significant portion of the loading being maintained while the healing takes place. Unfortunately, most of the specimens failed. The reason being that since the loading was paused at 0.15mm CMOD, it (the loading) tended to fluctuate to maintain a CMOD value of 0.15mm which led to failure during the reloading stages. The specimens also became stiffer and more brittle and thus, a CMOD rate of

0.001mm/s appeared to be too fast. The CMOD rate was later reduced and increased slowly to 0.001mm/s for specimens in Group B. Due to the high failure rate in this second trial test set, a new testing procedure was introduced in which the loading was controlled with the CMOD clip gauge until a crack opening of 0.15mm, then controlled with load while waiting, and back to CMOD control until the final CMOD of 0.45mm has been reached. This method was successful and the load-CMOD and load-deflection responses are shown in Figure 3.16. It can be seen the load reduces by a small amount in the fixed healing period; this is probably related to CA shrinkage and short-term concrete creep (relaxation). This final testing procedure was subsequently adopted for the main Group B set of tests.

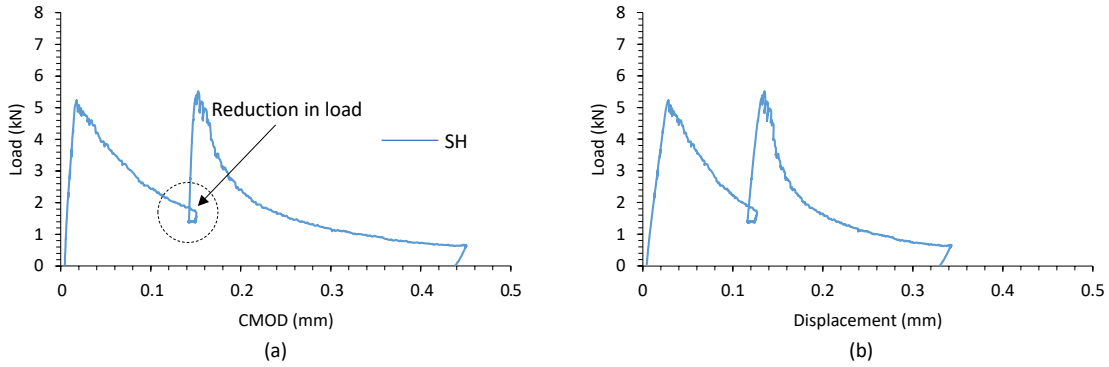

Figure 3.16. (a) Load-CMOD and (b) load-deflection responses at 10mins for the second trial test

3.5.2 Results and discussion

3.5.2.1 Effect of varying healing periods

The results for variable fixed healing periods are given in Figure 3.17(a-b), Figure 3.17(c-d), Figure 3.17(e-f), Figure 3.18(g-h), Figure 3.18(i-j) and Figure 3.18(k-l) for 2mins, 5mins, 10mins, 15mins, 30mins and 60mins respectively. Table 3.5 shows the influence of different healing periods on the healing recovery. The healing index for each specimen is calculated using the equation given in Section 3.4.1.4.

From the graphs in Figures 3.17 and 3.18, it may be seen that the post-healed softening branch of the load-CMOD and load-deflection was steeper than the corresponding pre-healed responses, which suggests that the fracture energy of the healed material is lower than that for the virgin material. All the SH specimens showed healing in terms of strength recovery. For example, at 2mins, the average peak load on the second loading cycle (post-healing) was 6.86kN as opposed to 5.61kN in the average peak load on the first loading cycle (pre-healing), which gives an average healing index of 130%. The average healing index recorded at 5mins and 10mins was 120% and 110% respectively. The response of the corresponding SH specimens that had a 15min healing period exhibited an average peak load on the second loading cycle (post-healing) of 5.79kN relative to an initial peak of 5.89kN, which equates to a healing index of 99%. The response of the other SH specimens (i.e. with 30min and 60min healing periods) gave similar healing indices of 105% and 109% respectively. The differences in their responses can be attributed to the natural variation in the concrete properties and it was suggested that 2mins was sufficient to allow CA to penetrate into the cracks and facilitate healing.

From visual observations (see Figure 3.19), it was apparent that the crack that occurred after the healing period was in a slightly different position from the first crack that formed. This meant that CA was able to hold the crack surfaces together since the tensile strength of cured CA was quoted being 21MPa (Cyanotec 2019), which was considerably stronger than the tensile strength of plain concrete of approximately 2.8MPa (see Table 3.3). This implied that the SH specimen will not re-crack directly through the cured healing agent but rather adjacent to the healed zone. As Joseph et al. (2010) suggested, when CA permeates into the microcracked zone adjacent to the macrocrack, it cures and creates a cementitious-polymer composite with a higher strength than the original material. Whilst it proved difficult to precisely measure the re-cracked area of the post-healed crack surfaces, approximate measurements suggested that between 80 to 95% of the crack had been healed.

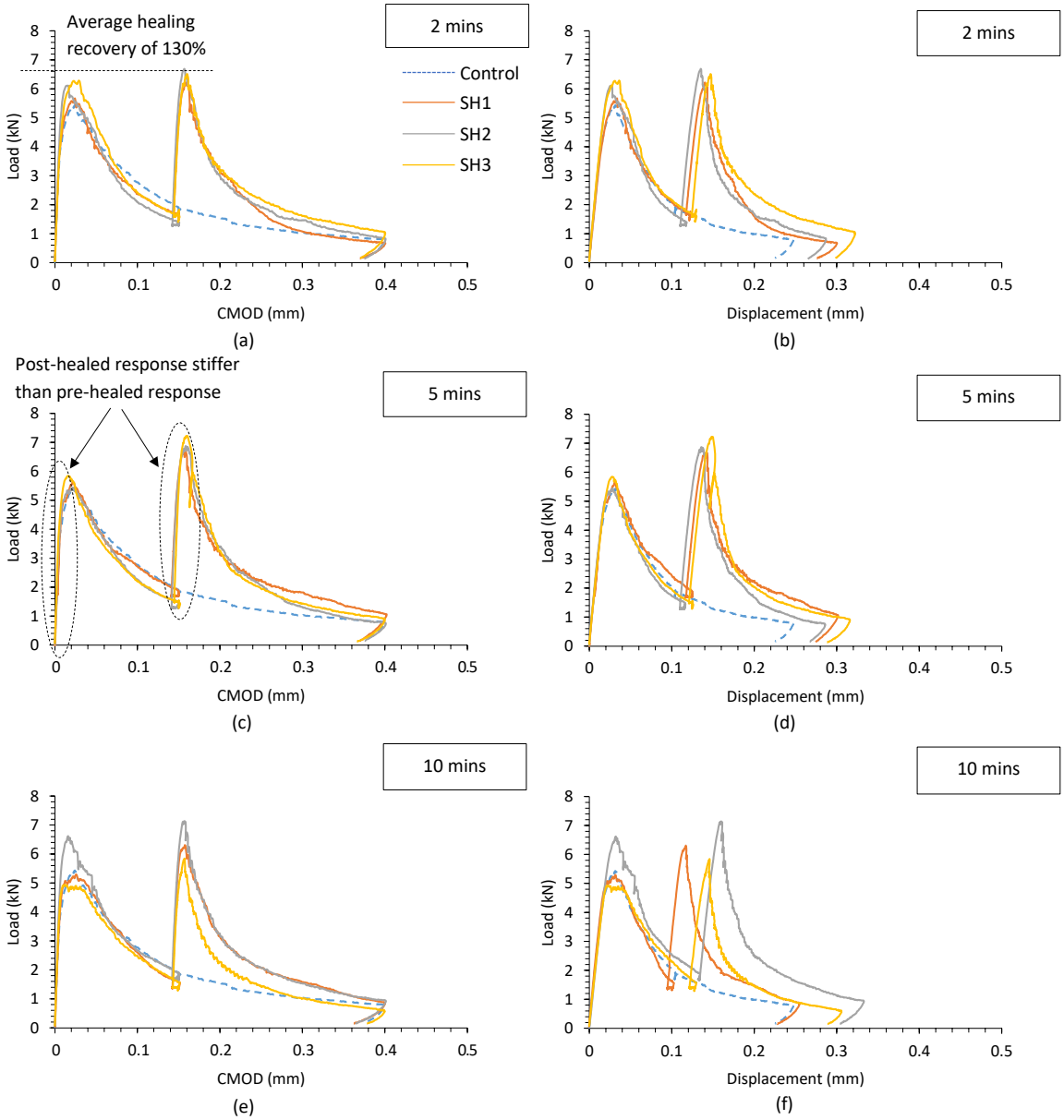

Figure 3.17. Load-CMOD and load-deflection responses at different healing periods for set 4 (a-b) 2mins, (c-d) 5mins and (e-f) 10mins (Group B)

Interestingly, the SH specimens had a significantly higher stiffness recovery in the reloading cycles. The stiffness during unloading also increased in comparison to the control specimens. As discussed for the second set of trial tests, there was reduction in load during the fixed healing period.

It was found that a healing period of between 2 to 5 minutes, with a CMOD of 0.15mm and the present concrete mix, was sufficient to obtain the healing recovery greater than 100%, although the results suggested that healing was substantially complete within the first 2 minutes. The average peak load on the second loading cycle (post-healing) exceeded the average peak load on the first loading cycle (pre-healing) in most cases except at 15mins (see Table 3.5).

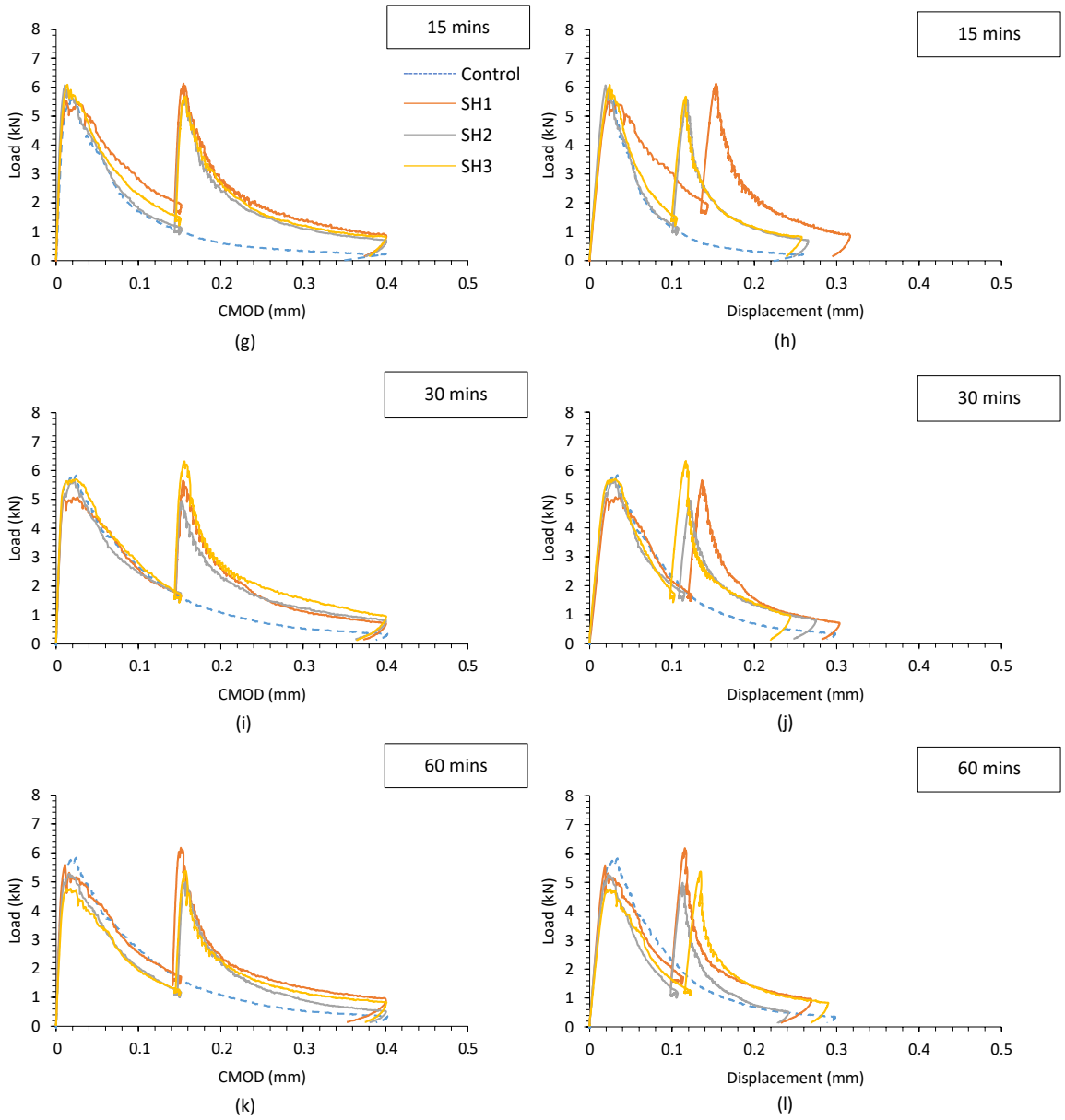

Figure 3.18. Load-CMOD and load-deflection responses at different healing periods for set 5 (g-h) 15mins, (i-j) 30mins and (k-l) 60mins (Group B)

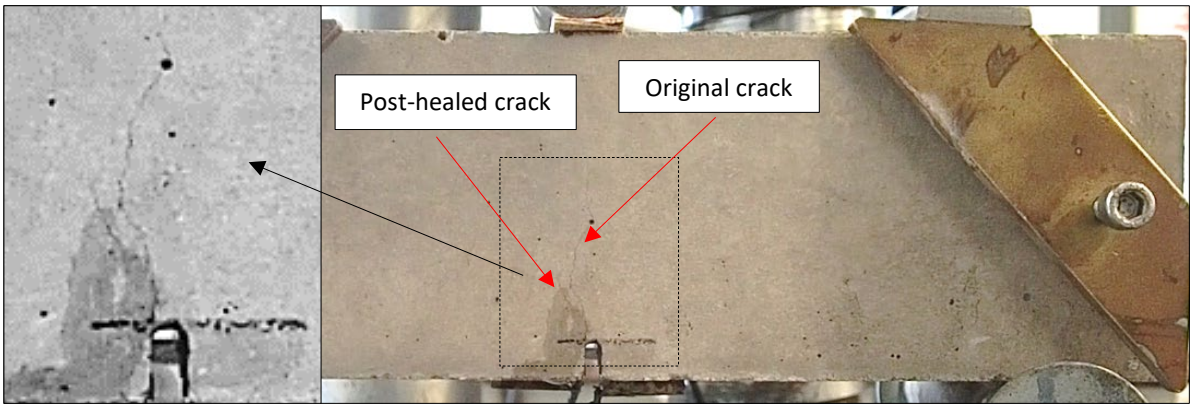

Figure 3.19. A representative SH specimen showing crack and CA on the surface

Table 3.5. Healing recovery for specimens in sets 4 and 5

Healing period	Specimen	Primary peak load, P_1 (kN)	Load at unloading, P_0 (kN)	Secondary peak load, P_2 (kN)	Healing recovery (%)	Average healing recovery (%)
2mins	SH1	5.58	1.70	6.57	126	130
	SH2	5.44	1.29	6.85	134	
	SH3	5.80	1.41	7.17	131	
5mins	SH1	5.29	1.33	6.30	126	120
	SH2	6.61	1.66	7.14	111	
	SH3	4.94	1.33	5.83	125	
10mins	SH1	5.67	1.64	6.22	114	110
	SH2	6.11	1.29	6.69	112	
	SH3	6.27	1.58	6.51	105	
15mins	SH1	5.54	1.67	6.12	115	99
	SH2	6.05	0.94	5.58	91	
	SH3	6.07	1.30	5.68	92	
30mins	SH1	5.05	1.58	5.65	117	105
	SH2	5.66	1.58	4.94	82	
	SH3	5.69	1.59	6.32	115	
60mins	SH1	5.58	1.46	6.18	115	109
	SH2	5.26	1.08	4.98	93	
	SH3	4.75	1.20	5.38	118	

3.6 Conclusions

A testing arrangement for an autonomic self-healing cementitious material system that produces a simultaneous damage and healing response was developed in this study. The overall conclusions drawn from this series of tests are as follows:

- The pressurised vascular healing system used for the experiment provides an effective method for delivering healing agent to discrete cracks and provided significant healing up to a crack opening of 0.4mm;
- Pressuring healing agent allowed greater penetration into cracks and increases the degree of healing;
- Low viscosity CA leads to losses in macrocracks;
- A healed specimen has the same characteristic fracture response as a plain concrete specimen;
- The post-healed fracture energy in healed cracks is lower than that of virgin cracks;
- Effectively full healing can be achieved in 2 minutes for a tapering crack with a CMOD of 0.15mm;
- Simultaneous damage and healing occur when the CMOD rate is in the range of 0.0002mm/s to 0.002mm/s;
- Multiple distinct healing peaks occur when the CMOD rate is in the range of 0.0002mm/s to 0.001mm/s;
- The irregularity of the load-CMOD and load-deflection responses increases as loading rate reduces;
- The optimum delivery pressure for the healing agent is between 0.3 bar to 0.5 bar;
- The CMOD and deflection (and time) at which measurable healing commences reduces as the delivery pressure increase;
- Healing indices in excess of 100% can be achieved using the vascular healing system for prisms loaded in flexure;
- This study provides a significant data set on the damage-healing behaviour of SHCMs that should be useful for those developing numerical models and/or design procedures.

Chapter 4 Damage-healing response in complex multiple cracks

4.1 Introduction

This chapter describes the Group C to F test series, which were designed to examine flow and healing behaviour in specimens that develop more complex crack patterns than those that occurred in the Group A and B tests (see Chapter 3). The vascular healing system used in this study to evaluate the damage-healing responses is shown in Figure 3.1 of Chapter 3. The specimens (100x100x500mm) in this study, which were larger than those used for the Group A and B tests, contained a vertically offset discontinuous arrangement of reinforcement embedded within the cementitious matrix, and either one (Group C) or two (Group D, E and F) layers of channels. An investigation of a more complex three-dimensional cracking problem by employing a vertically and laterally offset discontinuous arrangement of reinforcement will also be discussed (Group F). The objectives of the Group C to F tests were:

- To explore damage-healing behaviour in specimens that developed more complex crack patterns than those that occurred in the Groups A and B;
- To provide benchmark data for validating numerical models for SHCM systems.

The choice of the self-healing system and the healing agent was explained in sections 3.1 and 3.2 of Chapter 3. The following section describes some of the findings from the preliminary investigations.

4.2 Preliminary investigations

A preliminary investigation was undertaken to collect and review necessary information concerning the preparation of the specimens, the arrangement of reinforcement, and the testing procedure. The findings from this preliminary investigation were then used to guide the main experimental programme.

The concrete specimens in the preliminary programme of work were cured in water for a week and then tested immediately after this curing period, while they were still wet. However, it was then decided that it would be better to avoid too much interaction between liquid water and CA by drying the specimens in an oven prior to testing. This period of oven curing also accelerated the hydration reaction and produced more mature specimens. Therefore, for the main test series, the specimens underwent water curing for five days, heat curing for one day in an oven at 90°C, and air curing for further day. Two of the specimens were left to cure in the water tank at room temperature for an additional week to explore the effect of oven curing. The only difference between the 8-day specimens

(with one day of oven curing) and these 14-day specimens was that the latter showed higher initial peak loads (4.7% increase).

A trial reinforcement arrangement used in the first set of preliminary tests is illustrated in Figure 4.1(a), but this did not result in the desired multi-cracking response; therefore, an alternative arrangement, comprising two layers of offset reinforcing bars (see Figure 4.1(b)), was tested in a second set of the preliminary tests. This second reinforcement arrangement achieved the desired crack propagation sequence and was therefore adopted for the main series of tests.

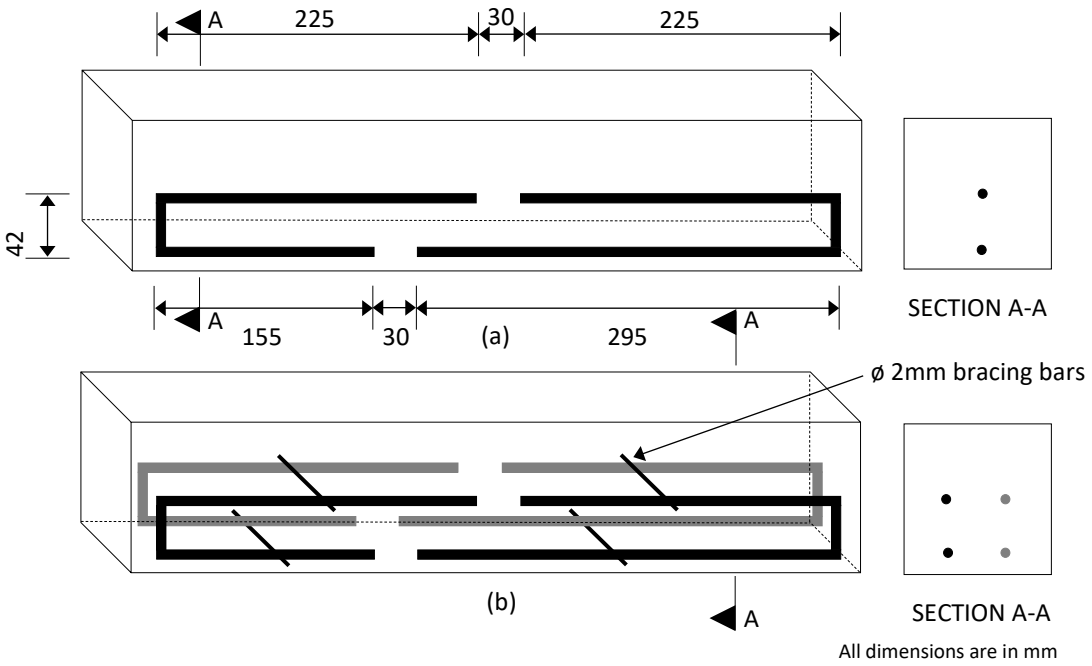

Figure 4.1. Reinforcement arrangement used in the (a) first and (b) second set of the preliminary tests (also in Groups C to E)

The details of the main test groups are now provided.

4.3 Details of Groups C to F test series

The general testing arrangement and specimen dimensions of the Group C, D, E and F test series are illustrated in Figure 4.2.

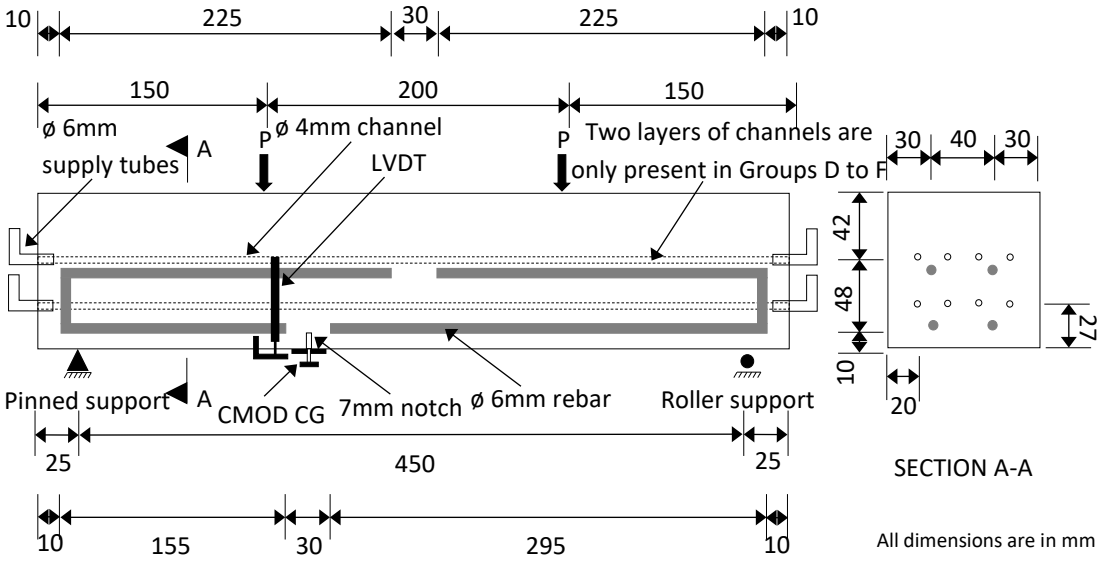

Figure 4.2. General arrangements for Group C, D, E and F

The details of the discontinuous reinforcement, which was essentially used to control or guide cracks, are given in Section 4.3.1 below. The experimental setup is shown in Figures 4.3 and 4.4. The hollow channels for the specimens in Groups C to F were created as illustrated in Figure 4.3. 10mm spacers were used to ensure the minimum required cover. The specimens in Groups C to F were subjected to four-point flexural bending tests using an Avery Denison 7152 Universal Hydraulics testing machine, as illustrated in Figure 4.4 (see Section 3.3.5 in Chapter 3). In contrast to the test series in Groups A and B reported in Chapter 3, the loading rate was controlled using feedback from the LVDT rather than the CMOD clip gauge. The reason for this was that the crack associated with the notch does not necessarily continuously increase throughout the test since there is a possibility that another crack becomes dominant. The loading rates (LVDT rate) and pressure used for the tests are given in Table 3.3 in Chapter 3. The notch for specimens in Groups C to F was introduced as shown in Figures 4.2 and 4.4. The outline of this study was previously explained in Section 3.3 in Chapter 3.

The experimental procedure for the test series with continuous loading of the test series in Groups C to F is as follows:

- The CA supply system was turned on (see Section 3.3.5 in Chapter 3) with a pressure of 0.5 bar;
- The specimens were loaded at an LVDT rate of 0.002mm/s until a maximum displacement of 2.5mm in Group C and a CMOD value of 2mm in Groups D to F; the latter value was lower because CA had seeped into the CMOD clip gauge;
- The CA supply was turned off following unloading and the remaining CA was drained from the specimen.

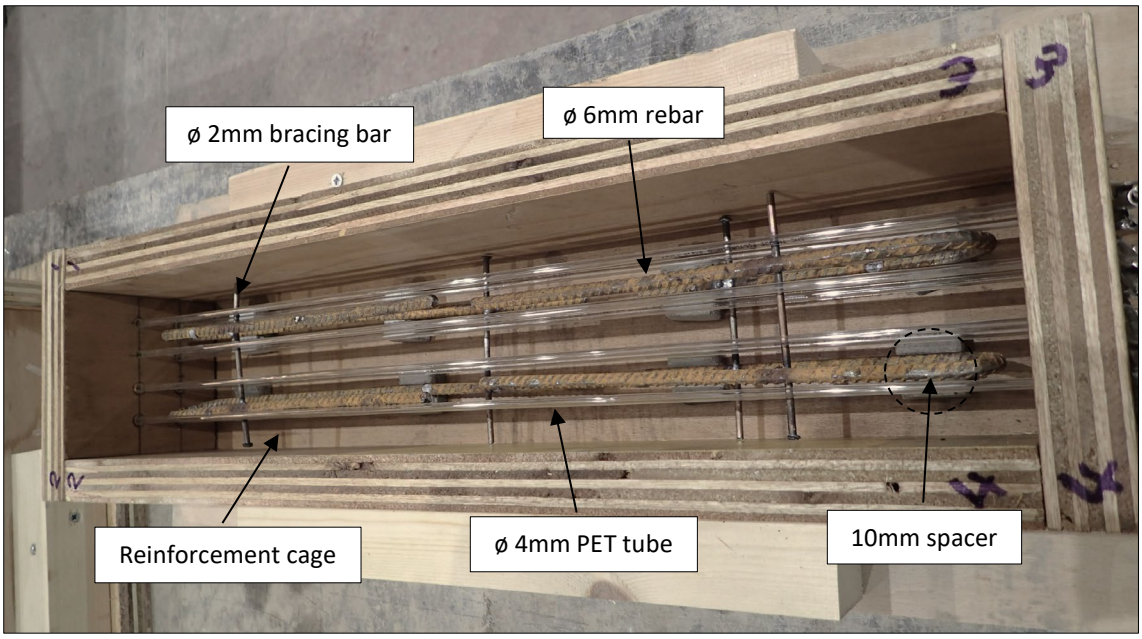

Figure 4.3. Specimen configurations for Group C to E

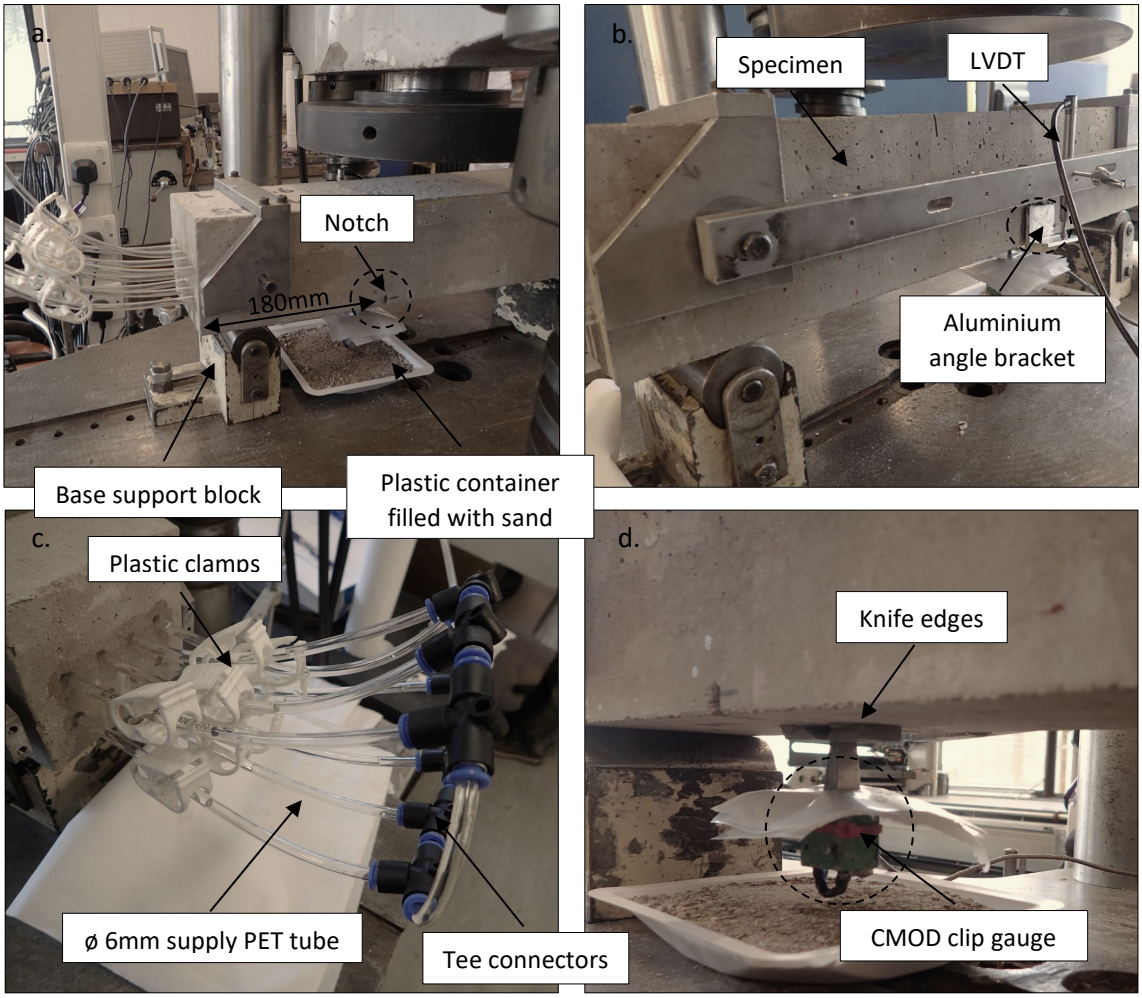

Figure 4.4. Experimental arrangements for Groups C to F

4.3.1 Reinforcement

As mentioned above, the reinforcement arrangement used in the present specimens was non-standard. Unlike conventional reinforcement layouts, there were gaps in the layers of reinforcement that were positioned to influence the cracking behaviour of the beam and achieve the desired crack patterns.

The specific arrangement of reinforcement and the position of the notch were designed so that, as the load increases, a mode I crack propagates from the notch until it reaches the bottom layer of reinforcement. At this point a shear crack should form, either diagonally or horizontally adjacent to the upper layer of reinforcement. Then, a second (near vertical) crack should form in the gap between the two halves of the upper layer of reinforcement whist other secondary cracks were also expected to form (see Figure 4.5).

As discussed earlier, two sets of 6mm diameter reinforcement bars were used to form prefabricated cages. Each of the cages was braced by two straight steel 2mm diameter bars, which were welded to the main bars, as illustrated in Figure 4.3. This ensured that the reinforcement cages remained stable in the mould during compaction. The specimens in Groups C to E consist of vertically offset discontinuous arrangement of reinforcement (see Figure 4.1(b)) whereas in the specimens in Group F involves vertically and laterally offset discontinuous arrangement of reinforcement (see Figure 4.6).

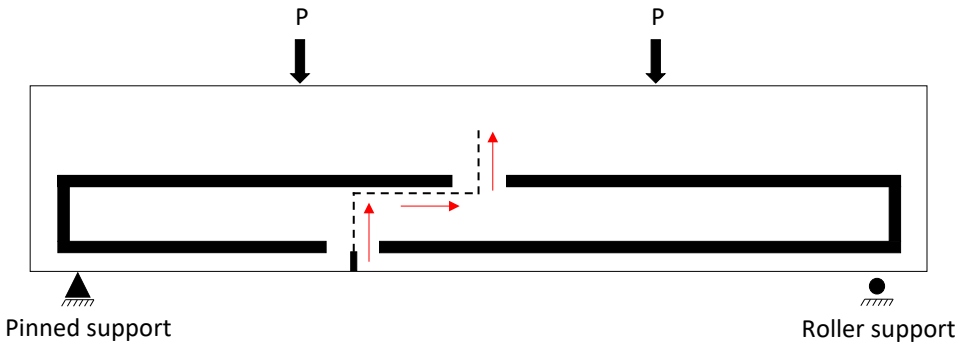

Figure 4.5. Arrows showing expected crack propagation upon loading

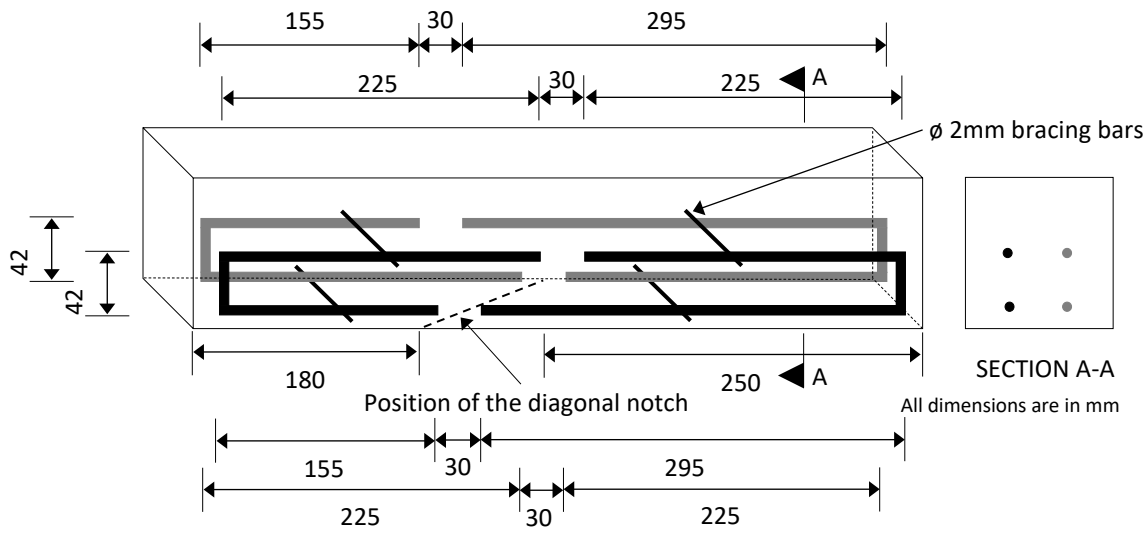

Figure 4.6. Reinforcement arrangement used in Group F

4.3.2 Compressive and tensile values

The average compressive and tensile strengths along with the CoV of the specimens in Groups C to F for sets 6 to 9 are shown in Table 4.1.

Table 4.1. Summary of concrete strengths after 8 days of curing in Chapter 4

Set	Average cube strength, f_{cu} (MPa)	CoV (%)	Average cylinder splitting strength, f_{cyl} (MPa)	CoV (%)	True uniaxial strength, f_c (MPa)	True tensile strength, f_t (MPa)
6	38.4	1.5	3.3	7.1	30.7	2.8
7	39.6	1.8	3.3	4.2	31.7	2.8
8	39.1	3.2	2.5	7.7	31.3	2.1
9	39.0	2.2	3.3	0.3	31.2	2.8

Specific details and the results from each group of tests will now be considered.

4.4 Group C: Single layer of channels notched concrete beams with vertically offset discontinuous reinforcement

4.4.1 Results and discussion

The main results for the test series in Group C are given below but some additional experimental results can be found in Appendix A. The tests on the control specimen with both single and double layers of empty channels as well as without channels were undertaken and it was found that the

presence of channels had a negligible impact on the response. The cracks developed in the control specimens according to the sequence described in Section 4.3.1. A number of labels were added to the response curves in Figures 4.7 to 4.11 (also in Figures 4.13 to 4.15 and 4.17 to 4.18) to signify the points at which either individual cracks became visible and/or there was a change in response phase. The cracking state at each of these points are also shown in the linked photographs. The details of the test series in Group C are summarised in Table 3.3 of Chapter 3. The load-CMOD and the load-displacement responses of a representative control and SH specimens are shown in Figures 4.7 to 4.11. The summary of the observations for each of these response phases is discussed in Table 4.2.

Table 4.2. Summary of Group C test series

Specimen	Phase (CMOD/time)	Observations
Control	0→0.023mm/ 0→30s Figure 4.7(a)	• The initial pre-peak loading phase (0 to a) ended (approximately) when the first macrocrack became visible; • A higher pre-peak non-linearity in the load-displacement responses recorded between the loads of 2kN to 7.25kN up to a displacement of 0.048mm, followed by a drop of approximately 2.45kN over a displacement of 0.12mm relative to 6kN to 7.25kN to 0.019mm CMOD before the drop over a 0.153mm CMOD in the load-CMOD responses as a result of crack growth (also occurred in SH1 to SH4).
	0.023→0.176mm/ 30→90s Figure 4.7(b)	• The first softening phase (a to b) coincided with the development and subsequent growth, of the first flexural crack that developed from the notch; • The upper layer of reinforcement prevented the crack from growing further.
	0.176→0.648mm/ 90→300s Figure 4.7(c)	• The reloading phase (b to c) started when the first crack reached the upper layer of reinforcement; • The crack opening increases with the loading before experiencing another drop.
	0.648→1.202mm/ 300→595s Figure 4.7(d)	• The first part of the second softening phase (c to d) commenced with the formation of a diagonal shear crack and softening continued as this crack developed; • Under the influence of flexural and shear stresses the crack tracked along the upper layer of reinforcement.
	1.202→1.769mm/ 595→905s Figure 4.7(e)	• A second flexural crack, that bifurcated from the end of the diagonal crack, became visible at (d) and continued to propagate both up and down in phase (d to e);
	1.7699→2.485mm/ 905→1305s Figure 4.7(f)	• The response plateaued in phase (e to f), during which the initial flexural crack below the reinforcement, the principal diagonal crack and the second flexural crack all continued to increase in width; • The test was stopped at (f) when the LVDT reading reached 2.5mm (as with SH1 to SH4).
SH1	0→0.023mm/ 0→30s Figure 4.8(a)	• The initial pre-peak loading phase (0 to a), which ended when the first macrocrack became visible, showed a higher pre-peak non-linearity in the loading range from 2kN to 8.18kN, over a displacement change of 0.048mm, compared to the load-CMOD responses for the load change from 6kN to 8.18kN over a CMOD of 0.016mm.
	0.023→0.229mm/ 30→150s Figure 4.8(b)	• A slight drop coincided with the first softening phase (a to b) where the first flexural crack was formed from the notch, followed by CA flowing out of the channels.
	0.229→0.388mm/ 150→260s Figure 4.8(c)	• The release of CA observed during the reloading phase (b to c); • A sudden drop associated with the growth of the diagonal shear crack as the first flexural crack continued to grow.
	0.388→0.775mm/ 260→570s Figure 4.8(d)	• A second flexural crack was developed on the opposite side of the first flexural crack at the unreinforced section in the second softening phase (c to d).
	0.775→1.177mm/ 570→900s Figure 4.8(e)	• The diagonal shear crack continued to develop until it reached the upper layer of reinforcement in phase (d to e) alongside the second flexural crack due to flexural and shear stresses.
	1.177→1.685mm/ 900→1310s Figure 4.8(f)	• The complex crack patterns were achieved at (f) when the response plateaued in phase (e to f).

SH2	0→0.026mm/ 0→30s Figure 4.9(a)	• The first flexural crack can be seen forming from the notch during the initial pre-peak loading phase (0 to a); • A slight drop occurred simultaneously.
	0.026→0.067mm/ 30→50s Figure 4.9(b)	• As the first flexural crack became more discrete during the first softening phase (a to b), CA can be seen flowing out; • A higher loading was observed as a result of the polymerisation of CA.
	0.067→0.396mm/ 50→200s Figure 4.9(c)	• The first flexural crack continued to travel upwards until the upper layer of reinforcement during the reloading phase (b to c).
	0.396→0.756mm/ 200→390s Figure 4.9(d)	• Since the first flexural crack could not propagate any further, this led to the formation of a diagonal shear crack and a second flexural crack due to shear and flexural stresses in second softening phase (c to d).
	0.756→1.746mm/ 390→1020s Figure 4.9(e)	• As the crack opening increases with loading so does the growth of the existing cracks in phase (d to e).
	1.746→2.149mm/ 1020→1290s Figure 4.9(f)	• The corresponding crack patterns were achieved at (f) in phase (e to f).
SH3	0→0.013mm/ 0→30s Figure 4.10(a)	• The first flexural crack initiated from the notch during the pre-peak loading phase (0 to a); • A more pronounced drop was seen due to cracking induced by increase loading as compared to SH1 and SH2 specimens.
	0.013→0.119mm/ 30→110s Figure 4.10(b)	• CA can be seen flowing out during the first softening phase (a to b) contributing to the increase in load.
	0.119→0.244mm/ 110→210s Figure 4.10(c)	• The first flexural crack widened until the upper layer of reinforcement; • The diagonal shear crack formed due to the combination of shear and flexural stresses in the reloading phase (b to c).
	0.244→0.673mm/ 210→540s Figure 4.10(d)	• Both the first flexural crack and diagonal shear crack became more obvious in the second softening phase (d to e); • At this time that there was some CA which had been cured and hardened around the notch which explained the lower CMOD in terms of displacement values;
	0.673→0.965mm/ 540→780s Figure 4.10(e)	• The second flexural crack which had developed from the existing cracks in phase (e to f), emerged.
	0.965→1.516mm/ 780→1260s Figure 4.10(f)	• The response plateaued as all the cracks continued to widen and complex crack pattern was achieved at (f) during phase (e to f).
SH4	0→0.054mm/ 0→55s Figure 4.11(a)	• The first flexural crack developed during the pre-peak loading phase (0 to a); • It reached and ruptured the channels allowing CA to flow out as a result improving the mechanical properties.
	0.054→0.237mm/ 55→150s Figure 4.11(b)	• The first flexural crack carried on upwards until the upper layer of reinforcement as during the first softening phase (a to b).
	0.237→0.381mm/ 150→220s Figure 4.11(c)	• Since the growth of the first flexural crack was deterred due to the upper layer of reinforcement, it sought the weakest region; • The formation of a diagonal shear crack can be seen in the reloading phase (b to c).
	0.381→0.789mm/ 220→470s Figure 4.11(d)	• The second flexural crack developed perpendicular to the first flexural crack in the second softening phase (c to d).
	0.789→0.976mm/ 470→600s Figure 4.11(e)	• All the cracks became more obvious in phase (d to e).
	0.976→1.830mm/ 600→1200s Figure 4.11(f)	• The existing cracks continued to open up as the loading increased in phase (e to f).

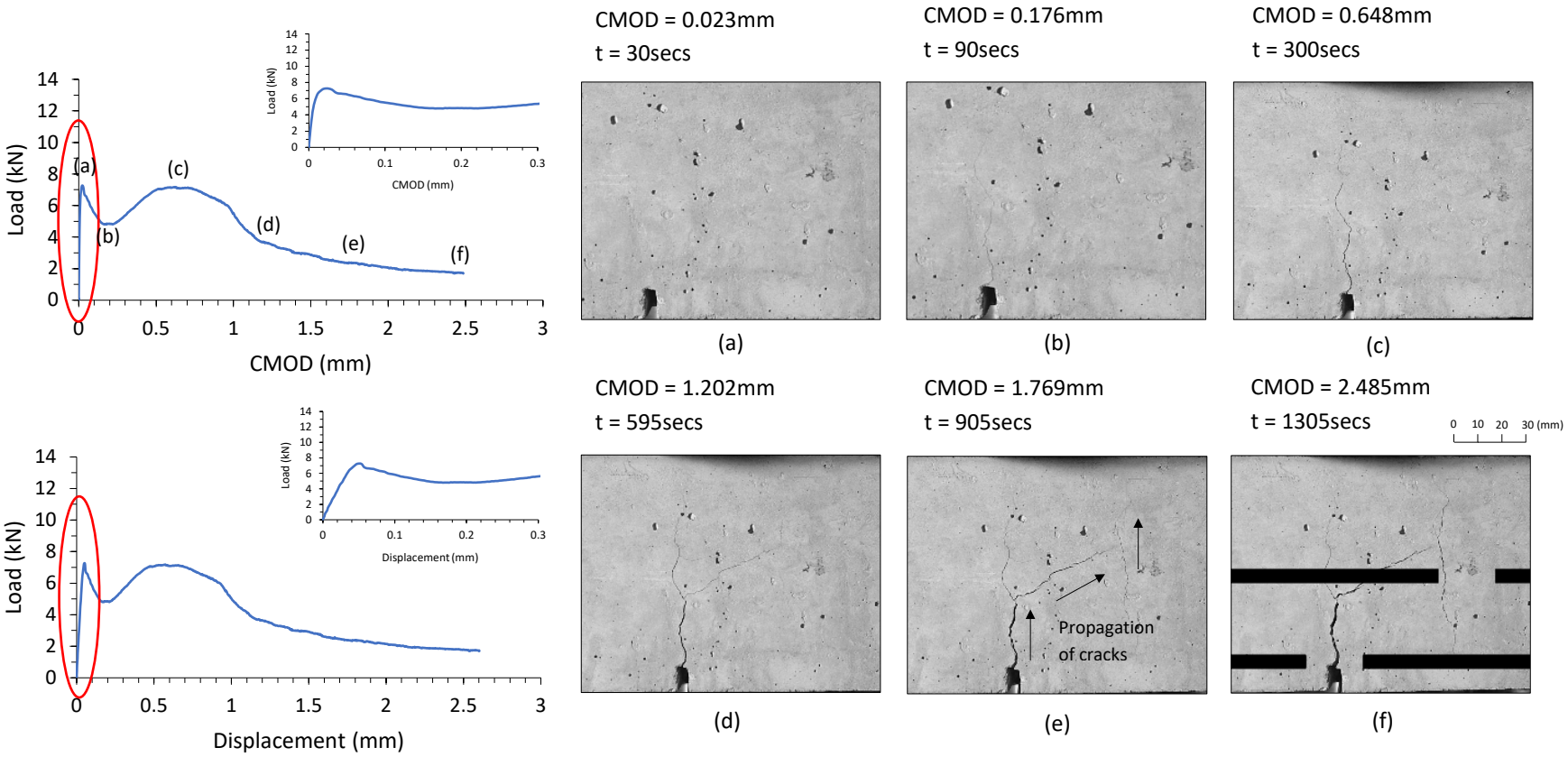

Figure 4.7. Load-CMOD and load-displacement responses of a representative control specimen (Group C)

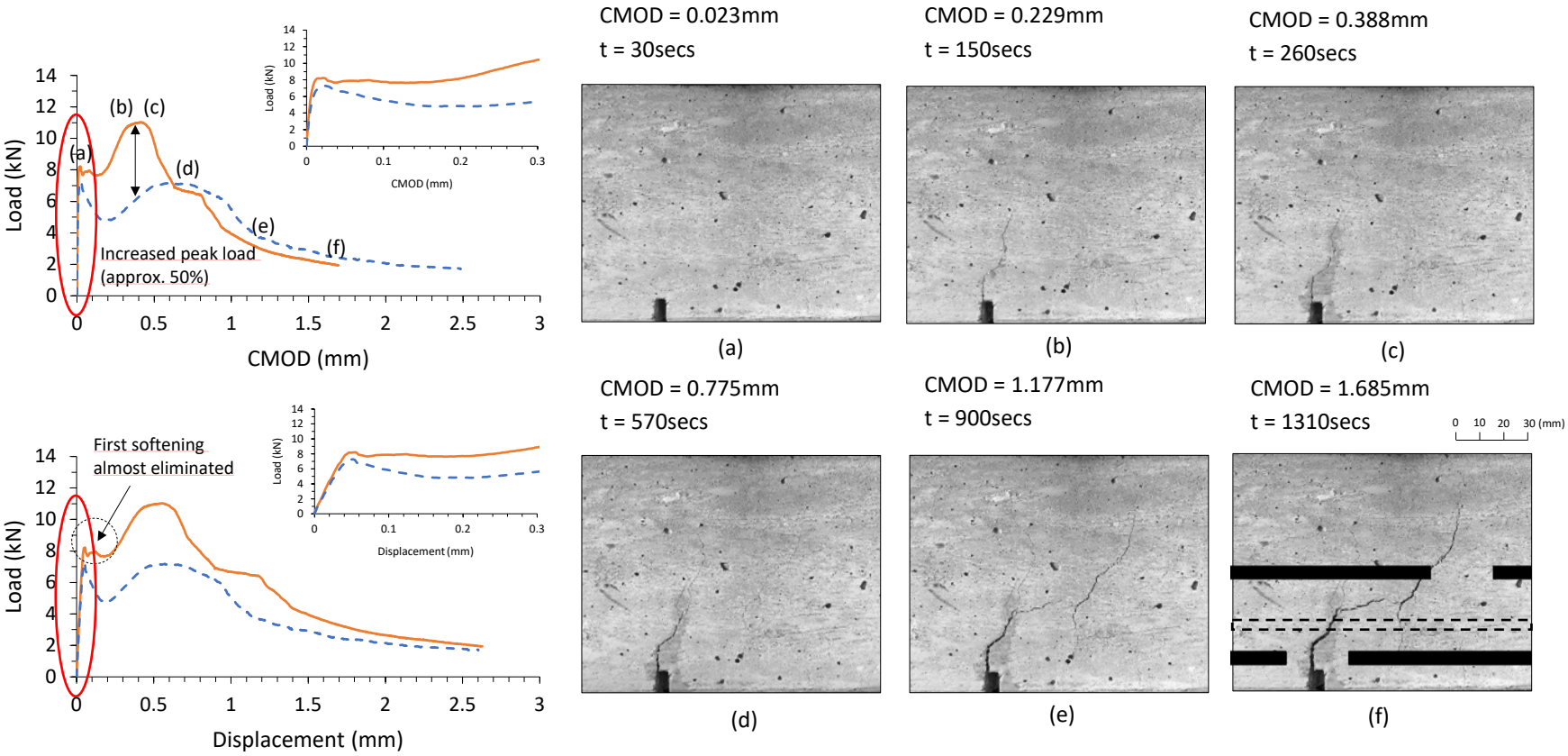

Figure 4.8. Load-CMOD and load-displacement responses for SH1 specimen (Group C)

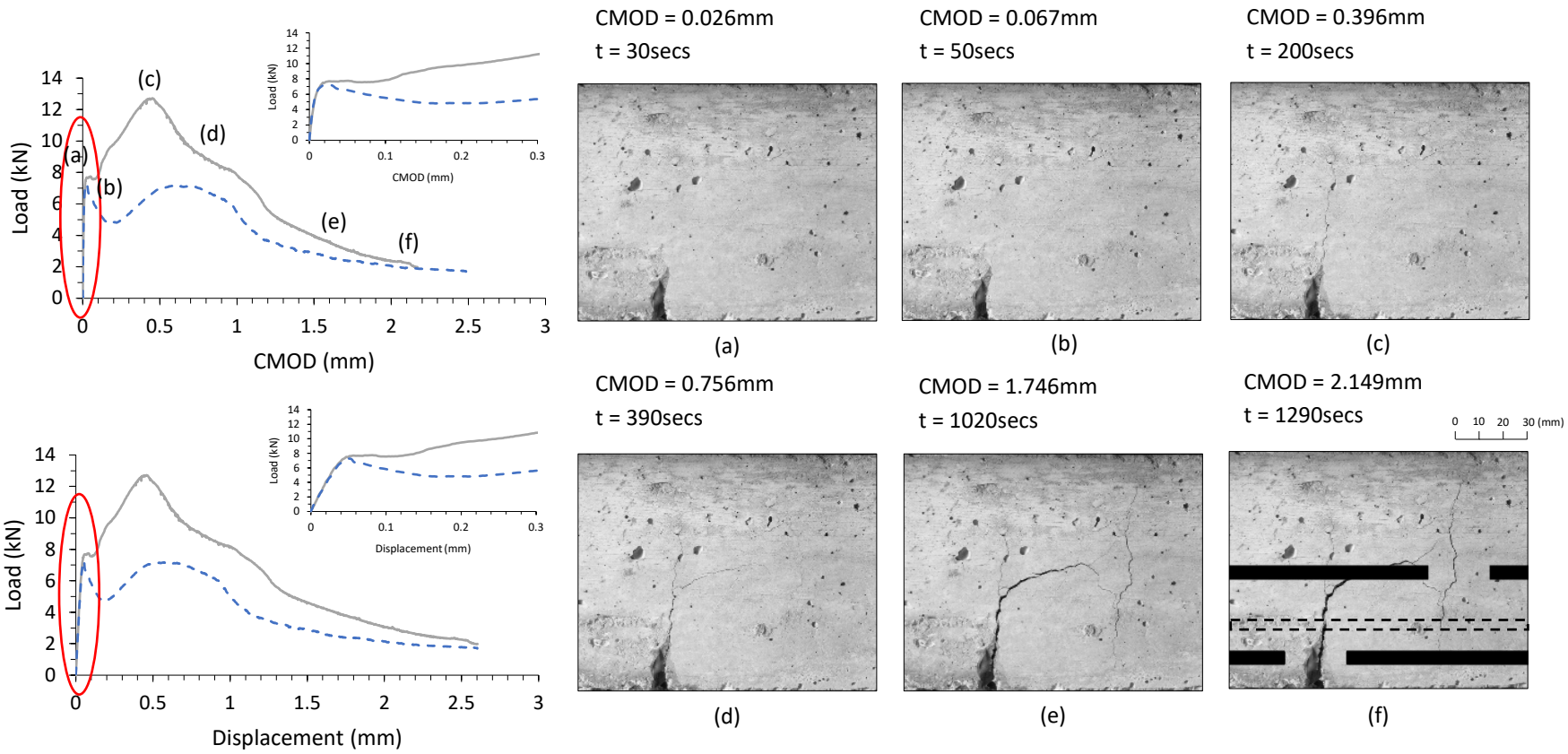

Figure 4.9. Load-CMOD and load-displacement responses for SH2 specimen (Group C)

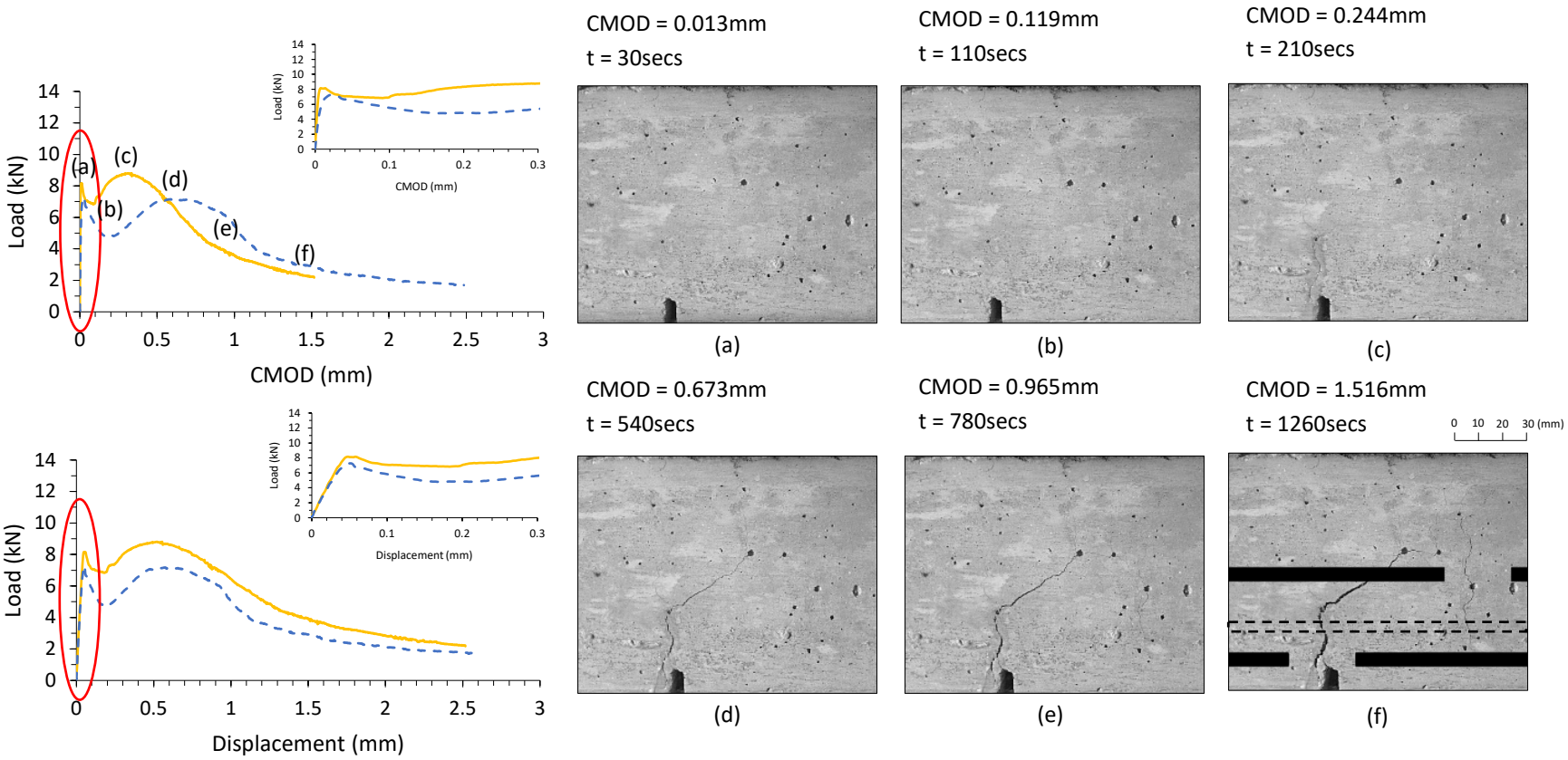

Figure 4.10. Load-CMOD and load-displacement responses for SH3 specimen (Group C)

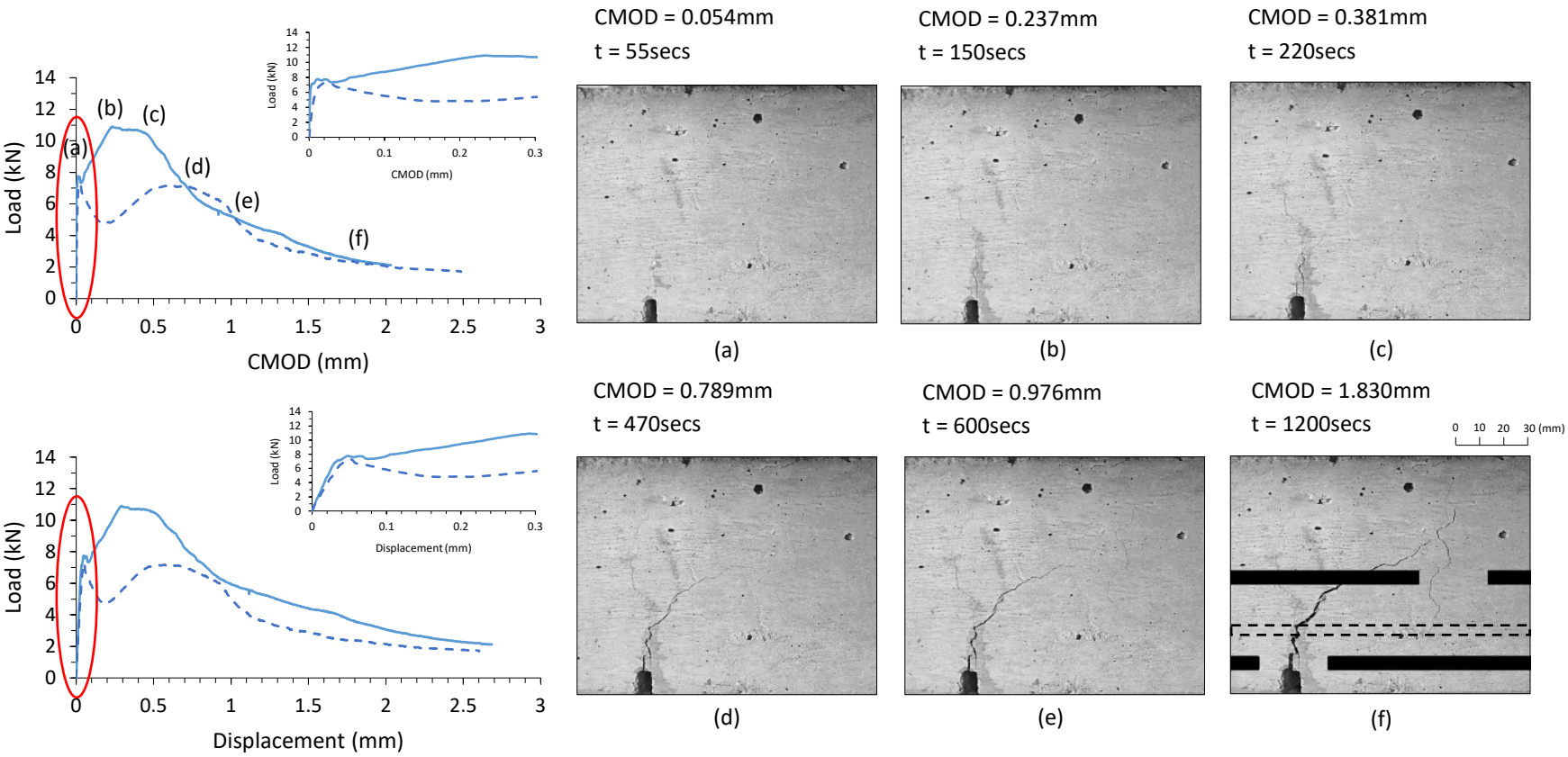

Figure 4.11. Load-CMOD and load-displacement responses for SH4 specimen (Group C)

It was found that healing had a major influence on the response, as illustrated by the fact that the peak load in the SH specimens increased by approximately 50% relative to the control specimen and the first softening phase was almost eliminated (see Figure 4.8). Even though the CA supply system was activated prior to the start of testing, CA was only able to penetrate when the crack reached an opening of 0.03mm, as previously discussed in Section 3.4.1.1 in Chapter 3. CA became visible on the surface when the CMOD reached approximately 0.2mm, which occurred between 110 and 120 seconds from the start of the test. There was also a time lag from when the CA was first transported into the propagating crack and the start of appreciable crack healing, which, from the results, was estimated to be approximately 2 seconds. A constant LVDT rate of 0.002mm/s was used in this test series, in which simultaneous damage-healing would be expected to occur as discussed in Section 3.4.1.1 in Chapter 3. By comparing the sequence of crack photographs for the SH specimens with those from the control specimen, it is suggested that healing strongly influenced the crack propagation sequence, with the diagonal crack forming later in time and merging with the two flexural cracks to form a single dominant crack. There was no evidence of the healing agent being transported into either the shear or the second flexural crack in these specimens, which had a single layer of channels.

The final crack patterns of the control and SH specimens in Group C, relative to the reinforcement and channels, are shown in Figure 4.12. The experiments performed in this test series allowed complex cracking and associated damage-healing responses to be achieved. These cracks usually occur at the weakest regions of the specimen and thus, complex cracking was obtained by tweaking the reinforcement arrangement. The SH specimens showed an increase in stiffness, peak strength, and post peak ductility due to the curing and hardening of the CA (that had low viscosity and fast curing properties) which flowed into the microcracks due to a combination of capillary action and driving pressure. It was also found that the LVDT rate of 0.002mm/s and supply pressure of 0.5 bar were sufficient to obtain a simultaneous damage-healing response.

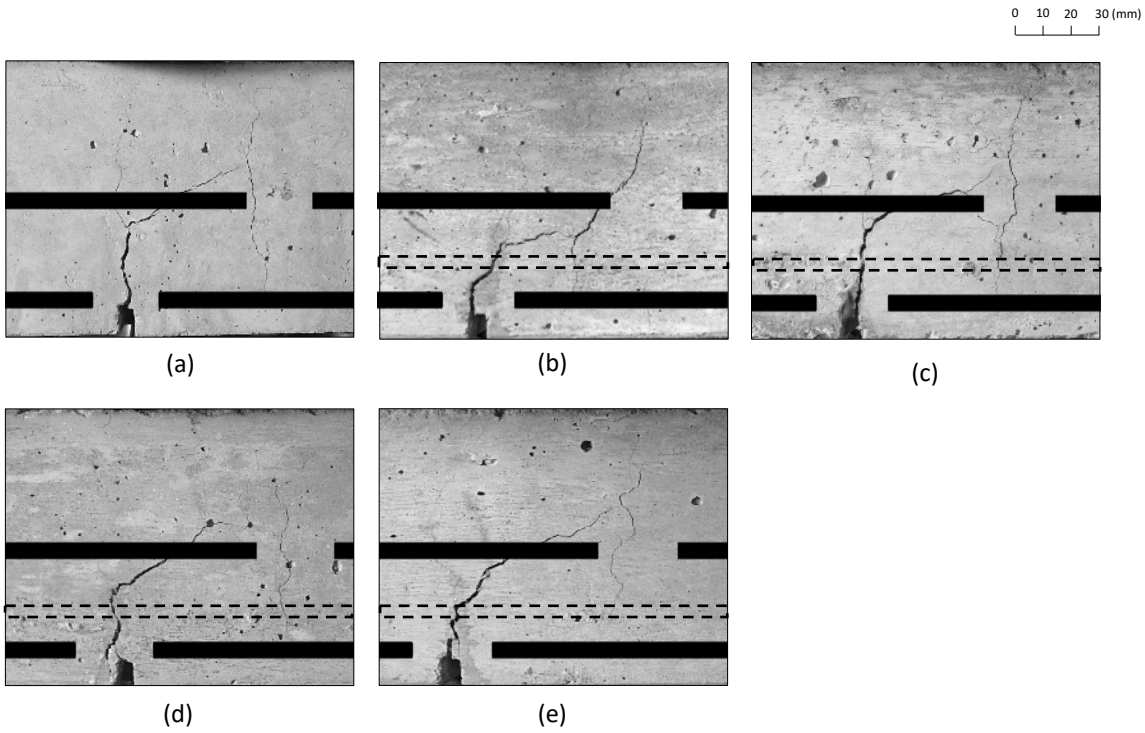

Figure 4.12. Crack growth, reinforcement and channels for (a) control specimen, (b) SH1 specimen, (c) SH2 specimen, (d) SH3 specimen and (e) SH4 specimen from Group C

4.5 Groups D and E: Double layers of channels notched concrete beams with vertically offset discontinuous reinforcement

The experimental parameters for the test series in Groups D and E (also in Group F) are similar to those in Group C as discussed in Section 4.3 but in Group E, a supply pressure of 0.3 bar was applied instead of 0.5 bar. A detailed discussion on the experiment is given in the following section.

4.5.1 Results and discussion

The details of the test series in Groups D and E can be found in Table 3.3 in Chapter 3. The load-CMOD and load-displacement responses of a representative control and SH specimens are shown in Figures 4.13 to 4.15. The summary of the observations is described in Table 4.3 below.

Table 4.3. Summary for Groups D and E test series

Specimen	Phase (CMOD/time)	Observations
Control	0→0.027mm/ 0→35s Figure 4.13(a)	• The first macrocrack became visible during the initial pre-peak loading phase (0 to a); • A pre-peak non-linearity influenced by microcracking occurred between 0 and 9.65kN which showed a significant shift from the initial stiffness in the load-displacement responses compared to the load-CMOD responses.
	0.027→0.135mm/ 35→195s Figure 4.13(b)	• A sudden drop occurred in the first softening phase (a to b) following the formation of the first flexural crack before skewing towards the opening of the unreinforced section due to both shear and flexural stresses.
	0.135→0.513mm/ 195→365s Figure 4.13(c)	• The increase in stiffness at (c) is the result of the steel reinforcement; • The first flexural crack continued to widen during the reloading phase (b to c).
	0.513→0.939mm/ 365→585s Figure 4.13(d)	• The second flexural crack developed during the second softening phase (c to d).
	0.939→1.481mm/ 585→885s Figure 4.13(e)	• The existing cracks continued to grow until the upper layer of reinforcement in phase (d to e).
	1.481→2.012mm/ 885→1185s Figure 4.13(f)	• The complex cracking was achieved at (f). • The test was stopped when the CMOD reading reached 2mm.
SH1	0→0.013mm/ 0→95s Figure 4.14(a)	• There was apparently more pre-peak non-linearity in load-displacement responses compared with load-CMOD responses (0 to a); • A slight drop occurred simultaneously after the formation of the first flexural crack.
	0.013→0.096mm/ 95→135s Figure 4.14(b)	• CA was seen flowing out due to the rupture of the bottom channels during the first softening phase (a to b).
	0.096→0.280mm/ 135→225s Figure 4.14(c)	• A peak load of 10.87kN was recorded; • The formation of the diagonal shear crack occurred during the reloading phase (b to c) which emanated from the first flexural crack due to polymerisation of CA.
	0.280→0.769mm/ 225→460s Figure 4.14(d)	• The diagonal shear crack propagated towards the gap in the upper layer reinforcement, due to shear and flexural stresses, during the second softening phase (c to d).
	0.769→1.204mm/ 460→720s Figure 4.14(e)	• The second flexural crack formed perpendicular to the first flexural crack; • CA can be seen flowing out due to the fracture of the top channels which coincided with the increase in stiffness.
	1.204→2.001mm/ 720→1160s Figure 4.14(f)	• The associated crack patterns shown at (f) relate to phase (d to e). • A load of 3.62kN as to 2.13kN in the control specimen was obtained following unloading.
SH2	0→0.018mm/ 0→35s Figure 4.15(a)	• A similar pre-peak non-linearity, due to microcracking, occurred in the load-displacement responses in the loading range 1.98kN and 9.44kN, which was followed by a drop in load associated to the development of the first flexural crack during the pre-peak loading phase (0 to a).
	0.018→0.088mm/ 35→65s Figure 4.15(b)	• The growth of the first flexural crack led to the fracture of the bottom channels allowing CA to flow out during the first softening phase (a to b).
	0.088→0.476mm/ 65→275s Figure 4.15(c)	• The curing and hardening of CA resulted in an increase in stiffness during the reloading phase (b to c); • A peak load of 12.34kN was reached.
	0.476→0.812mm/ 275→420s Figure 4.15(d)	• Since the first flexural crack was healed and repaired, a diagonal crack appeared due to shear and flexural stresses during the second softening phase (c to d).
	0.812→1.481mm/ 420→680s Figure 4.15(e)	• The existing cracks became more visible as the diagonal shear crack propagated towards the gap in the upper layer of reinforcement in phase (d to e); • The second flexural crack opened up and the CA could be seen on the adjacent surface, indicating fracture at the top channels.
	1.481→2.015mm/ 680→885s Figure 4.15(f)	• A load of 2.72kN was achieved at (f) prior to unloading.

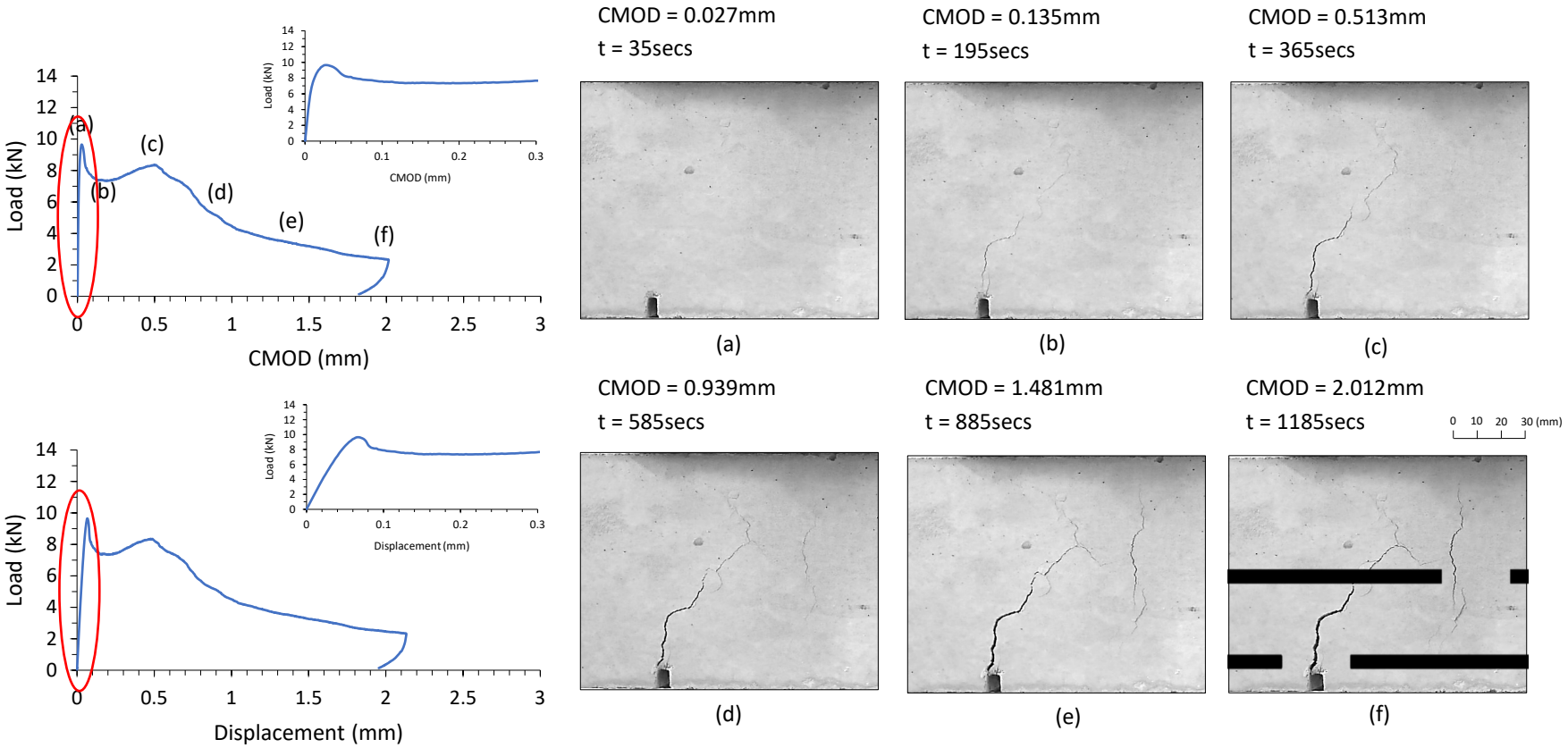

Figure 4.13. Load-CMOD and load-displacement responses of a representative control specimen (Groups D and E)

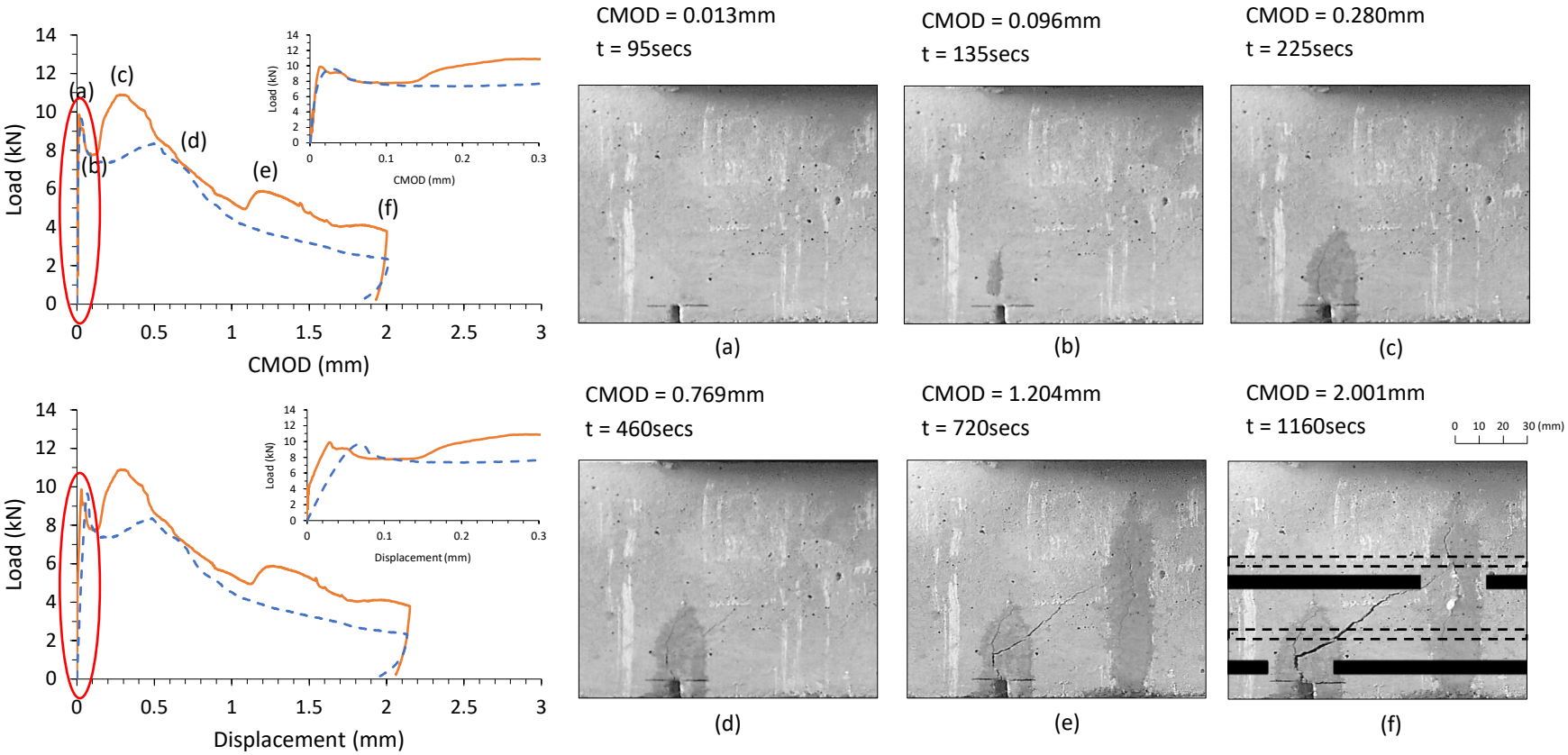

Figure 4.14. Load-CMOD and load-displacement responses for SH1 specimen (Group D)

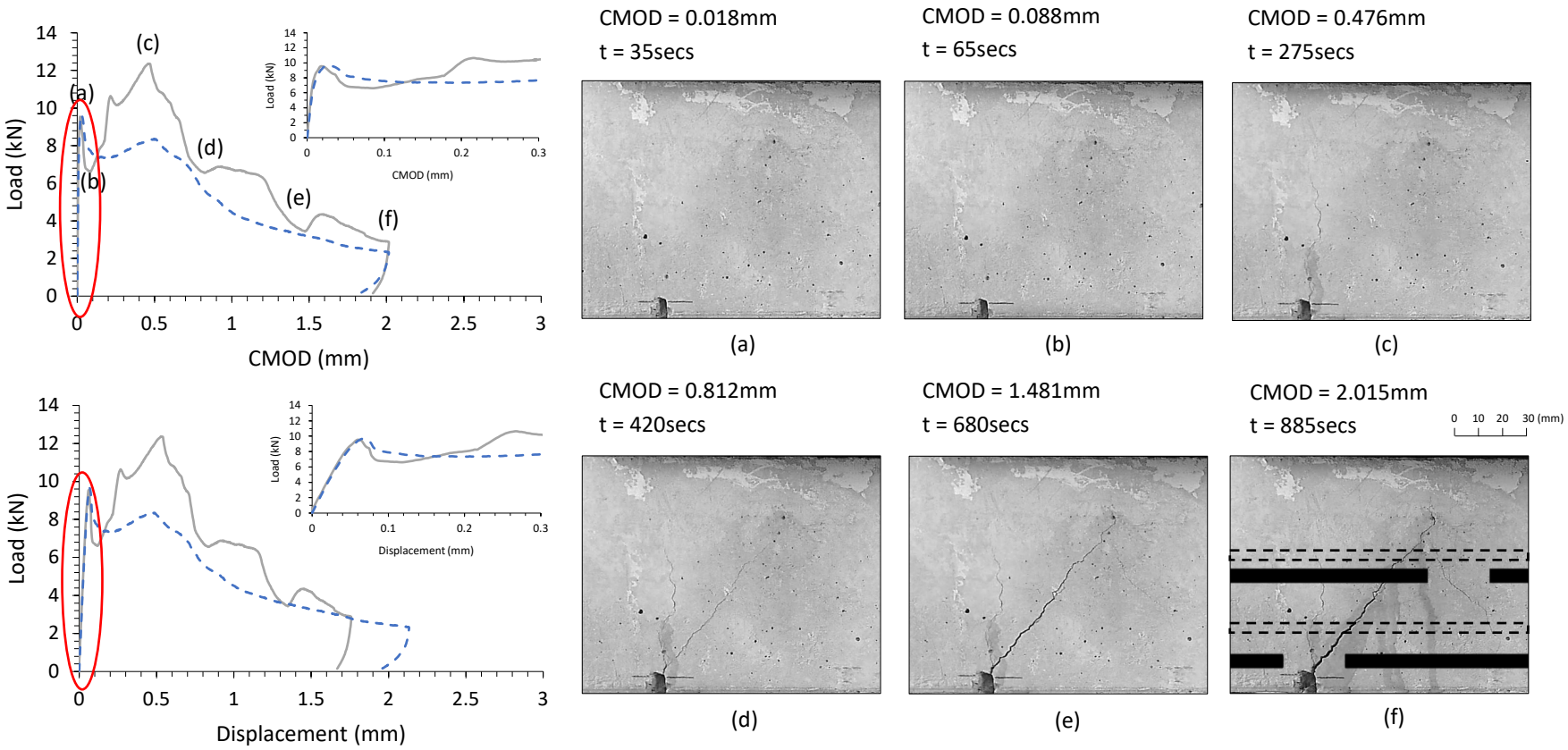

Figure 4.15. Load-CMOD and load-displacement responses for SH2 specimen (Group E)

Although the test series in Group C was considered a success in terms of achieving complex cracking and the apparent damage-healing responses, there was still the question of maximising the supply of CA. This was the case where the channels of the specimens in Group C were empty due to insufficient CA towards the end of the test period which led to the decision to include an additional layer of channels in the test series in Groups D and E as shown in Figure 4.2. Multiple channels also provide better coverage over a network of cracks.

It was suggested that the healing response for SH specimens in Groups D and E (see Figures 4.14 to 4.15) occurred a little later compared than in Group C (see Figures 4.8 to 4.11), since there was a more pronounced softening phase following the primary peak. This difference is attributed to variations in the crack opening at which healing agent is initially transported from the channels into the first crack, as discussed in Section 3.4.1.1 in Chapter 3. The shear crack bifurcated from the first flexural crack earlier than in the Group C specimens. The damage-healing response of the Group E specimens (i.e. SH2) had a higher peak (at c) that of the Group D specimens (i.e. SH1). The former used a supply pressure of 0.3 bar whereas the latter used 0.5 bar. It was previously shown (Section 3.4.1.2 in Chapter 3) that, for this system, maximum healing occurs when the supply pressure is close to 0.3 bar. These results appear to confirm this finding. The most significant effect of having two layers of channels was that healing occurred in the second flexural crack. This is believed to have occurred because CA could be seen on the surface around the second flexural crack and there was a second peak (at e) in the response curve that was not present in the response of the specimens that had a single layer of channels. The final crack patterns of the control and SH specimens in Groups D and E, relative to the reinforcement and channels are shown in Figure 4.16.

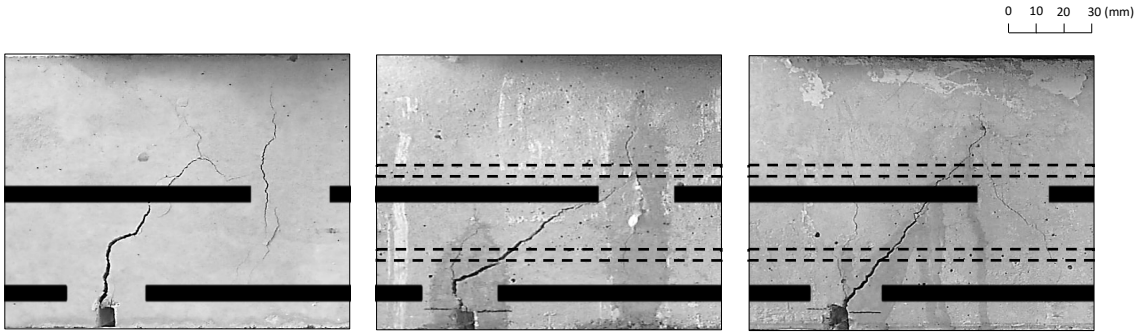

Figure 4.16. Crack growth, reinforcement and channels for (a) control specimen, (b) SH1 specimen from Group D and (c) SH2 specimen from Group E

It can be concluded that the healing agent flow was restricted to an initial flexural crack with one layer of channels whereas healing agents flowed throughout the macro-crack network with two layers of channels. The post-peak load for SH specimens in Groups D and E also remained higher throughout the post peak region than those in Group C. The overall conclusions from the Group C to E test series are as follows:

- The vertically offset discontinuous reinforcement used in the test series resulted in a complex crack propagation sequence that comprised of two flexural and one shear macro-cracks;
- The introduction of CA using the vascular healing system with one or two layers of channels can promote significant healing, with the peak load increased by at least 50%;
- CA was visible on the crack surfaces at a CMOD of approximately 0.2mm, which occurs 110 to 120 seconds from the start of the test;
- An LVDT rate of 0.002mm/s produces simultaneous healing and cracking;
- Multiple vascular channels distributed across the zone of potential cracking are required to ensure that healing agent flows into the majority of macro-cracks.

4.6 Group F: Double layers of channels notched concrete beams with vertically and laterally offset discontinuous reinforcement

This study was undertaken to investigate healing in a more complex three-dimensional crack growth. The information on the experimental procedure can be found in Section 4.3. The details related to the fabrication of the reinforcement cages are in Section 4.3.1. The notch was created diagonally across the bottom surface of the specimens as shown in Figure 4.6.

4.6.1 Results and discussion

The details of the test series in Groups F are given in Table 3.3 in Chapter 3. The load-CMOD and load-displacement responses of a representative control and SH specimen are shown in Figures 4.17 and 4.18. A summary of the observations is given in Table 4.4 below.

Table 4.4. Summary for Group F test series

Specimen	Phase (CMOD/time)	Observations
Control	0→0.014mm/ 0→15s Figure 4.17(a)	• A pre-peak non-linearity due to microcracking between loads of 12.0kN and 12.5kN was observed followed by a sudden drop of 2.86kN over a CMOD increase of 0.0181mm; • The first flexural crack occurred away from the notch during the pre-peak initial loading phase (0 to a).
	0.014→0.528mm/ 15→260s Figure 4.17(b)	• The first flexural crack widened until it reached the upper layer of reinforcement; • A diagonal shear crack developed due to the influence of shear and flexural stresses during the softening phase (a to b).
	0.528→2.003mm/ 260→365s Figure 4.17(c)	• A second flexural crack developed along the unreinforced section in phase (b to c); • The test was stopped at (f) when the CMOD reading reached 2mm (as with SH1).
SH1	0→0.0045mm/ 0→35s Figure 4.18(a)	• The pre-peak non-linearity observed was less than that of the control specimen in the loading range 11.36kN and 11.95kN over a CMOD of 0.0029mm, suggesting a higher initial stiffness during the pre-peak initial loading phase (0 to a) which was followed by a drop.
	0.0045→0.468mm/ 35→375s Figure 4.18(b)	• The first flexural crack again occurred away from the notch; • CA was visible in the initial crack and appeared come from both the top and bottom channels during the softening and reloading phases (a to b); • The formation of a diagonal shear crack occurred due to shear and flexural stresses making their way towards the upper layer reinforcement; • Multiple reloading and unloading jumps noticed.
	0.468→2.002mm/ 375→1885s Figure 4.18(c)	• The existing cracks continued to grow as loading increased in phase (b to c); • A load of 1.91kN as to 0.94kN for the control specimen was recorded at unloading.

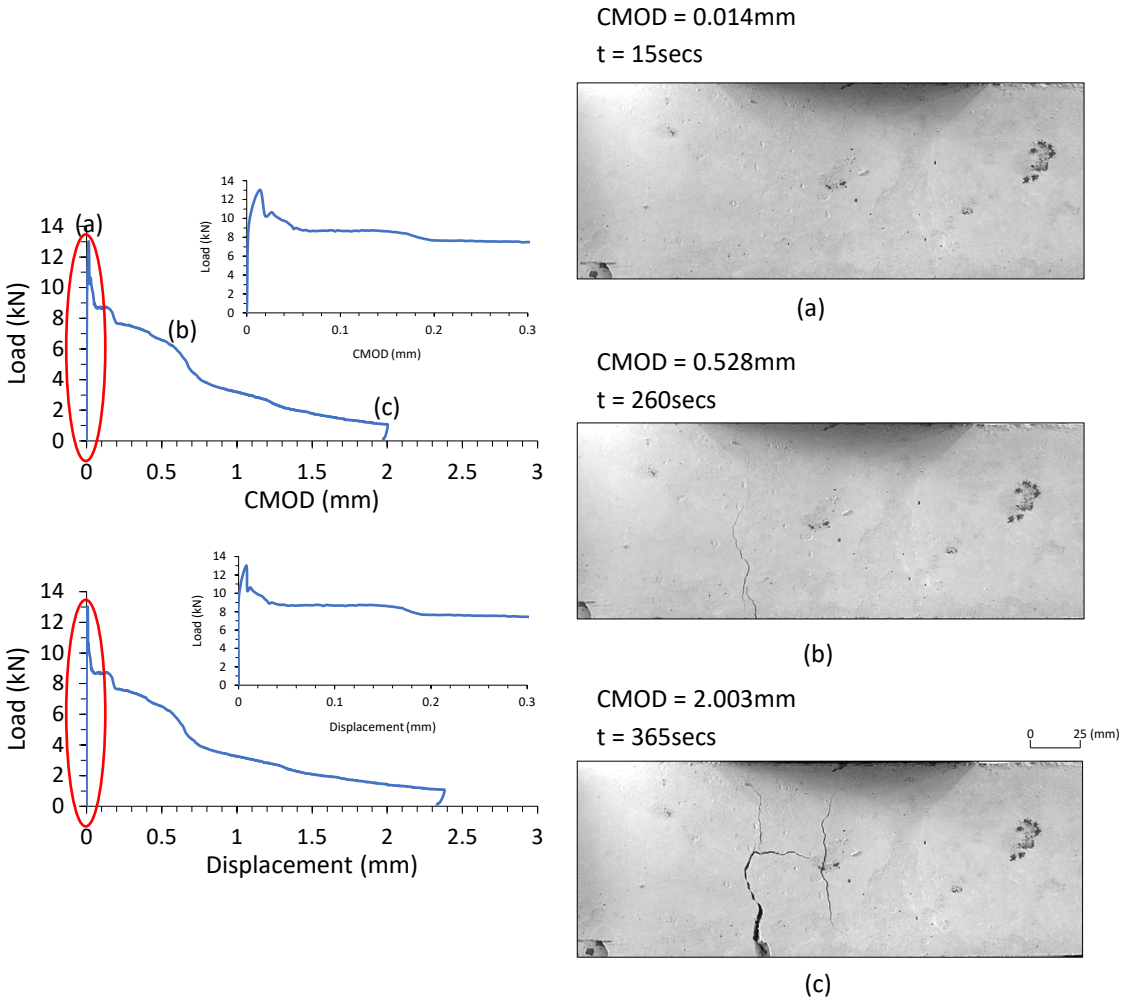

Figure 4.17. Load-CMOD and load-displacement responses of a representative control specimen (Group F)

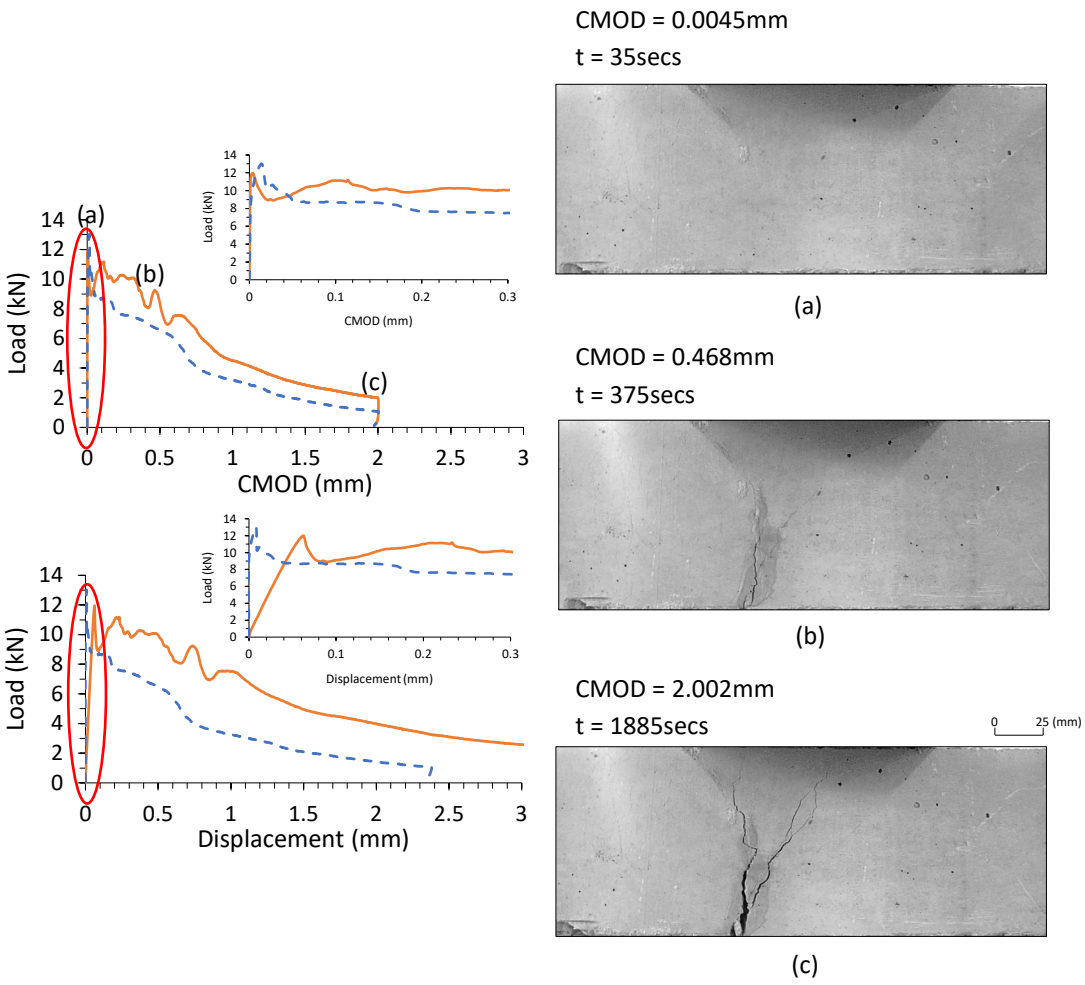

Figure 4.18. Load-CMOD and load-displacement responses for SH1 specimen from set 9 (Group F)

This attempt to achieve a curved crack proved to be unsuccessful, and it was concluded that this reinforcement arrangement was insufficient to control the crack. In both cases, the first flexural crack that formed remained perpendicular to the axis of the beam and was not steered or guided by the reinforcement to the degree expected. There were few factors that may have influenced the behaviour; including, the crack did not initiate from the notch because it was too far from the centreline. In fact, the first crack began and nucleated around the centre of the specimen. There was also a large central zone of unreinforced concrete in which the cracks propagated. Therefore, most of the specimens developed a mode I crack (near vertical). If this was to be pursued in the future, the recommendation is to have the offset discontinuous reinforcement closer to each other.

4.7 Conclusions

This study explored the development of the vascular healing system with embedded discontinuous reinforcement in order to achieve complex multiple cracks with a particular focus on multiple cracking, crack branching and the healing potential of the vascular system under such conditions. The main conclusions from the series of tests described are as follows:

- The vascular healing system with embedded channels as a delivery system for healing agent to the damage zones results in significant healing (> 30%) in crack openings up to 0.2mm;
- The vertically offset discontinuous reinforcement arrangement in Groups C, D and E was capable of controlling and guiding cracks to achieve complex multiple cracking;
- Multiple flow networks distributed across the zone of potential cracking are required to ensure that healing agent flows into the majority of macrocracks;
- The main difference between specimens with one or two layers of channels is that the latter showed an increase in stiffness during the first softening response and prior to unloading;
- Simultaneous damage-healing behaviour is less pronounced when the healing agent pressure is lower (~10 to 15%);
- Little healing is obtained when the reinforcement gap is laterally offset (as in Group F);
- These experimental results provide valuable information on the behaviour of self-healing cementitious material system that can be used for validating numerical models.

Chapter 5 Uniaxial tension

5.1 Introduction

This chapter describes a series of direct tension crack-healing tests undertaken to better understand the implied damage-healing behaviour observed in the notched beam crack-healing tests, reported in Chapter 3. The testing arrangement was designed to create a horizontal crack in a series of cube specimens, which were nominally of uniform opening. This is in contrast to the tapering cracks of the beam specimens described previously (see Section 3.5 in Chapter 3). The aim of this test series is to establish how the healing response changes with the crack opening displacement.

The work reported in this chapter describes the development of a direct tension crack-healing test. The geometry of the notched specimens used in the experiments was guided by the work of Jacobsen et al. (2012). A number of researchers have reported difficulties in achieving consistent results that capture a stable softening response in direct tension fracture tests (Reinhardt 1981, Van Mier 1997, Østergaard et al. 2007, Jacobsen et al. 2012). These difficulties become more severe when a static healing phase is introduced into the test procedure (Ferrara et al. 2018a). As highlighted in the introductory chapter of this thesis, the results obtained from this series of tests form part of an experimental programme of work undertaken to characterise the behaviour of a self-healing material system and to provide validation data for numerical and design models. Careful consideration was given in all stages of this test series to eliminate casting errors. A summary of the experiments discussed in the following sections of this chapter is presented in Table 5.1.

Table 5.1. Summary of the experimental details in Chapter 5

Description	Purpose	Set(s) and section no.	No. and size of specimens (mm)	CMOD rate (mm/s)	CA supply pressure (bar)	Healing period	CMOD during healing (mm)	Max CMOD (mm)
Preliminary investigation (Section 5.2)								
Direct tension pull off tests on notched prismatic specimens	To determine the bonded strength of CA at varying crack openings and healing periods	**Set 1** and **Set 2** (Section 5.2.1)	9 x controls[1] (75x75x255)	0.0333[2]	-	-	-	-
Direct tensions tests on notched cube control specimens	To determine the influence on the grooved surface	**Set 3** (Section 5.2.2.1)	6 x controls (100x100x100)	0.0001	-	-	-	0.15
	To determine the influence on the notch depth	**Set 4** (Section 5.2.2.2)	6 x controls (100x100x100)	0.0001	-	-	-	0.1
	To determine the influence on the max. agg. size and heat curing temp.	**Set 5** (Section 5.2.2.3)	6 x controls (100x100x100)	0.0001	-	-	-	0.15
	To determine the influence on the stiffness of the test setup	**Set 6** and **Set 7** (sections 5.2.2.4 and 5.2.2.5)	12 x controls (100x100x100)	0.0001	-	-	-	0.1
	To determine the influence on the concrete mix							
Experimental programme (Section 5.3)								
Direct tension crack-healing tests on notched cube specimens	To determine the characteristic healing behaviour of a horizontal crack at varying crack opernings and healing periods	**Set 8** (Section 5.4)	24 x self-healing (100x100x100) 12 x controls (100x100x100) 6 x cubes (100x100x100) 6 x cylinders (200xø100)	0.0001	0.5	0s 60s 300s	0.1	0.2
		Set 9 (Section 5.4)				0s 60s 600s 1200s	0.2	0.3

[1] 6 no. SH specimens (75x75x255mm) cast but set 2 tests were not carried out.

[2] Set 1 tests was controlled via machine stroke displacement.

5.2 Preliminary investigation

An extensive preliminary investigation was undertaken prior to the development of a successful experimental method. The various aspects investigated are discussed in detail in the following section and this is followed by a summary of the main findings from these preliminary tests.

5.2.1 Experimental trial 1

The trial tests include a series of direct tension pull off tests using the Zwick Roell Z100 and Avery Denison 7152 Universal Hydraulic testing machines on small scale laboratory prisms with dimensions 75x75x255mm (see Figure 5.1). The aim of this study was to determine the bonded strength of CA between two crack surfaces at varying crack openings and healing periods. The test setup is illustrated in Figure 5.2. The procedure for preparing moulds and forming flow channels in the SH specimens were previously discussed (see Section 3.3.1 in Chapter 3). Channels were not included in the control specimens. The mix ratio and curing regime are described in Section 5.3.3. The wooden moulds had

two 8.5mm diameter pre-drilled holes in the stop ends to allow for the 8mm diameter threaded reinforcement bars shown in Figure 5.1. The bars used in set 2 were 10mm in diameter with 10.5mm clearance holes. They were secured with modelling clay during casting. In addition, 40mm long perpendicular cross bars were welded to the ends of the main bars to form anchorages. As may be seen in Figure 5.1, the main and cross bars formed a tee shape.

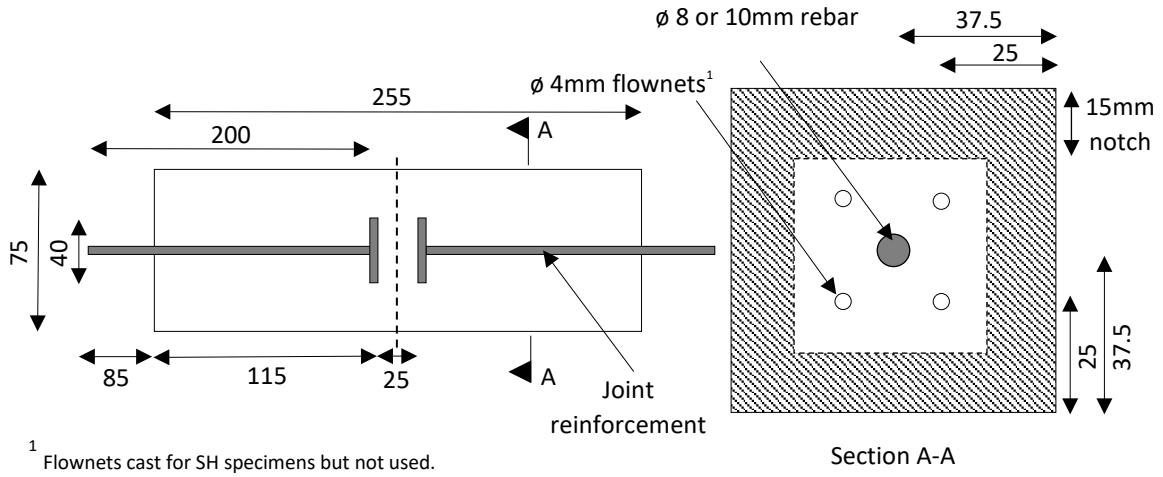

[1] Flownets cast for SH specimens but not used.

Figure 5.1. General arrangements for the direct tension pull off tests

3mm wide central notches were cut into the specimens on all sides, which were 7mm and 15mm deep for sets 1 and 2 respectively (see Figure 5.1). Therefore, the specimens in sets 1 and 2 had unnotched central cross-sectional areas of 1975mm^2 and 1896mm^2 respectively. Angle brackets were glued on all sides of the specimens 20mm from the notches to ensure equal spacings between the LVDT transducers (see Figure 5.2(c)). A frame designed to hold the LVDTs was used and the gauges were held in place with screws. The high resolution LVDTs are able to record 2400 readings per second, which was considered adequate to capture the response of the direct tension specimens. The ends of the reinforcement bars were then fixed to the grips on the machine. A preload of 100N was applied to the specimens and the loading was controlled with LVDTs instead of the machine stroke to negate slip effects (see Figure 5.2). A loading rate of 2mm per minute was used for all of the tests.

In set 1, the specimens were broken into two halves and the cracked surfaces were cleaned before CA was applied to both surfaces. The two halves were then pressed together and held in place with 10kg weights for periods of 2mins, 5mins, 8mins, 10mins and 12mins. The intended procedure for the set 2 specimens was as follows; load the specimens until a crack opens to 0.15mm; feed CA into the crack through the supply channels; re-load the specimens to close the crack and switch the machine to load control for the healing period (i.e. 2mins, 5mins, and 10mins); then reload the specimens until a crack opening of 0.3mm and then unload and remove the specimens from the rig.

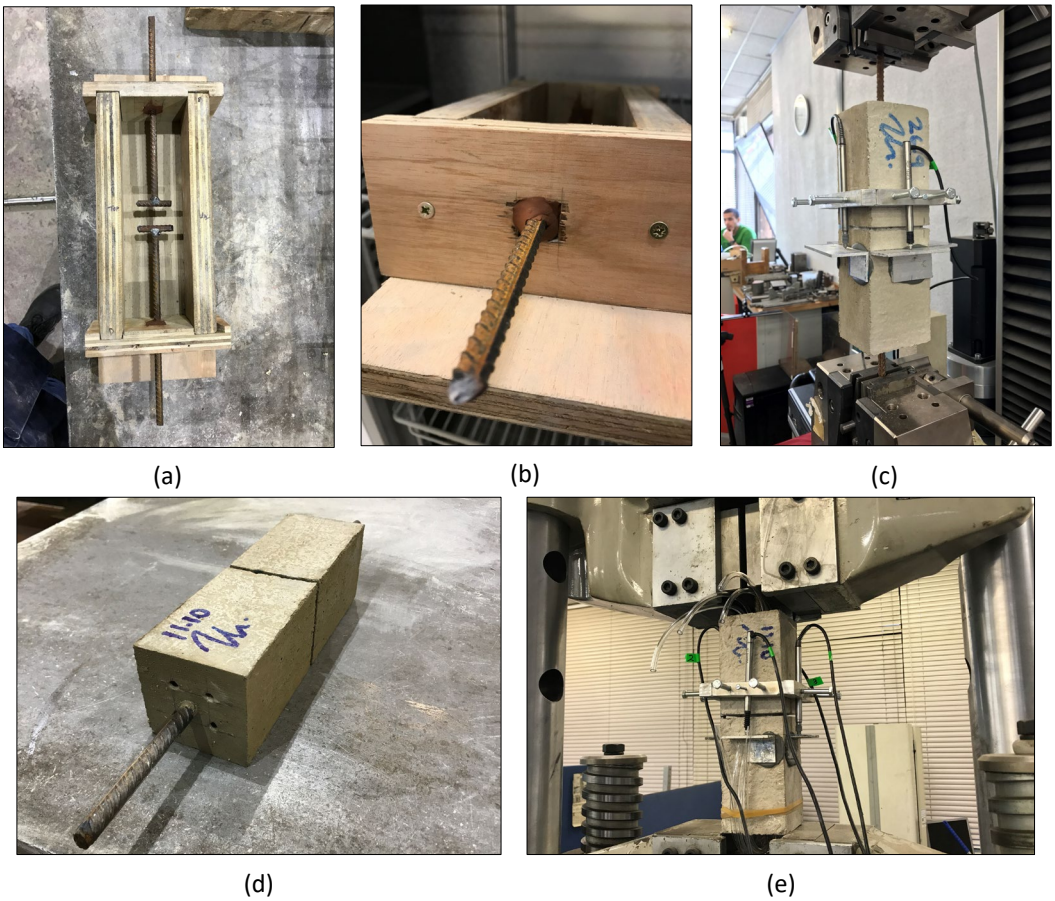

Figure 5.2. (a) Wooden mould with reinforcement bars, (b) modelling clay, (c) control specimen from set 1, (d) notch and channels and (e) SH specimen from set 2

The initial and post-healed responses of the set 1 specimens are given in Figures 5.3(a) and 5.3(b) respectively, and the specimens before and after failure are pictured in Figures 5.4(a) and 5.4(b) respectively. The results suggest that the specimens broke almost immediately after reaching their peak loads at an average stress of 2.8MPa. The energy released during failure of these specimens produced a snapback response that could not be captured in this testing arrangement. It is believed that the long and slender specimens and the relatively flexible testing machine had too much elastic energy, which made the post-peak behaviour unstable and very difficult to control (Jacobsen et al. 2012). There was also some evidence of slippage between the reinforcement bars and the machine grips.

From the results it is concluded that the average post-healed strength of 1.3MPa can be achieved if two cracked concrete surfaces are to be bonded together using CA with reasonable distribution. The tests to include CA within the cementitious matrix in set 2 did not proceed further since the results in set 1 proved that the post-peak behaviour could not be captured with this testing configuration.

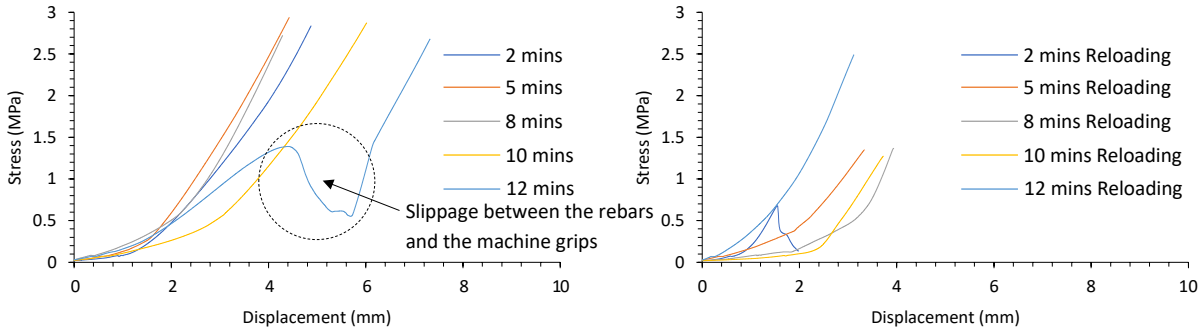

(a) (b)

Figure 5.3. Stress-displacement responses of the specimens in set 1 showing (a) initial strengths and (b) post-healed strengths

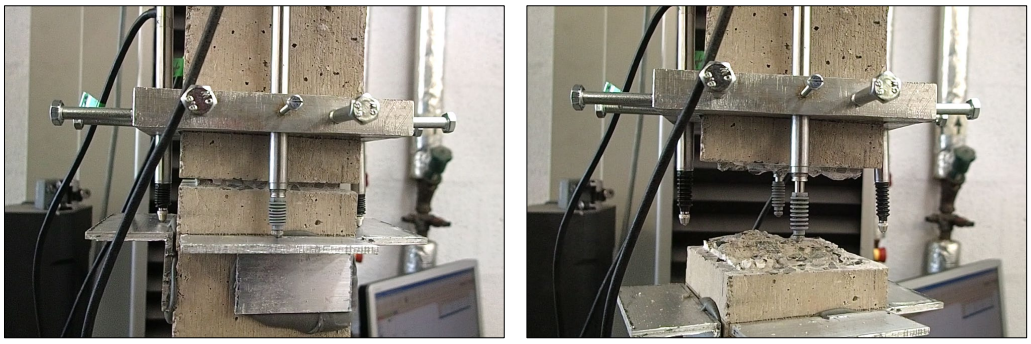

(a) (b)

Figure 5.4. (a) Before and (b) after

5.2.2 Experimental trial 2

A hydraulic Mayes universal test machine was used in order to achieve a higher overall stiffness and more control. This will be discussed further in sections 5.3.1 and 5.3.2. The overall test set up is illustrated in Figures 5.11 to 5.13 and 5.15. It is worth mentioning that the present tests did not include flow networks shown in Figure 5.15 and only control specimens were used with the aim of improving the testing procedure.

5.2.2.1 Influence on the grooved surface

The specimens in set 3 consisting of standard cubes, which were prepared in a similar manner to those described in sections 5.3.3 to 5.3.5 below. After curing and notching, the left and right surfaces of the specimens were cleaned and roughened to create a grid of grooves using an angle grinder, Air 4" grinderette. The grooves were approximately 2mm in depth with a spacing of 20mm. This is believed to improve the bond and to create mechanical interlocking between concrete, adhesive and steel plates. The roughness of the concrete surfaces allows adhesive to penetrate into the irregularities to form stronger interfacial layers. Both sides of the concrete surfaces were also roughen using a grinding

stone and cleaned using pressurised air to remove any dust before assembling it into the machine. More details on the bonding process can be found in Section 5.3.4.

However, most of the specimens did not perform as hoped, in that stable post-peak responses were not consistently obtained. There were few possible reasons for this; for example, the concrete surfaces were not levelled due to the variability in the grooves and the load also fluctuated too much during the setting of the adhesive. There was also a likelihood that some of the specimens were already broken since the hatching and notching were done a day after casting on a young concrete. There was also an issue relating to the noise which was primarily caused by tuning difficulties with the closed loop control. The frequency of the sampling rate was also increased from 10Hz to 100Hz.

Figure 5.5 shows the results from a successful test from set 3 where the softening behaviour of the specimen was captured. It can be seen that there some unloading and reloading behaviour occurred near the beginning of the test which may be due to issues related to the overall stiffness of the test setup. The potential stiffness reduction could be due to the missing bolts (see Figure 5.6) on the bottom plate, where only 4 out of 8 bolts were fastened. This situation resulted from an error in the manufacture of the bottom loading plate. Despite the above deficiencies, it was concluded that the present test setup with the closed control loop was able to achieve the post peak response of the specimens, but that a number of improvements were required. In future sets, grooves were not cut into the top and bottom surfaces and the specimens were allowed to mature for at least 7 days before notching to avoid any extra damage.

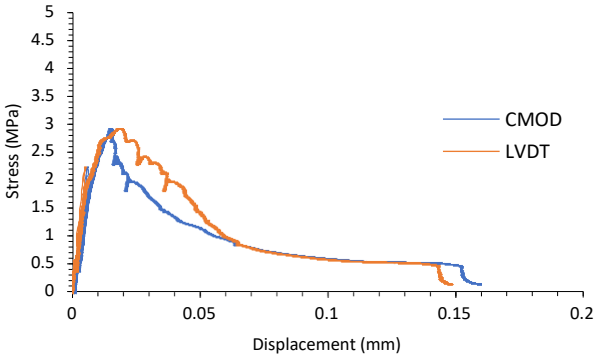

Figure 5.5. Load-displacement responses of the specimen in set 3

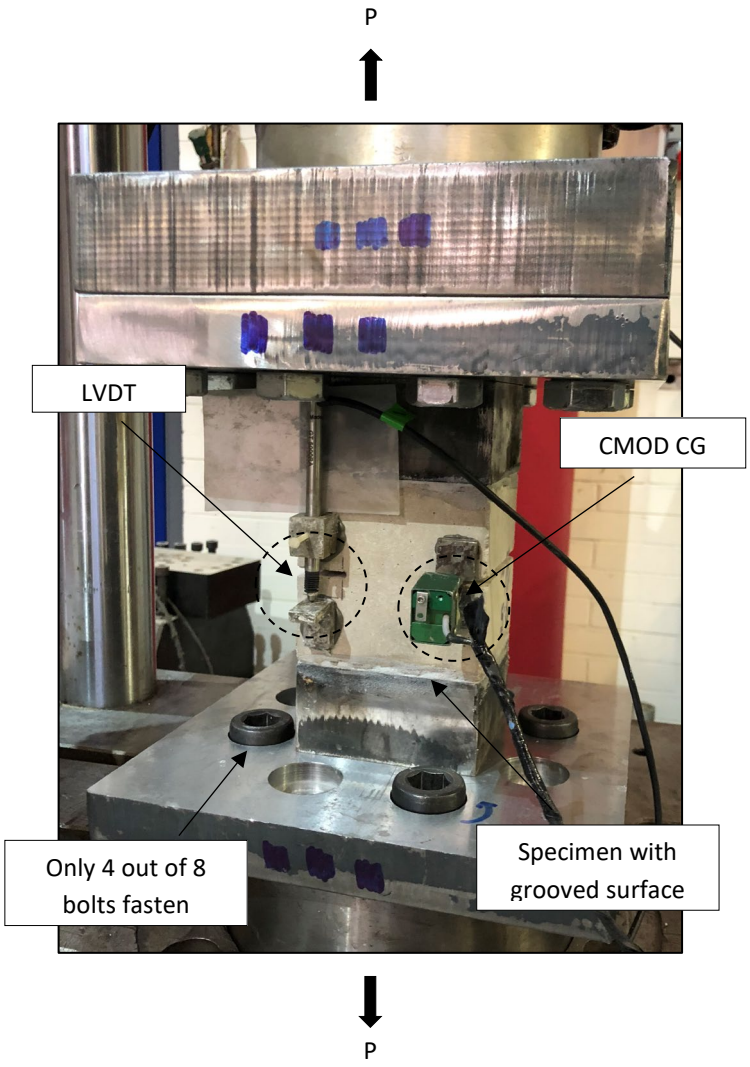

Figure 5.6. Testing arrangement showing the missing bolts

5.2.2.2 Influence of the notch depth

The specimens in set 4 used similar specimen preparation and testing procedures, to those described in sections 5.3.3 to 5.3.5. In this case, however, 35mm deep and 3mm wide notches were sawn on both sides of the specimen leaving an unnotched ligament area of 3000mm^2. This had the effect of reducing the stiffness of the specimen relative to that of the machine, which aimed to improve the stability of the post-peak response. Even though the test can be considered a success, there was still some difficulty in controlling the response, as may be seen from the unloading-reloading cycles in Figure 5.7. The author had some concern about the size of the coarse aggregate particles (i.e. 10mm) in relation to the width of the unnotched ligament area. This is because debonding tends to occur around these particles and when they are large in relation to a crack area, the position of the particles can have a strong influence on the behaviour (Karihaloo 1995). This implies that the measured behaviour is not representative of the material as a whole. Despite that, a straight crack or a mode I crack was achieved because of the deeper notches.

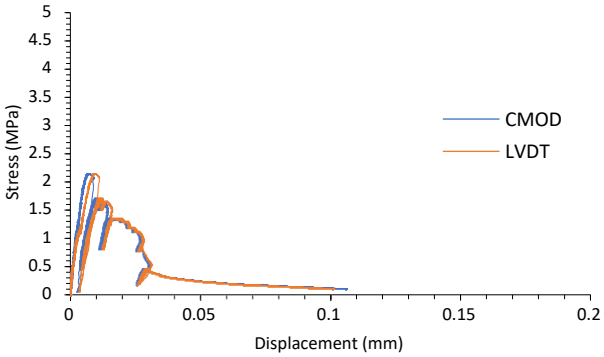

Figure 5.7. Load-displacement responses of the specimen in set 4

5.2.2.3 Influence on the maximum aggregate size and heat curing temperature

In order to explore the influence of coarse aggregate particle size and distribution, a set of tests (set 5) were undertaken with a different concrete mix, which had smaller coarse aggregate particles. The mix proportions used were 516kg/m^3: 1547kg/m^3: 237kg/m^3 of cement: aggregates: water with a maximum aggregate size of 4mm. A compressive strength of 40MPa was obtained at 7 days. The curing, notching and testing procedures were similar to those described in sections 5.3.4 and 5.3.5 except that the specimens were dried at a slightly lower temperature of 60°C instead of 90°C. In theory, smaller coarse aggregate particles result in a lower fracture energy (Karihaloo 1995), causing the response to be more difficult to control. However, the author believed that this disadvantage would be offset by having a more uniform dispersion of aggregate particles across the crack plane. The results are presented in Figure 5.8 below. A steeper pre-peak response was obtained due to the brittleness of the specimens as expected. The post peak response was also less ductile because of the smaller sized aggregates used. Although, there may be sufficient stiffness in the test setup, problems such as the test machine unloading and reloading before reaching the peak load was still an issue. This was apparent in control test 4, as shown in Figure 5.8(d). There was some scatter even after reaching the peak load during fracture initiation, which was most likely caused by the natural variation of concrete properties; nevertheless, the test setup was still able to capture the softening in all cases.

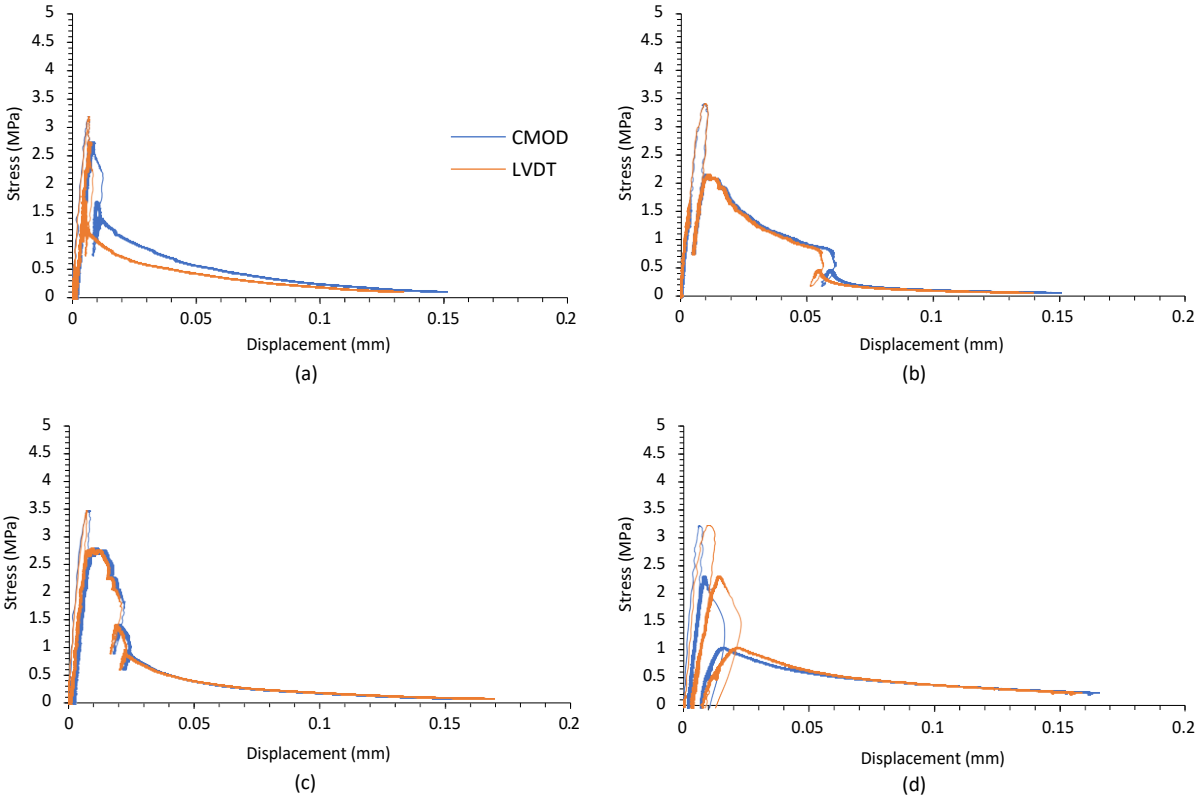

Figure 5.8. Load-displacement responses of the specimen in set 5 for (a) control 1, (b) control 2, (c) control 3 and (d) control 4

5.2.2.4 Influence on the stiffness of the loading rig

To obtain satisfactory results, the stiffness of the loading rig was increased by having a new lower plate machined, this time with all eight holes aligned to those in the machine platen (see Section 5.3.2). The test machine also underwent maintenance and recalibration. In sets 6 and 7, the specimens followed the same curing regime, notching, and bonding process as described in sections 5.3.3 to 5.3.5. The set 6 tests were carried out when the specimens were 5 weeks old due to the delays caused by the above maintenance.

Results from both of these test sets are presented in Figures 5.9 and 5.10. The results obtained were more promising and suggested that the test setup was adequately stiff, and that the response of the control unit was sufficient to reliably capture the post-peak response. It was also found that the load in control test 3 (see Figure 5.9(c)) drastically dropped after reaching the peak load but immediately regained a steady control. The different softening responses in the specimens were due to the natural variation and heterogenous nature of the concrete properties which are generally more apparent in a fixed head uniaxial test.

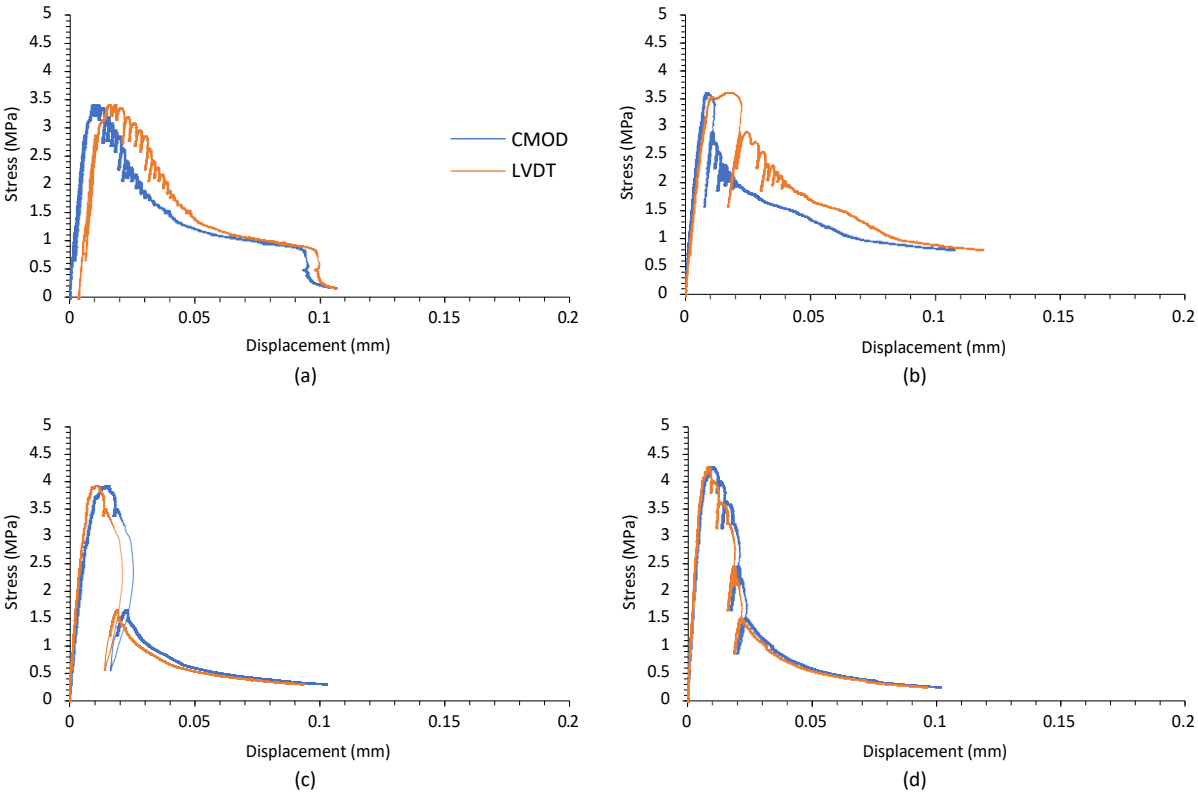

Figure 5.9. Load-displacement responses of the specimen in set 6 for (a) control 1, (b) control 2, (c) control 3 and (d) control

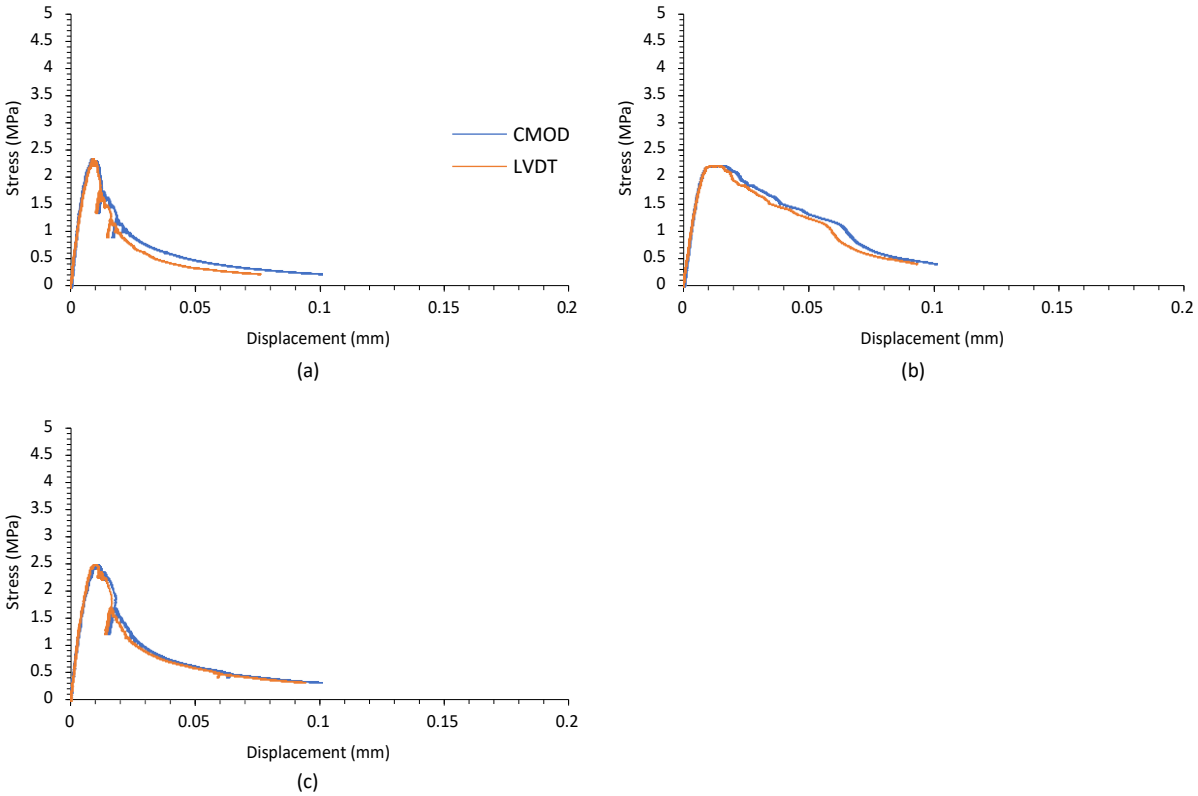

Figure 5.10. Load-displacement responses of the specimen in set 7 for (a) control 1, (b) control 2 and (c) control 3

5.2.2.5 Influence on the concrete mix

In set 6, the mix proportions were 406kg/m^3: 788kg/m^3: 983kg/m^3: 223kg/m^3 (cement: coarse aggregates: fine aggregates: water) with a maximum aggregate size of 10mm. However, in set 7 the concrete mix had a higher water-cement ratio of 0.67 compared to 0.55 in set 6 with mix proportions of 398kg/m^3: 772kg/m^3: 963kg/m^3: 267kg/m^3 (cement: coarse aggregates: fine aggregates: water). The average compressive strength obtained for the specimens in sets 6 and 7 were 49.3MPa at 10 weeks and 25.8MPa at 7 days respectively.

It was found that all the specimens in set 7 showed a smoother descending branch compared to the ones in set 6 (see Figures 5.9 and 5.10). It can be assumed that a weaker mix results in less brittle specimens due to the lower Young's modulus (E value), which reduces the possibility of snap-back behaviour occurring. However, the stronger mix resulted in a higher peak load and retained more of its stiffness on the descending branch. Although, there were humps after the peak load in the responses of both specimens in sets 6 and 7, the testing machine was able to recover from the drop, which suggested a stable closed loop control and a stiff test setup. It can be concluded that more unloading and reloading occurs when the specimens have higher strength and stiffness.

5.3 Experimental programme

As a result of the preliminary studies, several factors are taken into consideration in the main programme of study to ensure success in the following set of tests. The procedure deemed to be the most suitable will be discussed in this section.

5.3.1 Testing machine

A hydraulic Mayes universal test machine, certified for static and dynamic loads of up to 500kN and 400kN respectively, was used in this test series. This machine has a platen travel range of ±75mm and was controlled by an MTS FlexTest 100 closed loop control unit. A load cell with a capacity limit of 100kN in the vertical axis was used to measure the applied loads.

5.3.2 Manufacturing of steel plates

A sketch of the test setup is shown in Figure 5.11. The bespoke mild steel plates were supplied by Rycon Steels Ltd. Cardiff and comprised a 250x250x50mm machine platen, top and bottom plates of 250x250x30mm and specimen plates of 100x100x50mm. The steel plates were drilled, tapped and/or counterbored as per the CAD drawings with dimensions shown in Figures 5.12 and 5.13 by Metal Fabrication Co. Cardiff. Sufficient torque was applied to the M12 and M20 bolts to maintain compression between the plates at all times.

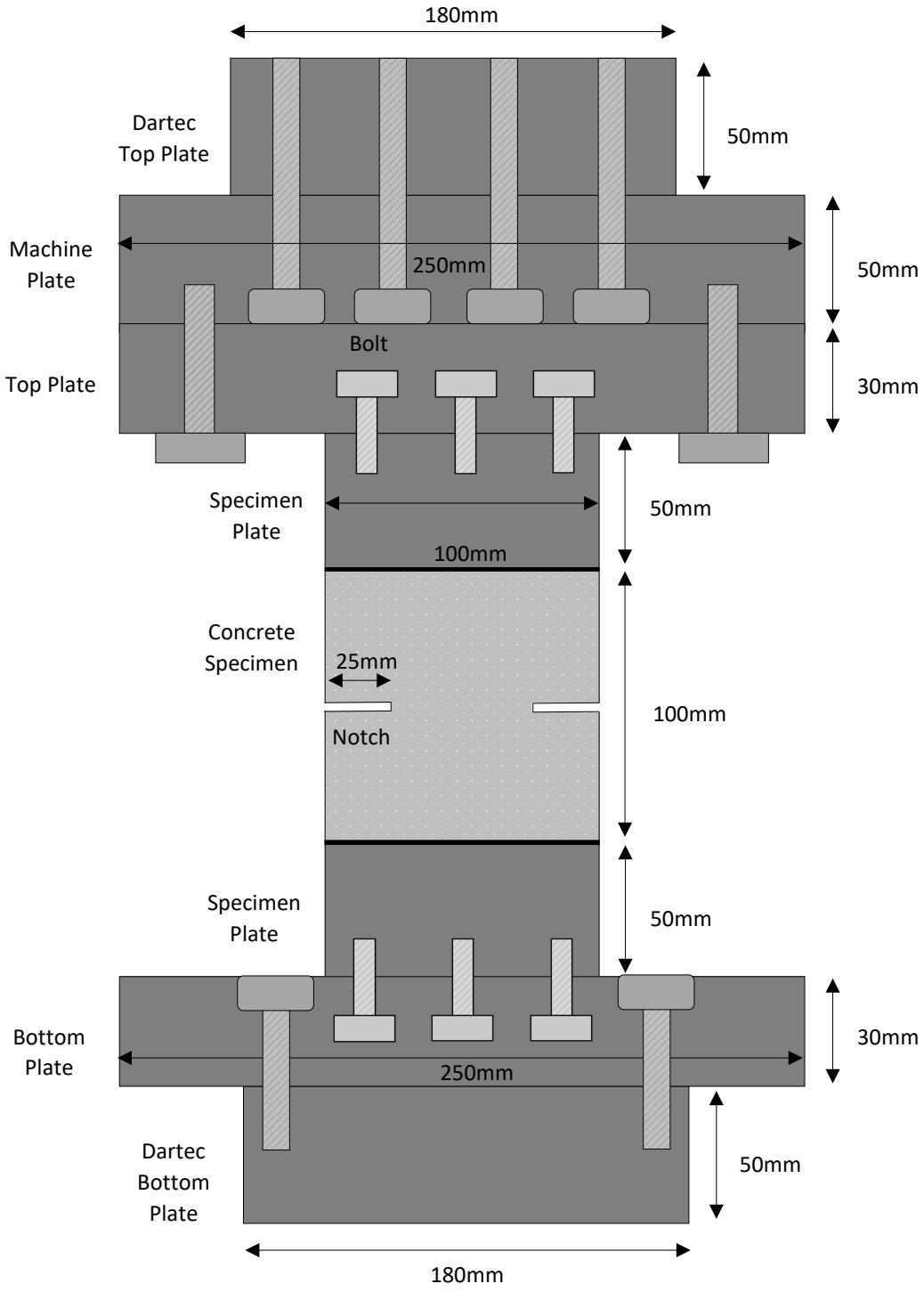

Figure 5.11. Schematic sketch of the direct tension test setup

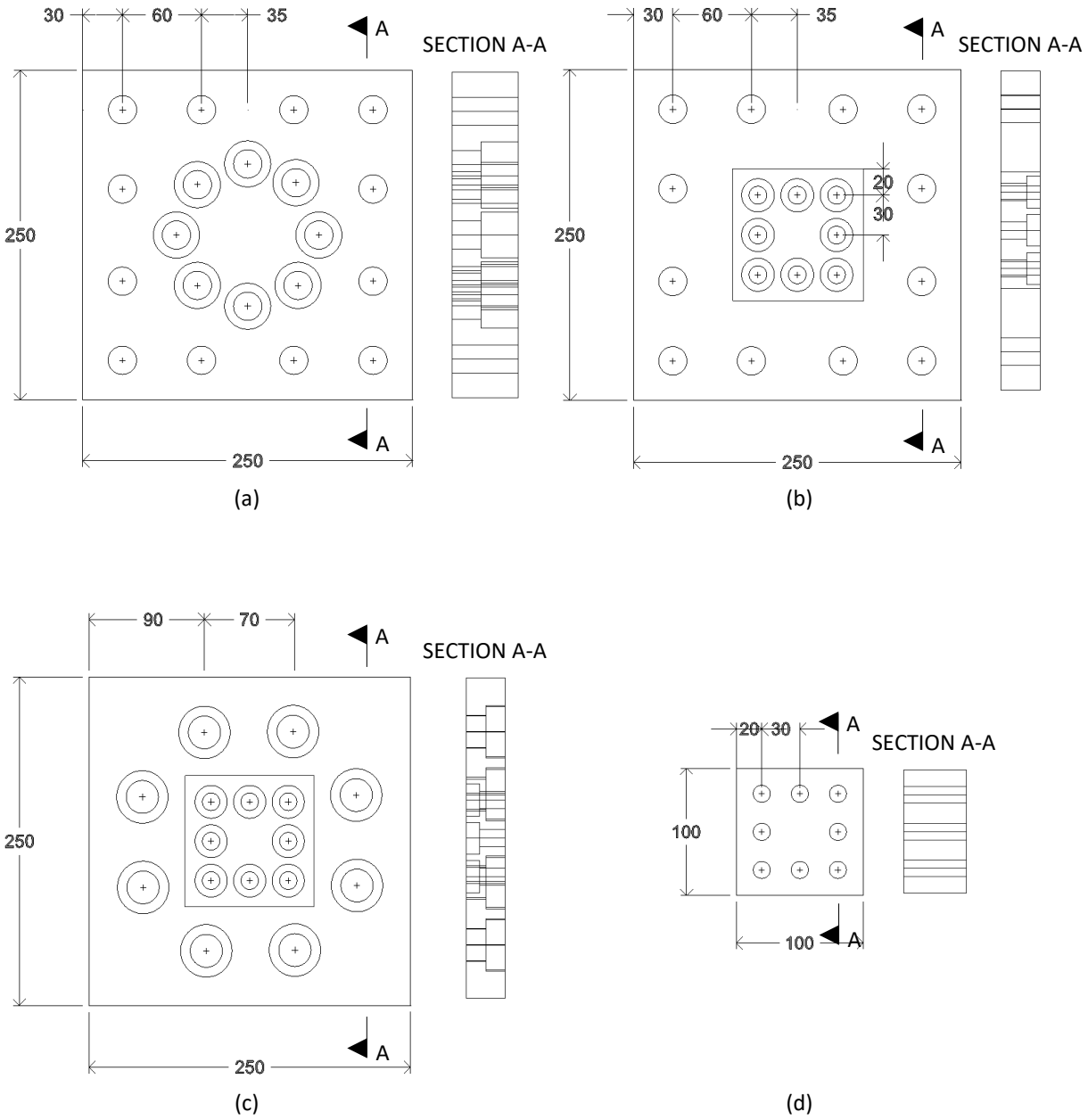

Figure 5.12. CAD drawings showing (a) machine plate, (b) top plate, (c) bottom plate and (d) specimen plate

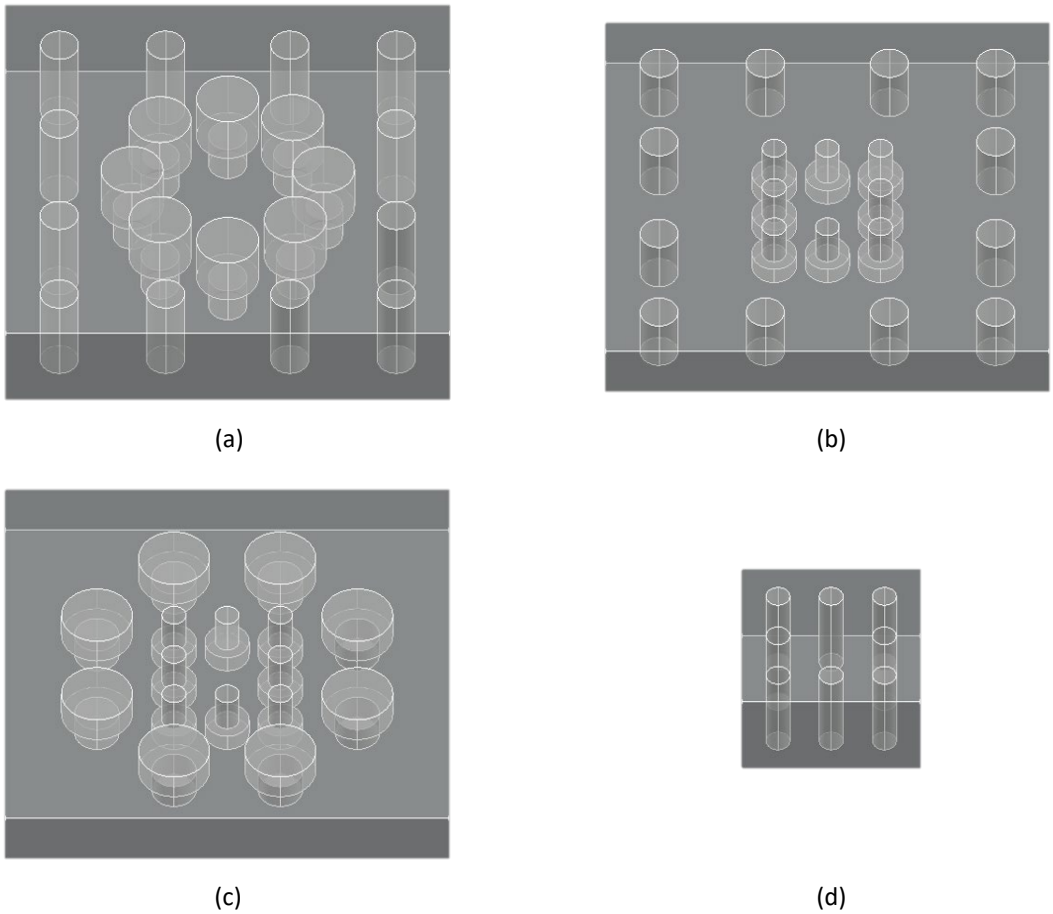

Figure 5.13. 3D CAD drawings showing (a) machine plate, (b) top plate, (c) bottom plate and (d) specimen plate

5.3.3 Concrete details and curing regime

The details of the mix design were the same to those given in Section 3.3.1 in Chapter 3. Testing was carried out between 8 to 24 days. After mixing, the fresh mix was transferred to the moulds. In this study nine 100x100x100mm concrete cube were cast, six of which included embedded channels. For every batch of concrete, three standard cubes and cylinders were also cast for determining the compressive and tensile strengths of the concrete respectively (see Section 5.3.6). The flow networks in the SH specimens were made using 4mm diameter PET tubes which were formed into a 'U' by threading 1mm diameter copper rods through the tubes and then bending the tube/rod combination into the required shape (see Figure 5.14). Two pre-drilled wooden blocks were placed on top of the mould and the PET tubes were secured with crocodile clips, which were then taped down to avoid any movement during compaction. The moulds, along with the PET tubes, were lightly coated with grease for easy removal. The concrete details and curing regime were given in sections 3.3.1 and 3.3.3 of Chapter 3. It was found that the PET tubes and copper rods could be readily removed using a plier from the specimens after 5 days of water curing. The holes on the surface of the specimens were then widened to 6mm and a depth of 10mm. After this, the channels were cleaned using pressurised air to eliminate any impurities and 6mm diameter 500mm long PET supply tubes were glued into the 10mm

deep recesses using CA (see Section 3.3.2 in Chapter 3). The pressure was supplied through an airline connected to a pressure gauge (see Section 3.3.4 in Chapter 3) and was attached to the 6mm diameter PET supply tubes. An Ashcroft 2089 precision digital test gauge was used to measure the required pressure prior to reloading to assist with the capillary action and the migration of CA into micro and macrocracks. This approach also minimised CA wastage, since only 25ml was needed to fill up all the channels rather than the conventional method of having a meter head to produce approximately 0.1bar pressure.

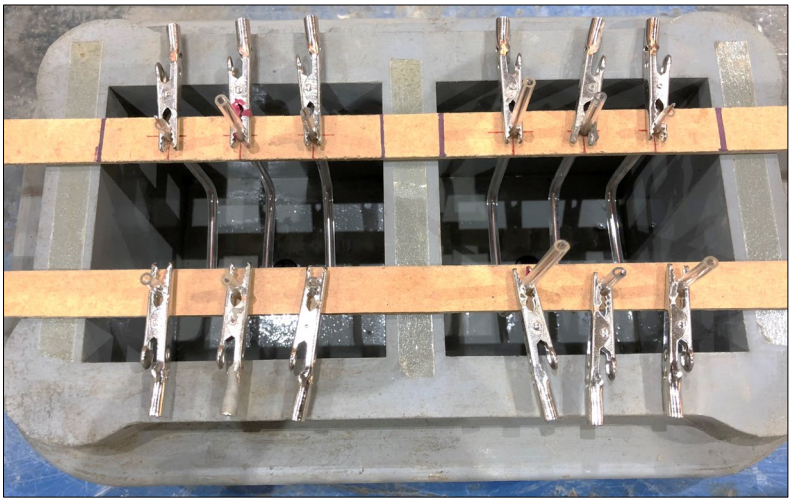

Figure 5.14. Prepared moulds for the SH specimens

5.3.4 Notching and bonding process

The specimens were notched either side to a depth of 25mm and a width of 3mm using a diamond blade masonry table saw, Controls Cernusco model 55-CO210/D after 5 days of water curing, thereby giving an unnotched ligament area of 50x97mm^2. Relatively deep notches were used to ensure that a single macro crack developed between those two notches, perpendicular to the maximum principal stress axis. This testing arrangement, guided by the work of Jacobsen et al. (2012), also reduces the potential for significant secondary cracks to form (see Figure 5.20). An LVDT, to measure the opening displacement, was mounted on one end of the notch and a CMOD transducer on the other side. The support brackets for the former and knife edges for the latter may be seen in Figure 5.16. The LVDT supports and knife edges were glued onto the specimen using a two-part epoxy resin with equal spacings of 20mm and 3mm across the notches respectively.

Before the specimen was mounted in the testing rig, the steel loading plates were sandblasted and cleaned with acetone to remove any grease or dust to prevent surface contamination. Sikadur-31 CF Rapid two-part thixotropic epoxy adhesive (SIKA) with an optimal working temperature of 5-15°C was used for bonding (see Table 5.2 and Appendix B). The adhesive was thoroughly mixed with a trowel and was evenly applied onto the top and bottom surfaces to a thickness of 1mm. The specimen was then glued to the pre-mounted on the 50mm thick specimen plates. A compressive force of 0.25kN was applied immediately after the specimen was mounted in the rig and maintained for 5.5 hours. This procedure facilitates the formation of a good bond.

Table 5.2. Properties of Sikadur-31 CF Rapid

Mechanical strengths	**After 10 days at 10-20°C**
Compressive strength • After 24 hours at 20°C • After 24 hours at 30°C	60-70N/mm^2 45-45N/mm^2 35-40N/mm^2
Flexural strength	30-40N/mm^2
Tensile strength	15-20N/mm^2
Bond strength to concrete	3.5N/mm^2
Bond strength to steel	15N/mm^2

5.3.5 Testing procedure and supplying CA

The relative displacement across the crack was measured on either side so that any relative rotation between the upper and lower parts of the specimens could be captured. The measurement of the crack opening was controlled by the CMOD clip gauge, which had a sensitivity of below 1µm at a constant rate of 0.0001mm CMOD per second which allows independent control of the vertical axis in a closed control loop. This relatively slow loading rate was used to facilitate the formation of a stable crack. A sampling rate of 100Hz was used. The PID (proportional-integral-derivative) controller on the closed loop control system for CMOD tuning was set on 400 for P Gain, 200 for I Gain and 0 for D Gain to obtain an optimal response and achieve a low steady state error (i.e. least noise). The testing arrangement and experimental setup are shown in Figures 5.15 and 5.16 respectively.

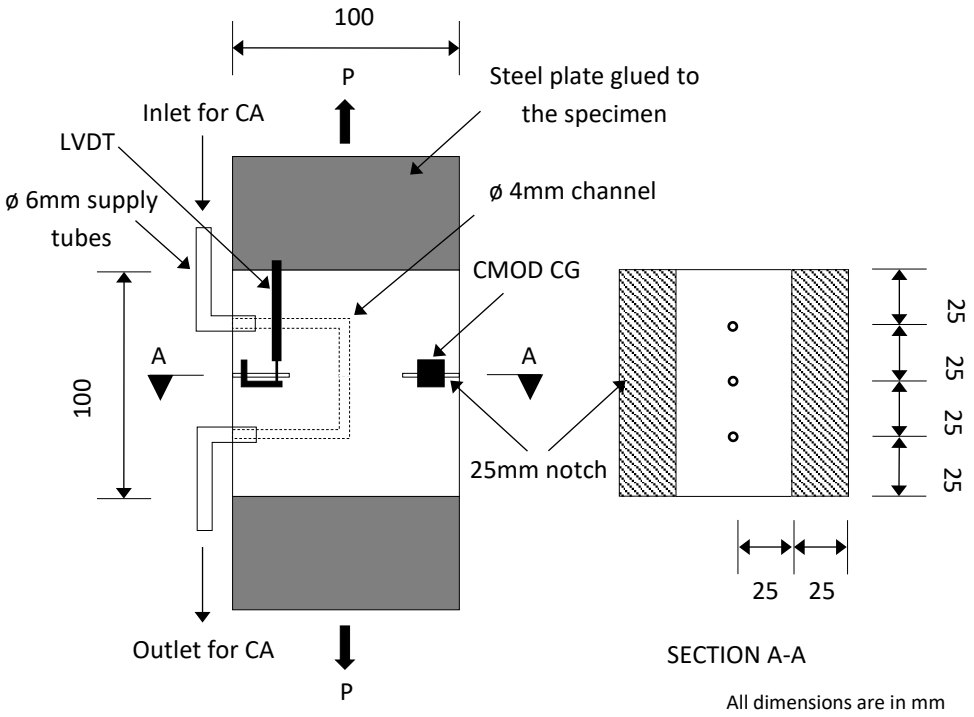

Figure 5.15. Testing arrangement for the direct tension crack-healing tests

CA was delivered through the 6mm diameter PET inlet supply tubes and secured with clamps to prevent flow prior to testing. The inlet supply tubes were clamped after filling, to ensure the pressure was contained within the system and stayed constant throughout, noting that a pressure of 0.5 bar was used for all of the current tests. The specimens were then subjected to loading until a specific crack opening (i.e. 0.1mm and 0.2mm for sets 8 and 9 respectively), as measured by the CMOD clip gauge (see Table 5.1). After pausing the load, the clamps on the inlet supply tubes were released to initiate flow of the CA. The specimens were reloaded after fixed healing periods (i.e. 0s, 60s, 300s, 600s and 1200s) until the crack opening was 0.2mm or 0.3mm for sets 8 and 9 respectively. The clamps on both the inlet and outlet supply tubes were later released to allow the remaining CA in the channels to flow out into an enclosed container to be disposed before unloading the test machine following the removal of the specimen. A few absorbent pads were also placed around the test setup to capture any excess CA that flowed out during the tests.

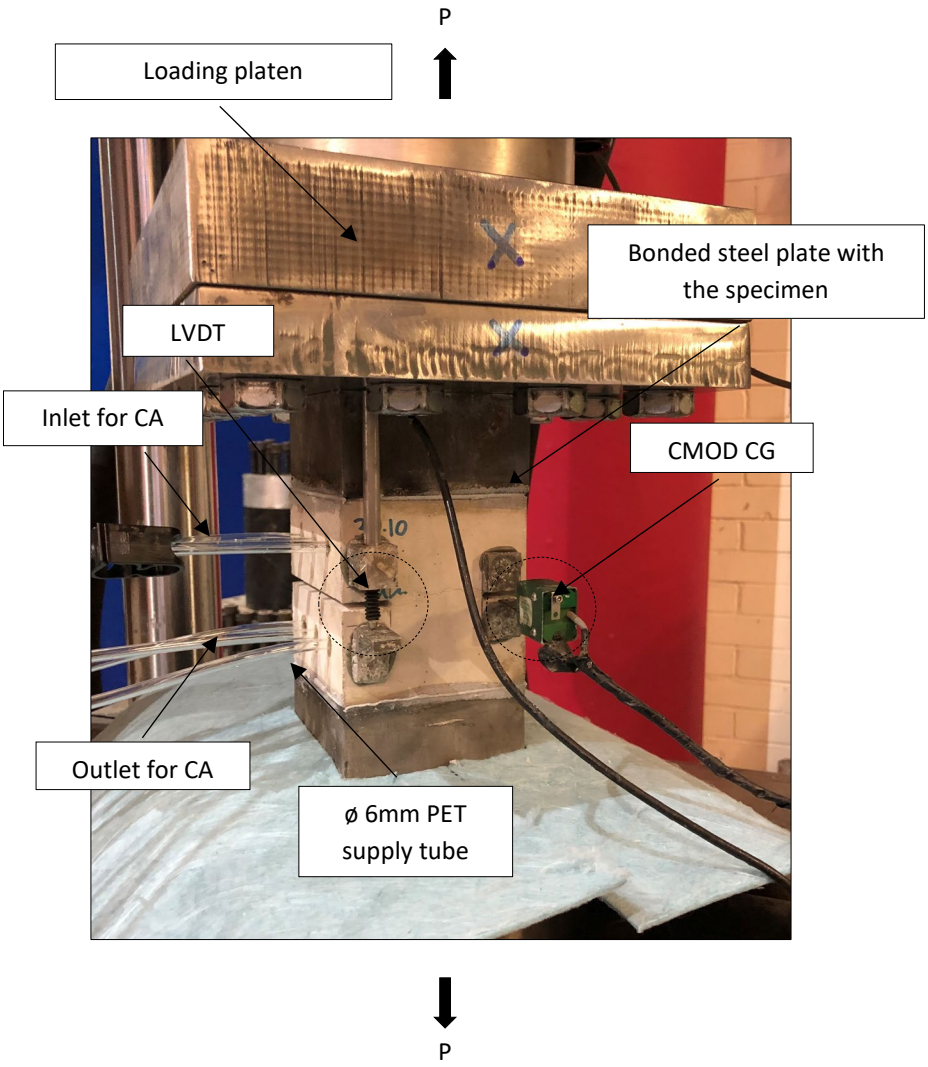

Figure 5.16. Experimental setup for the direct tension crack-healing tests

5.3.6 Compression and tensile values

The average compressive and tensile strengths along with the CoV of the specimens for this test series are shown in Table 5.3.

Table 5.3. Summary of concrete strengths after 8 days of curing in Chapter 5

Average cube strength, f_{cu} (MPa)	**CoV (%)**	**Average cylinder splitting strength, f_{cyl} (MPa)**	**CoV (%)**	**True uniaxial strength, f_c (MPa)**	**True tensile strength, f_t (MPa)**
39.5	6.5	3.5	9.6	31.6	3.0

5.4 Results and discussion

5.4.1 Load opening displacement

The results of the load-CMOD and load-displacement responses for the control specimens in sets 8 and 9 are shown in Figure 5.17. The stress, σ (MPa) is defined as the load, P (kN) divided by the ligament area (4850mm^2) and is plotted as a function of CMOD (mm) and LVDT (mm). The scatter in the responses is typical for concrete direct tension tests (Van Mier 1997). This is largely due to the heterogenous nature of the material and considerable local strength variations within the concrete matrix. The differences between the CMOD and displacement responses with respect to load (see Figure 5.17) were due to the nature of the upper platen of the loading rig, which had the freedom to rotate. The softening response is also affected by the manner in which the cracks from the notches on opposing faces propagate and join. For example, if there is a significant offset between the propagation lines of the opposing cracks (i.e. 20mm), then there tends to be a step in the load-displacement response when both cracks intersect, whereas when cracks from the two edges are closely aligned, the response is smoother. The unloading-reloading cycle in the softening phase, which occurs when the rate of the crack formation exceeds the response of the feedback loop; however, such cycles are not considered to invalidate the test provided that the softening branch is recaptured. The contrasting responses of the control specimens are illustrated in Figure 5.17, each of which exhibits one of the following characteristics; a smooth response (i.e. C1 and C2 from Figures 5.17(a) and 5.17(b) and C1 from Figures 5.17(c) and 5.17(d)), a response with a step (i.e. C3 from Figures 5.17(c) and 5.17(d)) and an unloading-reloading cycle (i.e. C3 from Figures 5.17(a) and 5.17(b) and C2 from Figures 5.17(c) and 5.17(d)).

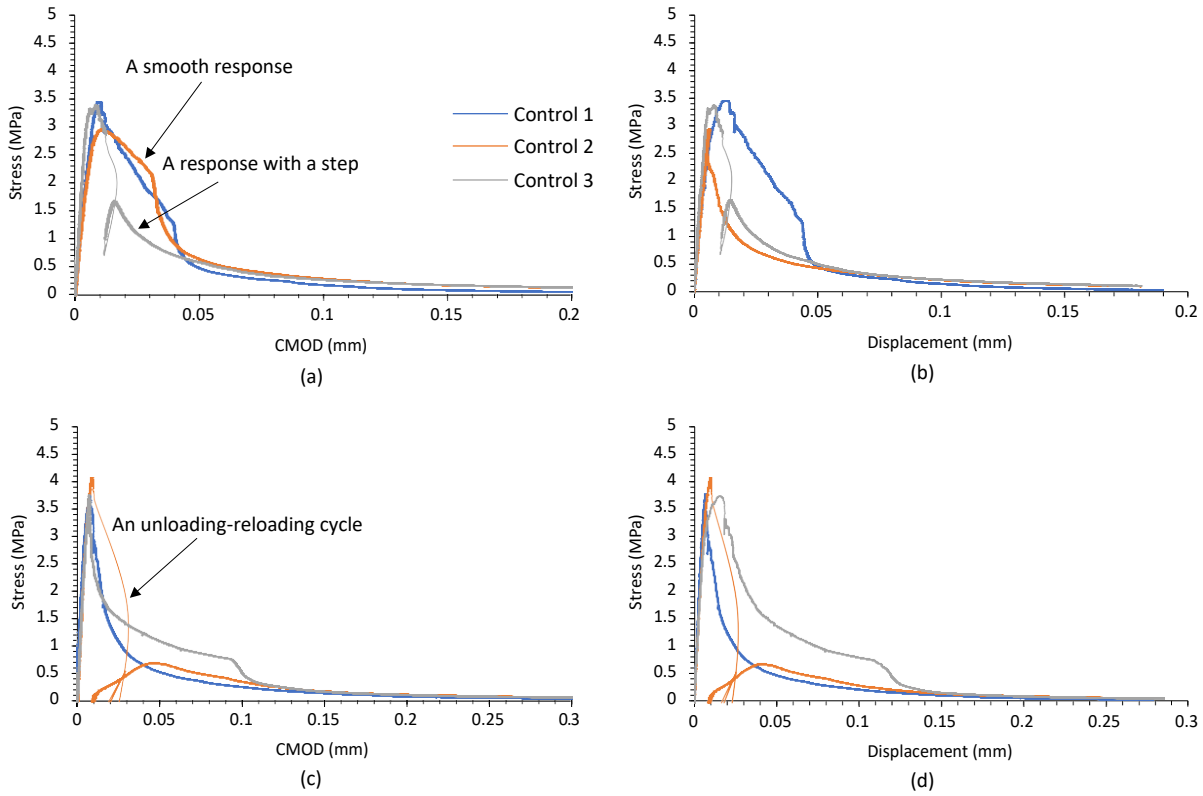

Figure 5.17. Load-CMOD and load-displacement responses of control specimens for (a-b) set 8 and (c-d) set 9

The results of load-CMOD and load-displacement responses for the SH specimens are presented in Figures 5.18 and 5.19. The fixed healing periods varied between 0 to 300 seconds in set 8 and 0 to 1200 seconds in set 9 respectively (see Table 5.1). An additional set of tests, with a healing period of 1200s, was undertaken in set 9 because it was apparent that CA had not fully cured after 600s. In the tests labelled 0s (i.e. Figures 5.18(a) and 5.18(b); Figures 5.19(a) and 5.19(b)), the inlet supply tubes were release immediately after the loading was paused (see Section 5.3.5), which took approximately 8 to 10s. It is estimated that CA reached the crack within 1s of the release time, noting that the supply pressure (0.5 bar) was also simultaneously applied. Therefore, the healing period labelled '0s' should be considered to be approximately 10s (±1s), though the quantity of CA in the crack would have been variable in this period. It was found by comparing the results from the test series in which healing took place within a 0.1mm crack opening in set 8 with those for a 0.2mm opening in set 9, that significantly more healing occurred at the smaller crack opening. This is evident from the increase in respective healing indices measured using the equation discussed in Section 3.4.1.4 in Chapter 3 for the associated crack openings (i.e. 0.1mm and 0.2mm) which recorded an average healing index of 50% and 15% respectively.

In both test series (see Figures 5.18 and 5.19), the initial slope of the reloading response curves (i.e. the response immediately after the healing period) increases with the duration of the healing period. Despite this, there was no corresponding increase in the peak post-healing loads. A more ductile response was obtained in the tests with shorter healing periods (i.e. 0s and 60s) which indicates that a significant proportion of CA was partially cured, and that re-healing and re-damage processes were occurring simultaneously during later stages.

The fact that the peak post-healed loads did not significantly increase in the same proportion to the reloading stiffness suggests that the proportion of the crack that is healed by fully cured agent is lower than the total area affected by it. This leads to the conclusion that CA did not stabilise and cure in some areas of the crack. This trend appears to increase as the crack opening increases. Another possible cause for this variation was small cyclic movements of the crosshead caused by the feedback control unit. These movements are likely to have disrupted the CA curing process. This effect was more pronounced in wider (see Figure 5.19) than narrower cracks (see Figure 5.18).

In summary, it was observed that the degrees of healing in both test series (i.e. 0.1mm and 0.2mm) were significantly lower than those for the comparable notched beam tests, for which the crack opening was 0.15mm (see Section 3.5 in Chapter 3). In the notched beam tests, the macro-crack tapers from a maximum value at the crack mouth to zero at the crack tip, although the area around the nominal crack tip will comprise a network of micro-cracks (Karihaloo 1995). It appears that the narrower the crack, the more effective the healing. Furthermore, the effectiveness of healing in the beams suggests that when healing agent flows upwards into a tapering vertical crack from a set of delivery channels, the healing agent stabilises and cures in a more effective way than when delivered via three channels into a horizontal uniform crack.

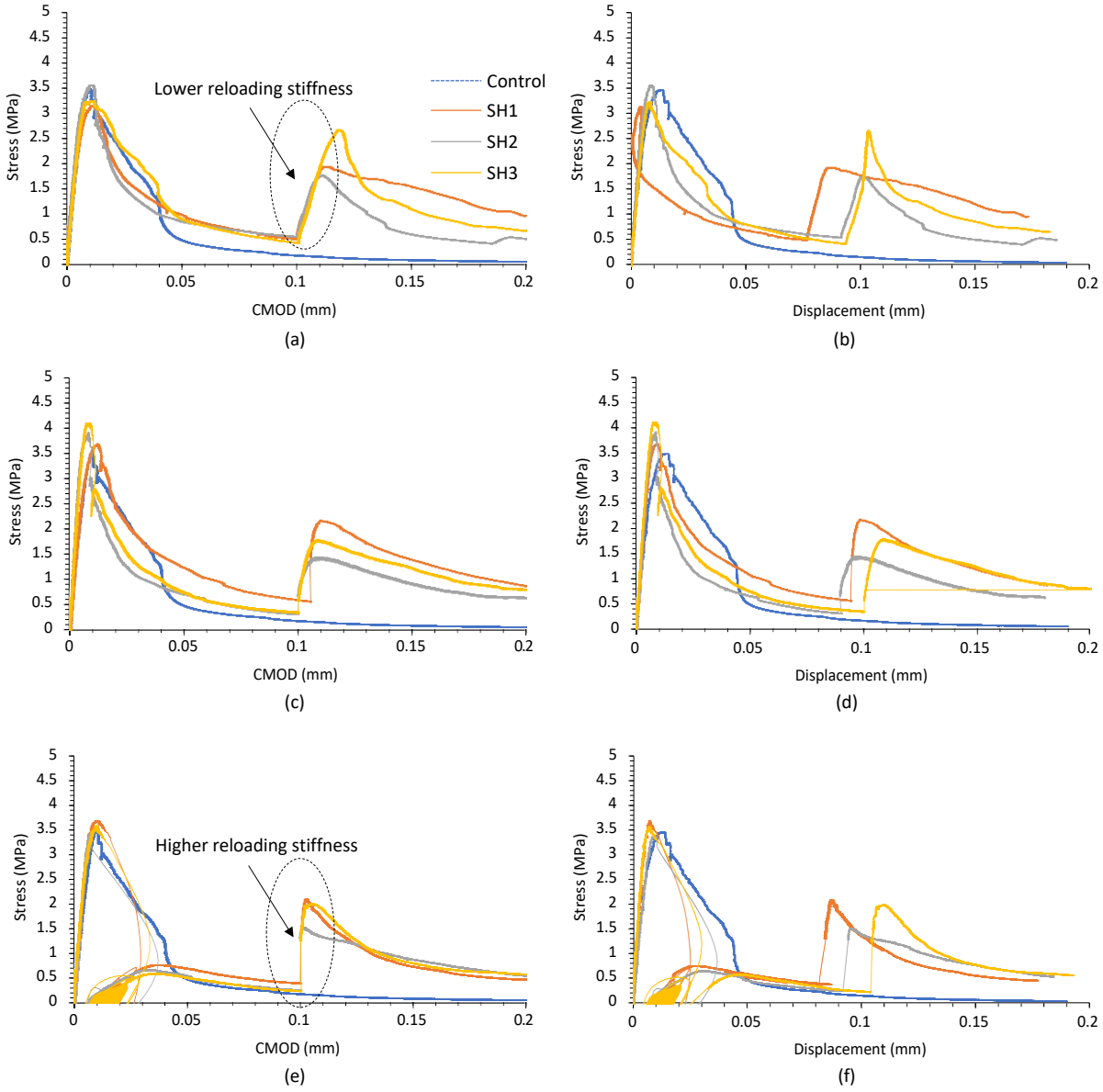

Figure 5.18. Load-CMOD and load-displacement responses of the SH specimens in set 8 (a-b) 0 second (c-d) 60 seconds and (e-f) 300 seconds

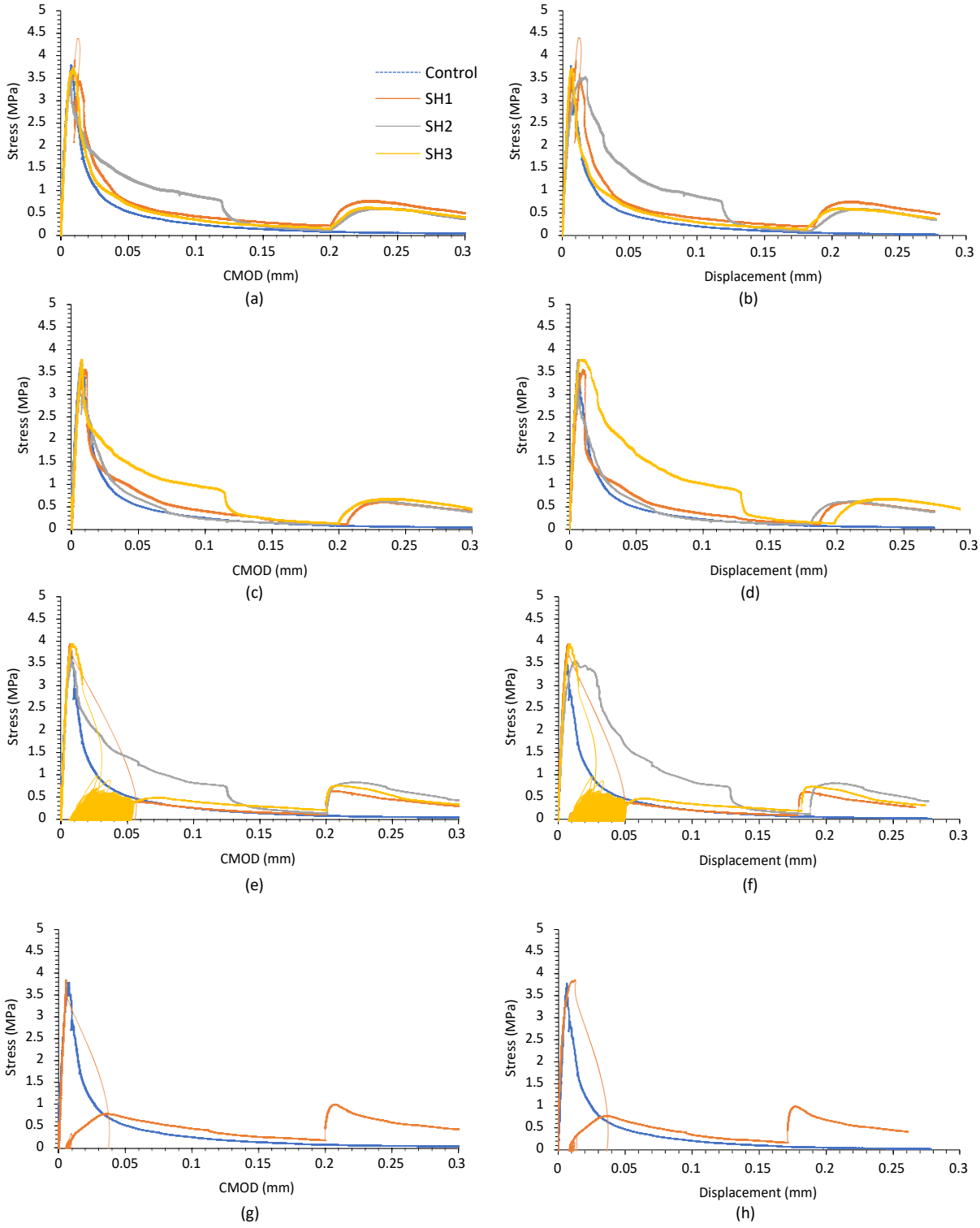

Figure 5.19. Load-CMOD and load-displacement responses of the SH specimens in set 9 (a-b) 0 second (c-d) 60 seconds, (e-f) 600 seconds and (g-h) 1200 seconds

5.4.2 Crack morphology and CA distribution

Given that concrete is a heterogenous material, a straight crack was nearly impossible to obtain. In spite of this, most specimens developed a single continuous crack between the notches with a variability of ± 5mm, as shown in Figure 5.20.

Additionally, there was evidence of multiple post-healed cracks, which developed around the fracture area. Visual observations during and after the tests suggests that re-cracking after healing often occurs in a slightly different location from the primary crack (see Figures 5.20(c) and 5.20(d)). This is consistent with the findings of Joseph et al. (2010).

Upon further investigation, it was found that the fracture was localised in between the aggregate particles (see Figure 5.21). This would suggest that the size of the aggregate particles has a major influence on the fracture properties of concrete in which the propagation of cracks is dominated by the aggregate distribution within the matrix. This is consistent with the well-established trend that the fracture energy of concrete increases with the maximum aggregate size (Van Mier 1997).

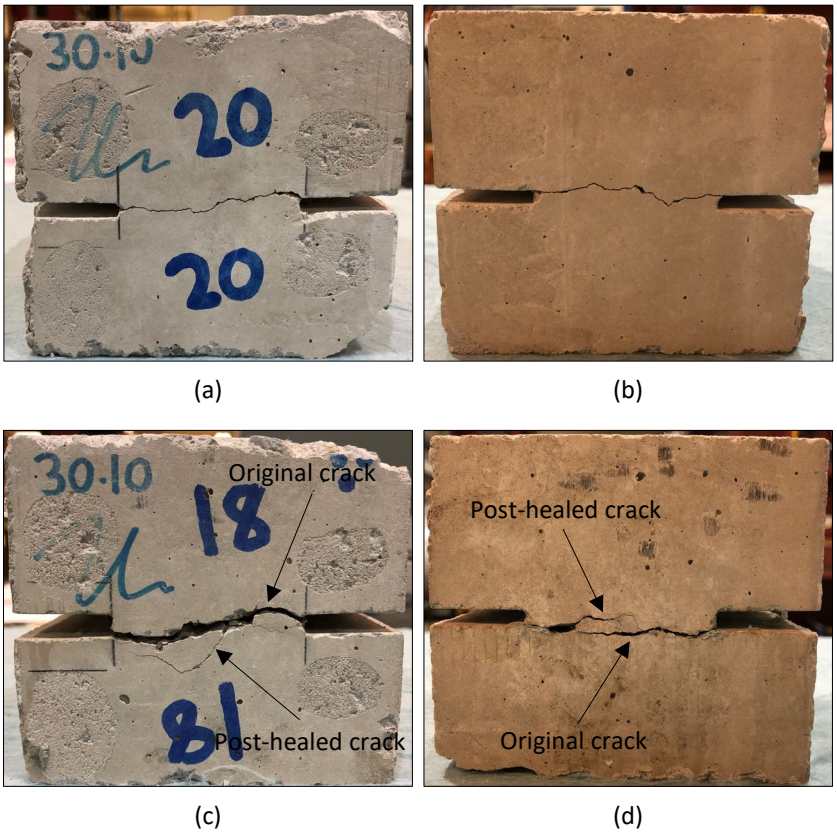

Figure 5.20. Front and back final crack patterns of a representative (a-b) control and (c-d) SH specimens

(a)

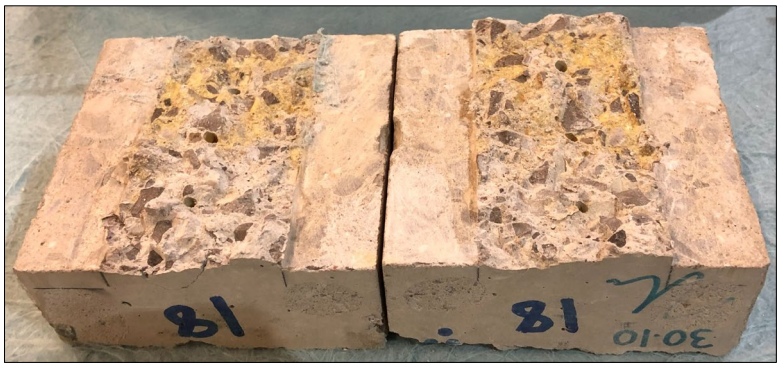

(b)

Figure 5.21. Close view of the crack surfaces of (a) a control specimen and (b) an SH specimen

Images taken of the cracked surfaces at the end of each tests showed that there were some discoloured zones, as illustrated in Figure 5.22. An attempt was made to measure the areas that had healed and re-cracked using an open source image editor, GNU Image Manipulation Program (GIMP 2019).

There were difficulties in approximating the amount of CA on the surfaces with any accuracy because the post-healed cracks always occurred at a different place especially for smaller crack openings (i.e. 0.1mm). These estimates were deemed to provide only qualitative evidence to support the computed healing indices. It was found that CA had completely healed a portion cracks at the 0.1mm CMOD crack opening (set 8) where only the upper half of the surface was covered with CA as oppose to the whole surface at 0.2mm CMOD crack opening (set 9). This would explain the higher load recovery for SH specimens in set 8 because cracking occurred elsewhere at reloading and at least half of the CA was fully cured. Although, a larger surface area was covered with CA for SH specimens in set 9, this had not resulted in greater healing, which suggests that a longer stable healing period was required. It was estimated that the spread of CA was up to 75% on the SH specimens in 0.2mm CMOD crack opening (set 9) and 50% in the 0.1mm CMOD crack opening (set 8).

The amount of CA in the reservoir was also found to decrease significantly during the healing phase of the tests with wider crack openings. It was found that a large portion of CA flowed into the

microcrack regions surrounding the macrocrack despite a small portion of CA can be seen flowing out onto the specimen. It was concluded that the viscosity of CA was too low to achieve a stable body of adhesive across the entire crack surface. It also appears that the crack boundary conditions and possibly the orientation of crack has a strong influence on the degree of healing.

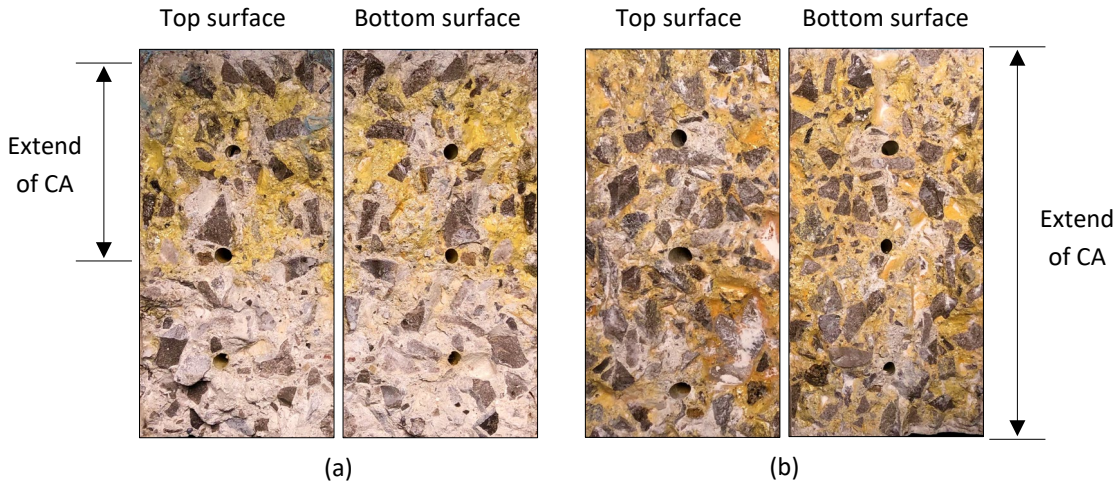

Figure 5.22. Differences on the spread of CA on the top and bottom surfaces at a crack opening of (a) 0.1mm CMOD after a healing period of 300s and (b) 0.2mm CMOD after a healing period of 600s

5.5 Conclusions

The study presented considers the direct tension behaviour of an autonomic self-healing cementitious system using CA as a healing agent at varying crack openings and healing periods. The overall conclusions from this series of tests are as follows:

- The test setup with the closed loop control has sufficient stiffness to capture the softening behaviour (with healing) in uniform cracks under tensile loading;
- The smoothness of the post-healing response of double notched concrete specimen is influenced by the manner in which opposite cracks intersect, where misaligned crack segments produce jumps in the response;
- More secondary post-healed cracks occurred when healing takes place in narrow crack openings (i.e. 0.1mm) than in wider crack openings (i.e. 0.2mm);
- A longer healing period (> 1200s) is required for CA to substantially cure (> 90%) in 0.1mm than 0.2mm wide respectively;
- The total area of crack filled by uncured or partially cured CA is less than the healed area;
- The low viscosity CA was unable to obtain a stable body of adhesive across the entire crack surface for the crack openings using the present delivery method;
- The degree of healing is greater in vertical tapered cracks in beams than in nominally uniform horizontal cracks.

In future work, it is recommended that the test machine be halted during the healing period (instead of paused) because the small vibrations caused by the feedback system may disrupt the formation of bonds within the healing agent and therefore affect the amount of healing.

Chapter 6 Flow and curing properties

6.1 Introduction and literature review

A series of tests were conducted to look at how the healing agent is being transported to damage sites and, how it cures and bonds to the surrounding matrix. This chapter focuses on the curing and transport properties of healing agent by analysing the experimental results from four separate studies (see Section 6.2).

Chapter 2 contains an extensive literature review on a range of healing agents and methods used by previous investigators to encapsulate, release and deliver these healing agents to damage sites (see sections 2.2.2.1 and 2.2.2.2 in Chapter 2). The advantages of vascular healing systems over other delivery systems are their potential to continually supply an unlimited quantity of healing agent and their ability to be pressurised to boost the flow of healing agent to micro and macrocracks regions (Davies et al. 2018). Vascular healing systems range from those that have isolated channels (Joseph et al. 2010) to systems with more complex interconnected networks (Minnebo et al. 2017). A detailed discussion on the vascular healing systems is given in Section 2.3 in Chapter 2. There have been many experimental methodologies proposed for the characterisation of the transport and mechanical properties of SHCMs. A more comprehensive review on the previous work can be found in Section 2.4 in Chapter 2 which also discusses non-destructive and imaging techniques used to provide useful insights into healing behaviour.

The following paragraphs discusses existing numerical studies conducted alongside the experiments in order to determine the flow and curing characteristics of healing agents. Gilabert et al. (2017) (see Section 2.4.2.1) simulated the flow of healing agent before and after capsule breakage by utilising the computational fluid dynamics program OpenFOAM and found a reasonable agreement between the model predictions and their experimental observations. The change in the healing-agent meniscus contact angle with time was also measured from the evolution of a PU drop on a concrete substrate. It is worth mentioning that the velocity dependence of the contact angle was not reported in the paper.

A combined experimental and numerical study was presented in Gardner et al. (2012; 2014) on the capillary flow of healing agents within discrete cracks in cementitious specimens. The study consists of the investigation of the flow of CA through artificial planar cracks after 7 and 28 days of curing. A range of crack openings and crack configurations (i.e. planar, inclined and tapered) were considered, and the capillary response was measured. The authors employed a modified Lucas-Washburn equation to simulate the discrete flow of healing agents that allowed for stick-slip of the meniscus, frictional dissipation and wall slip for the numerical simulation of the capillary flow. The work was extended in Gardner et al. (2017) in an investigation of the capillary flow properties of CA and GGBS solutions with time which included the measurement of the capillary meniscus contact angles of the two liquid agents on different substrates (i.e. glass, saturated concrete and unsaturated concrete). The time-viscosity relationship for these healing agents was determined using a custom viscometer that comprised of a concrete specimen with a cut horizontal rectangular channel, which was connected to transparent flexible tubes at either end of the channel. A time-dependent viscosity

relationship which is based on a momentum balance equation, was established for each healing-agent. This work was carried out for static cracks but did not consider evolving crack situations.

The curing process of CA on different substrates was studied by several investigators using a variety of techniques including Fourier transform infrared (FTIR) (Edwards and Day 2004; Brookes and Craston 1999), mid-infrared (mid-IR) (Katti and Krishnamurti 1999; Kusako and Suetaka 1980; Reynolds et al. 1982, Cambridge Polymer Group 2004), near-infrared (near-IR) (Tomlinson et al. 2006), electron tunnelling (Reynolds et al. 1982) and magnetic resonance (Katti and Krishnamurti 1999) spectroscopy. Tomlinson et al. (2006) explored the effects of CA film thickness and the type of substrate (i.e. dental and microscope glass slides) on the curing rate of CA at constant humidity using near-IR spectroscopy. The extents of cure with time for various film thickness was plotted. The authors suggested that the degree of cure was influenced by the presence of hydroxide ions (OH^-) ions. For example, the CA in contact with the substrate may stop curing when the moisture on the substrate is consumed. CA will also continuously cure from the upper surface downwards due to the infinite supply of OH^- ions in the air than on the substrate. There has not been any work on how curing fronts develop on cementitious substrates.

As highlighted previously by Jefferson et al. (2018), less attention has been paid to developing design procedures or numerical models for self-healing systems than to developing the systems themselves, although some progress has been made. There are usually inconsistencies between the information available from existing studies and the data required for numerical simulations. The motivation of this experimental programme is to provide the experimental data on the curing and transport behaviour of the healing agents in the vascular healing system which were identified as needing further investigation. Details on the experimental programme which addresses each of these aspects is provided in the following section. The associated modelling work from this study can be found in Freeman and Jefferson (2019) and Jefferson and Freeman (2019).

6.2 Scope of the study

A significant number of review articles have reported on self-healing systems that uses autonomic healing agents in SHCMs (Van Tittelboom et al. 2013; De Belie et al. 2018; Ferrara et al. 2018a). In some of these systems, the driving force of the healing agent only relied on capillary action whist pressurised networks were used in others (Davies et al. 2015). Additionally, in some scenarios, the damage and healing processes occur at different time scales but in other situations these processes overlap and interact. A comprehensive design procedure or numerical model for a SHCM system should be able to simulate all of the above using an idealised system in order to produce accurate and realistic representation of the self-healing behaviour (Jefferson et al. 2018); thus, the self-healing system and agent for the present experimental programme were chosen to consider all of these characteristics. As a result, the vascular healing system with embedded channels containing CA (Cyanotec 2019) described in Section 3.2 in Chapter 3 was selected because it ensured careful control of the delivery of healing agent, and it can be readily pressurised and easily monitored. The model self-healing system used for the present work is shown in Figure 3.1 in Chapter 3.

The experimental programme presented is as follows:

a. **Capillary flow in an evolving crack** (Section 6.3)
   The flow and transport characteristics of the healing agent under capillary pressure in an evolving crack in the cementitious specimens is essential to understand and predict the behaviour of vascular healing systems. This study investigates the capillary rise behaviour of the healing agent at varying loading rates and supply pressures.

b. **Sorptivity of cyanoacrylate** (Section 6.4)
   A proportion of the healing agent will always migrate into the micro-cracked region (or fracture process zone; see Karihaloo (1995) and van Mier (1997) adjacent to the crack. A series of tests were carried out to measure the healing agent uptake into cracked cementitious specimens in order to determine the sorptivity characteristics of this fracture process zone.

c. **Curing front properties of cyanoacrylate with a cementitious substrate** (Section 6.5)
   The polymerisation of CA is due to the presence of OH^- ions (Collins et al. 1966; Comyn 1998; Tomlinson et al. 2006) and its effect may be considered instantaneous with respect to the time scales considered in this study. Curing progresses as OH^- ions diffuse through the body of CA and this process is significantly slower than the polymerisation reaction. Tomlinson et al. (2006) suggested that polymerised material creates a barrier to further diffusion which makes the progress of healing highly dependent on the width between the surfaces being bonded (i.e. the crack width). The aim of this study was to provide an indication of whether a curing front model is appropriate for the vascular healing system, but no attempt was made to measure the curing rate of CA using such techniques as FTIR, which has been undertaken by others for different substrates (Tomlinson et al. 2006).

d. **Dynamic flow characteristics of CA in capillary channels** (Section 6.6)
   Blake (2006) suggested the contact angle between a moving meniscus and the adjacent substrate is velocity dependent. This issue was explored in a series of tests, which involved the healing agent being driven through a glass capillary tube. Specifically, with the aim of these tests was to determine the parameters associated with a velocity dependent dynamic meniscus contact angle (DCA) for CA.

The cementitious specimens in this study were formed from the same concrete mix as that given in sections 3.3.1 in Chapter 3. A nominal age of 8 days was chosen because neither the absolute strength of the specimens nor the degree of hydration was essential to the autonomic self-healing characteristics provided the specimens have general properties of a hardened concrete. Information on the curing regime can be found in Section 3.3.3 in Chapter 3.

6.2.1 Compressive and tensile values

The average compressive and tensile strengths along with the CoV of the specimens in this test series in sections 6.3 to 6.5 are shown in Table 6.1.

Table 6.1. Summary of concrete strengths after 8 days of curing in Chapter 6

Section	Average cube strength, f_{cu} (MPa)	CoV (%)	Average cylinder splitting strength, f_{cyl} (MPa)	CoV (%)	True uniaxial strength, f_c (MPa)	True tensile strength, f_t (MPa)
6.3	39.6	5.3	3.2	12.5	31.7	2.7
6.4	39.2	0.2	3.8	5.7	31.4	3.2
6.5	40.4	0.9	-	-	32.3	-

6.3 Capillary flow in an evolving crack

This study describes the capillary rise behaviour of CA in a vascular healing system exposed to CMOD rates of 0.0002mm to 0.002mm/s and supply pressures of 0 bar to 1 bar on small scale laboratory specimens of 75x75x255mm prisms under three-point flexural bending (see Figures 3.5 and 3.6 in Chapter 3). The experimental details for the Group A test series are given in Table 3.3. The characterisation of the mechanical healing properties in Group A was addressed in Section 3.4 in Chapter 3. The investigation presented here considers the flow and transport characteristics for such systems.

The capillary rise responses over time were recorded using a digital video camera directed at the notch from one side of the specimens. The capillary rise heights were measured as CA was seen flowing out from the surface of the crack. To facilitate the measurements, adjustable lighting was used in order to illuminate the growing crack. A pressure of 0.5 bar was used for all specimens whilst investigating the capillary rise at different loading rates and similarly, a CMOD rate of 0.001mm/s was used when varying the pressure.

6.3.1 Results and discussion

The time and capillary rise height responses at varying loading rates and supply pressures were extracted from the video recordings (see Figures 6.1 to 6.3) alongside the images shown to scale relative to the height of CA. The capillary rise height values during the continuous loading were measured from the bottom of the concrete prisms.

In Figures 6.1 and 6.2(d), the specimens recorded higher capillary rise heights with increasing loading rates. For example, at a CMOD rate of 0.002mm/s, a capillary rise height of 27.4mm was seen after 50 seconds, where it took 387 seconds at the CMOD rate of 0.0002mm/s to reach the same capillary rise height. It was found that the slower loading rate resulted in a more gradual glue flow into the cracks considering the delay from when the crack reaches the height of the channels (i.e. 20mm) thereby reaching a lower capillary rise height. Similarly, a faster capillary rise rate was recorded with higher pressure where a capillary rise height of 35.7mm after 97 seconds was shown at 1 bar of pressure

compared with 32.8mm after 92 seconds for 0.1 bar of pressure (see Figures 6.2(e-f) and 6.3). It is worth noting that the supply pressure had a significant influence on the capillary rise responses. This was apparent in the specimens without pressure (i.e. 0 bar), in which a capillary rise height of 9.1mm was observed after 310 seconds. This was because there were lower capillary forces to drive the CA upwards into the crack due to the absence of pressure. A maximum capillary rise height of 37.0mm was seen after 127 seconds in the specimens subjected to 0.5 bar of pressure. It was evident that the increase in loading rate and pressure facilitates CA penetration into micro and macrocracks.

It is necessary to extrapolate the capillary rise height data in order to investigate trends exhibited both in terms of varying loading rates and pressures. As discussed previously in Section 3.4.1.1 in Chapter 3, CA will flow into a crack when the crack opening reaches 0.03 to 0.05mm. This range for the breakthrough crack opening was based on when CA was first seen at the surface 25mm from the nearest delivery channel (see Figures 6.4 and 6.5). In addition, the slower loading rate the longer the time taken to reach a particular crack opening, and therefore the greater the time for the CA to cure in the channels, which may imply that a larger minimum opening would be required to initiate flow of CA (i.e. 0.05mm). Overall, it was found the loading rates did not significantly affect the response until it reached 0.001mm/s and a higher capillary rise height was recorded for a pressure of 0.3 bar, which coincides with the findings in sections 3.4.1.1 and 3.4.1.2 in Chapter 3.

Gardner et al. (2014) suggested that the capillary rise response is curtailed by CA curing. Since CA is known to cure rapidly in gaps less than 0.05mm (Joseph et al. 2010), with an accompanying increase in the viscosity, the capillary rise would expect to cease in a narrowing opening soon after the meniscus reaches this crack opening. In summary, this study, whist producing limited data, does provide an insight into the capillary rise behaviour in evolving cracks, and the effects of loading rates and pressures.

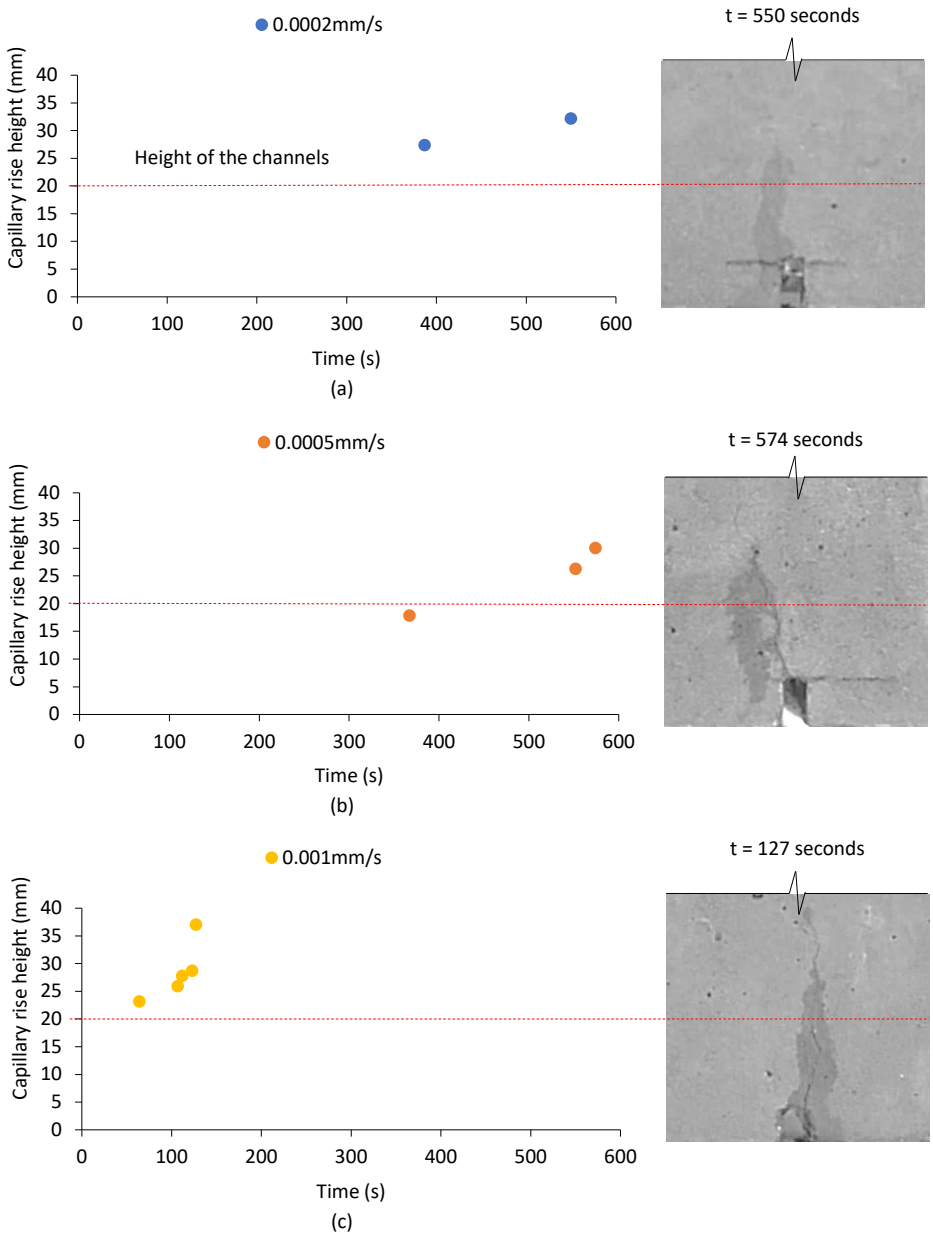

Figure 6.1. Capillary rise height measurements relative to the base of the specimen for loading rate of (a) 0.0002mm/s, (b) 0.0005mm/s and (c) 0.001mm/s

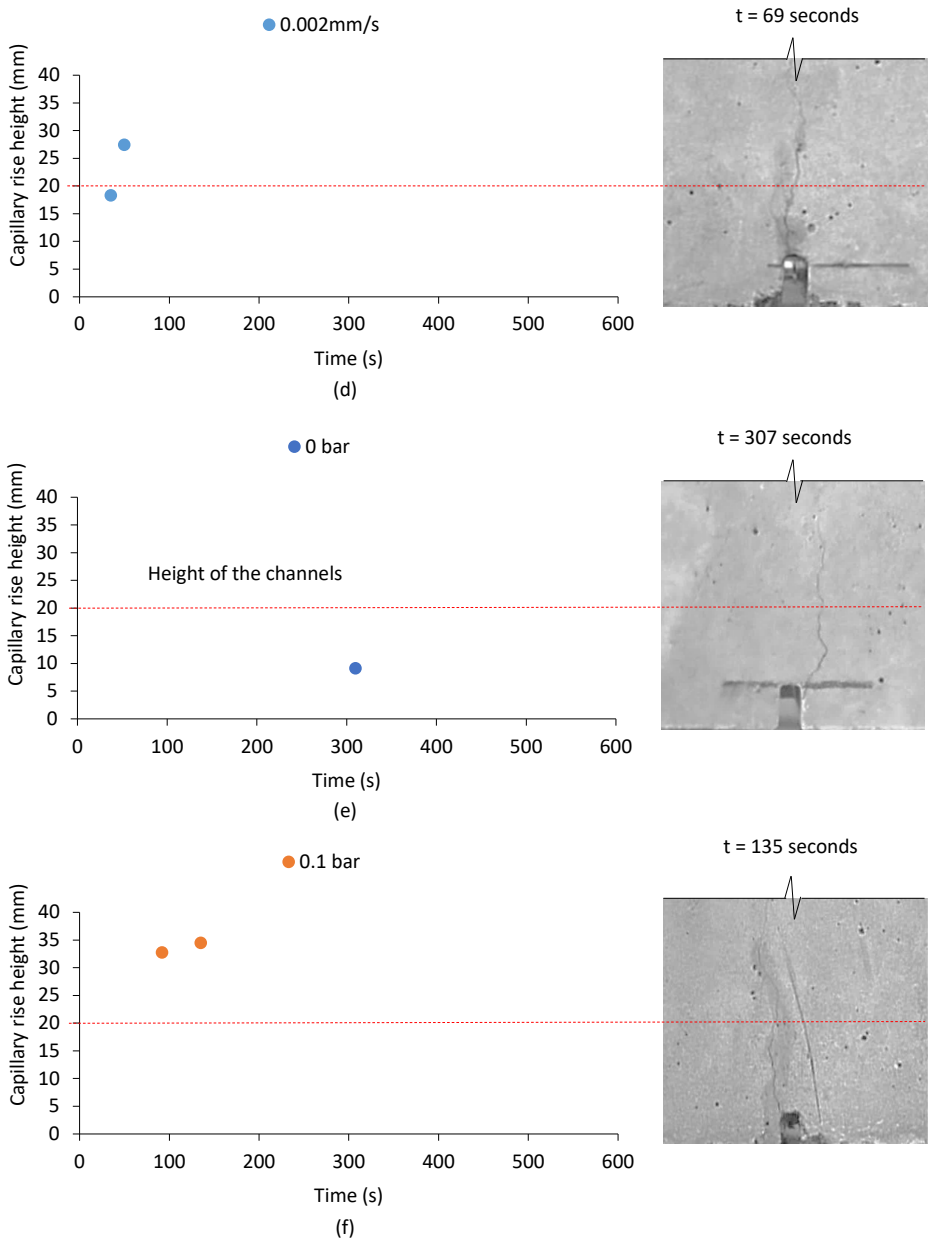

Figure 6.2. Capillary rise height measurements relative to the base of the specimen for (d) loading rate of 0.002mm/s, (e) pressure of 0 bar and (f) pressure of 0.1 bar

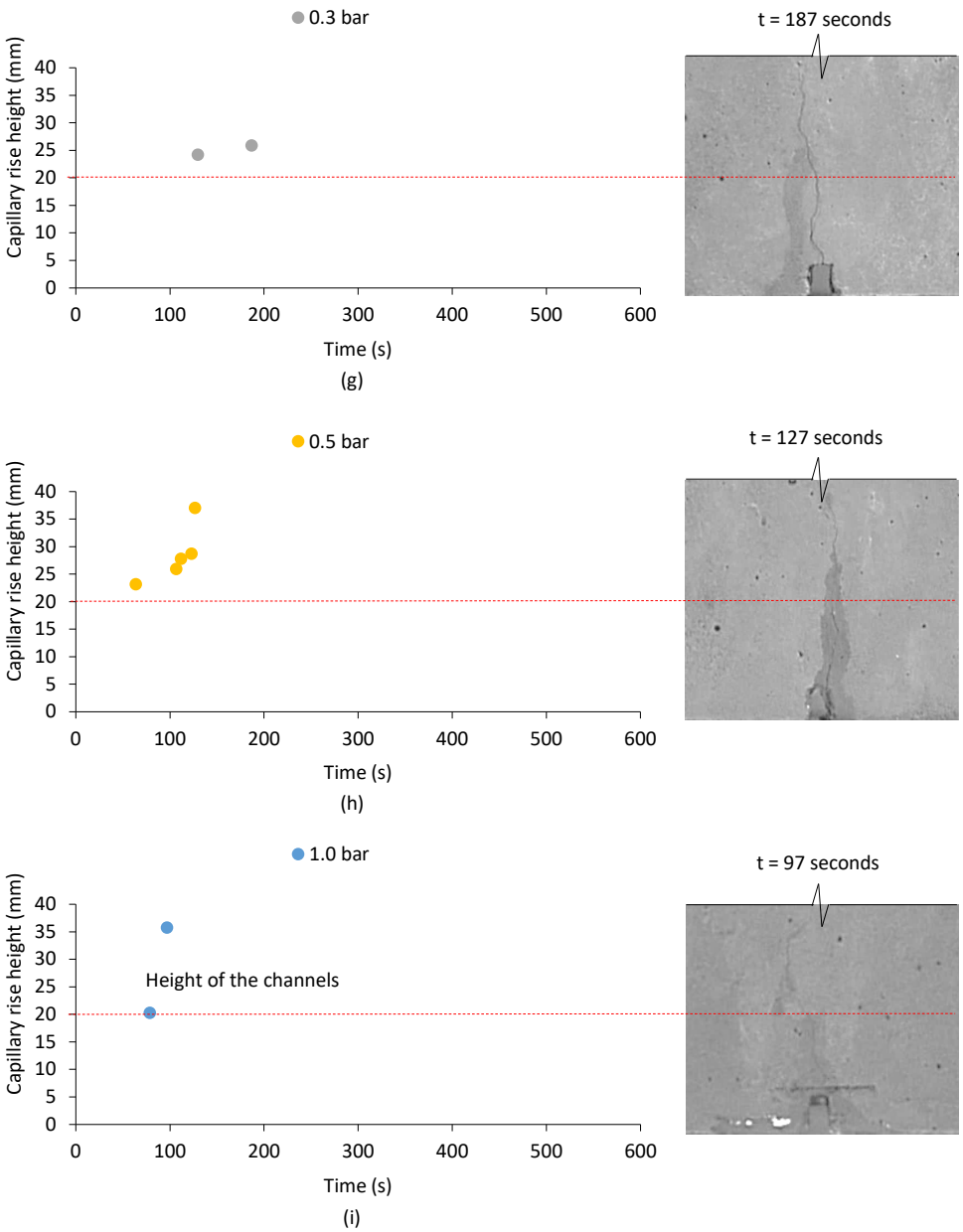

Figure 6.3. Capillary rise height measurements relative to the base of the specimen for pressure of (g) 0.3 bar, (h) 0.5 bar and (i) 1.0 bar

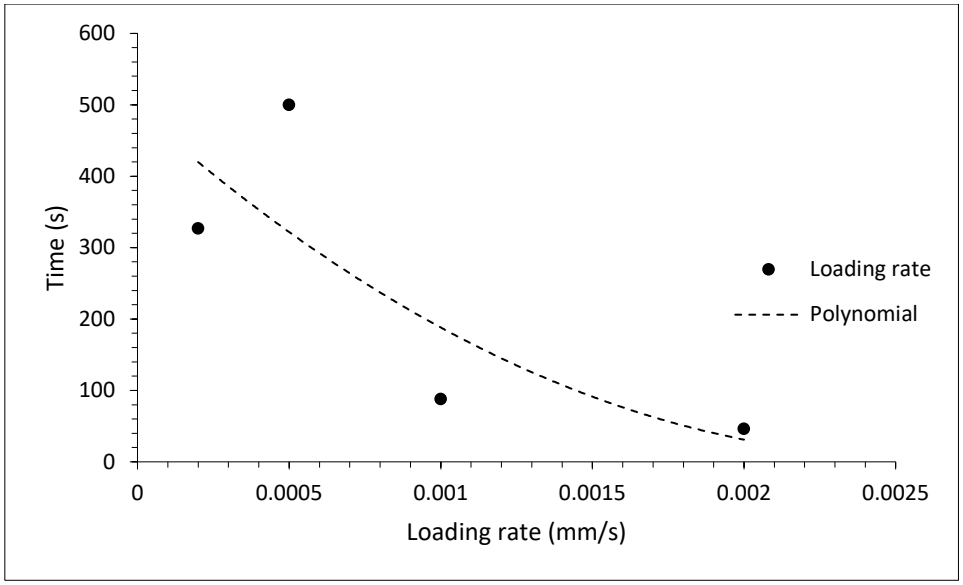

Figure 6.4. Effects of varying loading rates on the capillary rise height of 25mm

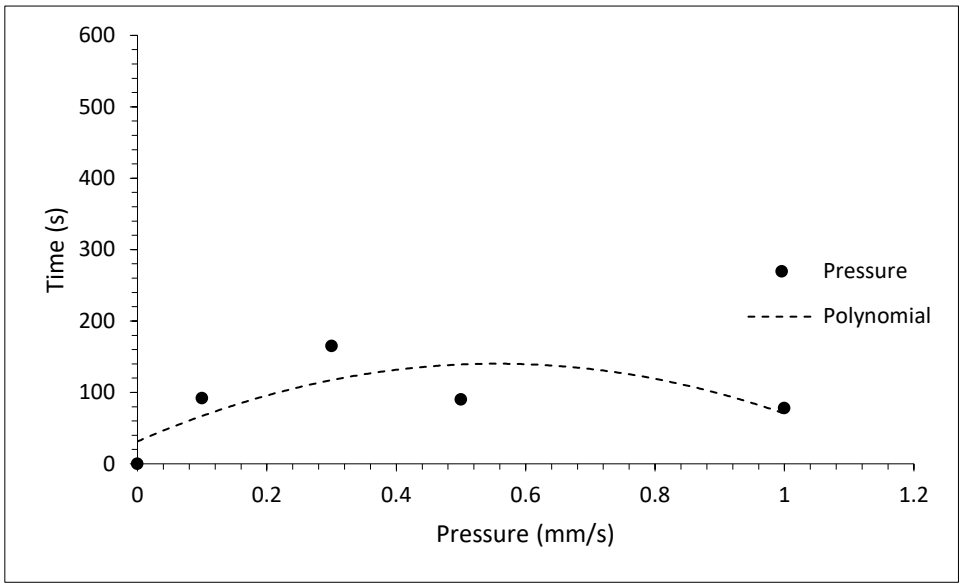

Figure 6.5. Effects of varying pressures on the capillary rise height of 25mm

6.4 Sorptivity of cyanoacrylate

This study examined the transport of CA into a cementitious specimen through a natural crack surface. The concrete prisms with dimensions of 75x75x255mm were cast with the same mix proportions, curing regime and specimen preparation as those detailed in sections 3.3.1 and 3.3.3 in Chapter 3. As discussed in Section 3.3.5 in Chapter 3, the specimens were loaded in three-point flexural bending to failure. The two halves of the broken beam formed two separate test specimens.

The experiment setup as illustrated in Figure 6.6, comprised a shallow bath of CA in a clear 500ml clear plastic container. The specimens, with the newly formed crack surface being placed vertically downwards and submerged in the CA pool. The capillary rise response was captured using a high-resolution digital video camera. A timer and a scale were placed within the viewing frame and LED lights were used to illuminate the test setup. The digital recording was started prior to the concrete specimen being placed in the bath and continued for a period of 5 minutes from the time that the specimen first touched the surface of the CA bath. Preliminary tests had previously shown that the visible rise height reached a steady state in under five minutes.

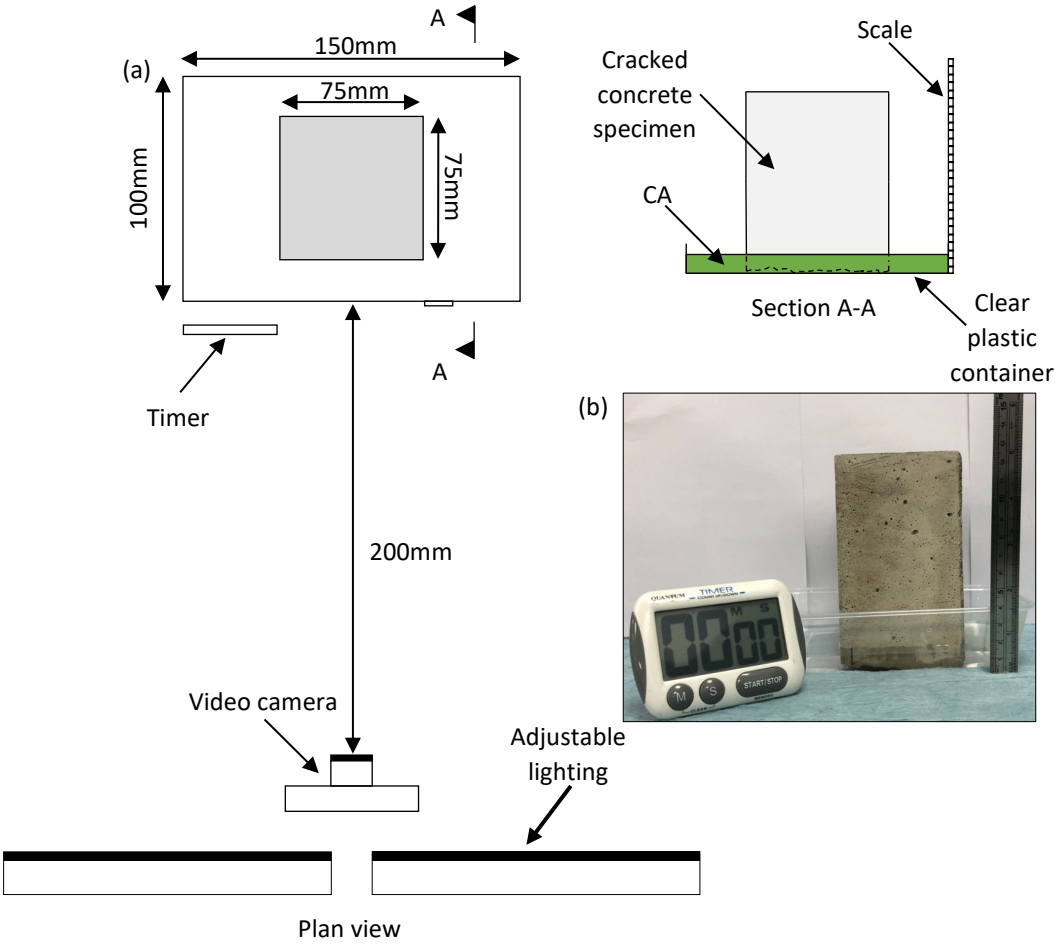

Figure 6.6. (a) Schematic representation and (b) photograph of the sorptivity test setup

6.4.1 Results and discussion

The capillary rise height responses, determined from the mean surface height of the CA visible on the side of the specimens, are given in Figure 6.7. As CA flows into the specimen under capillary action, the specimen becomes darker in colour, and the upper limit of the darker section is interpreted as the internal limit of the CA. It is acknowledged that this is an approximation used to determine the flow characteristics but, nonetheless, it can be readily simulated using a continuum flow model in which the driving force is capillary suction (Chitez and Jefferson 2016). The average immersion depth of the specimen in the CA bath was 10mm.

In all the specimens, the CA appeared to start rising immediately after the cracked surface touched the CA bath. The surface of the CA did not appear to remain plane but quickly became uneven, with the CA appearing to follow preferential paths and create *'flow fingers'*, which are characteristic of flow in heterogeneous materials (Neville 2012). There was also a significant variation in the rise-response observed in the different specimens, which has been found for other flow processes in concrete. There were also variations between the specimens in terms of surface areas in contact with the CA due to the tortuosity of the cracks which have an influence on the rate of the capillary rise and the sorptivity of CA (Collins and Sanjayan 2008; Gardner et al. 2012). The mean final rise height, from 4 specimens (S1-S4), was 3.1mm after 600 seconds with a CoV of 15%.

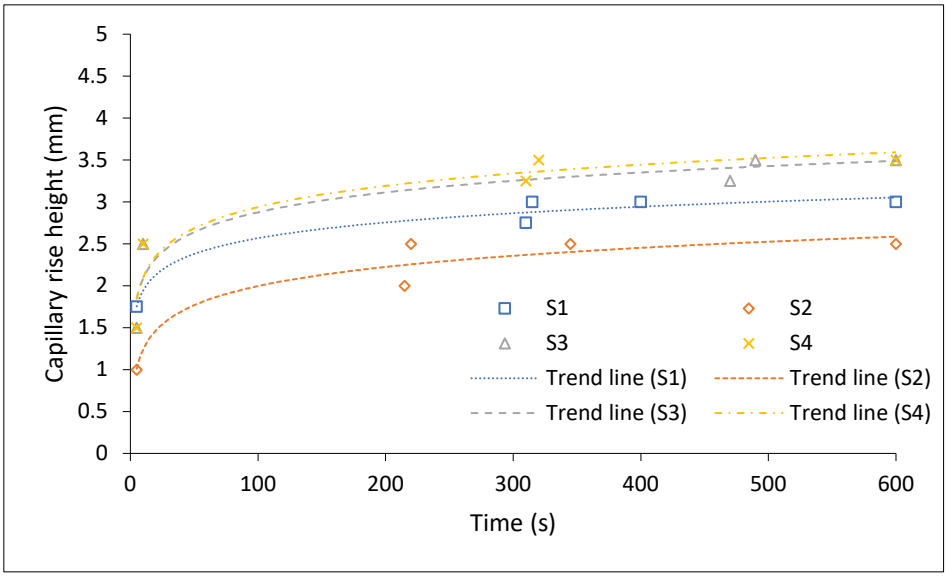

Figure 6.7. Sorption rise responses at 8 days

An attempt was made to determine the mass of CA absorbed by the specimen by weighing the specimens immediately before and after the immersion period. After the test, the surfaces were wiped with a damp cloth to remove excess CA, but this did not prove easy due to the nature of CA. Therefore, the results presented in Table 6.2 are given with a degree of caution. To determine the percentage of capillary pores filled with CA, the capillary porosity was assumed to be 12% (Baroghel-Bouny et al. 1999).

Table 6.2. CA sorption into concrete specimens at 8 days over 600s using weight before and after immersion

Specimen	Weight change (g)	CA uptake (ml)	Degree of saturation (%)
S1	0.72	0.68	0.77
S2	0.52	0.49	0.58
S3	0.48	0.45	0.50
S4	0.54	0.51	0.56
Mean	**0.56**	**0.53**	**0.60**
CoV (%)	**19**		

An additional set of tests for 4 specimens was carried out when the specimens were 15 days old (see Figure 6.8). These showed similar responses to those of the 8-day specimens. However, a slightly higher average capillary rise height of 3.5mm over 600 seconds was recorded for specimens S5 to S8, compared to an average capillary rise height of 3.1mm in S1 to S4. This is attributed to changes in the pore structure (becoming smaller) as a result of continued hydration and the associated increase the capillary rise potential (Neville 2012).

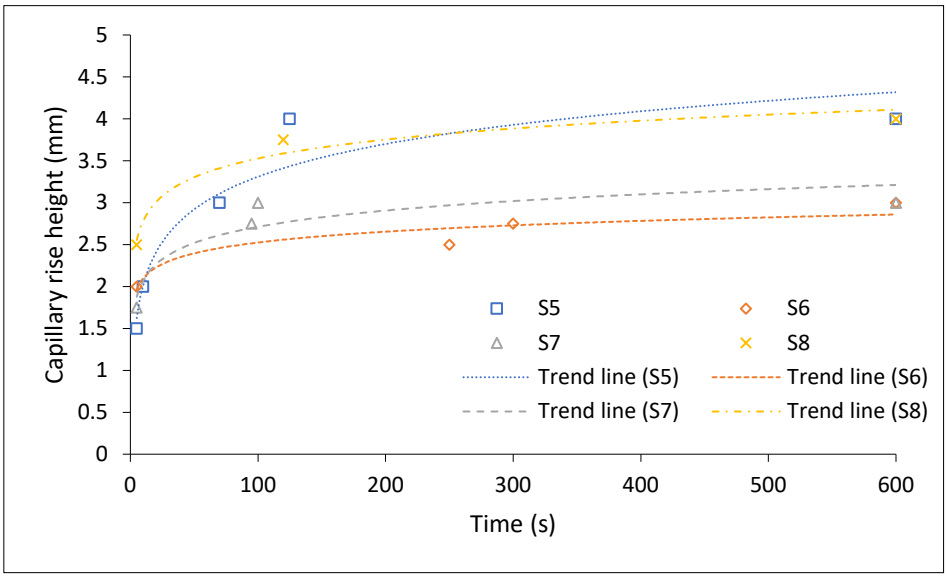

Figure 6.8. Sorption rise responses at 15 days

6.5 Curing front properties of CA with a cementitious substrate

The objective of this study was to provide experimental evidence for the existence and nature of a curing front in CA with a cementitious substrate. The tests rely on visual observations of a curing front and intermittent probes (using an indenter) to check that the observed front relates to cured material (see Figure 6.9).

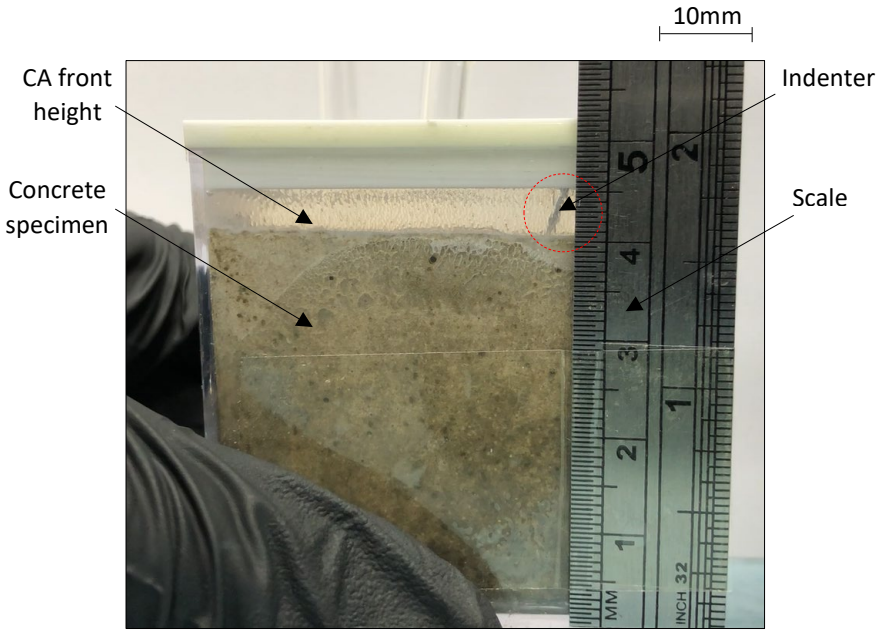

Figure 6.9. Curing front test photograph highlighting the indenter

The cracks considered in this research programme are typically 0.1mm to 0.5mm in width and therefore curing front properties are required for a relatively narrow layer of healing agent. It was therefore decided to use a small-scale testing arrangement in which curing in a 6mm layer of CA above a 50mm cube of concrete material was observed, as illustrated in Figure 6.10.

The specimen details are the same as those given in sections 3.3.1 and 3.3.3 in Chapter 3. The concrete cubes, of size 50x50x40mm, were cast in a Perspex box. After curing, the specimens were transferred to an identical clean Perspex box. Clear silicon sealant was applied around the edges to seal the specimens and eliminate any air gaps. The lid of the Perspex box was sealed with CA to ensure air tightness. The gap above the specimen was then filled with CA using a syringe that passed through a hole in the lid: a second temporary breathing hole was introduced into the lid during filling. One hole was then sealed and the other was used for the indenter, which had an airtight seal. CA curing was then recorded with a digital camera for a period of 30 minutes, with an indenter applied intermittently to verify that the visible curing front was being correctly interpreted. It is noted that the test was assumed to start (i.e. at t = 0), the moment that CA touched the substrate surface.

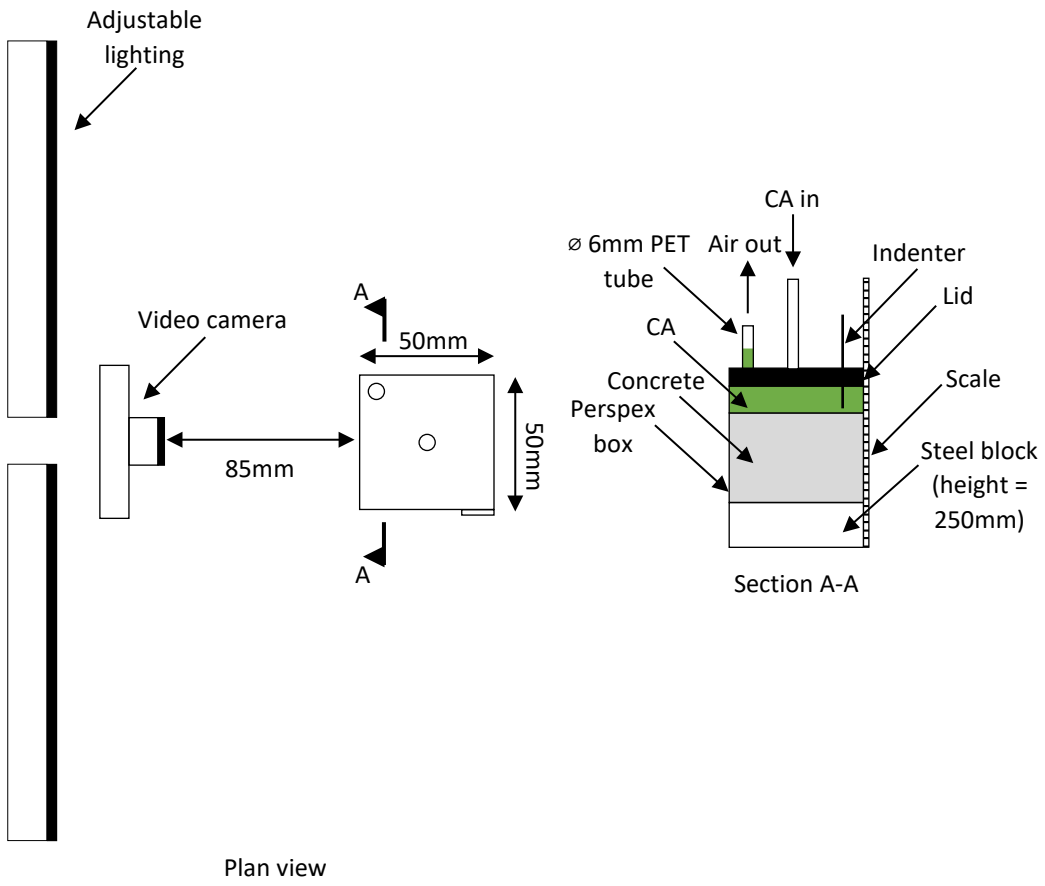

Figure 6.10. Curing front experimental setup

6.5.1 Results and discussion

CA becomes opaque when it is cured and the limit of cured (opaque) material adjacent to the substrate is interpreted as the curing front, as illustrated in Figure 6.11. For clarity, a dotted red line has been added to the figures to highlight the limit of the cured CA. It was found that initial polymerisation of CA occurred instantaneously. The video images suggested that the front does not remain plane and parallel to the substrate surface but becomes more irregular and increasingly diffused over time.

The curing of CA is a polymerisation reaction, initiated by OH^- ions, which propagates into the CA from the substrate. The curing mechanism can also be initiated by a source such as air causing diffusion of moisture which leads to the change in viscosity. Experimental evidence from Tomlinson et al. (2006), as well as the data measured here, shows that the depth of cure of the CA tends towards a limiting value, after which no more curing occurs. The polymerisation of CA formed a CA film on the on the cementitious substrate where, as the film gets thicker so does the extent of cure.

The data extracted from the video images are presented in Figure 6.12 in terms of curing front height (i.e. distance from substrate) versus time from the start of the experiment. The response suggests that the rate of progress of the curing front gradually diminishes over time. The spread of the experimental results showed that this process has a significant degree of variability and it is acknowledged that some judgement was required to discern the position of the front. These test results and observations

do provide an understanding of the nature and behaviour of CA curing adjacent to a cementitious substrate.

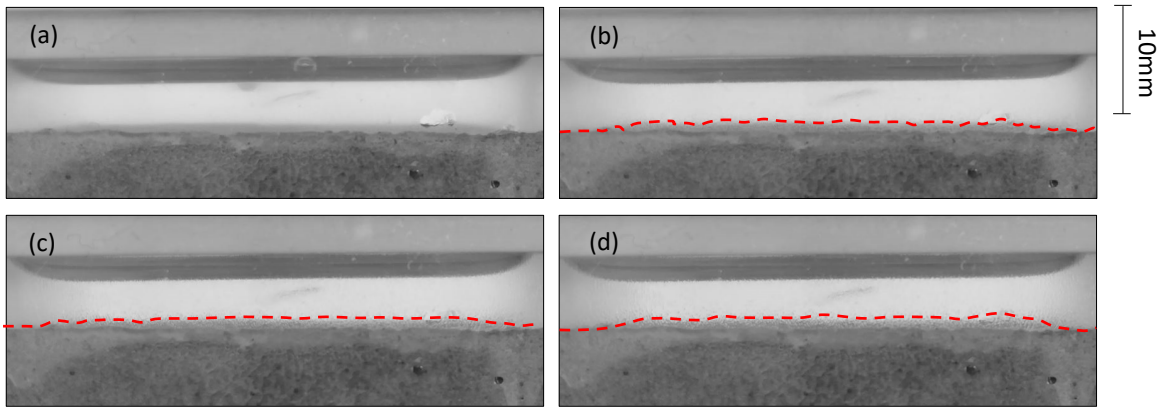

Figure 6.11. Curing front of specimen at (a) 5 seconds, (b) 210 seconds, (c) 570 seconds and (d) 810 seconds

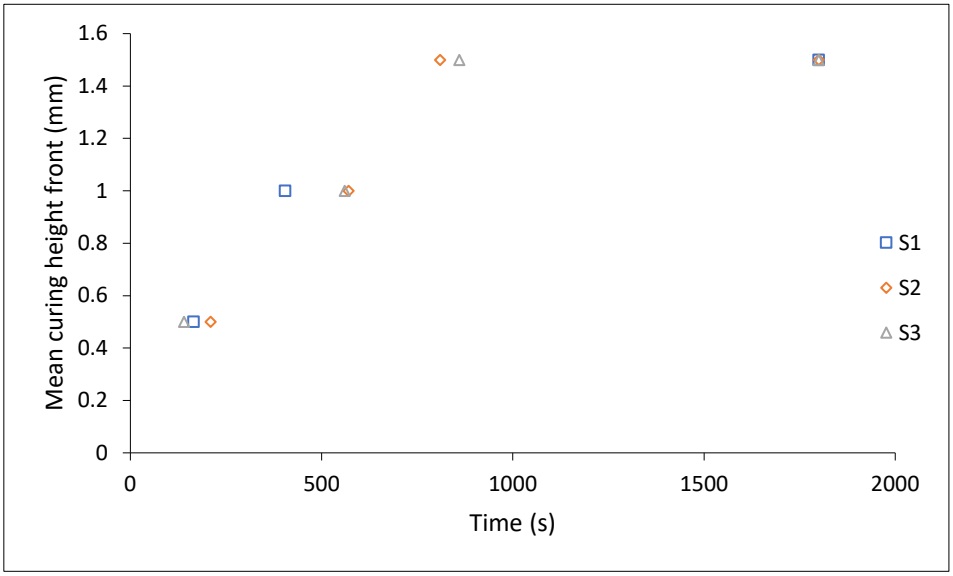

Figure 6.12. Mean curing height over time

6.6 Dynamic flow characteristics of CA in capillary channels

The following section presents a series of experimental studies on the dynamic flow of CA in 0.3mm glass capillary tube subjected to driving pressures of 0.1 bar, 0.3 bar, 0.5 bar and 1.0 bar and captured using a high-speed digital camera. Previous studies by other researchers have reported dynamic contact angle behaviour for silicone oils (Hoffman 1975), aqueous glycerol solution (Blake and Shikhmurzaev 2002), and di-n-butyl phthalate but, to the author's knowledge, no results have previously been published for CA. The preliminary investigations are discussed below.

6.6.1 Preparation and testing

The testing arrangement is illustrated in Figure 6.13 comprised CA in a glass capillary tube that was connected to an airline via a pressure regulator. The CA and the gas pressure from the airline were initially isolated from each other by a clamp. The glass capillary tubes were cleaned and dried prior to testing to remove any contaminants. The test setup was illuminated with adjustable high intensity lights which was reflected from a matt-white board to improve visibility. The LED lights were only switched on during the recording sequence to ensure that CA was maintained at room temperature. A 15cm ruler was also placed underneath the glass capillary tube to measure the distance travelled by the CA. A Motion BLITZ Cube 2 high speed digital camera produced by Mickotron which has a maximum resolution of 1280x1024 was used to capture the dynamic motion of the CA. A recording speed of 3012 fps was selected and the shutter time was reduced to 51µs to obtain sufficient clarity for data post-processing. A set of circular rings, perpendicular to the tube axis, were marked on the glass capillary tube at 10mm interval using a fine permanent marker. The test setup was placed on a platform at an elevated height of 10mm to ensure an even distribution of lighting.

The glass capillary tube was partially filled with CA using one end of the flexible PET tube and clamped to prevent flow. The airline and the regulator valve were connected to the flexible PET supply tube and the regulator was set to the appropriate pressure. The motion camera was activated, and the clamp released to initiate flow. Once the CA front (i.e. the meniscus) had passed the field of view of the camera, the flexible PET tube was re-clamped. After each test, the transient flow data and the meniscus contact angle at the centre of the glass capillary tube (i.e. central view, c in Figure 6.13) were extracted. Each of the glass capillary tubes were used only once and each test with the same parameters was repeated at least 3 times. The static contact angle was measured in the horizontal tube with the CA at rest. This condition was induced by partially filling the glass capillary tube with CA and applying the clamp to prevent further flow.

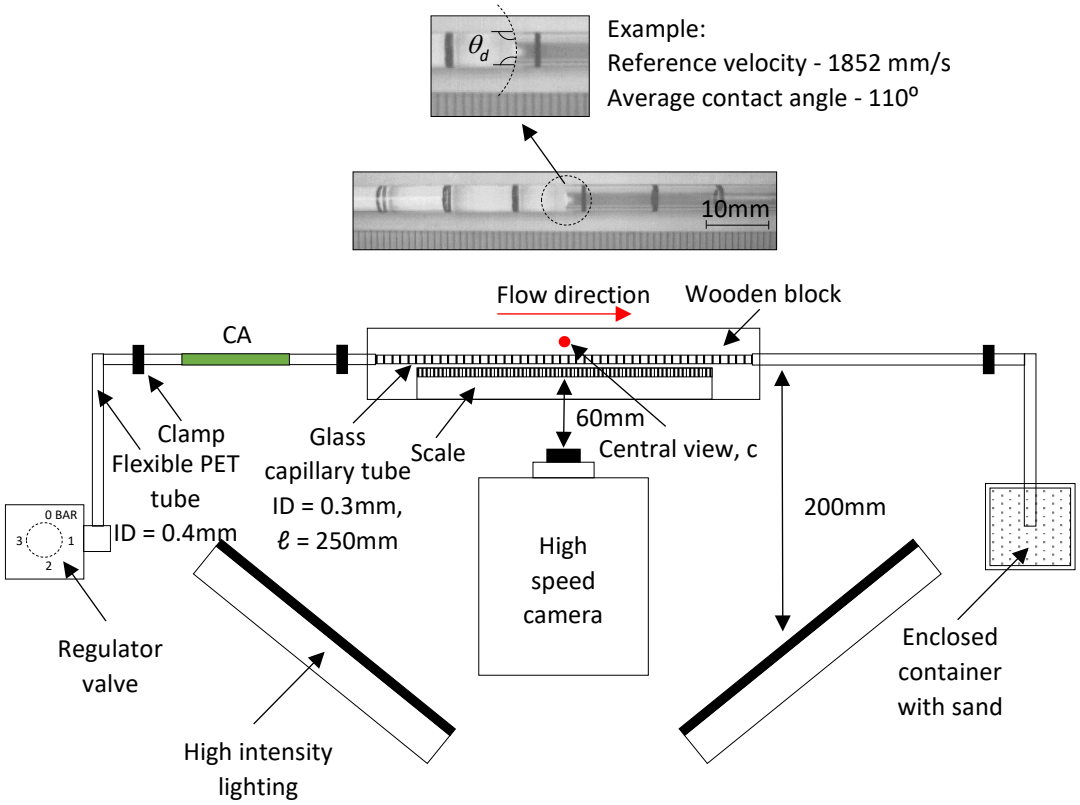

Figure 6.13. Dynamic CA flow testing arrangement

6.6.2 Preliminary investigations

For background, some details are now provided of a preliminary investigation that was used to refine the above testing procedure. During this preliminary investigation, a glass capillary tube of length of 500mm and 0.3mm in internal diameter was used. 1mm wide adhesive tape was wrapped around the glass capillary tubes at every 10mm intervals to form circular rings as shown in Figure 6.14. An X-Motion high speed digital camera as manufactured by AOS technologies at 2000 frames per second (fps) was used during testing. A more suitable high-speed camera was used in the main experimental programme. The remainder of the experimental procedures was as explained in Section 6.6.1. The healing agent subjected to pressures ranging from 0.1 bar to 2.0 bar.

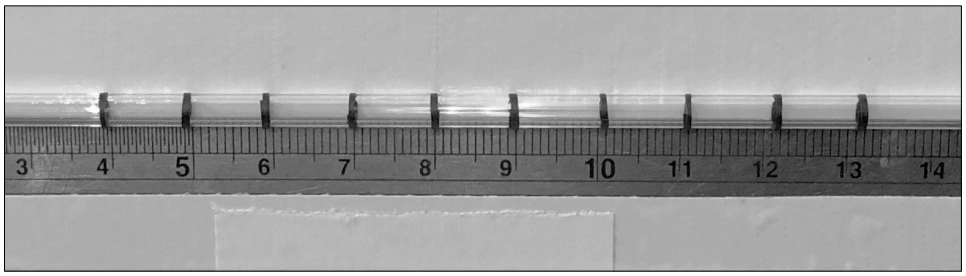

Figure 6.14. Glass capillary tube showing circular rings

There were some difficulties encountered during these preliminary tests. For example, the incorrect position of the spiral made it challenging to analyse the video files in AOS imaging studio during post processing because some of them were not exactly perpendicular to the tube axis. This caused complications during the interpretation when estimating contact angles. The low-resolution images obtained from the high-speed camera were also found to be unclear, thus affecting the accuracy of the measurements of the meniscus in motion at the central view, c (see Figure 6.13). An example is shown in Figure 6.15. There was also an issue with the glare from the reflection of the glass capillary tube caused by improper lighting. The raw data from the preliminary investigations are not reported here due to these inaccuracies, but steps were taken to improve the method of testing in the main experimental programme.

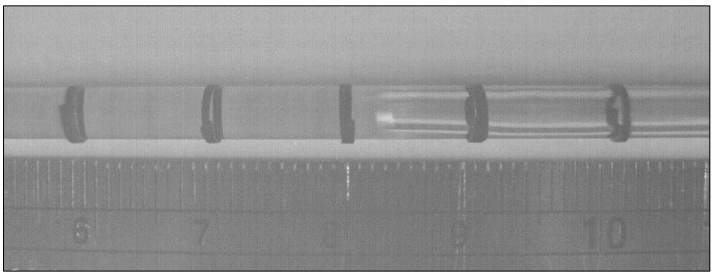

Figure 6.15. Low resolution image obtained from X-Motion high speed digital camera

6.6.3 Results and discussion

Transient capillary front graphs are presented in Figures 6.16 to 6.19 which also gives the average velocity of each pressure at the centre of the field of view (i.e. at the reference velocity). Images showing the meniscus for both static and dynamic contact angles are given in Figure 6.20. It was found that the reference velocity increases with pressure, as expected. It suggested that the flow approaches a steady state velocity towards the time when the meniscus reaches the end of the field of view, which is indicated by the gradient of the flow-front graphs becoming linear. An average CoV of 10.7% was recorded due to the natural degree of variation of such dynamic flow processes.

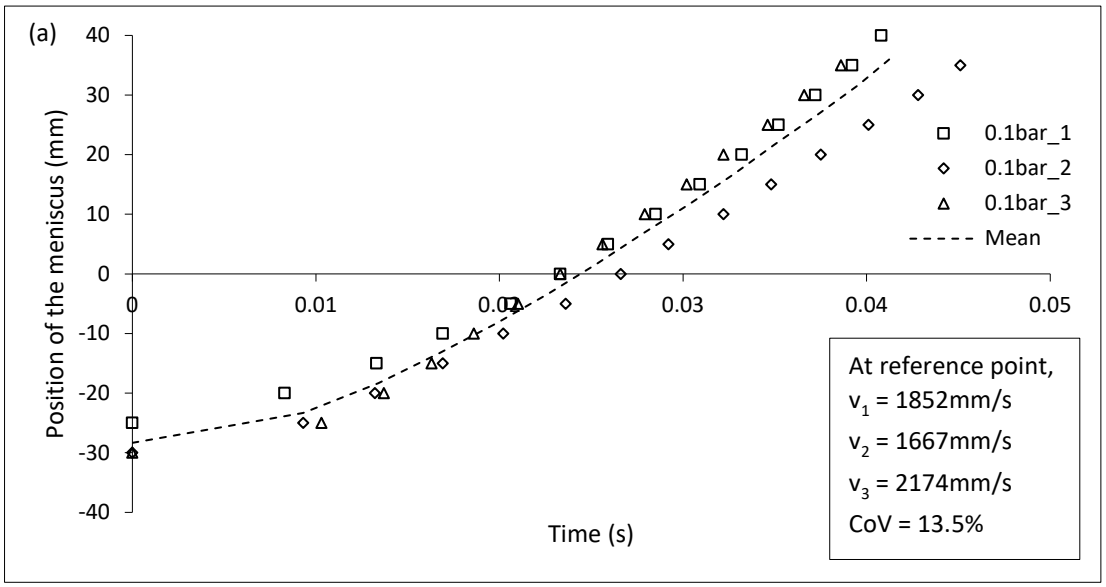

Figure 6.16. Position of the meniscus and time responses at 0.1 bar of pressure

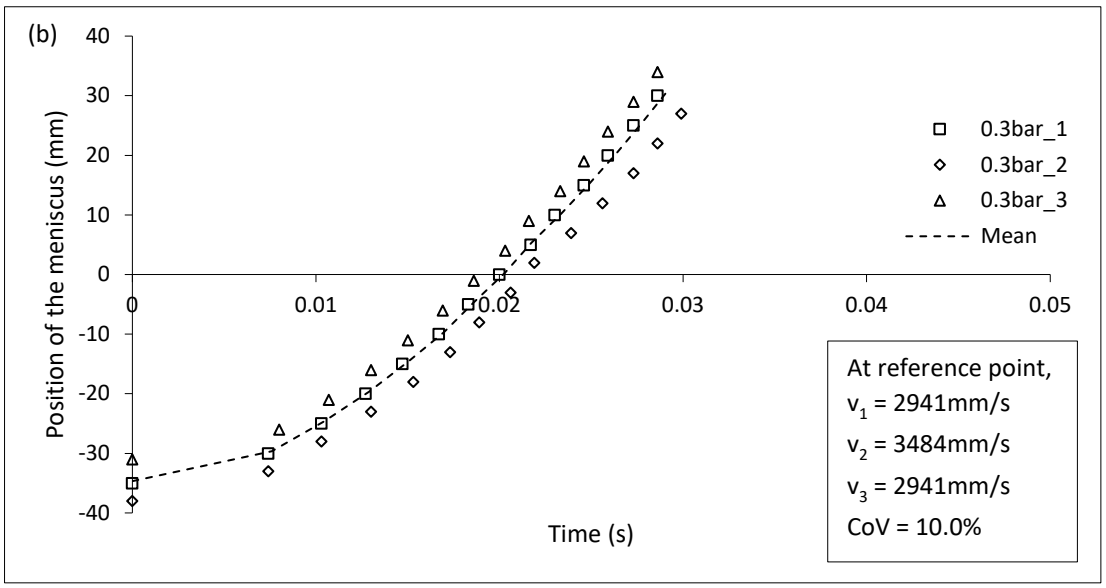

Figure 6.17. Position of the meniscus and time responses at 0.3 bar of pressure

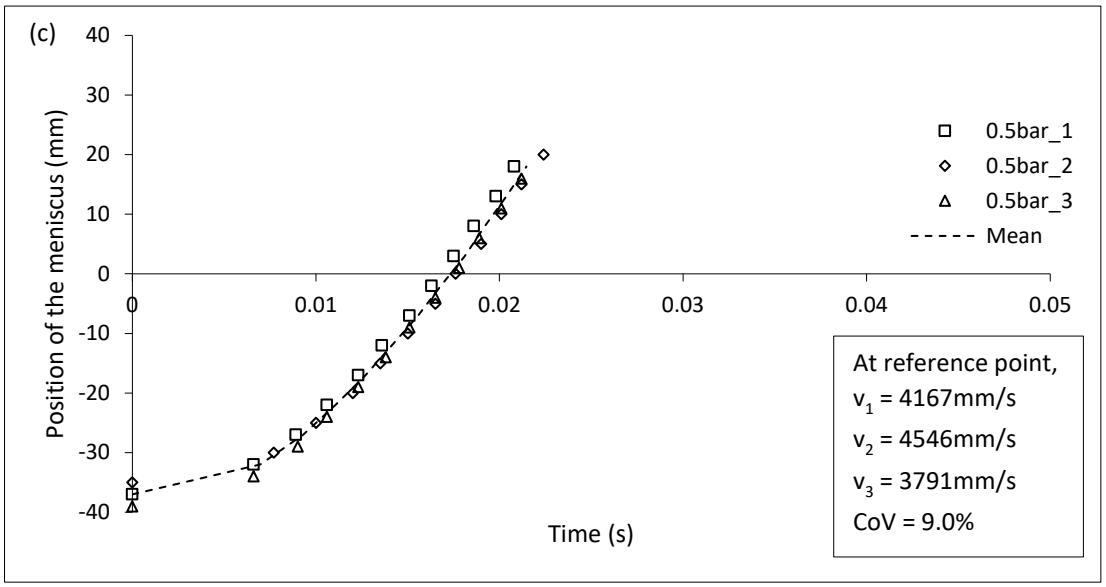

Figure 6.18. Position of the meniscus and time responses at 0.5 bar of pressure

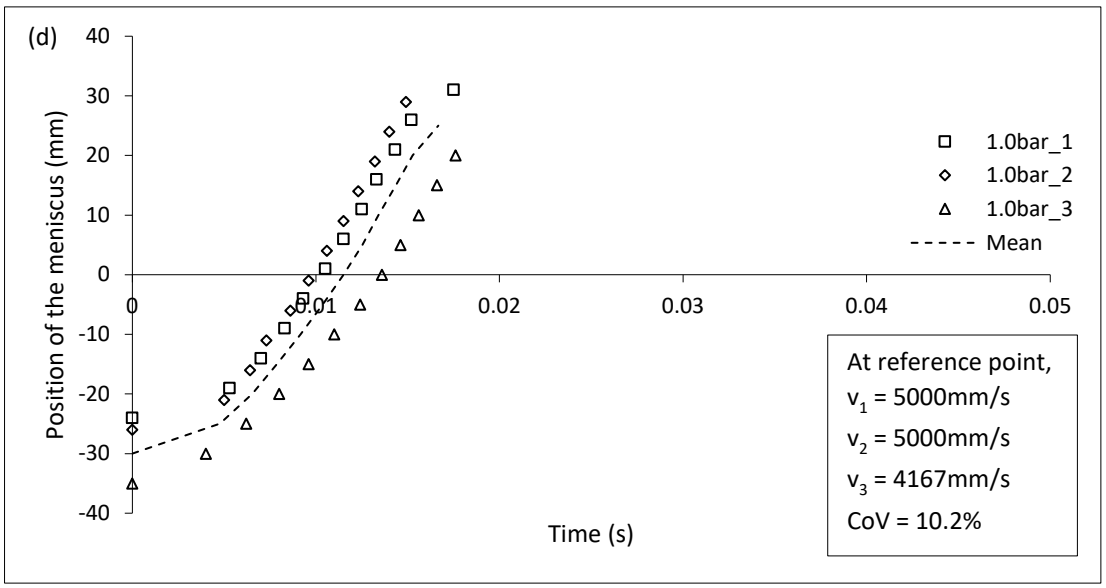

Figure 6.19. Position of the meniscus and time responses at 1.0 bar of pressure

Previous work on the dynamic flow behaviour of other liquids (Blake 2006; Jiang et al. 1979; Bracke et al. 1989; Cox 1986) suggests that the dynamic contact angle (θ_d) between the liquid meniscus and the substrate depends on the flow velocity. Therefore, the contact angles have been extracted from the high-speed camera images using a technique developed by Stalder et al. (2006). These were calculated at different velocities and analysed when the meniscus reached the centre of the field of view. The contact angles were measured directly from the wall of the glass capillary tube and these measurements were facilitated using a plugin for the software ImageJ, called *'drop snake'* (Biomedical Imaging Group 2019). The drop snake approach is similar to the polynomial fitting approach, but it also takes advantage of the global shape of the drop due to its elasticity which allows accurate detection of the contour of the drop to compute contact angles (Stalder et al. 2006).

From Figure 6.20 it is apparent that the meniscus is asymmetric relative to a vertical plane, which is attributed to the effects of gravity. This will lead to greater influence on static than dynamic behaviour since inertia forces are more dominant in the latter case.

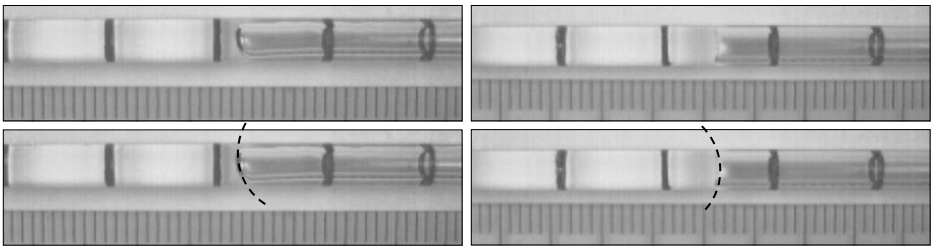

Contact angle (top)	30°	Contact angle (top)	122°
Contact angle (bottom)	44°	Contact angle (bottom)	124°
Average	37°	Average	123°
(a)		(b)	

Figure 6.20. ImageJ drop snake analysis for (a) static at 0mm/s velocity and (b) 0.5bar at 4546mm/s velocity

Contact angles (θ_d) are plotted as a function of velocity in Figure 6.21. The results suggest that there is a sharp transition from the low velocity region, for which the outer surface of the meniscus is concave (θ_d < 90°), to a higher velocity region where the meniscus is convex (θ_d > 90°). In all cases the meniscus had become convex by the time it reached the reference position but the points at which the meniscus flipped from a concave to a convex shape were visible on video images. However, because this abrupt transition occurred away from the centre of the field of view, the associated velocities were more difficult to determine accurately. A range of the approximate contact angles measured at θ_d = 90° is provided in Figure 6.21. This was estimated at a 45° angle from the central view, c.

A number of theorical models discussed in Blake (2006) have been developed for simulating dynamic capillary flow behaviour, including those of Jiang et al. (1979), Bracke et al. (1989), and Cox (1986). The contact angle models were proposed (see equations 6.1 to 6.3) based on experimental measurements and formulated in terms of capillary number, Ca which are only valid for positive contact line velocity. A comprehensive discussion on this is given in Shikmurzaev (1997). A Matlab

curve fitting function was applied to determine the constants c_1 and c_2 which were associated with the flow properties. All three models showed good agreement with the present experimental data. The resulting comparison between calculated responses, using equations 6.1 to 6.3, and the current experimental data are given in Figure 6.21.

Jiang's model (Jiang et al. 1979),

$$\tanh(c_1 Ca^{c_2}) = \frac{cos\theta_s - cos\theta_d}{cos\theta_s + 1} \quad (6.1)$$

in which the capillary number is defined by $C_a = \mu v/\gamma$ (Van Mourik et al. 2005); μ is the viscosity (0.004 Ns/m^2) (Gardner et al. 2014; Cyanotec 2019); v is the meniscus velocity (m/s); γ is the surface tension (0.034 N/m) (Cyanotec 2019); θ_s is the static contact angle (10°) (Gardner et al. 2017); θ_d is the dynamic contact angle; and the constants c_1 and c_2 are 1.205 and 0.2958 respectively. The density of CA is 1060 kg/m^3 (Cyanotec 2019).

Bracke's model (Bracke et al. 1989),

$$\theta_d = arccos(cos\theta_s - c_1(1 + cos\theta_s){C_a}^{c_2}) \quad (6.2)$$

where c_1 and c_2 are 0.8621 and 0.1947.

Cox's model (Cox 1986). A simplification of this model is given in Hoffman (1975).

$${\theta_d}^{c_2} - {\theta_s}^{c_2} = c_1 Ca \quad (6.3)$$

where c_1 and c_2 are 722.9 and 7.654.

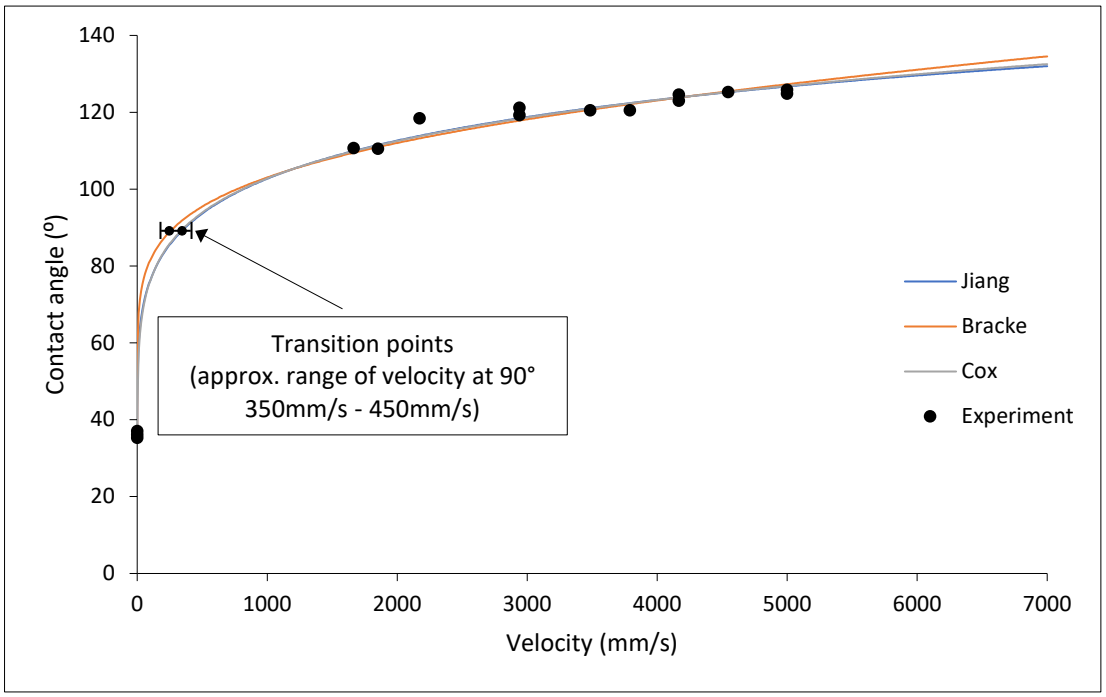

Figure 6.21. Dynamic contact angle data from the experiment with Jiang's, Bracke's and Cox's theoretical models

It is recognised that these values are for CA with a glass substrate whereas the study presented here is with a concrete substrate. This was necessary as cementitious materials are not transparent and current imaging techniques do not allow such high-speed images to be captured accurately through opaque materials. The contact angle formed between any given fluid and a substrate depends on the surface roughness and chemical composition of the substrate (Slepickova Kasalkova et al. 2015). The contact angle can therefore be expected to be different for CA-concrete than the measured CA-glass. However, Schwartz and Tejada (1972) suggested that surface roughness had no significant effect on predictions with a dynamic contact angle (DCA) model, provided that the roughness is random and that the physiochemical character of the surfaces is similar. Whilst Seebergh and Berg (1992) found that, for low capillary numbers, surface roughness produced significant stick-slip effects, but did not alter the constants in a DCA model, and that the static contact angle adequately accounts for the effect of acid-base (chemical) interactions. Therefore, in the present work the differences in substrate are addressed by adjusting the static contact angle, θ_s, using previously measured CA-concrete contact angle data (Gardner et al. 2017).

A coupled finite element model discussed in Jefferson and Freeman (2019) and Freeman and Jefferson (2019) was used to simulate the experimental behaviour presented here (see sections 6.3 to 6.6). The proposed numerical model was able to represent the characteristic continuum and discrete flow and allowed complex damage-healing behaviour in pressurised vascular healing systems to be reproduced accurately. These processes showed a significant degree of variability, but also exhibit strong behavioural trends. The experimental data obtained provided useful information for the development and validation of a coupled numerical model for vascular healing systems. It may also be helpful to others working in this field. In the next chapter, a validation study will be presented on healing agents

with various viscosity to determine the accuracy of the numerical simulations using the constitutive model for SHCM systems.

6.7 Conclusions

This study has provided new data and useful insights into the transport properties of CA in cementitious specimens within the context of a vascular healing system. The following conclusions are obtained from these series of tests:

- Improved capillary rise potential was observed on the capillary flow characteristic of CA in evolving cracks at a CMOD rate of 0.001mm/s and a pressure of 0.3 bar, consistent with previous observations in Section 3.4 in Chapter 3;
- Sorption of CA through a crack wall in a concrete specimen has been measured in order to determine the loss of CA from the crack domain into the cementitious matrix. An average capillary rise height of 3 to 3.5mm with a degree of variability of 15% was obtained in the sorption process in concrete;
- When CA cures with a cementitious substrate there is a visible curing front which develops adjacent to the substrate wall, which progresses over time but gradually becomes less planar and more diffuse. This rate of progress is shown to gradually reduce and this is believed to be due to cured CA providing an increasing wide barrier to the source of OH^- ions that are needed for curing to occur;
- Dynamic flow characteristics in a glass capillary tube have been determined and a relationship established for the velocity dependency of the dynamic contact angle of CA. It should be mentioned that this study is linked to previous work by Gardner et al. (2017) in which the effects of curing on CA flow characteristics were measured.

Chapter 7 Modelling and validation

7.1 Introduction

The study presented in this chapter relates to the autonomic healing system with embedded channels for the supply of CA described previously (see Figure 3.1 in Chapter 3). The experimental data from Chapters 3 and 6 were used to develop and calibrate a numerical model (developed by others) which simulates the mechanical damage-healing response and transport behaviour of the self-healing material system (Freeman and Jefferson 2019; Jefferson and Freeman 2019).

This chapter provides an overview of the model and then presents a set of model validation examples that are based on those given by Jefferson and Freeman (2019). The chapter then describes a material *'tailoring'* (or design) exercise, which aimed to find the *'best'* healing agent for a chosen structural configuration and loading scenario. Since this was the first time that the model had been used for this type of design exercise, a simplified situation was chosen that used the notched prismatic beams considered in Chapter 3 with an idealised CMOD rate of 0.0005mm/s. The tailoring study involved a sequence of analyses of notched prismatic beams for a range of healing agents. Each analysis set comprised a series of analyses at different crack opening rates. The properties of the agent that gave the best response for the selected loading scenario were then determined and a healing agent sourced that gave the best match to these idealised properties. A series of experiments were then carried out to determine the real response of the *'tailored'* system. The results from the experiments were compared with the numerical predictions and in this way the accuracy of the numerical model as a predictive tool for the design of SHCMs was assessed.

7.2 Constitutive damage-healing models

7.2.1 A scalar damage-healing model for a representative crack plane

Numerical simulations are useful for predicting the response of SHCM systems and for interpreting the results of SHCM experiments. A number of researchers have developed the type of damage-healing constitutive model discussed in Jefferson et al. (2018). A simplified representation of such a model when stress (σ) is applied across a crack band (Alfano and Sacco 2006), in terms of the relative displacement (u) across a crack for a single phase of healing can be expressed as:

$$\sigma = \sigma_v + \sigma_h = (1-\omega)\,Ku + \omega\, h(1-\omega_h)\,K\,(u-u_h) \tag{7.1}$$

in which $K{=}E/w_b$ is the stiffness of the crack band (E denotes Young's modulus and w_b the width of the crack band), ω is the damage variable ranging between 0 (no damage) to 1 (full damage), h is the degree of healing, u_h is the relative displacement at which healing takes place and ω_h is the damage variable for the healing material.

For this study, the term damage, derived from damage mechanics is associated with micro and macro cracking (Jefferson et al. 2018). A crack plane (defined in Jefferson and Mihai 2015) is the mid surface

of a narrow band which contains a number of micro and/or macro cracks. The width of the crack band (ω_b) equates to the thickness of the fracture process zone (Karihaloo 1995) and may be taken as three times the maximum aggregate size when applied to concrete or mortar. The area of the crack plane is assumed to be sufficiently large to represent the characteristic behaviour of the cementitious material under consideration. The mean stress across the crack plane consists of two components, the first of which is associated to the virgin material (*v*) and the second accounts for the stress transferred across the healed component (*h*) which may re-damage.

The inelastic components of the relative displacements, u and $(u - u_h)$ which are denoted u_{dam} and u_{redam} are given by the following relationships:

$$u_{dam} = u - u_{el} \tag{7.2a}$$

$$u_{redam} = u - u_h - u_{el} \tag{7.2b}$$

in which $u_{el} = \sigma/K$.

The damage evolution equations that define ω and ω_h depend on the maximum values of the inelastic relative displacements, ζ and ζ_h, and are given by:

$$\omega(\zeta) = 1 - \frac{f_t}{K \cdot \zeta} e^{\frac{-c\zeta}{\zeta_m}} \tag{7.3a}$$

$$\omega_h(\zeta_h) = 1 - \frac{f_{th}}{K \cdot \zeta_h} e^{\frac{-c\zeta_h}{\zeta_{mh}}} \tag{7.3b}$$

in which f_t is the tensile strength, $c = 5$ is a softening constant and ζ_m is the effective relative displacement at the end of the softening curve.

The softening constant was originally derived from a strength decay function (ϕ) as described in (Gopalaratnam and Shah 1985) such that:

$$\sigma = f_t\, \phi = (1 - \omega)\, K\, u \qquad For\ u \geq u_t \tag{7.4}$$

where noting that u_t is defined by $u_t = \frac{f_t}{K}$, and expressed as:

$$\phi(\zeta) = \big(1 - \omega(\zeta)\big)\frac{u}{u_t} \tag{7.5}$$

The model can be related to healing indices. Although, not employed in this chapter, these relationships provide a useful link between the healing indices seen in the model and the healing indices explained in Section 3.4.1.4 in Chapter 3. This comparison is given in Appendix C.

7.2.2 Matrix flow and capillary flow theories

The flow of healing agent in the concrete matrix is described using the type of nonlinear diffusion model given in Bazant and Najjar (1972). The governing mass balance equation is expressed as:

$$\frac{\partial S_h}{\partial t} + \nabla \cdot \mathrm{J_q} + Q = 0 \tag{7.6}$$

where S_h is the degree of healing agent saturation, Q (m/s) is the moisture source/sink term representing flow between the concrete matrix and discrete cracks and $\mathrm{J_q}$ is the moisture flux which is assumed to follow Fick's law and is given as:

$$\mathrm{J_q} = -D\nabla \cdot S_h \tag{7.7}$$

where D (m^2/s) is a diffusion coefficient given as:

$$D(S_h) = D_1\left(\alpha + \frac{1-\alpha}{1+\left(\frac{1-S_h}{1-S_{h_c}}\right)^n}\right) \tag{7.8}$$

where D_1 (m^2/s) is the maximum value of D, α, n and S_{h_c} are model parameters.

Q is given by:

$$\mathrm{Q} = 2\beta_c(S_h - 1) \tag{7.9}$$

where β_c (m/s) is a transfer coefficient and S_h is the degree of saturation in the porous medium.

The flow of healing agent in discrete cracks is described using a modified Lucas-Washburn model based on that found in Gardner et al. (2012; 2014). This approach simulates flow and transport for a range of crack apertures for a planar crack configuration which considers the stick-slip behaviour, frictional resistance and wall slip. The governing equation is expressed as:

$$\dot{z} = \frac{P_{app} + P_c(\theta_d)(1-\beta_s) - \rho g z sin(\varphi) - Q}{\frac{2\beta_m}{b} + \eta} \tag{7.10}$$

where the superior dot denotes time derivative, P_{app} (N/m^2) is the applied pressure, P_c (N/m^2) is the capillary pressure given by Young's equation, φ is the inclination of the capillary, b (m) is the capillary width (or crack width), z (m) is the meniscus height, β_s and β_m (Ns/m^2) are factors for stick-slip and frictional dissipation at the meniscus respectively, ρ (kg/m^3) is the density, g (m/s^2) is gravity, Q (m/s) is the source/sink through the crack faces and η (Ns/m^3) is the total viscous resistance given as:

$$\eta = A(z)\int_0^z \frac{1}{\left(\frac{k(x)}{\mu(\varphi)} + \frac{b\beta_w}{2}\right)A(x)}dx \tag{7.11}$$

where A (m^2) is the cross-sectional area, k (m^2) is the permeability, β_w (m^3/Ns) is the wall factor (Gardner et al. 2012) and μ (Ns/m^2) is the dynamic viscosity (which may be a function of the degree of cure). The capillary pressure (P_c) is given by Young-Laplace equation:

$$P_c = \frac{2\gamma\cos(\theta_d)}{b} \tag{7.12}$$

where γ (N/m) is the surface tension and θ_d is the dynamic contact angle. The permeability of a crack can be taken as $k = b^2/12$.

The contact angle is dynamic and is given as (Jiang et al. 1979):

$$tanh(c_1 {C_a}^{c_2}) = \frac{cos(\theta_s) - cos(\theta_d)}{cos(\theta_s) + 1} \tag{7.13}$$

where the capillary number can be defined as $C_a = \mu v/\gamma$, θ_s is the static contact angle and c_1 and c_2 are model parameters.

Q is given by:

$$\mathrm{Q} = -2\beta_c(S_h - 1) \tag{7.14}$$

where β_c (m/s) is a transfer coefficient and S_h is the degree of saturation in the porous medium.

7.2.3 Curing of cyanoacrylate

A full description of the CA curing model can be found in Freeman and Jefferson (2019) and Jefferson and Freeman (2019) and so only an overview is provided here.

CA cures by a polymerisation reaction initiated by hydroxide ions, which are transported from the edges of the specimen. To describe this propagating reaction front, the analytical solution to the advection diffusion equation is employed where, noting that propagation of the reaction front slows as the depth of cured material increases, until it eventually ceases, the position of the front, z, is given by:

$$z(t) = z_{c0}\left(1 - e^{\frac{-t}{\tau}}\right) \tag{7.15}$$

where z_{c0} (m) is a critical curing depth at which the transport ceases and τ (s) is a rate parameter (characteristic time).

The cure profile is given by:

$$\varphi_{x_c}(x_c, t) = \frac{1}{2}\left(1 - tanh\left(\left(\frac{2}{\sqrt{\pi}}\right)\left(\frac{x_c - z(t) - z_c}{z_c + \sqrt{\frac{z(t)}{D}}}\right)\right)\right) \tag{7.16}$$

where z_c (m) is a wall factor and D (m/m^2) is a spreading parameter.

This can be integrated across the crack width to give the total degree of cure at a point in the crack as:

$$\varphi(x_c, \mathrm{t}) = \frac{x_c}{2} - \frac{1}{2}\ln\left(\cosh\left(\frac{\frac{2}{\sqrt{\pi}}x_c - \frac{2}{\sqrt{\pi}}\mathrm{z_c} - \frac{2}{\sqrt{\pi}}z(t)}{\mathrm{z_c} + \sqrt{\frac{z(t)}{D}}}\right)\right)\left(\frac{\sqrt{\pi}}{2}\sqrt{\frac{z(t)}{D}} + \frac{\sqrt{\pi}}{2}\mathrm{z_c}\right) + \mathrm{c} \tag{7.17}$$

The effect of curing on the rheology is considered using the following chemo-rheological model (Castro and Macosko 1980):

$$\mu = \mu_0 \left(\frac{\varphi_g}{\varphi_g - \varphi} \right)^{nv} \tag{7.18}$$

where φ is the degree of cure, μ_0 (Ns/m^2) is the initial viscosity, φ_g is the degree of cure at the gel point (where a rapid increase of viscosity is observed) and nv is an exponent which defines the rate of change of μ with φ.

The degree of mechanical healing is given as the degree of cure at the centre of the crack:

$$\mathrm{h}(w_c, t) = \frac{1}{2}\left(1 - tanh\left(\left(\frac{2}{\sqrt{\pi}} \right) \left(\frac{\frac{w_c}{2} - z(t) - z_c}{z_c + \sqrt{\frac{z(t)}{D}}} \right) \right) \right) \tag{7.19}$$

7.3 Validation of the model

In this section, the proposed constitutive model was used to simulate multiple damage-healing behaviours of Group A test series (see Jefferson and Freeman 2019) previously discussed in Section 3.4 in Chapter 3. A summary of the test series in Group A is provided in Table 3.3 in Chapter 3. Continuous loading at a constant CMOD rate was applied to notched beam specimens with pressurised healing agent (i.e. PC20) until a CMOD of 0.3mm was reached. Results from the numerical simulations using the constitutive model described in Section 7.2 for varying CMOD rates of 0.0005mm/s, 0.001mm/s and 0.002mm/s are presented in Figure 7.1. In order to reproduce the experimental responses, the model parameters were calibrated (see Table 7.2) with some corrections given in Table 7.1 to provide a close match to the experimental data.

Table 7.1. Correction parameters for PC20 at varying CMOD rates

	Variables (units)		
CMOD rate (mm/s)	$\boldsymbol{w_{crit}}$ (mm)	$\boldsymbol{f_t}$ (N/mm^2)	$\boldsymbol{\zeta_m}$ (mm)
0.0005	0.060	2.75	0.15
0.001	0.055	3.00	0.13
0.002	0.044	2.80	0.20

7.3.1 Results and discussion

It may be seen from Figure 7.1 that the numerical model is able to reproduce the responses for control and SH specimens with reasonable accuracy. The experimental results show that the healing response was influenced by the CMOD rate (see also Section 3.4.1.1 in Chapter 3). This trend is captured reasonably well by the numerical model, which predicts a higher post healing peak at a slower CMOD rate (i.e. 0.0005mm/s) than at a faster CMOD rate (i.e. 0.002mm/s).

It is concluded that the numerical model is able to simulate the damage-healing behaviour of such systems and can be reliably used to predict the responses for other healing agents with different physical and chemical properties (see Section 7.4).

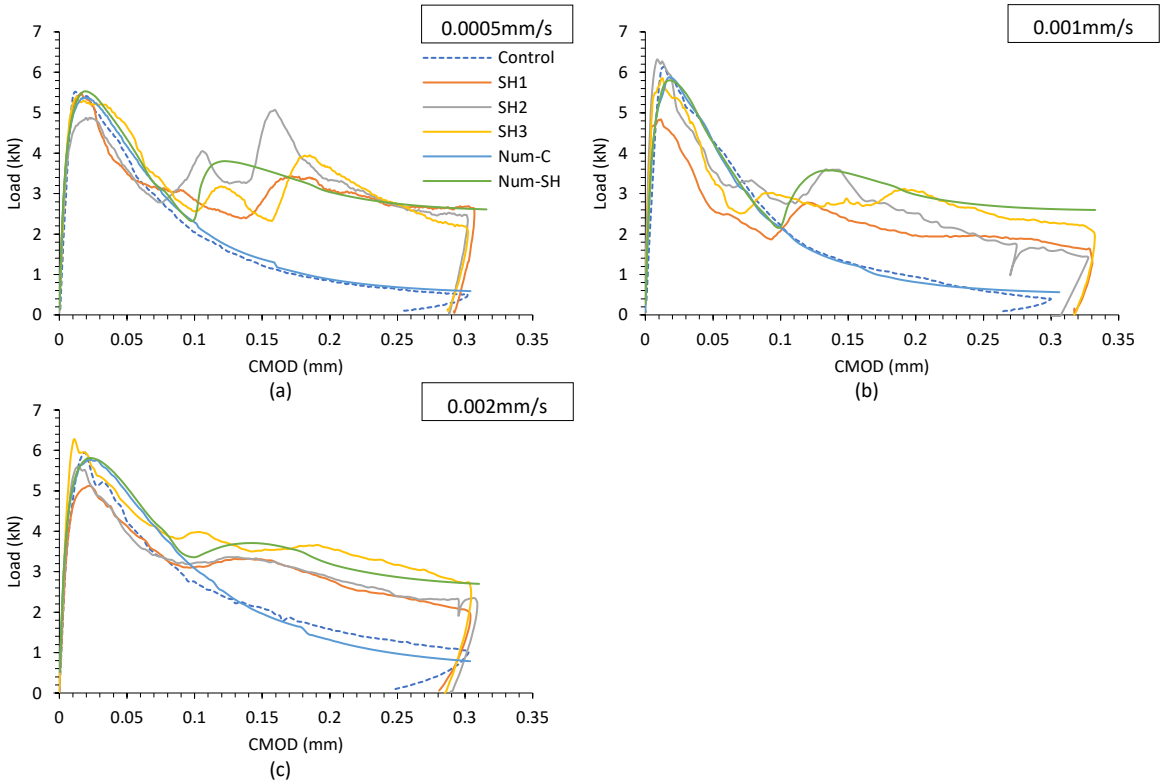

Figure 7.1. Comparison of load-CMOD responses between the experimental data of Group A test series and the numerical simulations for loading rates of (a) 0.0005mm/s, (b) 0.001mm/s and (c) 0.002mm/s (Jefferson and Freeman 2019)

7.4 Application of the model

In order to investigate the influence of using different healing agents on the damage-healing response of the SH beam system considered in Chapter 3, and in Section 7.3 of this chapter, a series of numerical simulations were performed. The healing agents used in this study had viscosities ranging from 0.004 to 2.5Ns/m^2, as follows:

- Procure PC20 (PC20), a very low viscosity (0.004Ns/m^2) modified Ethyl Cyanoacrylate adhesive;
- Procure PC22 (PC22), a high viscosity modified (2.5Ns/m^2) modified Ethyl Cyanoacrylate adhesive;
- Procure PC24 (PC24), a medium viscosity (0.12Ns/m^2) modified Ethyl Cyanoacrylate adhesive;
- Sodium silicate (SS), a silicon-oxygen polymer (0.06Ns/m^2) consisting of ionic sodium (Na+) components.

The safety and technical data sheets for these healing agents are available in Appendix B.

The model parameters for different healing agents are given in Table 7.2. The values quoted were extracted from available manufacture data or otherwise assumed. The model parameters were tuned and calibrated, with consideration given to different crack release values (i.e. the crack opening at which the agent starts to flow into a discrete crack). It was assumed that higher viscosity healing agents would be released at larger crack openings than lower viscosity agents. The predicted damage-healing responses from the numerical simulations are provided in the following section.

Table 7.2. Summary of model parameters and definitions

Variable (units)	**Desc. in FORTRAN**	**Physical meaning**	**PC20**	**PC22**	**PC24**	**SS**
μ (Ns/m^2)	visc	Viscosity	0.004	2.5	0.12	0.06
θ (rad)	theta	Static contact angle	0.1745	0.1745	0.1745	0.257
γ (N/m)	gamma	Capillary surface tension	0.033	0.033	0.033	0.0498
ρ_h (kg/m^3)	dense	Density	1060	1060	1060	1390
w_{crit} (mm)	wcrit	Healing agent release at crack opening	0.05	0.1	0.1	0.075
β_m (Ns/m^2)	betam	Frictional dissipation at meniscus	0	0	0	0
β_s (-)	betas	Stick-slip factor	0	0	0	0
β_w (m^3/Ns)	betaw	Wall slip factor	0.0025	0.0025	0.0025	0.0025
c_1 (-)	c1	Softening constant	1.138	1.138	1.138	1.138
c_2 (-)	c2	Softening constant	0.2397	0.2397	0.2397	0.2397
φ_g (-)	phig	Degree of cure at the gel point (where a rapid increase of viscosity is observed)	1	1	1	1
nv (-)	Nv	An exponent in the velocity formula	2.193	2.193	2.193	2.193
D_1 (mm^2/s)	diffx/diffy	Maximum value of the diffusion coefficient	1.4	1.4	1.4	1.4
β_c (mm/s)	betac	Transfer coefficient	0.001	0.001	0.001	0.001
α (-)	ad	Calibrated parameter in the diffusion function	0.9	0.9	0.9	0.9
S_{h_c} (-)	hc	Calibrated parameter in the diffusion function	0.8	0.8	0.8	0.8
n (-)	nd	Calibrated parameter in the diffusion function	15	15	15	15
z_{c0} (mm)	zc0	Critical curing depth	0.1	0.85	0.1	0.25
τ (s)	tauc	Curing time parameter or healing rate	10	150	50	25
D (mm/mm^2)	zc1	Diffusivity at saturation	25	25	25	25
z_c (mm)	zc2	Curing front position	0.0001	0.0001	0.0001	0.0001
E (N/mm^2)	young	Young's modulus	30000	30000	30000	30000
ν (-)	poiss	Poisson's ratio	0.2	0.2	0.2	0.2
f_t (N/mm^2)	ftens	Tensile strength	3	3	3	3
ζ_m (mm)	dulim	Relative displacement at the effective end of the softening curve	0.13	0.13	0.13	0.13
w_b (mm)	hsdzo	Width of the crack band	4	4	4	4
E_h (N/mm^2)	younh	Young's modulus of the healed material	30000	30000	30000	30000
ν_h (-)	poish	Poisson's ratio of the healed material	0.2	0.2	0.2	0.2
f_{th} (N/mm^2)	ftenh	Tensile strength of the healed material	3	3	3	2.5
ζ_{mh} (mm)	dulih	Relative displacement at the effective end of the softening curve of the healed material	0.15	0.15	0.15	0.15

7.4.1 Results and discussion

The numerical load-CMOD responses for the different cases are shown in Figure 7.2. In order to explore the response of the system with different healing agents to different loading rates, analyses were undertaken with CMOD rates ranging from 0.0001mm/s to 0.01mm/s. The healing agent supply pressure was set to a constant value of 0.5 bar.

The results from the numerical simulations are shown in Figure 7.2. These appear to be reasonable when considered in the light of previous results presented in Chapter 3. The smooth responses and general trends are consistent with these previous findings and it is concluded that the change in healing agent properties did not result in any numerical problems with the model.

From the results, PC20, PC22 and SS appear to produce the most effective simultaneous damage-healing response at CMOD rates of between 0.0005mm/s and 0.001mm/s, whilst PC24 appears more suited to slower loading rates (i.e. 0.0001 to 0.0005mm/s). This is judged from the degree of healing and the amount of post-healing ductility.

To illustrate the differences in the model predictions, PC22 and SS were selected for comparison. A deformed mesh plot showing the healing agent in the crack and degree of healing for each case are given in Figures 7.3 and 7.4 respectively; whist the saturation contours for the corresponding healing agents are shown in Figures 7.5 and 7.6. It was also found that the crack tip almost reaches the top of the prisms and that the healing agents filled the majority of the crack (~95%), as illustrated in Figures 7.3 and 7.4. Curing progresses (with time) from the notch where a higher degree of healing was recorded at the crack tip due to the narrow layer of glue. It can also be seen from Figures 7.5 and 7.6 that the healing agent was distributed across the microcracked region. In the solutions, SS achieved a higher healing recovery (6.7%) and degree of saturation (12%) compared with those of PC22. This was expected as the glue can be seen spreading throughout the cementitious matrix and achieving a higher degree of healing due to its less viscous properties.

The author now considers a material design or tailoring exercise in which it has been assumed that, in a particular structural element, the main surface cracks will open at a rate of 0.0005mm/s. The preceding analyses have shown that PC24 is the best healing-agent (among those considered) for this rate. The author then wanted to check whether the model predictions for this agent were reasonable and, in this way, establish whether the model is a reliable tool for designing materials. Therefore, a final series of experiments were undertaken to replicate the system simulated with PC24 as the healing agent. The results of these experiments and further discussion on the tailoring exercise are given in the next section of this chapter.

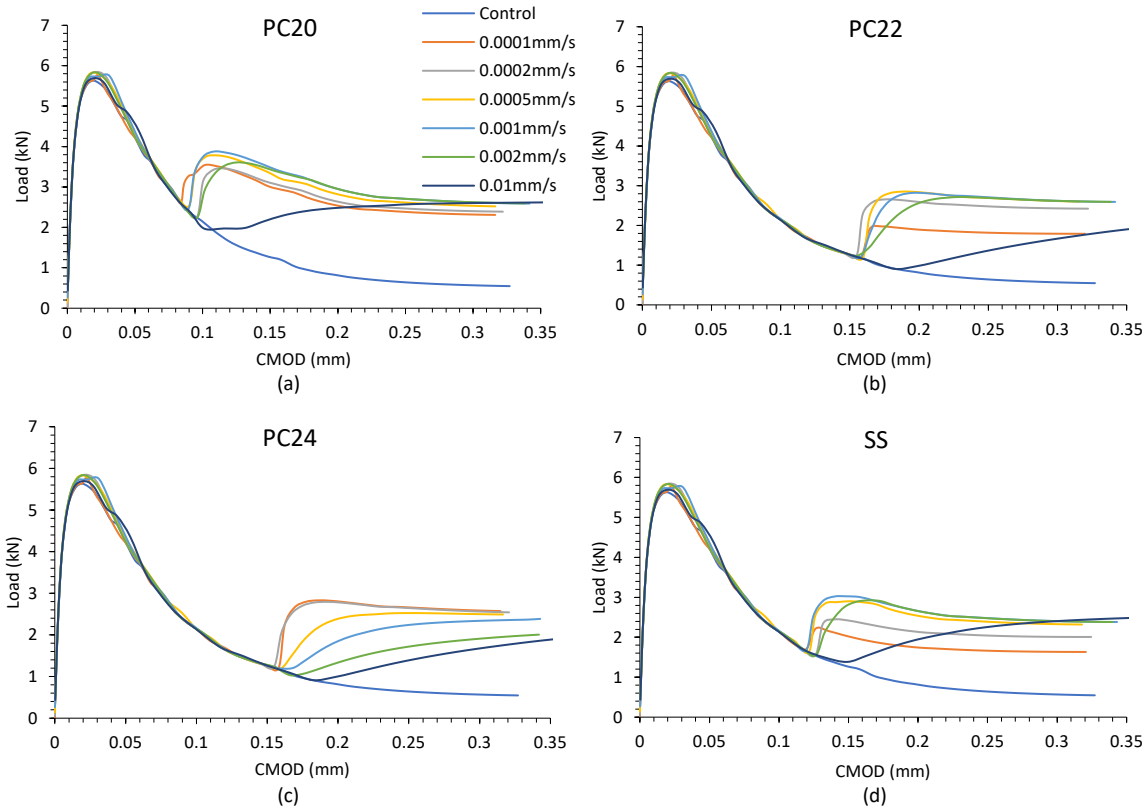

Figure 7.2. Load-CMOD responses for loading rates 0.0001mm/s to 0.01mm/s for (a) PC20, (b) PC22, (c) PC24 and (d) SS

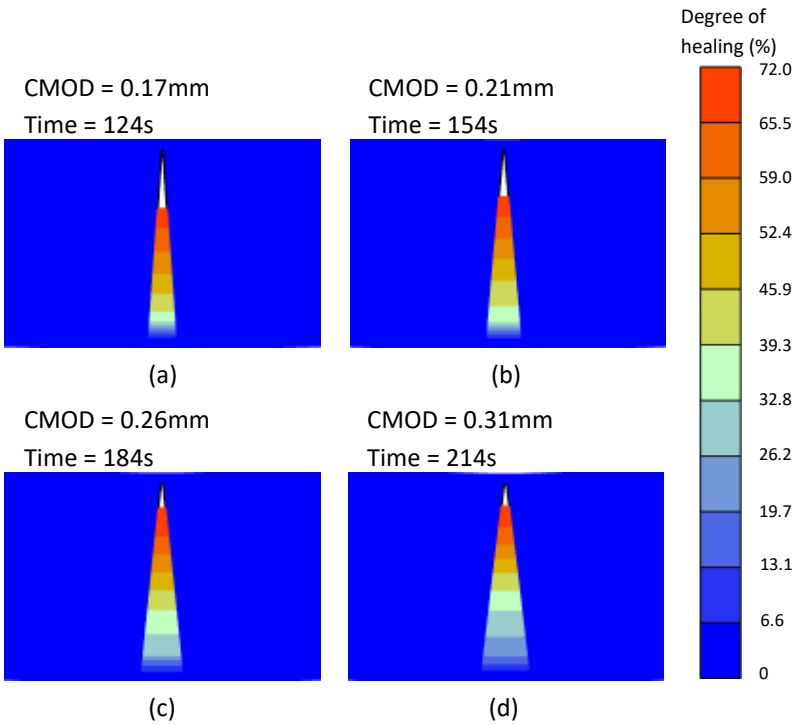

Figure 7.3. Deformed colour contours on the degree of healing for PC22

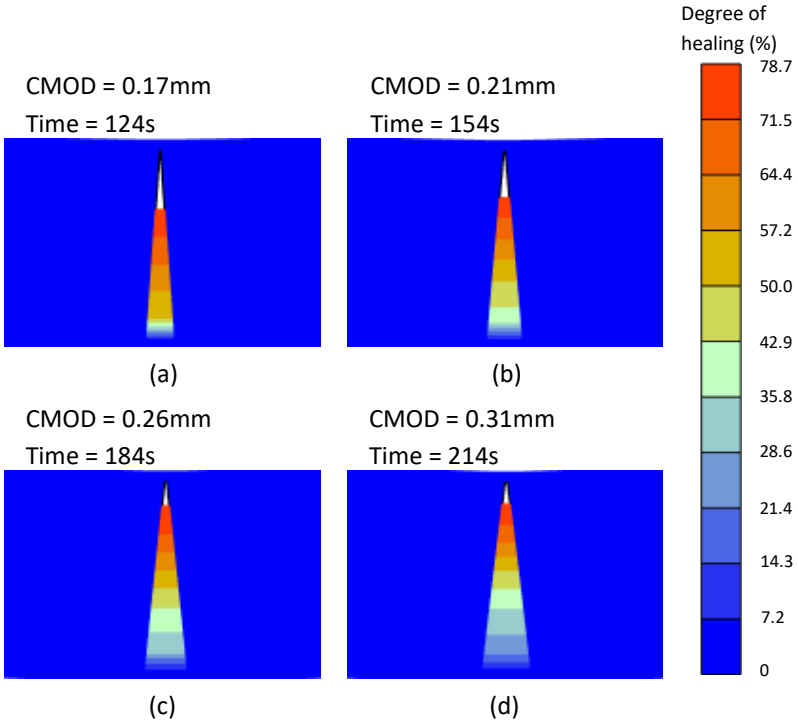

Figure 7.4. Deformed colour contours on the degree of healing for SS

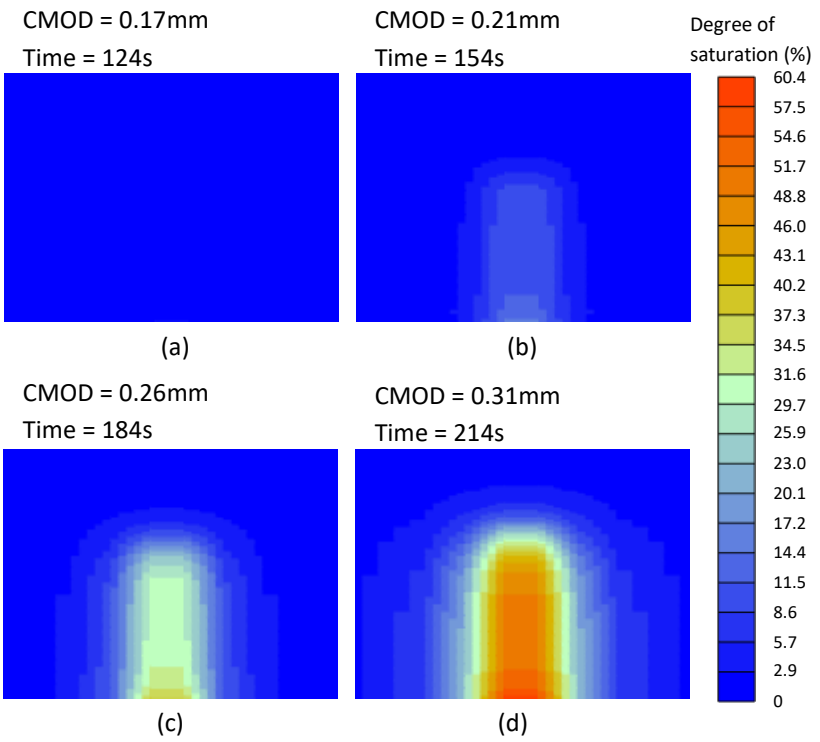

Figure 7.5. Colour contours on the degree of saturation for PC22

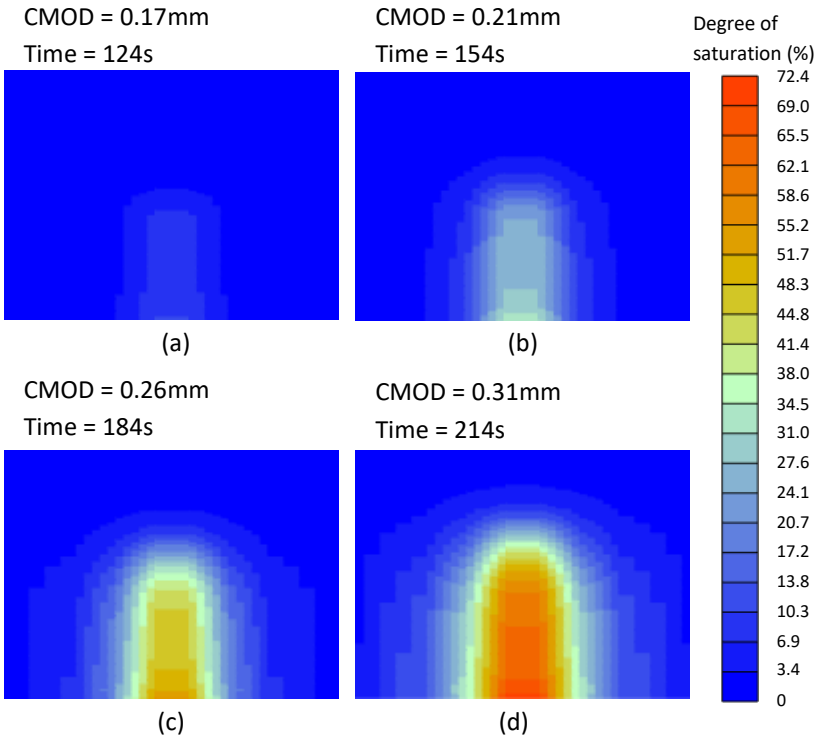

Figure 7.6. Colour contours on the degree of saturation for SS

7.5 Combined experimental-numerical studies

The purpose of this test series was to assess whether the predictions made in the preceding material tailoring exercise were valid. For this exercise, a crack opening rate of 0.0005mm/s was selected. This would be approximately consistent with a crack opening to 0.3mm in a principal structural element in a multiple storey carpark if the portion of slab being supported by the structural element was loaded over a 10-minute period. For ease of comparison, the same self-healing beam arrangement considered in Chapter 3 was used for this exercise. It is acknowledged that this is very different in scale from the structural elements used to support carpark decks, but it is the crack opening rate that is important in this exercise. As shown in the previous section, amongst the available healing agents considered, PC24 gave the most favourable response at this crack opening rate.

The validation experiments comprised tests on 21 laboratory specimens (i.e. 75x75x255mm notched prismatic beams), 9 of which were self-healing specimens. 3 concrete cubes and cylinders were also cast and tested for compressive and tensile strengths. The details on the experimental procedures were given in Section 3.3 in Chapter 3. The specimens were subjected to continuous loading at different crack opening rates at a pressure of 0.5 bar under three-point flexural bending tests until a CMOD of 0.3mm was reached. The experimental setup is shown in Figures 3.5 and 3.6 in Chapter 3.

Although the selected rate crack opening rate for the tailoring exercise was 0.0005mm/s, the author decided to conduct additional tests at a higher rate (0.001mm/s) and lower rate (0.0002mm/s) in order to check that the numerical simulations with this healing agent gives the correct trend with respect to loading rate.

7.5.1 Compression and tensile values

The average compressive and tensile strengths along with the CoV of the specimens in this test series are shown in Table 7.3.

Table 7.3. Summary of concrete strengths after 8 days of curing in Chapter 7

Average cube strength, f_{cu} (MPa)	**CoV (%)**	**Average cylinder splitting strength, f_{cyl} (MPa)**	**CoV (%)**	**True uniaxial strength, f_c (MPa)**	**True tensile strength, f_t (MPa)**
38.2	8.6	3.1	8.3	30.6	2.6

7.5.2 Results and discussion

The results for the load-CMOD responses of the tests series are presented in Figure 7.7. Each graph, relating to a CMOD rate, includes the results from the associated numerical computation (see Section 7.4).

The graphs show that there are significant differences between the experimental responses of the three SH beams in each set. This variability is a feature of self-healing systems that has been discussed in the earlier chapters of this thesis. This variability is not captured in the single analysis undertaken for each CMOD rate. Nevertheless, the numerical predictions are considered sufficiently accurate to be useful for material design.

As discussed in Section 7.4, it was necessary to select the crack opening at which the healing agent was released (w_{crit}) and it was assumed that this increases with the viscosity of the healing agent. Here, a value of 0.115mm was selected, although a small amount of calibration was involved in the choice of this value. From visual observations (see Figure 7.8) it was also found that PC24 did not form a strong enough bond as re-cracking (after healing) did not occur elsewhere.

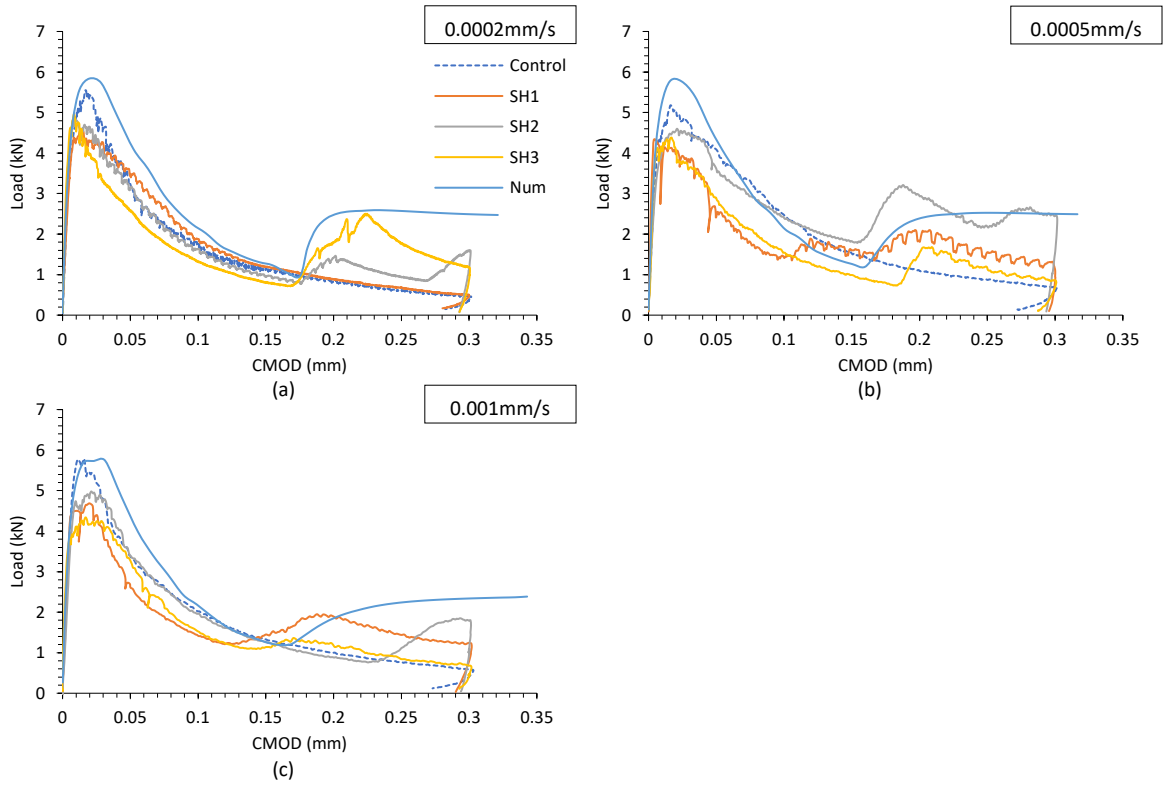

Figure 7.7. Comparison of experimental data and numerical simulations of load-CMOD responses for loading rates of (a) 0.0002mm/s, (b) 0.0005mm/s and (c) and 0.001mm/s

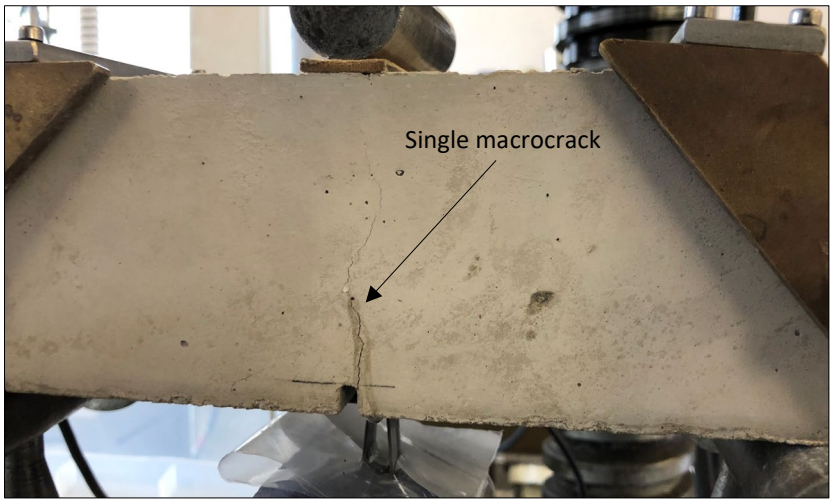

Figure 7.8. A representative specimen showing surface crack and healing agent PC24

7.6 Conclusions

The application of the numerical model presented here suggests that is it possible to predict the behaviour of the vascular healing system using the model. The conclusions drawn from these numerical and the associated experimental studies are as follows:

- The numerical model is able to represent the damage-healing behaviour of a cementitious vascular healing system with reasonable accuracy;
- The model gives the correct trends with respect to changing healing agents;
- The model can be used to tailor the design of an SH system to a particular loading scenario;
- The model requires healing-agent parameters than are not normally provided in material data sheets and, where possible, these parameters (i.e. the crack opening at which the healing agent is first transported into a crack) are best determined by calibration.

Specific conclusions from the experiments with the PC24 healing agent are as follows:

- The degree of healing increases as the CMOD rate reduces;
- A more viscous healing agent (i.e. PC24) requires a larger opening to initiate flow;
- A higher delivery pressure (i.e. > 0.5 bar) is necessary to accelerate the flow and transport of PC24 into discrete cracks.

Chapter 8 Conclusions and future work

8.1 Conclusions

This chapter presents the main conclusions from the work described in this thesis and gives recommendations for future work on SHCMs. Before proceeding with the conclusions the author considers it is valuable to revisit the objectives set out in Chapter 1, as follows:

- Develop an experimental methodology for characterising the behaviour of a vascular self-healing cementitious material system;
- Understand different aspects of the mechanical and transport behaviour of the healing system;
- Determine a consistent set of mechanical damage and healing, and transport parameters for the chosen cementitious material system;
- Devise and validate a set of constitutive relationships that could form the basis of a design procedure and/or numerical model of the selected material system;
- Validate a numerical model, developed by others in the M4L Group at Cardiff, and then use the model to determine the most ideal healing agent for a selected structural element under a predetermined loading scenario;
- Assess the accuracy of the above material design exercise by conducting experimental tests on the structural element designed.

The objectives were met by the following work:

a. An experimental programme comprising a series of three and four-point flexural bending tests which was undertaken to explore simultaneous damage-healing behaviour of a vascular healing system. This study evaluated healing under transient and fixed crack opening conditions. The influence of varying crack opening rates, supply pressures and healing periods within small scale laboratory specimens were investigated. Additionally, the influence of cracking and healing in multiple interconnected micro and macrocracks was also considered. The specimens used in the latter tests included vertically and/or laterally offset discontinuous reinforcement with one or two layers of channels. The following conclusions were drawn from these three and four-point flexural bending tests are:

    - A vascular healing system with embedded channels is able to transport healing agents to damage zones;
    - Healing agent transport was enhanced by the application of pressure to the liquid agent;

- The continuous supply of CA from an external reservoir allowed significant healing in cracks up to 0.2mm in width, which recovery indices of 50% and 90% (or greater) for continuous and paused loadings respectively;
- Healing indices in excess of 100% are possible with CA;
- A healing system with CA as the agent can fully heal a tapering crack, with a maximum surface opening of 0.15mm, in two to three minutes;
- A discontinuous offset arrangement of reinforcement is able to produce a complex cracking pattern;
- Multiple channels are required to ensure that healing agent reaches the majority of micro and macrocracks;
- The optimum CMOD rate and applied healing-agent pressure are between 0.0005 and 0.001mm/s and 0.3 and 0.5 bar respectively for the materials considered in this programme of work.

b. A series of direct tension tests on notched cubes with embedded channels was carried out in order to supplement the above study and explore the influence of the crack opening and healing period on the damage healing response. The conclusions from the direct tension tests are:

- It is necessary to have relatively deep notches ($\geq$ 50mm of the cross-section) in the cube to ensure that a single (nominally horizontal) macro crack forms;
- The testing configuration with closed loop control has sufficient stiffness and speed of reaction to allow stable post-peak responses to be captured;
- More healing occurs in narrow crack openings (i.e. 0.1mm) than wider openings (i.e. 0.2mm) although the proportion of crack area that is reached by the healing agent is similar in both cases;
- At larger openings, a significant proportion of CA flows out of the specimen or permeates into the matrix adjacent to the crack;
- The degree of healing is higher in beams with tapering vertical cracks than in cubes with (nominally) uniform horizontal cracks;
- A longer healing period is required to achieve substantial healing in direct tension specimens than in the comparable beam samples;
- The smoothness in the post-peak response depends on how the cracks from both side notches intersect;
- A healing agent with higher viscosity is recommended to ensure reasonable distribution across the crack surface.

c. A series of tests to characterise the transport and curing behaviour of the vascular self-healing system studied in this programme of work was also undertaken. This study examined the capillary flow in an evolving crack, the CA sorptivity, the curing front properties of CA with a cementitious substrate and the dynamic flow characteristics of CA in capillary channels. The following conclusions are drawn from the work:

- The capillary rise response of CA in a discrete crack is strongly dependent on the crack opening and the supply pressure;
- CA is drawn by capillary action into the micro-cracked region adjacent to a macro crack and the average vertical capillary rise response from a nominally horizontal crack immersed in a bath of CA is between 3 and 3.5mm;
- CA develops a curing front adjacent to a cementitious substrate, which progresses over time, but which gradually becomes less planar and more diffuse;
- The meniscus dynamic contact angle for CA is velocity dependent.

d. A numerical model, developed by others in the M4L team at Cardiff, was validated. A series of predictive analyses of notched self-healing beams were undertaken using this model for different crack opening rates and different healing agents. A crack opening rate was selected and the healing agent with the *'best'* performance for this rate was chosen from amongst the agents considered in the analysis series just described. The agent selected, which had the properties of PC24 cyanoacrylate, was then used in a set of tests and the experimental response compared with that predicted by the numerical analysis. The comparison showed that the model predictions were relatively accurate. The following conclusions are drawn from this study:

- The numerical model is able to represent the damage-healing behaviour of SHCMs with reasonable accuracy;
- The model correctly predicts the change in response due to a change in healing agent;
- The model is reliable enough to design of an SHCM system;
- The model requires healing agent parameters than are not normally provided in material data sheets and therefore these should be calibrated using a test on a cementitious SH specimen;

8.2 Recommendations for future work

This research has provided useful information on the nature of simultaneous damage-healing behaviour in cementitious vascular healing systems. The study was motivated by problems encountered with the durability of cementitious materials (as explained in Chapter 1). It is recommended that more extensive studies be undertaken in this ever-evolving field of advanced material science before the material systems are used by the construction industry. The following future work is recommended:

- Mechanical and flow tests for a larger range of healing agents;
- Direct tension tests with transient crack openings;
- Long-term tests on the healing systems under fixed and variable loading conditions;
- Tests with different reinforcement configurations to explore healing in more complex crack patterns;
- Tests under different environmental conditions for example, at different temperatures, relative humidities and under equivalent marine conditions (i.e. offshore or coastal);
- Developing standardised tests for characterising healing behaviour;
- 2D and 3D model validations for more complex cases and further material *'tailoring'* exercises;
- Full-scale site trials;
- Exploration of the potential of the healing systems for repair and maintenance.

8.3 Practical implications

The viability of vascular healing systems to be employed in a full-scale structure on a construction site has been proven (Davies et al. 2018). In these trials, the healing agent was pumped under pressure through a vascular network embedded in a concrete wall panel. The main challenges identified in this work were to:

- Find better healing agents that remain stable and viable for relatively long periods of time;
- Establish ways of properly storing and disposing healing agents;
- Modify the network system such that it can be flushed using air or water to allow for repeated cycles of healing;
- Better position the vascular channels in zones susceptible to cracking to maximize the effectiveness of the healing system;
- Find ways of attaching an external reservoir to allow for more supply of healing agents;
- Seal or secure vascular networks when not in use;
- Design a method to remotely activate the vascular networks without human intervention.

Appendices

Appendix A: Experimental results

Chapter 3: Mechanical damage and healing properties

Chapter 4: Transport properties in complex multiple cracks

Chapter 7: Modelling and validation

Appendix B: Safety and technical datasheets

The front pages of each material datasheets have been provided along with a link for the full document and the associated safety information.

- Cyanoacrylate, Procure PC20, Safety and technical datasheets
  URL: http://www.cyanotec.com/procure/
- Cyanoacrylate, Procure PC24, Safety and technical datasheets
  URL: http://www.cyanotec.com/procure/
- Cyanoacrylate, Procure PC22, Safety and technical datasheets
  URL: http://www.cyanotec.com/procure/
- Sodium silicate, Safety datasheet
  URL:
  https://www.fishersci.co.uk/store/msds?partNumber=10060470&productDescription=2.5LT+Sodium+silicate%2C+technical%2C+solution%2C+d%3D1.5&countryCode=GB&language=en
- Sikadur-31 CF Rapid, Product datasheet
  URL: http://www.epms-supplies.co.uk/admin/products/documents/Sika/Data/Sikadur%2031%20CF%20Rapid%20TDS.pdf

Appendix C

Chapter 7: Relationship between healing indices and healing parameters

Figure C1. Typical damage-healing response in uniaxial tension

Appendix D: Glossary of terms

D1.1 Definition of terms

D1.2 Self-healing systems

Appendix A: Experimental results

Chapter 3: Mechanical damage and healing properties

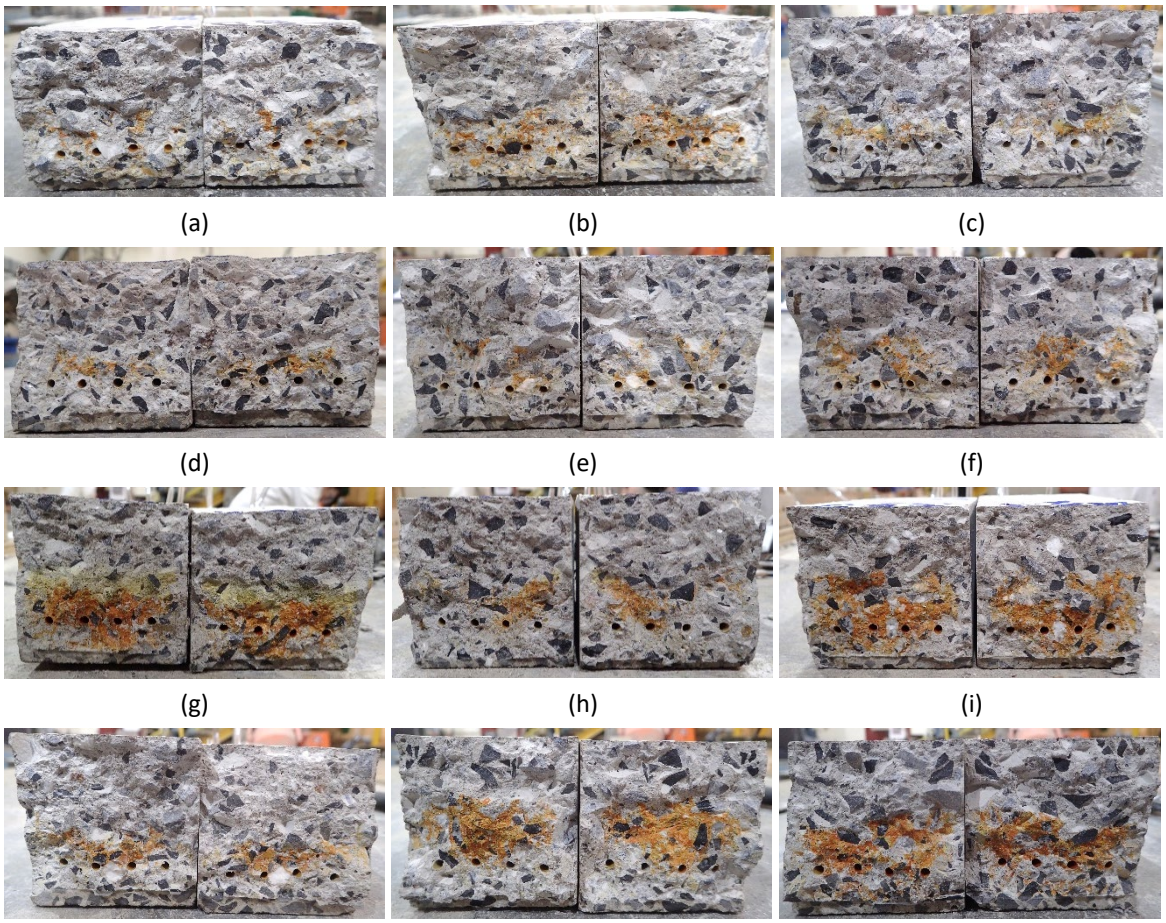

Figure A1. CA migration and zone of healing at loading rate of (a-c) 0.0002mm/s for SH1-3, (d-f) 0.0005mm/s for SH1-3, (g-i) 0.001mm/s for SH1-3 and (j-l) 0.002mm/s for SH1-3 with 0.5 bar of pressure

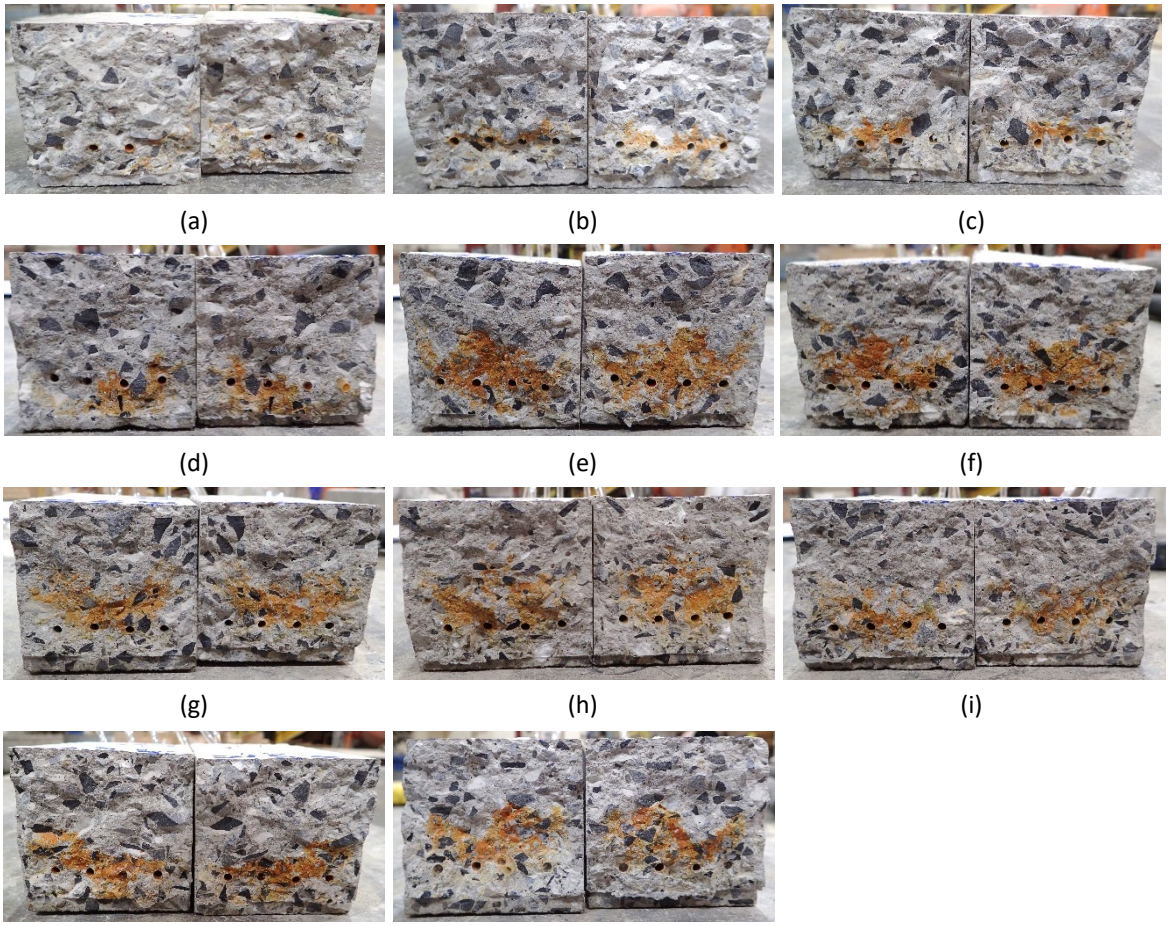

Figure A2. CA migration and zone of healing at loading rate of 0.001mm/s with pressure of (a-c) 0 bar for SH1-3, (d-f) 0.1 bar for SH1-3, (g-i) 0.3 bar for SH1-3 and (j-k) 1.0 bar for SH1-3

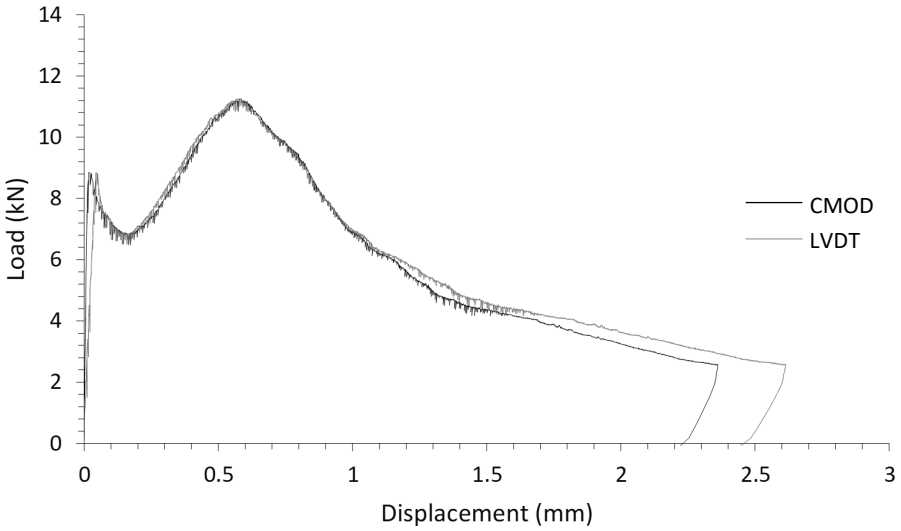

Figure A3. Load-CMOD-LVDT responses of the C1 specimen from set 6, Group C

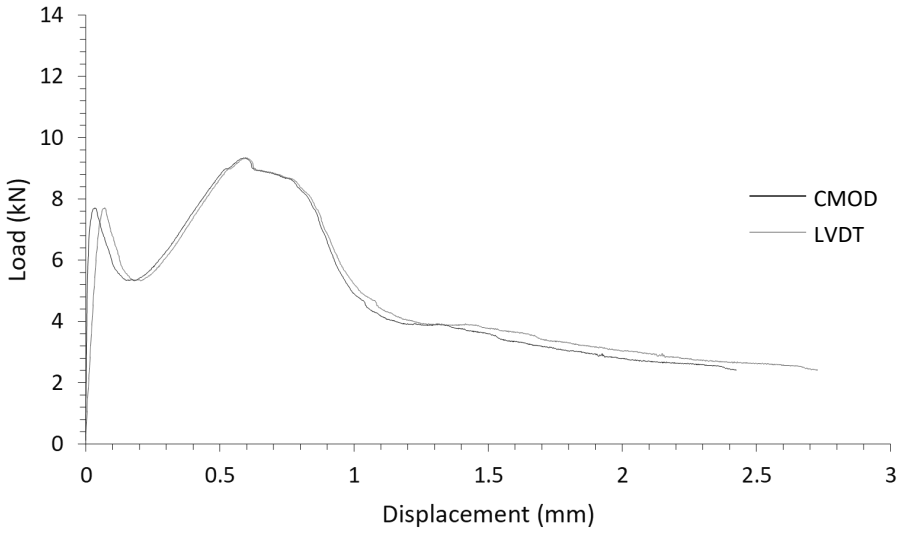

Figure A4. Load-CMOD-LVDT responses of the C3 specimen from set 6, Group C

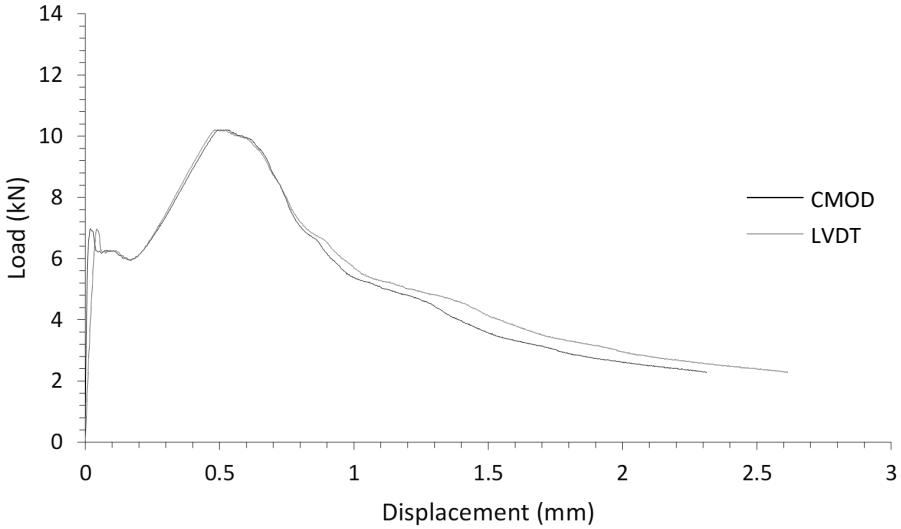

Figure A5. Load-CMOD-LVDT responses of the C4 specimen from set 6, Group C

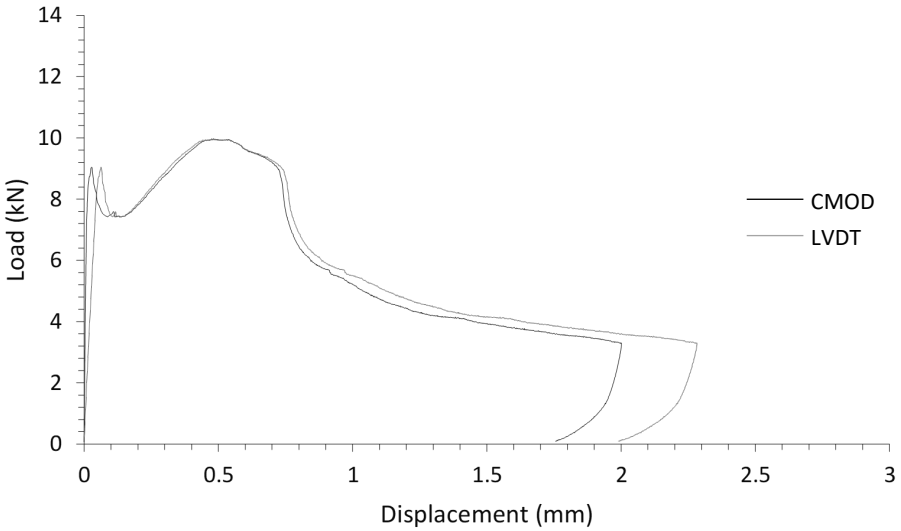

Figure A6. Load-CMOD-LVDT responses of the C1 specimen from set 7, Group D

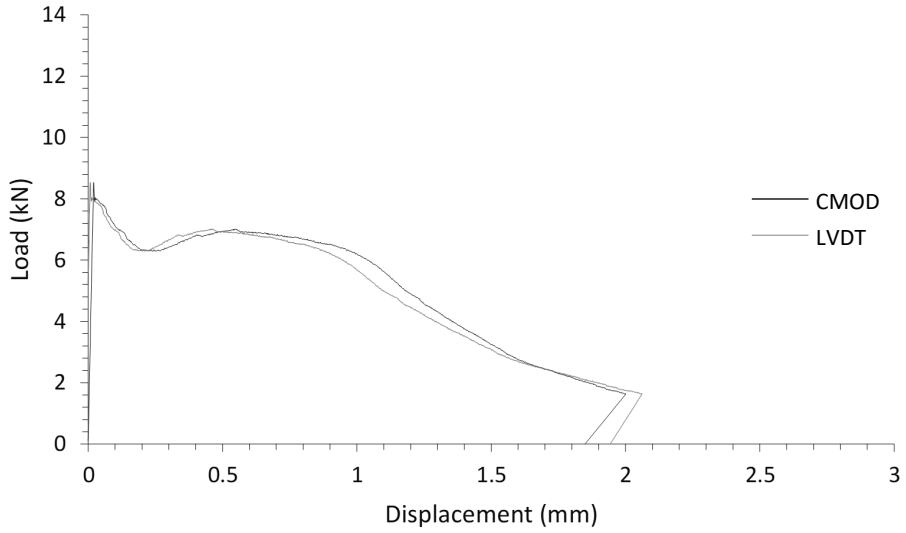

Figure A7. Load-CMOD-LVDT responses of the C1 specimen from set 7, Group D

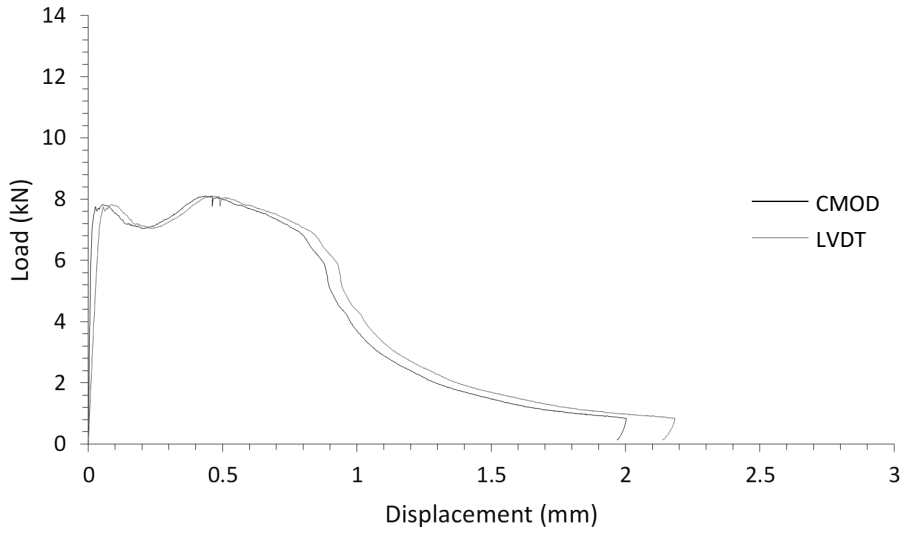

Figure A8. Load-CMOD-LVDT responses of the C4 specimen from set 7, Group D

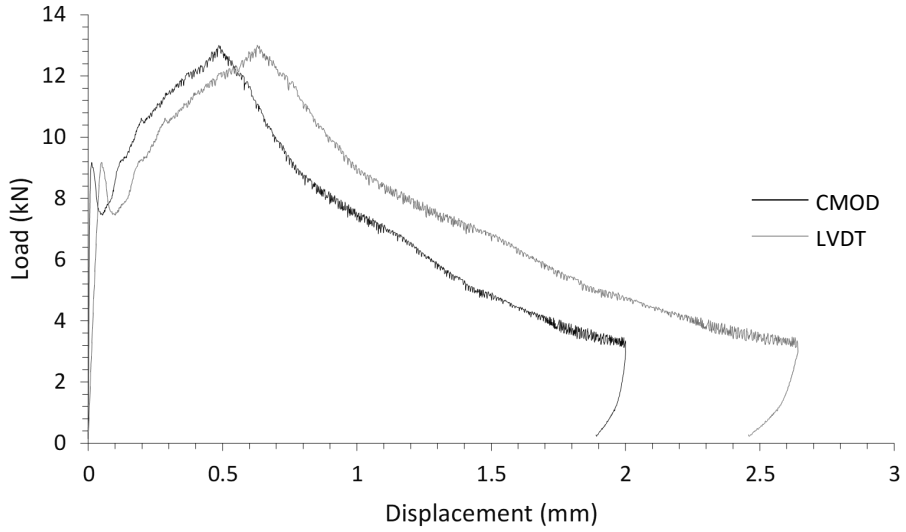

Figure A9. Load-CMOD-LVDT responses of the SH2 specimen from set 7, Group D

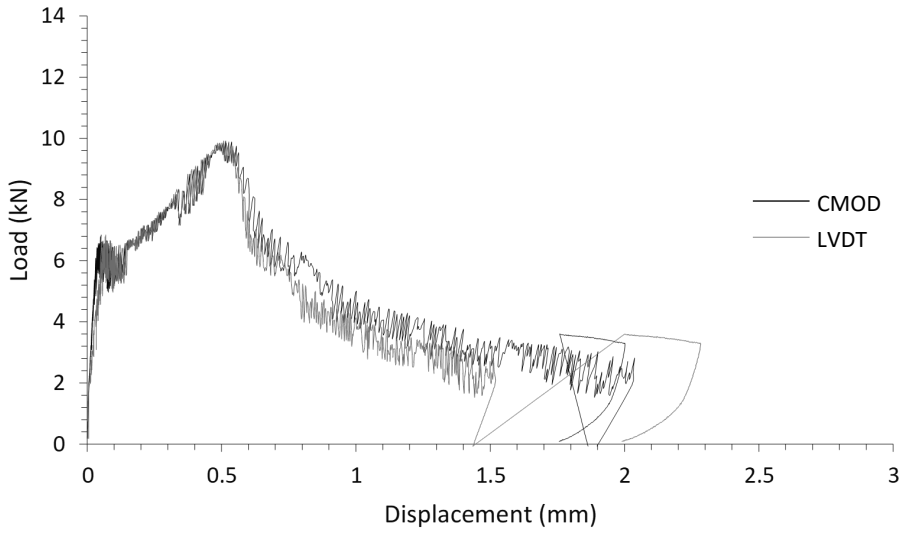

Figure A10. Load-CMOD-LVDT responses of the C2 specimen from set 8, Group E

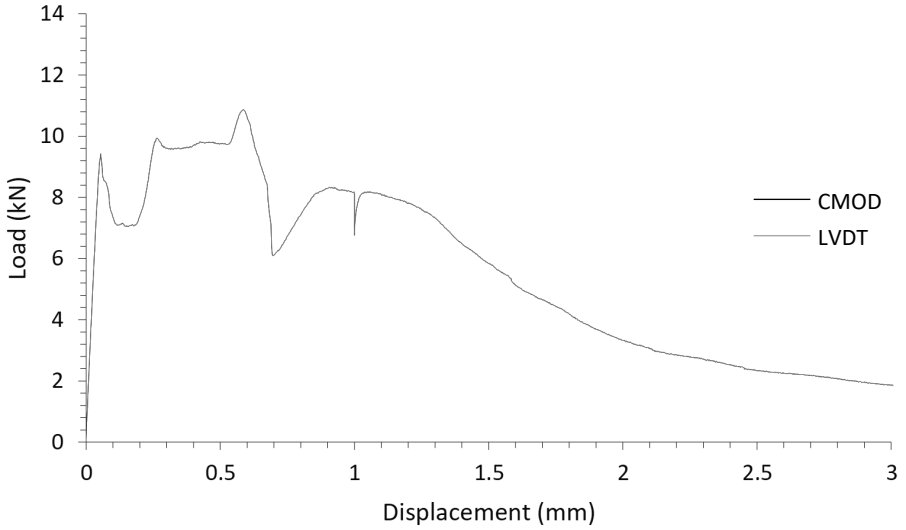

Figure A11. Load-CMOD-LVDT responses of the SH2 specimen from set 8, Group E

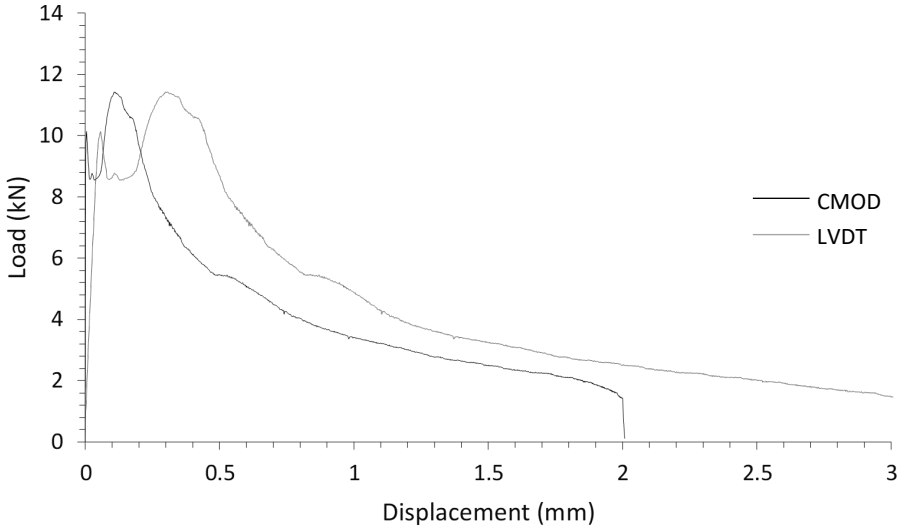

Figure A12. Load-CMOD-LVDT responses of the SH3 specimen from set 8, Group E

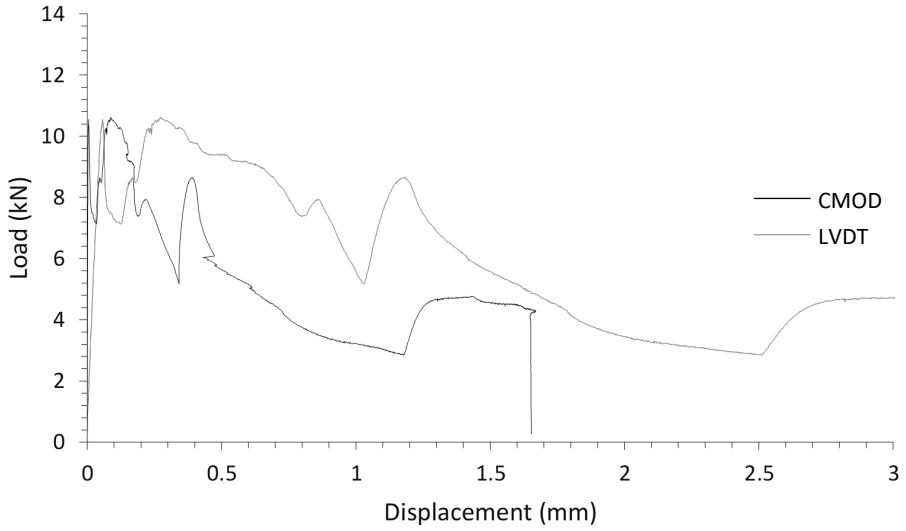

Figure A13. Load-CMOD-LVDT responses of the SH4 specimen from set 8, Group E

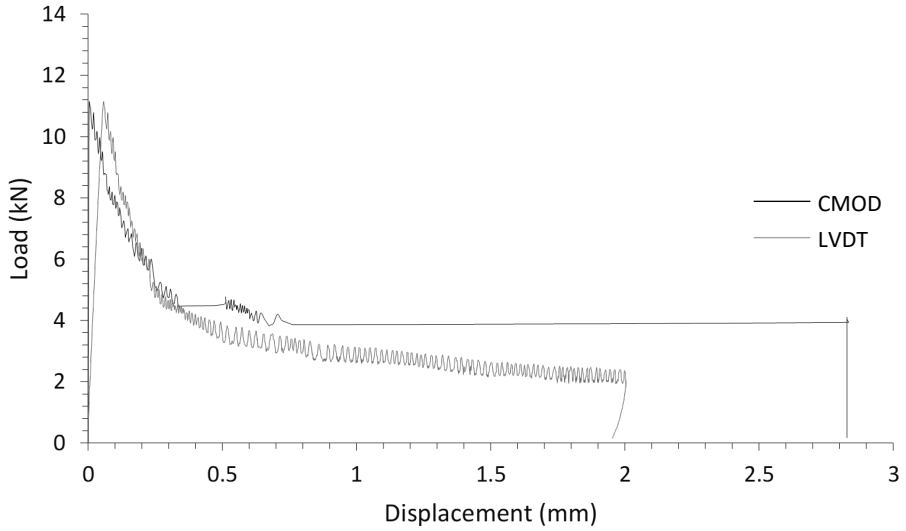

Figure A14. Load-CMOD-LVDT responses of the C1 specimen from set 9, Group F

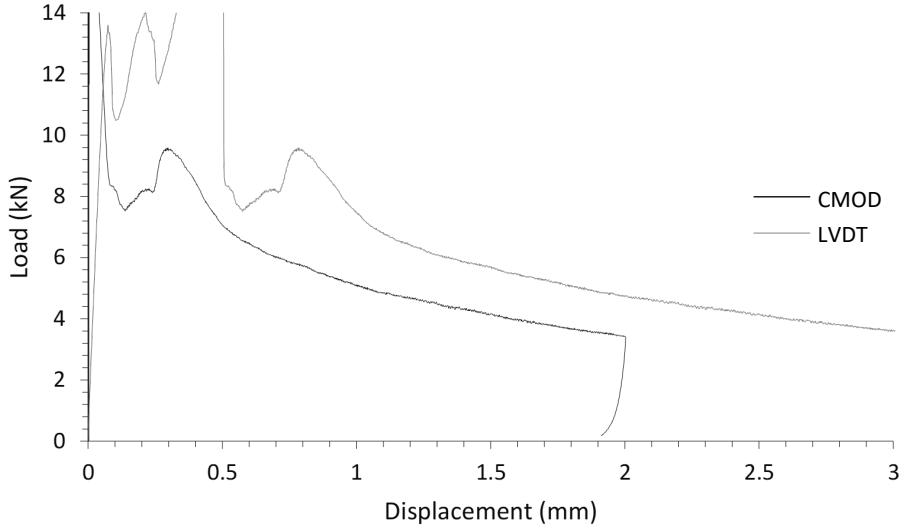

Figure A15. Load-CMOD-LVDT responses of the SH1 specimen from set 9, Group F

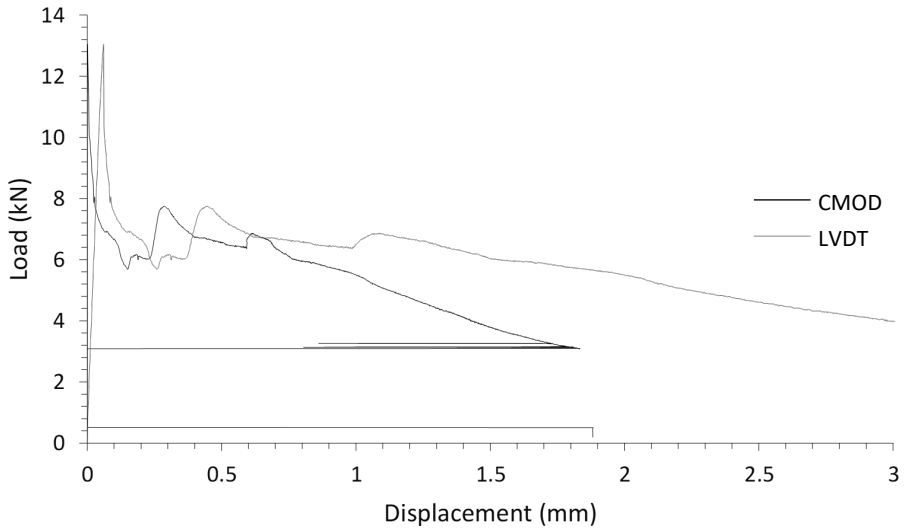

Figure A16. Load-CMOD-LVDT responses of the SH2 specimen from set 9, Group F

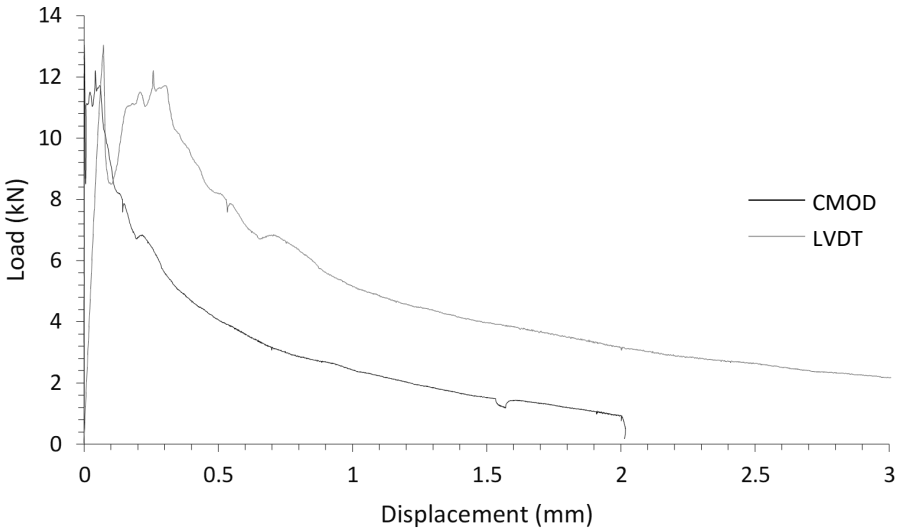

Figure A17. Load-CMOD-LVDT responses of the SH4 specimen from set 9, Group F

Chapter 7: Modelling and validation

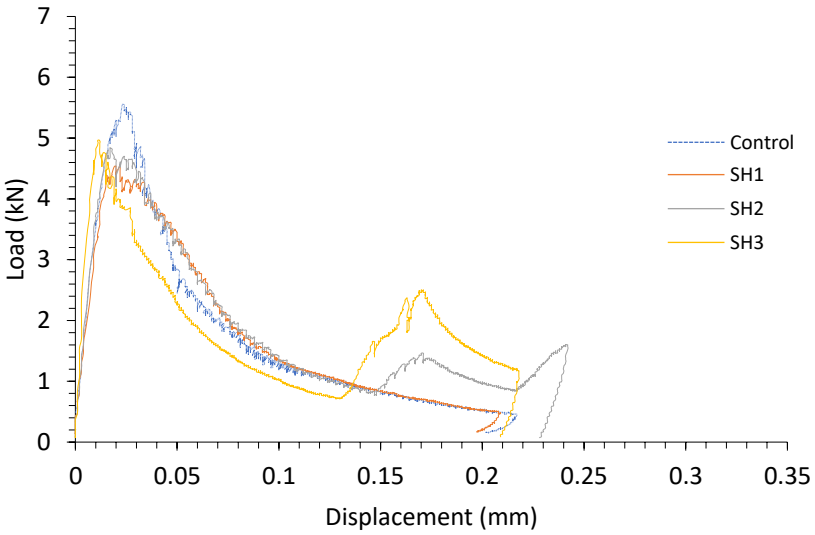

Figure A18. Load-displacement responses for loading rates of 0.0002mm/s for PC24

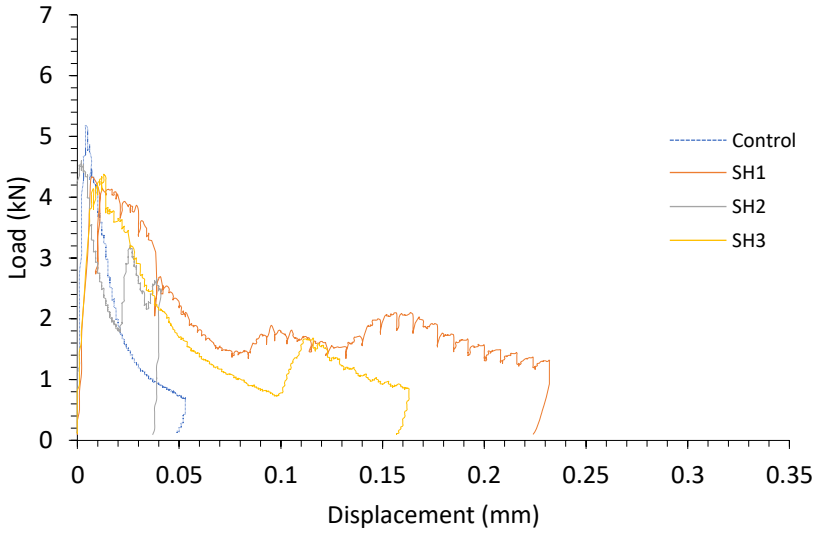

Figure A19. Load-displacement responses for loading rates of 0.0005mm/s for PC24

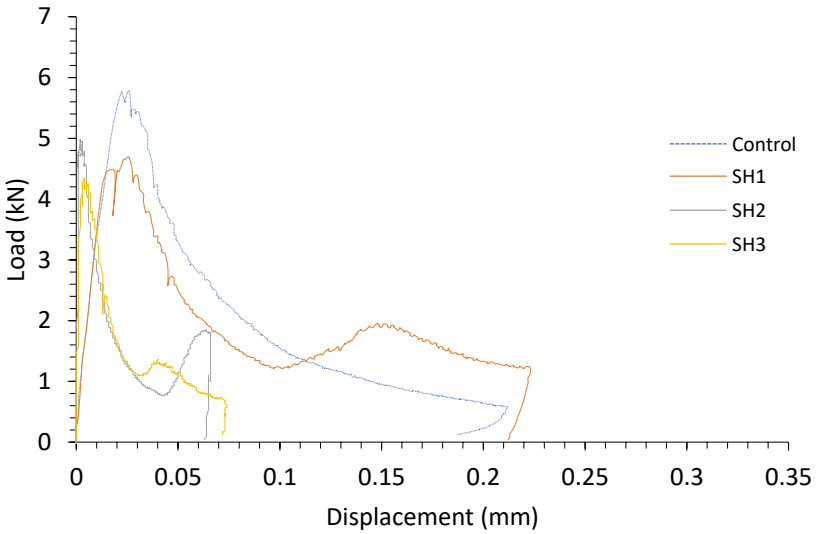

Figure A20. Load-displacement responses for loading rates of 0.001mm/s for PC24

CYANOTEC Creating Bonds

PROCURE PC20

TECHNICAL DATA SHEET FOR PROCURE PC20

TYPICAL APPLICATIONS

PC 20 is specially formulated for the bonding of plastics, rubbers, wood, metals and other common substrates. Recommended for use on assemblies with very close fitting parts and smooth, even surfaces.
Can be used as a post-assembly adhesive to wick into parts.

PRODUCT DESCRIPTION

Procure PC 20 is a very low viscosity (5cPs) modified Ethyl Cyanoacrylate adhesive.
PC 20 is suitable for bonding a very wide range of materials, including some porous ones, where very fast cure speed is required.

PROPERTIES OF UNCURED MATERIAL

Chemical type		Ethyl
Appearance		Clear
Specific Gravity		1.06
Viscosity cPs[1]		
– range		2-5
– typical value		4
Tensile Strength[2]	(N/mm^2)	21
Fixture Time	(secs)	1-20
Full Cure	(hours)	24
Flash Point	(°C)	> 85
Shelf Life @ 5°C	(months)	12
Max Gap Fill	(mm)	0.05
Operating Temperature Range	(°C)	-50 to +80

[1] ISO 3104/3105
[2] ISO 6922

TYPICAL CURING PERFORMANCE

Typical Speed:

Steel/steel	<15 seconds
ABS/ABS	<5 seconds
Rubber/Rubber	<5 seconds
Wood (balsa)	<3 seconds

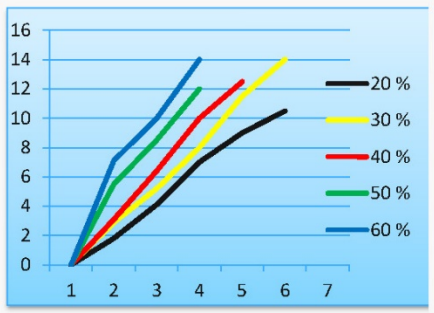

CURE VS. HUMIDITY

CURE SPEEDS VS. ENVIRONMENTAL CONDITIONS

Cyanoacrylates require surface moisture on the substrates in order to initiate the curing mechanism. The speed of cure is reduced in low-humidity conditions. Low temperatures will also reduce cure speed. All figures relating to cure speed are tested at 21°C.

CURE SPEED VS. SUBSTRATE

The speed of cure of cyanoacrylates varies according to the substrates to be bonded. Acidic surfaces such as paper and leather will have longer cure times than most plastics and rubbers. Some plastics with very low surface energies, such as polyethylene, polypropylene and Teflon® require the use of Procure 77 Primer
(See PC 77 TDS for further info).

CURE SPEED VS.ACTIVATOR

Activators 780 and 750 may be used in conjunction with cyanoacrylates where cure speed needs to be accelerated.

Cure speeds of less than 2 seconds can be obtained with most cyanoacrylates.

The use of an activator can reduce the final bond strength by up to 30% Testing on the parts to measure the effect is recommended.

CURE SPEED VS. BOND GAP

PROCURE / REACT cyanoacrylates give best results on close fitting parts. The product should be applied in a very thin line in order to ensure rapid polymerisation and a strong bond. Excessive bond gaps will result in slower cure speeds. PROCURE / REACT cyanoacrylate activators may be used to greatly increase cure speeds (see PC780 and PC750 TDS for further info).

CYANOTEC LTD
Bay 2, Building 62, Third Avenue, Pensnett Trading Estate, Kingswinford DY6 7XT
TEL 0845 618 3120 FAX 0845 618 3121 EMAIL sales@cyanotec.com

PC 20
V1.3
JUN 16

CYANOTEC Creating Bonds

PROCURE PC24

TECHNICAL DATA SHEET FOR PROCURE PC24

TYPICAL APPLICATIONS

PC 24 is specially formulated for the bonding of plastics, rubbers, wood, paper, leather, metals and other common substrates.

PC 24 relies less on surface moisture for cure speed than standard cyanoacrylates. Recommended for use on close-fitting parts and fairly smooth, even surfaces

PRODUCT DESCRIPTION

PC 24 is a medium viscosity modified Ethyl Cyanoacrylate adhesive. PC24 is suitable for bonding a very wide range of materials, including some porous ones, where a fast cure speed is required.

PROPERTIES OF UNCURED MATERIAL

Chemical type		Ethyl
Appearance		Clear
Specific Gravity		1.06
Viscosity cPs[1]		
– range		80-120
– typical value		100
Tensile Strength[2]	(N/mm^2)	21
Fixture Time	(secs)	3-20
Full Cure	(hours)	24
Flash Point	(°C)	> 85
Shelf Life @ 5°C	(months)	12
Max Gap Fill	(mm)	0.15
Operating Temperature Range	(°C)	-50 to +80

TYPICAL CURING PERFORMANCE

Typical Speed:

Steel/steel	<20 seconds
ABS/ABS	<10 seconds
Rubber/Rubber	<5 seconds
Wood (balsa)	<3 seconds

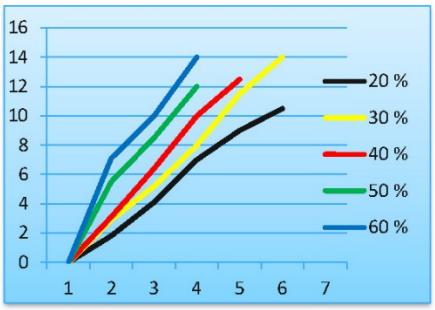

CURE VS HUMIDITY

CURE SPEED VS. ENVIRONMENTAL CONDITIONS

Cyanoacrylates require surface moisture on the substrates in order to initiate the curing mechanism. The speed of cure is reduced in low-humidity conditions. Low temperatures will also reduce cure speed. All figures relating to cure speed are tested at 21°C.

CURE SPEED VS.SUBSTRATE

The speed of cure of Cyanoacrylates varies according to the substrates to be bonded. Acidic surfaces such as paper and leather will have longer cure times than most plastics and rubbers. Some plastics with very low surface energies, such as polyethylene, polypropylene and Teflon® require the use of Procure 77 Primer
(See PC 77 TDS for further info).

CURE SPEED VS.ACTIVATOR

Activators 780 and 750 may be used in conjunction with cyanoacrylates where cure speed needs to be accelerated.

Cure speeds of less than 2 seconds can be obtained with most cyanoacrylates.

The use of an activator can reduce the final bond strength by up to 30% Testing on the parts to measure the effect is recommended.

CURE SPEED VS. BOND GAP

PROCURE/REACT Cyanoacrylates give best results on close fitting parts. The product should be applied in a very thin line in order to ensure rapid polymerisation and a strong bond. Excessive bond gaps will result in slower cure speeds. PROCURE/REACT Cyanoacrylate Activators may be used to greatly increase cure speeds (see PC780 and PC750 TDS for further info).

CYANOTEC LTD
Bay 2, Building 62, Third Avenue, Pensnett Trading Estate, Kingswinford DY6 7XT
TEL 0845 618 3120 FAX 0845 618 3121 EMAIL sales@cyanotec.com

PC 24
V1.3
JUN 16

CYANOTEC Creating Bonds

PROCURE

PC22

TECHNICAL DATA SHEET FOR PROCURE PC22

TYPICAL APPLICATIONS

PC 22 is specially formulated for high strength, general purpose bonding of most plastics, rubbers and other common substrates. Recommended for use on assemblies where parts are not close fitting, for uneven or porous surfaces, or when time is required to align parts before curing.

PRODUCT DESCRIPTION

PC 22 Instant Superglue is a high viscosity Ethyl Cyanoacrylate based adhesive.
PC 22 is suitable for bonding a wide range of materials.

PROPERTIES OF UNCURED MATERIALS

Chemical type		Ethyl
Appearance		Clear
Specific Gravity		1.06
Viscosity cPs[1]		
– range		2175- 2750
– typical value		2500
Fixture Time	(secs)	20
Full Cure	(hours)	20 - 60
Flash Point	(°C)	24
Shelf Life @ 5°C	(months)	> 85
Max Gap Fill	(mm)	12
Operating Temperature Range	(°C)	0.20
[1] Brookfield LVF, spindle 3, speed 30rpm		-50 to +80
[2] ISO 6922		

TYPICAL CURING PERFORMANCE

Typical Speed:	
Steel/steel	<60 seconds
ABS/ABS	<40 seconds
Rubber/Rubber	<30 seconds

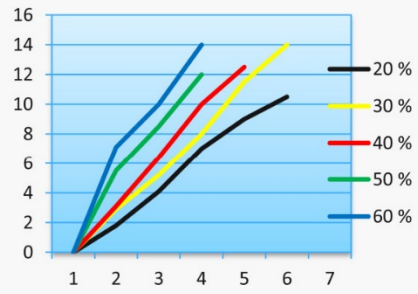

CURE VS HUMIDITY

CURE SPEED VS. ENVIRONMENTAL CONDITIONS

Cyanoacrylates require surface moisture on the substrates in order to initiate the curing mechanism. The speed of cure is reduced in low-humidity conditions. Low temperatures will also reduce cure speed. All figures relating to cure speed are tested at 21°C.

CURE SPEED VS. SUBSTRATE

The speed of cure of Cyanoacrylates varies according to the substrates to be bonded. Acidic surfaces such as paper and leather will have longer cure times than most plastics and rubbers. Some plastics with very low surface energies, such as polyethylene, polypropylene and Teflon® require the use of Procure 77 Primer (see PC 77 TDS for further info).

CURE SPEED VS. ACTIVATOR

Activators 780 and 750 may be used in conjunction with cyanoacrylates where cure speed needs to be accelerated.

Cure speeds of less than 2 seconds can be obtained with most cyanoacrylates.

The use of an activator can reduce the final bond strength by up to 30% Testing on the parts to measure the effect is recommended

CURE SPEED VS. BOND GAP

PROCURE/REACT Cyanoacrylates give best results on close fitting parts. The product should be applied in a very thin line in order to ensure rapid polymerisation and a strong bond. Excessive bond gaps will result in slower cure speeds.
PROCURE/REACT Cyanoacrylate Activators may be used to greatly increase cure speeds (see PC780 and PC750 TDS for further info).

CYANOTEC LTD
Bay 2, Building 62, Third Avenue, Pensnett Trading Estate, Kingswinford DY6 7XT
TEL 0845 618 3120 FAX 0845 618 3121 EMAIL sales@cyanotec.com

PC22
V1.3
JUN 16

SAFETY DATA SHEET

Creation Date 10-Feb-2011 **Revision Date** 15-Feb-2019 **Revision Number** 5

SECTION 1: IDENTIFICATION OF THE SUBSTANCE/MIXTURE AND OF THE COMPANY/UNDERTAKING

1.1. Product identification

Product Description: Sodium silicate solution about 1.5 S.G.
Cat No. : S/6340/25, S/6340/17

1.2. Relevant identified uses of the substance or mixture and uses advised against

Recommended Use Laboratory chemicals.
Uses advised against No Information available

1.3. Details of the supplier of the safety data sheet

Company

UK entity/business name
Fisher Scientific UK
Bishop Meadow Road, Loughborough,
Leicestershire LE11 5RG, United Kingdom

EU entity/business name
Acros Organics BVBA
Janssen Pharmaceuticalaan 3a
2440 Geel, Belgium

E-mail address begel.sdsdesk@thermofisher.com

1.4. Emergency telephone number

Tel: 01509 231166
Chemtrec US: (800) 424-9300
Chemtrec EU: 001 (202) 483-7616

SECTION 2: HAZARDS IDENTIFICATION

2.1. Classification of the substance or mixture

CLP Classification - Regulation (EC) No 1272/2008

Physical hazards

Based on available data, the classification criteria are not met

Health hazards

Skin Corrosion/irritation	Category 2 (H315)
Serious Eye Damage/Eye Irritation	Category 1 (H318)

Environmental hazards
Based on available data, the classification criteria are not met

Construction

Sikadur®-31 CF Rapid

2-part thixotropic epoxy adhesive

Product Description	Sikadur®-31 CF Rapid is a moisture tolerant, thixotropic, structural two part adhesive and repair mortar, based on a combination of epoxy resins and special fillers, designed for use at temperatures between +5°C and +20°C.
Uses	As a structural adhesive and mortar for: ■ Concrete elements ■ Hard natural stone ■ Ceramics, fiber cement ■ Mortar, Bricks, Masonry ■ Steel, Iron, Aluminium ■ Wood ■ Polyester, Epoxy ■ Glass As a repair mortar and adhesive: ■ Corners and edges ■ Holes and void filling ■ Vertical and overhead use Joint filling and crack sealing: ■ Joint and crack arris / edge repair
Characteristics / Advantages	Sikadur®-31 CF Rapid has the following advantages: ■ Easy to mix and apply ■ Very good adhesion to most construction materials ■ High strength adhesive ■ Thixotropic: non-sag in vertical and overhead applications ■ Hardens without shrinkage ■ Different coloured components (for mixing control) ■ No primer needed ■ High initial and ultimate mechanical strength ■ Good abrasion resistance ■ Impermeable to liquids and water vapour ■ Good chemical resistance

Appendix C

Chapter 7: Relationship between healing indices and healing parameters

Having considered the constitutive model described in the preceding section it was felt interesting to explore how the healing parameters related to more standard healing indices. This work is not applied to any healing situations presented here but was used in one of the author's publications (Selvarajoo et al. 2020).

A healing index was proposed by Homma et al. (2009) as shown in equation (7.20) which had also been adopted by other investigators (Davies et al. 2018; Ferrara et al. 2014). An explanation on its use to measure the healing recovery from the experimental data is also provided in Section 3.4.1.4 in Chapter 3.

$$H_\sigma = \frac{\sigma_3 - \sigma_2}{\sigma_1 - \sigma_2} \tag{7.20}$$

in which the average uniaxial stress (σ_1) defined in Figure C1 and it is noted that $\sigma_1 = f_t$.

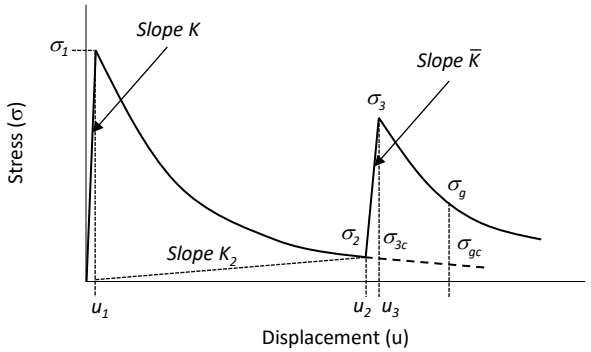

Figure C1. Typical damage-healing response in uniaxial tension

Assuming that damage occurs continuously in the virgin part of the material during the reloading phase (i.e. from points 2 to 3), a more logical definition of H_σ would be to replace σ_{3c} with σ_2 in equation 7.20. The challenge of this approach is that the control curves needs to be fully consistent with the damage-healing curve which is difficult to achieve due to the statistical variation of concrete. Since the amount of virgin damage that occurs between points 2 and 3 is negligible, the definition given in equation 7.20 can only be adopted in experiments with single phase healing. When considering simultaneous damage-healing processes, this assumption is no longer reasonable and therefore equation 7.20 is presented. It is acknowledged that the indices measured will be affected by the aforementioned statistical variation in behaviour.

$$H_\sigma = \frac{\sigma_g - \sigma_{gc}}{\sigma_1 - \sigma_{gc}} \tag{7.21}$$

in which σ_g and σ_{gc} is defined in Figure C1.

The indices defined in equations 7.20 and 7.21 relate to strength recovery but a stiffness recovery index is also defined as follows:

$$H_K = \frac{\bar{K} - K_2}{K - K_2} \tag{7.22}$$

in which K is the initial (pre-cracked) slope and $\bar{K}$ is the slope from points 2 to 3, as illustrated in Figure C1.

When considering the relationship between healing indices and healing parameters, in terms of the stiffness index; using the theoretical terms from equations 7.1 to 7.5 and 7.20 to 7.22 leads to the following expression for H_K:

$$H_K = \frac{\big((1-\omega_2)K + \omega_2\, h_\omega\, \mathrm{K}\big) - (1-\omega_2)K}{K - (1-\omega_2)K} = h_\omega \tag{7.23}$$

It is suggested that the stiffness healing index, H_K defined in equation 7.22 is consistent with the healing parameter, h_ω in equation 7.23.

Using the same process for strength healing index, H_σ gives the following:

$$H_\sigma = \frac{(\phi_2 f_t + \omega_2 h_\omega K \Delta u) - \phi_2 f_t}{f_t - \phi_2 f_t} = \frac{\omega_2}{(1-\phi_2)} \frac{f_{th}}{f_t} h_\omega \tag{7.24}$$

in which $\Delta u = u_3 - u_2$ and the strength of the healed material is related to the change of stress in the healed proportion of material in the reloading step i.e. $f_{th} = K\Delta u$.

It is noted that, if a fully healing crack had the same strength as the virgin material and the crack was fully formed at the time of healing (i.e. $\omega = 1$ and $\phi = 0$) then H_σ would be equal to h_ω.

Appendix D: Glossary of terms

D1.1 Definition of terms

The following is a brief overview of the basic terminology and definitions used within the literature in the field of advanced material science. The material ability to self-heal essentially depends on the level of intelligence displayed (Mishahi et al. 2000; Sharp and Clemena 2004). The vast majority of materials fall into basic materials group, where they are unable to respond to stimuli (de Rooij et al. 2013).

- ***Sensory structures*** are the least intelligent structure among all. It has the capability but lacks in actuators and therefore, is not able to respond to environmental changes. Examples of sensory structures include smart paint and piezoelectric paint that have the capability to examine the remaining life of the structures due to degradations and hence, protect the metal substrate which it is applied on (Sharp and Clemena 2004).

- ***Smart structures*** are engineered composites of basic materials, which exhibit sensing and actuation properties of smart materials (Joseph 2008). Unlike intelligent materials, they can only react and respond to certain changes occurring in its surrounding environment.

- ***Smart materials*** are engineered to respond positively to stimuli and changing environments where they are able to activate compensating adjustments to fit these changes (Sharp and Clemena 2004). Examples of smart materials include magnetostrictive materials, shape-memory materials that are able to retain memory of two different shapes, smart spoons made of temperature-responsive polymers which change colour with different temperatures, piezoelectric materials that sense for weigh-in-motion and structural monitoring, and smart gels that have the ability to shrink or swell by a factor of 1000. According to Joseph (2008), the difference between an intelligent material and a smart material is the degree to which the material can gather information, process the information and react accordingly. Most of the current self-healing processes are in the midst of basic to some smart intelligence.

- ***Intelligent materials*** as defined by Mihashi et al. (2000) are materials which *'incorporate the notion of information as well as physical index such as strength and durability'*. The level of intelligence of these materials is achieved by systematic incorporation of various individual functions, hence allowing them to adapt and respond to various external stimuli. Natural materials for example, have a higher adaptability to outside environment due to their organized hierarchal structure, which are present at all levels (length scale) of the material. Given the complexity nature of these hierarchies, such materials are not currently being used in practice.

D1.2 Self-healing systems

SHCMs consist of autogenic healing (naturally) and autonomic healing (artificially) both of which are categorised as *'smart materials'* which rely on previous knowledge of the damage mechanisms. This could also further include activated repairing that can be considered as *'intelligent materials'*. The self-healing processes can be described with the following definitions by the RILEM committee TC-211 (de Rooij et al. 2013). There is usually an overlap between different self-healing systems where a combination of techniques is often employed to enhance their healing mechanisms.

- ***Autogenic healing*** *(naturally)* occurs when the recovery process uses its own material components that could otherwise be found even without the purpose for self-healing (own generic materials);

- ***Autonomic healing*** *(artificially)* occurs when the recovery process uses material components that would not otherwise be found in the material (engineered additions);

- ***Activated repairing*** using artificial devices such as sensors and actuators to promote repairing by providing supplementary materials other than those in concrete.

References

Ahn, T.H. and Kishi, T. (2010). Crack self-healing behavior of cementitious composites incorporating various mineral admixtures. *Journal of Advanced Concrete Technology* **8**(2):171–186.

Al-Tabbaa, A., Lark, B., Paine, K., Jefferson, T., Litina, C., Gardner, D. and Embley, T. (2018). Biomimetic cementitious construction materials for next-generation infrastructure. *Proceedings of the Institution of Civil Engineers - Smart Infrastructure and Construction* **171**(2):67–76.

Al-Tabbaa, A., Litina, C., Giannaros, P., Kanellopoulos, A. and Souza, L. (2019). First UK field application and performance of microcapsule-based self-healing concrete. *Construction and Building Materials* **208**:669–685.

Alderete, N., Villagrán Zaccardi, Y., Snoeck, D., Van Belleghem, B., Van den Heede, P., Van Tittelboom, K. and De Belie, N. (2019). Capillary imbibition in mortars with natural pozzolan, limestone powder and slag evaluated through neutron radiography, electrical conductivity, and gravimetric analysis. *Cement and Concrete Research* **118**(December 2018):57–68.

Alfano, G. and Sacco, E. (2006). Combining interface damage and friction in a cohesive-zone model. *International Journal for Numerical Methods in Engineering* **68**(5):542–582.

Alghamri, R., Kanellopoulos, A. and Al-Tabbaa, A. (2016). Impregnation and encapsulation of lightweight aggregates for self-healing concrete. *Construction and Building Materials* **124**:910–921.

Alghamri, R., Kanellopoulos, A., Litina, C. and Al-Tabbaa, A. (2018). Preparation and polymeric encapsulation of powder mineral pellets for self-healing cement based materials. *Construction and Building Materials* **186**:247–262.

American Concrete Institute (2010). Report Chemical Admixtures for Concrete, https://www.concrete.org/ [Accessed 25 April 2019].

Araújo, M., Chatrabhuti, S., Gurdebeke, S., Alderete, N., Van Tittelboom, K., Raquez, J.M., Cnudde, V., Van Vlierberghe, S. and Gruyaert, E. (2018). Poly(methyl methacrylate) capsules as an alternative to the proof-of-concept'' glass capsules used in self-healing concrete. *Cement and Concrete Composites* **89**:260–271.

Baroghel-Bouny, V., Mainguy, M., Lassabatere, T. and Coussy, O. (1999). Characterization and identification of equilibrium and transfer moisture properties for ordinary and high-performance cementitious materials. *Cement and Concrete Research* **29**(8):1225–1238.

Basaran Bundur, Z., Kirisits, M.J. and Ferron, R.D. (2015). Biomineralized cement-based materials: Impact of inoculating vegetative bacterial cells on hydration and strength. *Cement and Concrete Research* **67**:237–245.

Bazant, Z.P. and Gettu, R. (1992). Rate effects and load relaxation in static fracture of concrete. *ACI Materials Journal* **89**(5):457–468.

Bažant, Z.P. and Najjar, L.J. (1972). Nonlinear water diffusion in nonsaturated concrete. *Matériaux et Constructions* **5**(1):3–20.

Beglarigale, A., Seki, Y., Demir, N.Y. and Yazıcı, H. (2018). Sodium silicate/polyurethane microcapsules used for self-healing in cementitious materials: Monomer optimization, characterization, and fracture behavior. *Construction and Building Materials* **162**(December 2017):57–64.

De Belie, N., Gruyaert, E., Al-Tabbaa, A., Antonaci, P., Baera, C., Bajare, D., Darquennes, A., Davies, R., Ferrara, L., Jefferson, T., Litina, C., Miljevic, B., Otlewska, A., Ranogajec, J., Roig-Flores, M., Paine, K., Lukowski, P., Serna, P., Tulliani, J.M., Vucetic, S., Wang, J. and Jonkers, H.M. (2018). A Review of Self-Healing Concrete for Damage Management of Structures. *Advanced Materials Interfaces* **5**(17):1–28.

Van Belleghem, B., Kessler, S., Van den Heede, P., Van Tittelboom, K. and De Belie, N. (2018). Chloride induced reinforcement corrosion behavior in self-healing concrete with encapsulated polyurethane. *Cement and Concrete Research* **113**(December 2017):130–139.

Van Belleghem, B., Montoya, R., Dewanckele, J., Van Den Steen, N., De Graeve, I., Deconinck, J., Cnuddle, V., Van Tittelboom, K. and De Belie, N. (2016). Capillary water absorption in cracked and uncracked mortar - A comparison between experimental study and finite element analysis. *Construction and Building Materials* **110**:154–162.

Biomedical Imaging Group (2019). Drop Snake Analysis, http://bigwww.epfl.ch/demo/dropanalysis/, 2013 [Accessed 15 October 2018].

Blake, T.D. (2006). The physics of moving wetting lines. *Journal of Colloid and Interface Science* **299**(1):1–13.

Blake, T.D. and Shikhmurzaev, Y.D. (2002). Dynamic wetting by liquids of different viscosity. *Journal of Colloid and Interface Science* **253**(1):196–202.

Borg, R.P., Cuenca, E., Gastaldo Brac, E.M. and Ferrara, L. (2018). Crack sealing capacity in chloride-rich environments of mortars containing different cement substitutes and crystalline admixtures. *Journal of Sustainable Cement-Based Materials* **7**(3):141–159.

Bracke, M., De Voeght, F. and Joos, P. (1989). The kinetics of wetting: the dynamic contact angle. *Progress in Colloid and Polymer Science* **79**:142–149.

van Breugel, K. (2007). Is there a market for self-healing cement-based materials? *1St International Conference on Self-Healing Materials*(April):1–9.

van Breugel, K. (2012). Self-healing material concepts as solution for aging infrastructure. *37th Conference on Our World in Concrete & Structures*:1–17. doi: https://doi.org/100037009.

British Standard Institution (2004). BS EN 1992-1-1:2004 Eurocode 2: Design of Concrete Structures – Part 1-1: General Rules and Rules of Buildings. London, UK: BSI.

Brookes, A. and Craston, D. (1999). The application of Raman Spectroscopy to reacting systems. The Internet Journal of Vibration Spectroscopy **3**(3).

Cailleux, E. and Pollet, V. (2009). Investigations on the development of self-healing properties in protective coatings for concrete and repair mortars. *2nd International Conference on Self Healing Materials* **32**(0):1–4.

Cambridge Polymer Group (2004). Determination of the kinetics of curing of cyanoacrylate-based adhesives with Fourier Transform Infrared Spectroscopy. *Cambridge Polymer Group, Inc*.

Castro, J.M. and Macosko, C.W. (1980). Kinetics and rheology of typical polyurethane reaction injection molding systems. *Society of Plastics Engineers*:434–438.

Chen, P.W., Brignoli, J. and Studart, A.R. (2014). Mechanics of thick-shell microcapsules made by microfluidics. *Polymer* **55**(26):6837–6843.

Chen, P.W., Erb, R.M. and Studart, A.R. (2012). Designer polymer-based microcapsules made using microfluidics. *Langmuir* **28**(1):144–152.

Chitez, A.S. and Jefferson, A.D. (2016). A coupled thermo-hygro-chemical model for characterising autogenous healing in ordinary cementitious materials. *Cement and Concrete Research* **88**:184–197.

Collins, F. and Sanjayan, J. (2008). Unsaturated capillary flow within alkali activated slag concrete. *Journal of Materials in Civil Engineering* **20**(9):565–570.

Collins, J.A., Pani, K.C., Lehman, R.A. and Leonard, F. (1966). Biological Substrates and Cure Rates of Cyanoacrylate Tissue Adhesives. *Archives of Surgery* **93**(3):428–432.

Comyn, J. (1998). Moisture cure of adhesives and sealants. *International Journal of Adhesion and Adhesives* **18**(4):247–253.

Cox, R. G. (1986). The dynamics of the spreading of liquids on a solid surface. Part 1. Viscous flow. *Journal of Fluid Mechanics* **168**:169–194.

Crossin, E. (2015). The greenhouse gas implications of using ground granulated blast furnace slag as a cement substitute. *Journal of Cleaner Production* **95**:101–108.

Cuenca, E., Tejedor, A. and Ferrara, L. (2018). A methodology to assess crack-sealing effectiveness of crystalline admixtures under repeated cracking-healing cycles. *Construction and Building Materials* **179**:619–632.

Currie, R.J. and Crammond, N.J. (1994). Assessment of existing high alumina cement construction in the UK. *Proceedings of the Institution of Civil Engineers: Structures and Buildings* **104**(1):83–92.

Cyanotec (2019). Technical Data Sheet for Procure PC20, http://www.gluesdirect.co.uk/catalog/product_info.php?products_id=151,%202016 [Accessed 5 July 2019].

Darquennes, A., Olivier, K., Benboudjema, F. and Gagné, R. (2016). Self-healing at early-age, a way to improve the chloride resistance of blast-furnace slag cementitious materials. *Construction and Building Materials* **113**:1017–1028.

Datta, S.S., Abbaspourrad, A., Amstad, E., Fan, J., Kim, S.H., Romanowsky, M., Shum, H.C., Sun, B., Utada, A.S., Windbergs, M., Zhou, S. and Weitz, D.A. (2014). 25th anniversary article: Double emulsion templated solid microcapsules: Mechanics and controlled release. *Advanced Materials* **26**(14):2205–2218.

Davidovits, J. (2010). Geopolymer Cement and Mitigation of Global Warming, http://www.geopolymer.org/applications/global-warming/ [Accessed: 15 September 2018].

Davies, R., Jefferson, A., Lark, R. and Gardner, D. (2015). A novel 2D vascular network in cementitious materials. *Concrete - Innovation and Design: fib Symposium Proceedings*:249–250.

Davies, R., Pilegis, M., Kanellopoulos, A., Sharma, T., Teall, O., Gardner, D., Jefferson, T. and Lark, R. (2016). Multi-scale cementitious self-healing systems and their application in concrete structures. *Proceedings of the 9th International Concrete Conference 2016 – Environment, Efficiency and Economic Challenges for Concrete*, Dundee, UK.

Davies, R., Teall, O., Pilegis, M., Kanellopoulos, A., Sharma, T., Jefferson, A., Gardner, D., Al-Tabbaa, A., Paine, K. and Lark, R. (2018). Large scale application of self-healing concrete: Design, construction, and testing. *Frontiers in Materials* **5**(September):1–12.

Department of Trade and Industry (2014). Construction Statistics Annual Report. London: TSO.

Dejonghe, P., De Belie, N., Steuperaert, S. and Snoeck, D. (2011). The behaviour of superabsorbing polymers as a sealing agent in concrete: Absorption kinetics, degradation and water permeability. *Proceedings on the 3rd International Conference on Self-healing Materials*, Bath, United Kingdom, 27-

29 June 2011.

Djerbi, A., Bonnet, S., Khelidj, A. and Baroghel-bouny, V. (2008). Influence of traversing crack on chloride diffusion into concrete. *Cement and Concrete Research* **38**(6):877–883.

Dong, B., Ding, W., Qin, S., Han, N., Fang, G., Liu, Y., Xing, F. and Hong, S. (2018). Chemical self-healing system with novel microcapsules for corrosion inhibition of rebar in concrete. *Cement and Concrete Composites* **85**:83–91.

Dry, C. (1994). Matrix cracking repair and filling using active and passive modes for smart timed release of chemicals from fibers into cement matrices. *Smart Materials and Structures* **3**(2):118–123.

Dry, C., Corsaw, M. and Bayer, E. (2003). A comparison of internal self-repair with resin injection in repair of concrete. *Journal of Adhesion Science and Technology* **17**(1):79–89.

Dry, C. and McMillan, W. (1996). Three-part methylmethacrylate adhesive system as an internal delivery system for smart responsive concrete. *Smart Materials and Structures* **5**(3):297–300.

Dry, C.M. (2000). Three designs for the internal release of sealants, adhesives, and waterproofing chemicals into concrete to reduce permeability. *Cement and Concrete Research* **30**(12):1969–1977.

Edvardsen, C. (1999). Water permeability and autogenous healing of cracks in concrete. *ACI Materials Journal-American Concrete Institute* **96**(4):448–454.

Edwards, H.G.M. and Day, J.S. (2004). Fourier transform Raman spectroscopic studies of the curing of cyanoacrylate glue. *Journal of Raman Spectroscopy* **35**(7):555–560.

Ersan, Y.C., Palin, D., Yengec Tasdemir, S.B., Tasdemir, K., Jonkers, H.M., Boon, N. and De Belie, N. (2018). Volume fraction, thickness, and permeability of the sealing layer in microbial self-healing concrete containing biogranules. *Frontiers in Built Environment* **4**(November):1–11.

European Cement Association (2017). Key facts and figures, https://cembureau.eu/ [Accessed 15 May 2019].

European Commission DG (2018). A new approach to evaluating the sustainability of substituting raw materials: Science for Environmental Policy.

Farrugia, C., Borg, R.P., Ferrara, L. and Buhagiar, J. (2019). The application of Lysinibacillus sphaericus for surface treatment and crack healing in mortar. *Frontiers in Built Environment* **5**(May):1–10.

Feiteira, J., Gruyaert, E. and De Belie, N. (2016). Self-healing of moving cracks in concrete by means of encapsulated polymer precursors. *Construction and Building Materials* **102**:671–678.

Feiteira, J., Tsangouri, E., Gruyaert, E., Lors, C., Louis, G. and De Belie, N. (2017). Monitoring crack movement in polymer-based self-healing concrete through digital image correlation, acoustic emission analysis and SEM in-situ loading. *Materials and Design* **115**:238–246.

Ferrara, L. (2018). Self-healing cement-based materials: An asset for sustainable construction industry. *IOP Conference Series: Materials Science and Engineering* **442**(1):0–12.

Ferrara, L., Cuenca, E., Tejedor, A. and Brac, E.G. (2018b). Performance of concrete with and without crystalline admixtures under repeated cracking/healing cycles. *MATEC Web of Conferences* **199**.

Ferrara, L., Krelani, V. and Carsana, M. (2014). A 'fracture testing' based approach to assess crack healing of concrete with and without crystalline admixtures. *Construction and Building Materials* **68**:535–551.

Ferrara, L., Krelani, V. and Moretti, F. (2016a). On the use of crystalline admixtures in cement based construction materials: From porosity reducers to promoters of self healing. *Smart Materials and*

Structures **25**(8).

Ferrara, L., Krelani, V. and Moretti, F. (2016b). Autogenous healing on the recovery of mechanical performance of high performance fibre reinforced cementitious composites (HPFRCCs): Part 2 - Correlation between healing of mechanical performance and crack sealing. *Cement and Concrete Research* **73**:299–315.

Ferrara, L., Krelani, V., Moretti, F., Roig Flores, M. and Serna Ros, P. (2017). Effects of autogenous healing on the recovery of mechanical performance of High Performance Fibre Reinforced Cementitious Composites (HPFRCCs): Part 1. *Cement and Concrete Composites* **83**:76–100.

Ferrara, L., Van Mullem, T., Alonso, M.C., Antonaci, P., Borg, R.P., Cuenca, E., Jefferson, A., Ng, P.L., Peled, A., Roig-Flores, M., Sanchez, M., Schroefl, C., Serna, P., Snoeck, D., Tulliani, J.M. and De Belie, N. (2018a). Experimental characterization of the self-healing capacity of cement based materials and its effects on the material performance: A state of the art report by COST Action SARCOS WG2. *Construction and Building Materials* **167**:115–142.

Formia, A., Irico, S., Bertola, F., Canonico, F., Antonaci, P., Pugno, N.M. and Tulliani, J.M. (2016). Experimental analysis of self-healing cement-based materials incorporating extruded cementitious hollow tubes. *Journal of Intelligent Material Systems and Structures* **27**(19):2633–2652.

Formia, A., Terranova, S., Antonaci, P., Pugno, N.M. and Tulliani, J.M. (2015). Setup of extruded cementitious hollow tubes as containing/releasing devices in self-healing systems. *Materials* **8**(4):1897–1923.

Freeman, B.L. and Jefferson, A.D. (2019). The simulation of transport processes in cementitious materials with embedded healing systems. *International Journal for Numerical and Analytical Methods in Geomechanics*:1–34.

Gardner, D., Herbert, D., Jayaprakash, M., Jefferson, A. and Paul, A. (2017). Capillary flow characteristics of an autogenic and autonomic healing agent for self-healing concrete. *Journal of Materials in Civil Engineering* **29**(11).

Gardner, D., Jefferson, A. and Hoffman, A. (2012). Investigation of capillary flow in discrete cracks in cementitious materials. *Cement and Concrete Research* **42**(7):972–981.

Gardner, D., Jefferson, A., Hoffman, A. and Lark, R. (2014). Simulation of the capillary flow of an autonomic healing agent in discrete cracks in cementitious materials. *Cement and Concrete Research* **58**:35–44.

Gardner, D., Lark, R., Jefferson, T. and Davies, R. (2018). A survey on problems encountered in current concrete construction and the potential benefits of self-healing cementitious materials. *Case Studies in Construction Materials* **8**(January):238–247.

Gardner, D.R., Lark, R.J. and Barr, B. (2005). Effect of conditioning temperature on the strength and permeability of normal- and high-strength concrete. *Cement and Concrete Research* **35**(7):1400–1406.

Gartner, E. (2004). Industrially interesting approaches to 'low-CO2' cements. *Cement and Concrete Research* **34**(9):1489–1498.

Ghosh, P., Mandal, S., Chattopadhyay, B.D. and Pal, S. (2005). Use of microorganism to improve the strength of cement mortar. *Cement and Concrete Research* **35**(10):1980–1983.

Gilabert, F.A., Van Tittelboom, K., Van Stappen, J., Cnudde, V., De Belie, N. and Van Paepegem, W. (2017). Integral procedure to assess crack filling and mechanical contribution of polymer-based healing agent in encapsulation-based self-healing concrete. *Cement and Concrete Composites* **77**:68–80.

GIMP (2019). GNU Image Manupulation Programme. https://www.gimp.org/ [Accessed 25 May 2017].

Gopalaratnam, V. and Shah, S. (1985). Softening response of plain concrete in direct tension. *ACI Structural Journal* **82**:310–323.

Granger, S., Loukili, A., Pijaudier-Cabot, G. and Chanvillard, G. (2007). Experimental characterization of the self-healing of cracks in an ultra high performance cementitious material: Mechanical tests and acoustic emission analysis. *Cement and Concrete Research* **37**(4):519–527.

Gruyaert, E., Debbaut, B., Snoeck, D., Díaz, P., Arizo, A., Tziviloglou, E., Schlangen, E. and De Belie, N. (2016). Self-healing mortar with pH-sensitive superabsorbent polymers: Testing of the sealing efficiency by water flow tests. *Smart Materials and Structures* **25**(8).

Hazelwood, T. (2015). Investigation of a Novel Self-Healing Cementitious Composite Material System PhD Thesis, Cardiff University.

Hearn, N. (1998). Self-sealing, autogenous healing and continued hydration: What is the difference? *Materials and Structures/Materiaux et Constructions* **31**(212):563–567.

Van den Heede, P., Van Belleghem, B., Alderete, N., Van Tittelboom, K. and De Belie, N. (2016). Neutron radiography based visualization and profiling of water uptake in (Un)cracked and autonomously healed cementitious materials. *Materials* **9**(5).

ter Heide, N. and Schlangen, E. (2007). Self-healing of Early Age Cracks in Concrete. *Proceedings of the First International Conference on Self-healing Materials*, Noordwijk aan Zee, The Netherlands.

Hoffman, R.L. (1975). A study of the advancing interface. I. Interface shape in liquid-gas systems. Journal of Colloid and Interface Science **50**(2):228–241.

Homma, D., Mihashi, H. and Nishiwaki, T. (2009). Self-healing capability of fibre reinforced cementitious composites. *Journal of Advanced Concrete Technology* **7**(2):217–228.

Hu, J., Ren, Q., Jiang, Q., Gao, R., Zhang, L. and Luo, Z. (2018). Strength characteristics and the reaction mechanism of stone powder cement tailings backfill. *Advances in Materials Science and Engineering* **2018**.

Huang, H. and Ye. G. (2011). Application of sodium silicate solution as self-healing agent in cementitious materials. *Proceedings of the International Conference on Advances in Construction Materials through Science and Engineering*, Hong Kong, China.

Huang, H., Ye, G., Qian, C. and Schlangen, E. (2016). Self-healing in cementitious materials: Materials, methods and service conditions. *Materials and Design* **92**:499–511.

Huang, H., Ye, G. and Shui, Z. (2014). Feasibility of self-healing in cementitious materials - By using capsules or a vascular system? *Construction and Building Materials* **63**:108–118.

Hyde, G.W. and Smith, W.J. (1889). Results of experiments made to determine the permeability of cement and cement mortars. *Journal of the Franklin Institute*.

International Energy Agency (2018). Technology Roadmap - Low-Carbon Transition in the Cement Industry.

Isaacs, B., Lark, R., Jefferson, T., Davies, R. and Dunn, S. (2013). Crack healing of cementitious materials using shrinkable polymer tendons. *Structural Concrete* **14**(2):138–147.

Jacobsen, S., Marchand, J. and Boisvert, L. (1996). Effect of cracking and healing on chloride transport in OPC concrete. *Cement and Concrete Research* **26**(6):869–881.

Jacobsen, J.S., Poulsen, P.N. and Olesen, J.F. (2012). Characterization of mixed mode crack opening in concrete. *Materials and Structures/Materiaux et Constructions* **45**(1–2):107–122.

Jefferson, A., Joseph, C., Lark, R., Isaacs, B., Dunn, S. and Weager, B. (2010). A new system for crack closure of cementitious materials using shrinkable polymers. *Cement and Concrete Research* **40**(5):795–801.

Jefferson, A.D. and Freeman, B.L. (2020). The simulation of cracking and healing events in cementitious materials with embedded healing systems.

Jefferson, T., Javierre, E., Freeman, B., Zaoui, A., Koenders, E. and Ferrara, L. (2018). Research Progress on Numerical Models for Self-Healing Cementitious Materials. *Advanced Materials Interfaces* **5**(17):1–19.

Jefferson, A.D. and Mihai, I.C. (2015). The simulation of crack opening-closing and aggregate interlock behaviour in finite element concrete models. *International Journal for Numerical Methods in Engineering* **104**:48–78.

Jiang, T., Oh. S. and Slattery, J.C. (1979). Correlation for dynamic contact angle. *Journal of Colloid and Interface Science* **68**:74–77.

Jones, R., Mccarthy, M. and Newlands, M. (2011). Fly ash route to low embodied CO_2 and implications for concrete construction. *World of Coal Ash (WOCA) Conference*.

Jonkers, H.M. (2007). *Self-healing Concrete: A Biological Approach. In Self-healing Materials – An Alternative Approach to 20 Centuries of Material Science*, Springer, The Netherlands.

Jonkers, H.M. (2011). Bacteria-based self-healing concrete. *Heron* **56**:1–12.

Jonkers, H.M., Thijssen, A., Muyzer, G., Copuroglu, O. and Schlangen, E. (2010). Application of bacteria as self-healing agent for the development of sustainable concrete. *Ecological Engineering* **36**(2):230–235.

Joseph, C. (2008). Experimental and numerical study of the fracture and self-healing of cementitious materials. PhD Thesis, Cardiff University.

Joseph, C., Gardner, D., Jefferson, T., Isaacs, B. and Lark, B. (2011). Self-healing cementitious materials: A review of recent work. *Proceedings of Institution of Civil Engineers: Construction Materials* **164**(1):29–41.

Joseph, C., Jefferson, A.D., Isaacs, B., Lark, R. and Gardner, D. (2010). Experimental investigation of adhesive-based self-healing of cementitious materials. *Magazine of Concrete Research* **62**(11):831–843.

Kanellopoulos, A., Giannaros, P. and Al-Tabbaa, A. (2016). The effect of varying volume fraction of microcapsules on fresh, mechanical and self-healing properties of mortars. *Construction and Building Materials* **122**:577–593.

Kanellopoulos, A., Giannaros, P., Palmer, D., Kerr, A. and Al-Tabbaa, A. (2017). Polymeric microcapsules with switchable mechanical properties for self-healing concrete: Synthesis, characterisation and proof of concept. *Smart Materials and Structures* **26**(4).

Kanellopoulos, A., Qureshi, T.S. and Al-Tabbaa, A. (2015). Glass encapsulated minerals for self-healing in cement based composites. *Construction and Building Materials* **98**:780–791.

Karihaloo, B.L. (1995). *Fracture mechanics and structural concrete*, Longman Scientific & Technical, New York.

Katti, D. and Krishnamurti, N. (1999). Anionic polymerization of alkyl cyanoacrylates: In vitro model studies for in vivo applications. *Journal of Applied Polymer Science* **74**(2):336–344.

Kennett, S. (2009). Green Cement: An Industry Revolution, https://www.building.co.uk/green-cement-an-industry-revolution?/3133227.article [Accessed: 10 December 2018].

Kim, J.S. and Schlangen, E. (2011). Self-healing in ECC stimulated by SAP under flexural cyclic load. *Proceedings of 3rd International Conference on Self Healing Materials, Bath, UK*(June):27–29.

Kishi, T., Ahn, T., Hosoda, A., Suzuki, S. and Takaoka, H. (2007). Self-Healing Behaviour By Cementitious Recrystallization of Cracked Concrete Incorporating Expansive Agent. *First International Conference on Self Healing Materials*(April):1–10.

Kuang, Y. and Ou, J. (2008a). Self-repairing performance of concrete beams strengthened using superelastic SMA wires in combination with adhesives released from hollow fibers. *Smart Materials and Structures* **17**(2):0–7.

Kuang, Y. and Ou, J. (2008b). Passive smart self-repairing concrete beams using shape memory alloy wires and fibers containing adhesives. *Journal of Central South University* **15**:411–417.

Kusaka, I. and Suëtaka, W. (1980). Infrared spectrum of α-cyanoacrylate adhesive in the first monolayer on a bulk aluminum surface. *Spectrochimica Acta Part A: Molecular Spectroscopy* **36**(7):647–648.

Lee, H.X.D., Wong, H.S. and Buenfeld, N.R. (2010). Potential of superabsorbent polymer for self-sealing cracks in concrete. *Advances in Applied Ceramics* **109**(5):296–302.

Lee, H.X.D., Wong, H.S. and Buenfeld, N.R. (2016). Self-sealing of cracks in concrete using superabsorbent polymers. *Cement and Concrete Research* **79**(January 2016):194–208.

Lepech, M.D. and Li, V.C. (2009). Water permeability of engineered cementitious composites. *Cement and Concrete Composites* **31**(10):744–753.

Li, C., Sun, H. and Li, L. (2010). A review: The comparison between alkali-activated slag (Si + Ca) and metakaolin (Si + Al) cements. *Cement and Concrete Research* **40**(9):1341–1349.

Li, F., Yuan, Y. and Li, C. Q. (2011). Corrosion propagation of prestressing steel strands in concrete subject to chloride attack. *Construction and Building Materials* **25**:3878–3885.

Li, M. and Li, V.C. (2011). Cracking and healing of engineered cementitious composites under chloride environment. *ACI Materials Journal* **108**(3):333–340.

Li, V.C., Lim, Y.M. and Chan, Y.W. (1998). Feasibility study of a passive smart self-healing cementitious composite. *Composites Part B: Engineering* **29**(6):819–827.

Li, V.C., Lepech, M., Wang, S., Weimann, M. and Keoleian, G. (2004). Development of green ECC for sustainable infrastructure systems. *Proceedings of the International Workshop on Sustainable Development and Concrete Technology*, Beijing, China:181–192.

Li, W., Jiang, Z. and Yang, Z. (2017). Acoustic characterization of damage and healing of microencapsulation-based self-healing cement matrices. *Cement and Concrete Composites* **84**:48–61.

Li, W., Jiang, Z., Yang, Z., Zhao, N. and Yuan, W. (2013). Self-healing efficiency of cementitious materials containing microcapsules filled with healing adhesive: Mechanical restoration and healing process monitored by water absorption. *PLoS ONE* **8**(11):1–18.

Liu, S., Bundur, Z.B., Zhu, J. and Ferron, R.D. (2016). Evaluation of self-healing of internal cracks in biomimetic mortar using coda wave interferometry. *Cement and Concrete Research* **83**:70–78.

Lv, Leyang, Schlangen, E., Yang, Z. and Xing, F. (2016). Micromechanical properties of a new polymeric microcapsule for self-healing cementitious materials. *Materials* **9**(12):1–16.

Lv, L., Yang, Z., Chen, G., Zhu, G., Han, N., Schlangen, E. and Xing, F. (2016). Synthesis and characterization of a new polymeric microcapsule and feasibility investigation in self-healing cementitious materials. *Construction and Building Materials* **105**:487–495.

Ma, H., Qian, S. and Zhang, Z. (2014). Effect of self-healing on water permeability and mechanical property of Medium-Early-Strength Engineered Cementitious Composites. *Construction and Building Materials* **68**:92–101.

Maes, M., Van Tittelboom, K. and De Belie, N. (2014). The efficiency of self-healing cementitious materials by means of encapsulated polyurethane in chloride containing environments. *Construction and Building Materials* **71**:528–537.

van Mier, J.C.W. (1997). *Fracture Processes of Concrete*, first ed., CRC Press, London.

Mignon, A., Vermeulen, J., Snoeck, D., Dubruel, P., Van Vlierberghe, S. and De Belie, N. (2017). Mechanical and self-healing properties of cementitious materials with pH-responsive semi-synthetic superabsorbent polymers. *Materials and Structures/Materiaux et Constructions* **50**(6):1–12.

Mihashi, H., Kaneko, Y., Nishiwaki, T. and Otsuka, K. (2000). Fundamental study on development of intelligent concrete characterized by self-healing capability for strength. *Transactions of the Japan Concrete Institute* **22**:441–450.

Minnebo, P., Thierens, G., De Valck, G., Van Tittelboom, K., Belie, N. De, Van Hemelrijck, D. and Tsangouri, E. (2017). A novel design of autonomously healed concrete: Towards a vascular healing network. *Materials* **10**(1):1–23.

Mostavi, E., Asadi, S., Hassan, M.M. and Alansari, M. (2015). Evaluation of self-healing mechanisms in concrete with double-walled sodium silicate microcapsules*. Journal of Materials in Civil Engineering* **27**(12):1–8.

Van Mourik, S., Veldman, A.E.P. and Dreyer, M.E. (2005). Simulation of capillary flow with a dynamic contact angle. *Microgravity Science and Technology* **17**(3):87–94.

Muhammad, N.Z., Shafaghat, A., Keyvanfar, A., Majid, M.Z.A., Ghoshal, S.K., Mohammadyan Yasouj, S.E., Ganiyu, A.A., Kauchaksaraei, M.S., Kamyab, H., Taheri, M.M., Shirdar, M.R. and McCaffer, R. (2016). Tests and methods of evaluating the self-healing efficiency of concrete: A review. *Construction and Building Materials* **112**:1123–1132.

Van Mullem, T., Gruyaert, E., Debbaut, B., Caspeele, R. and De Belie, N. (2019). Novel active crack width control technique to reduce the variation on water permeability results for self-healing concrete. *Construction and Building Materials* **203**:541–551.

Naqi, A. and Jang, J.G. (2019). Recent progress in green cement technology utilizing low-carbon emission fuels and raw materials: A review. *Sustainability (Switzerland)* **11**(2).

De Nardi, C., Bullo, S., Ferrara, L., Ronchin, L. and Vavasori, A. (2017b). Effectiveness of crystalline admixtures and lime/cement coated granules in engineered self-healing capacity of lime mortars. *Materials and Structures/Materiaux et Constructions* **50**(4).

De Nardi, C., Cecchi, A. and Ferrara, L. (2018). Assessing the influence of self-healing capacity of lime-based mortars on brick-mortar interface strength in masonry units. *MATEC Web of Conferences* **199**.

De Nardi, C., Cecchi, A., Ferrara, L., Benedetti, A. and Cristofori, D. (2017a). Effect of age and level of damage on the autogenous healing of lime mortars. *Composites Part B: Engineering* **124**:144–157.

Neville, A.M. (2012). *Properties of Concrete*, fifth ed., Prentice Hall, London.

Newlands, M.D. and Paine, K.A. (2010). Research Collaboration: Sustainable high performance concrete infrastructure. *Indian Concrete Journal* **84**(10):25–26.

Nishiwaki, T., Kwon, S., Homma, D., Yamada, M. and Mihashi, H. (2014). Self-healing capability of fiber-reinforced cementitious composites for recovery of watertightness and mechanical properties. *Materials* **7**(3):2141–2154.

Nishiwaki, T., Mihashi, H., Jang, B.K. and Miura, K. (2006). Development of self-healing system for concrete with selective heating around crack. *Journal of Advanced Concrete Technology* **4**(2):267–275.

Office of National Statistic (2019). Construction output in Great Britain: April 2019, https://www.ons.gov.uk [Accessed 15 April 2019].

Olivier, K., Darquennes, A., Benboudjema, F. and Gagné, R. (2016). Early-age self-healing of cementitious materials containing ground granulated blast-furnace slag under water curing. *Journal of Advanced Concrete Technology* **14**(11):717–727.

Van Oss, H.G. (2005). Background Facts and Issues Concerning Cement and Cement Data Open-File Report 2005-1152.

Østergaard, L., Olesen, J.F. and Poulsen, P.N. (2007). Biaxial testing machine for mixed mode cracking of concrete. *Proceedings of the Fracture Mechanics of Concrete and Concrete Structures: New Trends in Fracture Mechanics of Concretes*, The Netherlands:263–270.

Özbay, E., Şahmaran, M., Yücel, H.E., Erdem, T.K., Lachemi, M. and Li, V.C. (2013a). Effect of sustained flexural loading on self-healing of engineered cementitious composites. *Journal of Advanced Concrete Technology* **11**(5):167–179.

Özbay, E., Şahmaran, M., Lachemi, M. and Yücel, H.E. (2013b). Self-Healing of Microcracks in High-Volume Fly-Ash-Incorporated Engineered Cementitious Composites. *ACI Materials Journal* **110**(1):33–43.

Paine, K. (2016). Bacteria-Based Self-Healing of Concrete: Effects of Environment, Exposure and Crack Size. *Proceedings of the RILEM Conference on Microorganisms-Cementitious Materials Interactions*(1):1–15.

Palin, D., Wiktor, V. and Jonkers, H.M. (2015). Autogenous healing of marine exposed concrete: Characterization and quantification through visual crack closure. *Cement and Concrete Research* **73**:17–24.

Palin, D., Wiktor, V. and Jonkers, H.M. (2017). A bacteria-based self-healing cementitious composite for application in low-temperature marine environments. *Biomimetics* **2**(13).

Pareek, S., Shrestha, K.C., Suzuki, Y., Omori, T., Kainuma, R. and Araki, Y. (2014). Feasibility of externally activated self-repairing concrete with epoxy injection network and Cu-Al-Mn superelastic alloy reinforcing bars. *Smart Materials and Structures* **23**(10).

Pelletier, M. (2019). Smart Concrete, https://www.archdaily.com/62357/smart-concrete-michelle-pelletier [Accessed 5 June 2018].

Perez, G., Erkizia, E., Gaitero, J.J., Kaltzakorta, I., Jiménez, I. and Guerrero, A. (2015). Synthesis and characterization of epoxy encapsulating silica microcapsules and amine functionalized silica nanoparticles for development of an innovative self-healing concrete. *Materials Chemistry and Physics* **165**:39–48.

Pilegis, M., Teall, O., Hazelwood, T., Jefferson, A., Gardner, D. and Lark, R. (2015). Delayed concrete

prestressing with shape memory polymer tendons; *Concrete - Innovation and Design: fib Symposium Proceedings*:247–248.

Qian, S., Zhou, J., de Rooij, M.R., Schlangen, E., Ye, G. and van Breugel, K. (2009). Self-healing behavior of strain hardening cementitious composites incorporating local waste materials. *Cement and Concrete Composites* **31**(9):613–621.

Qian, S.Z., Zhou, J. and Schlangen, E. (2010). Influence of curing condition and precracking time on the self-healing behavior of Engineered Cementitious Composites. *Cement and Concrete Composites* **32**(9):686–693.

Qureshi, T., Kanellopoulos, A. and Al-Tabbaa, A. (2018). Autogenous self-healing of cement with expansive minerals-I: Impact in early age crack healing. *Construction and Building Materials* **192**:768–784.

Qureshi, T., Kanellopoulos, A. and Al-Tabbaa, A. (2019). Autogenous self-healing of cement with expansive minerals-II: Impact of age and the role of optimised expansive minerals in healing performance. *Construction and Building Materials* **194**:266–275.

Qureshi, T.S., Kanellopoulos, A. and Al-Tabbaa, A. (2016). Encapsulation of expansive powder minerals within a concentric glass capsule system for self-healing concrete. *Construction and Building Materials* **121**:629–643.

Ramachandran, S.K., Ramakrishnan, V. and Bang, S.S. (2001). Remediation of Concrete Using Micro-organisms. *ACI Materials Journal* **98**:3–9.

Ranaivomanana, H., Verdier, J., Sellier, A. and Bourbon, X. (2013). Sealing process induced by carbonation of localized cracks in cementitious materials. *Cement and Concrete Composites* **37**(1):37–46.

Reinhardt, H.W. (1981). Similitude of brittle fracture of structural concrete. *Proceedings of the IABSE Colloquium Advanced Mechanics of Reinforced Concrete*, Delft, The Netherlands:201–210.

Reinhardt, H.W. and Jooss, M. (2003). Permeability and self-healing of cracked concrete as a function of temperature and crack width. *Cement and Concrete Research* **33**(7):981–985.

Reynolds, S., Oxley, D.P. and Pritchard, R.G. (1982). An adhesive study by electron tunnelling: Ethyl α-cyanoacrylate adsorbed on an oxidized aluminium surface. Spectrochimico Ado **38A**(1):103–111.

Roig-Flores, M., Moscato, S., Serna, P. and Ferrara, L. (2015). Self-healing capability of concrete with crystalline admixtures in different environments. *Construction and Building Materials* **86**:1–11.

Roig-Flores, M., Pirritano, F., Serna, P. and Ferrara, L. (2016). Effect of crystalline admixtures on the self-healing capability of early-age concrete studied by means of permeability and crack closing tests. *Construction and Building Materials* **114**:447–457.

de Rooij, M.R., Van Tittelboom, K., De Belie, N. and Schlangen, E. (2013). *Self-Healing Phenomena in Cement-Based Materials: State-of-the-Art Report of RILEM Technical Committee 221-SHC: Self-Healing Phenomena in Cement-Based Materials*, vol. 11, Springer, Bagneux, France.

Sabir, B.B., Wild, S. and O'Farrell, M. (1998). A water sorptivity test for mortar and concrete. *Materials and Structures/Materiaux et Constructions* **31**(212):568–574.

Şahmaran, M., Keskin, S.B., Ozerkan, G. and Yaman, I.O. (2008). Self-healing of mechanically-loaded self consolidating concretes with high volumes of fly ash. *Cement and Concrete Composites* **30**(10):872–879.

Sahmaran, M., Yildirim, G. and Erdem, T.K. (2013). Self-healing capability of cementitious composites

incorporating different supplementary cementitious materials. *Cement and Concrete Composites* **35**(1):89–101.

Şahmaran, M., Yildirim, G., Noori, R., Ozbay, E. and Lachemi, M. (2015). Repeatability and pervasiveness of self-healing in engineered cementitious composites. *ACI Materials Journal* **112**(4):513–522.

Şahmaran, M., Yildirim, G., Ozbay, E., Ahmed, K. and Lachemi, M. (2014). Self-healing ability of cementitious composites: Effect of addition of pre-soaked expanded perlite. *Magazine of Concrete Research* **66**(8):409–419.

Sangadji, S. (2017). Can Self-healing Mechanism Helps Concrete Structures Sustainable? *Procedia Engineering* **171**:238–249.

Sangadji, S. and Schlangen, E. (2012). Self healing of concrete structures - Novel approach using porous network concrete. *Journal of Advanced Concrete Technology* **10**(5):185–194.

Schneider, M., Romer, M., Tschudin, M. and Bolio, H. (2011). Sustainable cement production-present and future. *Cement and Concrete Research* **41**(7):642–650.

Schwartz, A.M. and Tejada, S.B. (1972). Studies of dynamic contact angles on solids. *Journal of Colloid and Interface Science* **2**:359–375.

Scrivener, K.L., John, V.M. and Gartner, E.M. (2018). Eco-efficient cements: Potential economically viable solutions for a low-CO 2 cement-based materials industry. *Cement and Concrete Research* **114**(March):2–26.

Seebergh, J.E. and Berg, J.C. (1992). Dynamic wetting in the low capillary number regime. *Chemical Engineering Science* **47**:4455–4464.

Selvarajoo, T., Davies, R.E., Freeman, B.L. and Jefferson, A.D. (2020). Mechanical response of a vascular self-healing cementitious material system under varying loading conditions. *Construction and Building Materials*.

Sharp, S.R. and Clemena, G. (2004). State-of-the-Art Survey of Advanced Materials and Their. (November):44.

Shikhmurzaev, Y.D. (1997). Moving contact lines in liquid/liquid/solid systems. *Journal of Fluid Mechanics* **334**(March 1997):211–249.

Siad, H., Alyousif, A., Keskin, O.K., Keskin, S.B., Lachemi, M., Sahmaran, M. and Hossain, K.M.A. (2015). Influence of limestone powder on mechanical, physical and self-healing behavior of Engineered Cementitious Composites. *Construction and Building Materials* **99**:1–10.

Silva, E.F., Moreira, M., R Manzano, M.A. and Blanco, R. (2017). Case study of permeability-reducing admixture use in anti-flotation slabs: building in Brasilia, Brazil. *Journal of Building Pathology and Rehabilitation* **2**(1):1–9.

Sisomphon, K., Copuroglu, O. and Fraaij, A. (2011). Application of encapsulated lightweight aggregate impregnated with sodium monofluorophosphate as a self-healing agent in blast furnace slag mortar. *Heron* **56**(1–2):17–36.

Slepickova Kasalkova, N., Slepicka, P., Kolska, Z. and Svorcik, V. (2015). Wettability and other surface properties of modified polymers. Wetting and Wettability:324–352.

Snoeck, D. and De Belie, N. (2012). Mechanical and self-healing properties of cementitious composites reinforced with flax and cottonised flax, and compared with polyvinyl alcohol fibres. *Biosystems Engineering* **111**(4):325–335.

Snoeck, D. and De Belie, N. (2015). From straw in bricks to modern use of microfibers in cementitious composites for improved autogenous healing - A review. *Construction and Building Materials* **95**:774–787.

Snoeck, D. and De Belie, N. (2016). Repeated autogenous healing in strain-hardening cementitious composites by using superabsorbent polymers. *Journal of Materials in Civil Engineering* **28**(1): 04015086.

Snoeck, D. and De Belie, N. (2019). Autogenous healing in strain-hardening cementitious materials with and without superabsorbent polymers: An 8-year study. *Frontiers in Materials* **6**(March):1–12.

Snoeck, D., Dewanckele, J., Cnudde, V. and De Belie, N. (2016). X-ray computed microtomography to study autogenous healing of cementitious materials promoted by superabsorbent polymers. *Cement and Concrete Composites* **65**:83–93.

Snoeck, D., Van den Heede, P., Van Mullem, T. and De Belie, N. (2018b). Water penetration through cracks in self-healing cementitious materials with superabsorbent polymers studied by neutron radiography. *Cement and Concrete Research* **113**(November 2017):86–98.

Snoeck, D., Pel, L. and De Belie, N. (2017). The water kinetics of superabsorbent polymers during cement hydration and internal curing visualized and studied by NMR. *Scientific Reports* **7**(1):1–14.

Snoeck, D., Schaubroeck, D., Dubruel, P. and De Belie, N. (2014b). Effect of high amounts of superabsorbent polymers and additional water on the workability, microstructure and strength of mortars with a water-to-cement ratio of 0.50. *Construction and Building Materials* **72**:148–157.

Snoeck, D., De Schryver, T. and De Belie, N. (2018a). Enhanced impact energy absorption in self-healing strain-hardening cementitious materials with superabsorbent polymers. *Construction and Building Materials* **191**:13–22.

Snoeck, D., Smetryns, P.A. and De Belie, N. (2015). Improved multiple cracking and autogenous healing in cementitious materials by means of chemically-treated natural fibres. *Biosystems Engineering* **139**(1998):87–99.

Snoeck, D., Steuperaert, S., Van Tittelboom, K., Dubruel, P. and De Belie, N. (2012). Visualization of water penetration in cementitious materials with superabsorbent polymers by means of neutron radiography. *Cement and Concrete Research* **42**(8):1113–1121.

Snoeck, Didier, Van Tittelboom, K., Steuperaert, S., Dubruel, P. and De Belie, N. (2014a). Self-healing cementitious materials by the combination of microfibres and superabsorbent polymers. *Journal of Intelligent Material Systems and Structures* **25**(1):13–24.

Soltmann, U., Nies, B. and Böttcher, H. (2011). Cements with embedded living microorganisms - A new class of biocatalytic composite materials for application in bioremediation, biotechnology. *Advanced Engineering Materials* **13**(1–2):25–31.

Song, H.W. and Kwon, S.J. (2007). Permeability characteristics of carbonated concrete considering capillary pore structure. *Cement and Concrete Research* **37**(6):909–915.

Souza, L. and Al-Tabbaa, A. (2018). Microfluidic fabrication of microcapsules tailored for self-healing in cementitious materials. *Construction and Building Materials* **184**:713–722.

Stalder, A.F., Kulik, G., Sage, D., Barbieri, L. and Hoffmann, P. (2006). A snake-based approach to accurate determination of both contact points and contact angles. *Colloids and Surfaces A: Physicochemical and Engineering Aspects* **286**(1–3):92–103.

Sun, L., Yu, W. and Ge, Q. (2011). Experimental research on the self-healing performance of micro-cracks in concrete bridge. *Advanced Materials Research* **250**:28–32.

Supino, S., Malandrino, O., Testa, M. and Sica, D. (2016). Sustainability in the EU cement industry: The Italian and German experiences. *Journal of Cleaner Production* **112**:430–442.

Teall, O., Davies, R., Pilegis, M., Kanellopoulos, A., Sharma, T., Paine, K., Jefferson, A., Lark, R., Gardner, D. and Al-Tabbaa, A. (2016). Self-healing concrete full-scale site trials. *Proceedings of the 11th fib International PhD Symposium in Civil Engineering*, FIB 2016 Balkema, Rotterdam, The Netherlands:639–646.

Teychenné, D. C., Nicholls, J. C., Franklin, R. E. and Hobbs, D. W. (1997). *Design of Normal Concrete Mixes*, second ed., Building Research Establishment, United Kingdom.

Thao, T.D.P., Johnson, T.J.S., Tong, Q.S. and Dai, P.S. (2009). Implementation of Self-healing in Concrete – Proof of Concept. *The IES Journal Part A: Civil and Structure Engineering* **2**(2)116–125.

Van Tittelboom, K. and De Belie, N. (2010). Self-healing Concrete: Suitability of Different Healing Agents. *International Journal of 3R's* **1**:12–21.

Van Tittelboom, K. and De Belie, N. (2013). *Self-Healing in Cementitious Materials - A review*. *Materials* **6**:2182–2217.

Van Tittelboom, K., De Belie, N., Lehmann, F. and Grosse, C.U. (2012b). Acoustic emission analysis for the quantification of autonomous crack healing in concrete. *Construction and Building Materials* **28**(1):333–341.

Van Tittelboom, K., De Belie, N., Van Loo, D. and Jacobs, P. (2011). Self-healing efficiency of cementitious materials containing tubular capsules filled with healing agent. *Cement and Concrete Composites* **33**(4):497–505.

Van Tittelboom, K., De Belie, N., De Muynck, W. and Verstraete, W. (2010). Use of bacteria to repair cracks in concrete. *Cement and Concrete Research* **40**(1):157–166.

Van Tittelboom, K., Gruyaert, E., Rahier, H. and De Belie, N. (2012a). Influence of mix composition on the extent of autogenous crack healing by continued hydration or calcium carbonate formation. *Construction and Building Materials* **37**:349–359.

Van Tittelboom, K., Tsangouri, E., Van Hemelrijck, D. and De Belie, N. (2015). The efficiency of self-healing concrete using alternative manufacturing procedures and more realistic crack patterns. *Cement and Concrete Composites* **57**:142–152.

Van Tittelboom, K., Wang, J., Araújo, M., Snoeck, D., Gruyaert, E., Debbaut, B., Derluyn, H., Cnudde, V., Tsangouri, E., Van Hemelrijck, D. and De Belie, N. (2016). Comparison of different approaches for self-healing concrete in a large-scale lab test. *Construction and Building Materials* **107**:125–137.

Tomlinson, S.K., Ghita, O.R., Hooper, R.M. and Evans, K.E. (2006). The use of near-infrared spectroscopy for the cure monitoring of an ethyl cyanoacrylate adhesive. *Vibrational Spectroscopy* **40**(1):133–141.

Turner, L.K. and Collins, F.G. (2013). Carbon dioxide equivalent (CO2-e) emissions: A comparison between geopolymer and OPC cement concrete. *Construction and Building Materials* **43**:125–130.

Tziviloglou, E., Wiktor, V., Wang, J., Paine, K., Alazhari, M., Richardson, A., Gueguen, M., De Belie, N., Schlangen, E. and Jonkers, H. (2016). Evaluation of experimental methodology to assess the sealing efficiency of bacteria-based self-healing mortar: round robin test. *RILEM Conference on Microorganisms-Cementitious Materials Interactions*, RILEM:156–170.

Valipour, M., Yekkalar, M., Shekarchi, M. and Panahi, S. (2014). Environmental assessment of green concrete containing natural zeolite on the global warming index in marine environments. *Journal of Cleaner Production* **65**:418–423.

Vilanova, N., Rodríguez-Abreu, C., Fernández-Nieves, A. and Solans, C. (2013). Fabrication of novel silicone capsules with tunable mechanical properties by microfluidic techniques. *ACS Applied Materials and Interfaces* **5**(11):5247–5252.

Wang, J., Dewanckele, J., Cnudde, V., Van Vlierberghe, S., Verstraete, W. and De Belie, N. (2014b). X-ray computed tomography proof of bacterial-based self-healing in concrete. *Cement and Concrete Composites* **53**:289–304.

Wang, J., Mignon, A., Snoeck, D., Wiktor, V., Van Vliergerghe, S., Boon, N. and De Belie, N. (2015). Application of modified-alginate encapsulated carbonate producing bacteria in concrete: A promising strategy for crack self-healing. *Frontiers in Microbiology* **6**(OCT):1–14.

Wang, J., Van Tittelboom, K., De Belie, N. and Verstraete, W. (2012a). Use of silica gel or polyurethane immobilized bacteria for self-healing concrete. *Construction and Building Materials* **26**(1):532–540.

Wang, J.Y., De Belie, N. and Verstraete, W. (2012b). Diatomaceous earth as a protective vehicle for bacteria applied for self-healing concrete. *Journal of Industrial Microbiology and Biotechnology* **39**(4):567–577.

Wang, J.Y., Snoeck, D., Van Vlierberghe, S., Verstraete, W. and De Belie, N. (2014a). Application of hydrogel encapsulated carbonate precipitating bacteria for approaching a realistic self-healing in concrete. *Construction and Building Materials* **68**:110–119.

Wang, J.Y., Soens, H., Verstraete, W. and De Belie, N. (2014c). Self-healing concrete by use of microencapsulated bacterial spores. *Cement and Concrete Research* **56**:139–152.

Wang, X., Fang, C., Li, D., Han, N. and Xing, F. (2018a). A self-healing cementitious composite with mineral admixtures and built-in carbonate. *Cement and Concrete Composites* **92**(March):216–229.

Wang, X., Xing, F., Zhang, M., Han, N. and Qian, Z. (2013b). Experimental study on cementitious composites embedded with organic microcapsules. *Materials* **6**(9):4064–4081.

Wang, X., Zhang, M., Xing, F. and Han, N. (2018b). Effect of a healing agent on the curing reaction kinetics and its mechanism in a self-healing system. *Applied Sciences (Switzerland)* **8**(11).

Wang, Xianfeng, Guo, Y., Su, J., Zhang, X., Han, N. and Wang, Xinyu (2018c). Microstructure and thermal reliability of microcapsules containing phase change material with self-assembled graphene/organic nano-hybrid shells. *Nanomaterials* **8**(6):1–20.

Wang, Y., Zhu, Q. and Geng, Y. (2013a). Trajectory and driving factors for GHG emissions in the Chinese cement industry. *Journal of Cleaner Production* **53**:252–260.

White, S.R., Sottos, N.R., Geubelle, P.H., Moore, J.S., Kessler, M.R., Sriram, S.R., Brown, E.N. and Viswanathan, S. (2001). Autonomic healing of polymer composites. *Nature* **409**(6822):794–797.

Wiktor, V. and Jonkers, H.M. (2011). Quantification of crack-healing in novel bacteria-based self-healing concrete. *Cement and Concrete Composites* **33**(7):763–770.

Wiktor, V. and Jonkers, H.M. (2015). Field performance of bacteria-based repair system: pilot study in a parking garage. *Case Studies in Construction Materials* **2**:11–17.

Win, P.P., Watanabe, M. and Machida, A. (2004). Penetration profile of chloride ion in cracked reinforced concrete. *Cement and Concrete Research* **34**(7):1073–1079.

Worrell, E., Price, L., Martin, N., Hendriks, C. and Meida, L.O. (2001). Carbon dioxide emissions from the global cement industry. *Annual Review of Environment and Resources* **26**:303–329.

Wu, M., Johannesson, B. and Geiker, M. (2012). A review: Self-healing in cementitious materials and

engineered cementitious composite as a self-healing material. *Construction and Building Materials* **28**(1):571–583.

Xu, S., Liu, X., Tabaković, A. and Schlangen, E. (2019a). Investigation of the potential use of calcium alginate capsules for self-healing in porous asphalt concrete. *Materials* **12**(1):1–13.

Xu, S., Tabaković, A., Liu, X., Palin, D. and Schlangen, E. (2019b). Optimization of the calcium alginate capsules for self-healing asphalt. *Applied Sciences (Switzerland)* **9**(3):0–12.

Xue, C., Li, W., Li, J., Tam, V.W.Y. and Ye, G. (2019). A review study on encapsulation-based self-healing for cementitious materials. *Structural Concrete* **20**(1):198–212.

Yang, K.H., Jung, Y.B., Cho, M.S. and Tae, S.H. (2015). Effect of supplementary cementitious materials on reduction of CO_2 emissions from concrete. *Journal of Cleaner Production* 103:774–783.

Yang, P., Han, S., Su, J.F., Wang, Y.Y., Zhang, X.L., Han, N.X. and Li, W. (2018). Design of self-healing microcapsules containing bituminous rejuvenator with nano-$CaCO_3$/organic composite shell: Mechanical properties, thermal stability, and compactability. *Polymer Composites* **39**:E1441–E1451.

Yang, Y., Lepech, M.D., Yang, E.H. and Li, V.C. (2009). Autogenous healing of engineered cementitious composites under wet-dry cycles. *Cement and Concrete Research* **39**(5):382–390.

Yang, Y., Yang, E.H. and Li, V.C. (2011a). Autogenous healing of engineered cementitious composites at early age. *Cement and Concrete Research* **41**(2):176–183.

Yang, Z., Hollar, J., He, X. and Shi, X. (2011b). A self-healing cementitious composite using oil core/silica gel shell microcapsules. *Cement and Concrete Composites* **33**(4):506–512.

Yao, Y., Zhu, Y. and Yang, Y. (2012). Incorporation superabsorbent polymer (SAP) particles as controlling pre-existing flaws to improve the performance of engineered cementitious composites (ECC). *Construction and Building Materials* **28**(1):139–145.

Ye, H., Jin, N., Jin, X. and Fu, C. (2012). Model of chloride penetration into cracked concrete subject to drying-wetting cycles. *Construction and Building Materials* **36**:259–269.

Yildirim, G., Keskin, Ö.K., Keskin, S.B.I., Şahmaran, M. and Lachemi, M. (2015a). A review of intrinsic self-healing capability of engineered cementitious composites: Recovery of transport and mechanical properties. *Construction and Building Materials* **101**:10–21.

Yildirim, G., Sahmaran, M., Balcikanli, M., Ozbay, E. and Lachemi, M. (2015b). Influence of cracking and healing on the gas permeability of cementitious composites. *Construction and Building Materials* **85**:217–226.

Zhang, Z., Qian, S. and Ma, H. (2014). Investigating mechanical properties and self-healing behavior of micro-cracked ECC with different volume of fly ash. *Construction and Building Materials* **52**:17–23.

Zhu, Y., Yang, Y. and Yao, Y. (2012a). Use of slag to improve mechanical properties of engineered cementitious composites (ECCs) with high volumes of fly ash. *Construction and Building Materials* **36**:1076–1081.

Zhu, Y., Yang, Y. and Yao, Y. (2012b). Autogenous self-healing of engineered cementitious composites under freeze-thaw cycles. *Construction and Building Materials* **34**:522–530.